Characterization of Open Pool Fires and Study of Heat Transfer in Bodies Engulfed in Pool Fires

Submitted in partial fulfillment of the requirements

of the degree of

Doctor of Philosophy

by

Siddapureddy Sudheer

(Roll No. 08410006)

Supervisor

Prof. S.V. Prabhu

Department of Mechanical Engineering

INDIAN INSTITUTE OF TECHNOLOGY BOMBAY

(2013)

Dedicated to

The Grand Weaver of my life,

JESUS CHRIST

Approval Sheet

This dissertation entitled **Characterization of Open Pool Fires and Study of Heat Transfer in Bodies Engulfed in Pool Fires** by Mr. Siddapureddy Sudheer, Roll no. 08410006, is approved for the degree of Doctor of Philosophy.

Examiners

Prof. H.S. Mukunda

Prof. R.P. Vedula

Supervisor

Prof. S.V. Prabhu

Chairman

Prof. T.I. Eldho

Date: 23-07-2013

Place: Mumbai

Declaration

I declare that this written submission represents my ideas in my own words and where others' ideas or words have been included, I have adequately cited and referenced the original sources. I also declare that I have adhered to all principles of academic honesty and integrity and have not misrepresented or fabricated or falsified any idea/data/fact/source in my submission. I understand that any violation of the above will be cause for disciplinary action by the Institute and can also evoke penal action from the sources which have thus not been properly cited or from whom proper permission has not been taken when needed.

(Siddapureddy Sudheer)

Roll No: 08410006

Date: 23-07-2013

Place: Mumbai

Indian Institute of Technology-Bombay, India
Certificate of Course Work

This is to certify that Mr. Siddapureddy Sudheer was admitted to the candidacy of the Ph.D. degree on 01/01/2009, after successfully completing all the courses required for the Ph.D. programme. The details of the course work are given below:

SI No.	Course code	Course name	Credits
1	ME 415	Computational Fluid Dynamics and Heat Transfer	6.0
2	ME 412	CFD and HT Lab	6.0
3	HS 699	Communication and Presentation Skills	4.0
4	MES801	Seminar	4.0

Dated: Dy. Registrar (Academic)

I.I.T. Bombay

Abstract

The aim of the present study is to develop a simplified methodology of predicting the heat transfer to a body engulfed in pool fire. The body represents a thermal cask simulated as a stainless steel cylinder filled with insulation. To begin with, pool fires are studied without any body immersed in them. The fuels used for this study are diesel, gasoline and hexane. The pool diameters considered are in the range of 0.3 m to 1.0 m.

Some of the important properties are flame emissivity, radiative fraction, gas velocity, temperature and emissive power distributions. Flame emissivity along the height of the pool fire is measured using the Infrared thermography. Radiation fraction is measured using single-location and multi-location measurements. Gas velocity of the pool fires is measured using a bidirectional probe.

Subsequently, pool fires are studied with casks engulfed in them. In this study, the ratio of the projected area of the cask to the pool surface area is less than 14.4%. There is no significant change in the mass burning rate of the pool fire in spite of the presence of the cask. Thermocouples are welded inside the cask to measure the subsurface temperature. Inverse heat conduction methodology is applied to the measured subsurface temperature to estimate the heat flux to the cask.

The heat flux to the cask engulfed in a pool fire is also predicted using numerical simulations. Adiabatic surface temperature (AST) is measured for pool fires using plate thermometers. This measured AST along with the convective heat transfer coefficient is given as mixed boundary condition in the numerical simulations of the cask. A good conservative estimate is obtained from numerical simulations. The radiative heat transfer to the cask predominates the convective heat transfer due to the low gas velocities.

Adiabatic surface temperature for a given diesel pool fire is also computed using Fire dynamics simulator (FDS). Numerical simulations of the cask are carried out using this computed AST to obtain the heat flux to the cask. The maximum deviation of the heat flux computed is less than 10% as compared to experimental results. Thus, using AST computed from FDS along with a conduction model circumvents the need for pool fire experiments.

Table of Contents

List of Symbols

Variables

A	Surface area (m^2)
a	A constant in Eq. (3.14)
B	Blockage
b	A constant in Eq. (3.14)
C_p	Specific heat capacity (kJ/kg.K)
C_s	Smogorinsky constant
D	Pool diameter (m)
d	Diameter (mm)
D_α	Diffusion coefficient
D_e	Characteristic length (m)
E	Emissive power (kW/m^2)
f	Puffing frequency (Hz)
F, f	Configuration/view factor
$f(\varepsilon)$	A function of emissivity in Eq. (3.13)

f_b	External force (N)
f_h	Flame height (m)
f_n	Angle increment
f_t	Time step increment
G	Constant in Eq. (4.3)
h	Convective heat transfer coefficient (W/m^2.K)
h	Height (mm)
h_1	Distance between dV and dA along the axis of the pool(m)
I	Intensity
K	Calibration constant of bidirectional probe
k	Thermal conductivity (W/m.K)
l	Length of the cask (mm)
$\dot{m}'''_\alpha$	Bulk production rate of species α per unit volume (kg/m^3.s)
$\dot{m}'''_b$	Bulk mass source per unit volume (kg/m^3.s)
$\dot{m}'''_{b\alpha}$	Bulk production rate of species α by evaporating droplets/particles per unit volume (kg/m^3.s)
$\dot{m}''$	Mass loss rate per unit area (kg/m^2.s)
Nu	Nusselt number
OS	Object signal of the camera
p	Pressure (Pa)
Pr	Prandtl number
Q	Heat release rate (kW)
$\dot{q}''$	Heat flux (kW/m^2)
$\dot{q}'''_b$	Heat transferred to evaporating liquid droplet per unit volume (kW/m^3)
R	Non dimensional grid resolution

Re	Reynolds number
s	Distance between dV and dA (m)
T	Temperature (K)
t	Thickness of the cask (mm)
t	Time (s)
T_∞	Ambient temperature (K)
u, v, w	Velocity (m/s)
w	Width (mm)
W_α	Molecular weight of species α
x, y	Coordinate axis
Y_α	Mass fraction of species α
Y_i	Distance from the base of the pool to the center of i_{th} reference body (mm)
Z	Mixture fraction

Greek Symbols

α	Absorptivity
β	Mean beam length corrector
Δ	Kronecker delta
δ	Thickness of the plate thermometer (m)
δ_{ij}	Constant
ε	Dissipation rate
ε	Emissivity
η	Efficiency of combustion
η, ξ	Coordinate axis
ΔH_c	Effective heat of combustion (kJ/kg)
Δh_g	Total heat of vaporization or gasification (kJ/kg)

κ	Absorption extinction coefficient
λ	Wavelength (μm)
μ	Viscosity (kg/m.s)
ν	Kinematic viscosity (m^2/s)
ϕ, θ	Angles of inclination
ρ	Density of flue gases (kg/m^3)
τ	Transmissivity
τ_{ij}	Viscous stress tensor
$\upsilon_F, \upsilon_O, \upsilon_P$	Stoichiometric coefficients

Subscripts

1, 2	Surfaces 1, 2
abs	Absorption
avg	Average
cond	Conduction
conv	Convection
emi	Emitted
f	Flame
gas	Gas
i, *j*	Indices
inc	Incident
recv	Received
loss	Miscellaneous loss
net	Net
out	Outside the body
rad	Radiation

$rad - CV$	Radiation from a control volume
ref	Reflection
rr	Re-radiation
s	surface of the body body
$s300$	Heated body at 300 °C
$s400$	Heated body at 400 °C
$soot$	Soot
sto	Stored
t	Total
TC	Thermcouple

Acronyms

AST	Adiabatic surface temperature
CAFE	Container analysis fire environment
CFEES	Centre for fire, environment and explosive safety
CFL	Courant Friedrichs Lewy number
FDS	Fire dynamics simulator
FSD	Fire safety distance
IAEA	International atomic energy agency
IHCP	Inverse heat conduction problem
LES	Large eddy simulation model
PT	Plate thermometer
SODDIT	Sandia one-dimensional direct and inverse thermal
VN	Von Neumann number

List of Figures

List of Tables

CHAPTER 1

Introduction

1.1 Motivation

As man started using fire as fuel, safety has been at stake. On October 29, 2009 at 7:30 PM, a fire broke out at Indian Oil Corporation depot in Sitapura of Jaipur, Rajasthan. This incident killed 12 people, leaving over 300 injured. In about 6 minutes, fire spread from the leaking petrol tank to the other nearby fuel tanks with flames rising 30 m to 35 m height (Fig. 1.1). This huge fire wiped out nearly one lakh kiloliters of fuel that includes diesel, petrol and kerosene (Mukta, 2011). Liquid fuel fires represent potential hazards in many applications ranging from accidents during transportation to accidents at industrial plants.

Fig. 1.1 Fire explosion at oil depot Jaipur, Rajasthan
(Mail online, 1 November 2009)

In 1997, a cargo truck was hit by a car in a overpass of New York, releasing 8800 gallons of gasoline from the truck. The ensuing fire destroyed the cargo tank semitrailer, Eagle Premier sedan and the overpass with an estimated damage of $7 million. Fire accidents form an important part of all accidents which occur in the chemical industry and in the transport of hazardous materials: fire is involved in 41.4% of all these events, according to a historical analysis based on a survey of 6099 cases (Cuchi *et al.*, 1997). The same analysis shows that of the different types of fire (jet fire, flash fire, etc.); pool fire is the most frequent. This is in good agreement with the fact that liquids were involved in 53% of accidents.

The action of flames on process equipment can result in escape of hazardous substances and cause a much more serious accident. The situation becomes dangerous if the flames impinge on the surface of equipment, as in this case the heat flux is very high. Hence, these materials are packed in specially designed containers called transportation packages.

1.2 Transportation Packages

Transportation had become a part of human life since the man scattered all over the surface of the earth. The importance of radioactive material cannot be over emphasized as it finds it's usage in several fields throughout the globe, to name a few fields: engineering industry, agriculture and medicine. The radioactive material is generated in a location with sophisticated facilities. Then they are transported to desired locations (road, rail, air and sea). Several packages of radioactive materials are being transported yearly. Any accident during the transportation, makes the public vulnerable to danger. A radioactive material packaging is a container that is used to safely transport radioactive material from one location to another. The container alone is called as packaging and the packaging together with its contents is called as package.

There are four types of packaging that are being designed for specific purposes. They are explained below and are shown in Fig. 1.2 (Sandia, 2013):

1. **Expected Packaging** are designed to survive normal conditions of transportation. These packages are used for materials that are of low specific activity.

2. **Industrial Packaging** are designed to survive normal conditions of transport and are also equipped to withstand drop test. These are used for materials with very small amounts of radioactivity.

3. **Type A Packaging** are designed to survive normal transportation and minor accidents. These are used for radioactive materials that would not result in significant health effects if they were released.

Fig. 1.2 Different types of radioactive material packages (Sandia, 2013)

4. **Type B Packaging** are designed to survive severe accidents. These packages are used to transport radioactive materials in large quantities. These are usually made up of stainless steel 304L cylinders. The radioactive material is surrounding by several protecting layers. Type B packaging must require to pass through the standard requirements provided by any international agency.

1.3 Safety of Transportation Packages

In view of safety, these casks must be certified by any internationally accepted regulations. In 1957, International Atomic Energy Agency (IAEA) was established to provide safety regulations for the transport of radioactive materials. Since then, these standards have been updated periodically. These regulations basically state that each cask must meet certain requirement when it is subjected to a specified hypothetical accident conditions. Hypothetical accident thermal requirements stated in Para-728 of TS-R-1 (IAEA, 2005) that "*Exposure of a specimen for a period of 30 minutes to a thermal environment which provides a heat flux at least equivalent to that of a hydrocarbon fuel/air fire in sufficiently quiescent ambient conditions to give a minimum average flame emissivity coefficient of 0.9 and an average temperature of at least* $800\,^{\circ}C$*, fully engulfing the specimen, with a surface absorptivity coefficient of 0.8 or that value which the package may be demonstrated to possess if exposed to the fire specified.*"

Fig. 1.3 Large circular cylinder engulfed in a pool fire (Kramer *et al.*, 2003)

These regulations do not provide the specific information on how to generate these hypothetical conditions. Accidents fire scenarios can be classified as open pool fires. The fire is left to burn until there is availability of oxygen that aids the combustion. Simulating such an uncontrolled environment for a testing a cask is difficult, if not impossible. Studies have been made to model a furnace that would replicate pool fire conditions (Logenbaugh *et al.*, 1990). The transportation package of radioactive material is generally idealized as a circular cask. Kramer *et al.* (2003) measured the heat transfer to a massive cylindrical calorimeter engulfed in a circular pool fire (Fig. 1.3). In the pool fire tests, temperature distribution within the cask and the heat flux on to the cask are measured. The aim of these studies to prescribe the furnace conditions that replicate these measured parameters in a furnace. The challenge lies here is that for each pool fire size, there needs to have an effort to measure these parameters.

Majority of the transporting vehicles are run on diesel fuel and hence there is a need to understand the diesel pool fires and how they compare with other fuels. Though several pool fire experiments are reported in the past, there is no systematic study on the radiative parameters with pool sizes. Hence, the present work focuses on systematic study of various radiative parameters in different diesel pool sizes. This work is also aimed to reduce some of the rigorous computations to prescribe pool fire parameters for furnaces. These studies are in general and hence applied to any transportation package but not just radioactive transportation package.

1.4 Open Pool Fires

This section details the challenges in dealing with fire accidents. Most of the accidents involve burning of fuel in an open atmosphere. These types of fires are called open pool fires. Pool fires are classified into premixed and diffusion flames basing on the way the fuel and oxidizer are mixed (Mukunda, 2009).

- In a **premixed flame**, the fuel and oxidizer are mixed before reacting each other. The air-fuel ratio can be controlled by changing the fuel to oxidizer ratio. The reaction rate is slow compared to the rates of heat and species diffusion.

- In a **diffusion flame**, only fuel is supplied to the burner and the oxidizer is supplied from the ambient air. The mixing and combustion take place together. The reaction rate in diffusion flames is much faster than the rate of diffusion. The central fuel core and the outer reaction zone can be seen by looking at the colors associated with these regions. Soot appears yellow in color and acts as a source of radiation.

A pool fire may be defined as "*the turbulent diffusion fire burning above a horizontal pool of vaporizing hydrocarbon fuel where buoyancy is the controlling transport mechanism*". The fuel can be on the floor or on the roof (stagnation flow pattern). Oxidizer (air) diffuses into the reacting zone from surroundings. Pool fires are classified into two, basing on the quality of ventilation:

1. **Open pool fires** are well ventilated pool fires. These are also known as fuel controlled. There is plenty of oxidizer (air) available for burning and hence, these fires are controlled by fuel.

2. **Enclosure pool fires** are under ventilated open pool fires. The amount of oxidizer available is limited in the enclosure and hence, these fires are ventilation controlled. Though there is enough fuel to burn, but the lack of oxidizer makes incomplete combustion.

1.4.1 Pool Fire Mechanism

Flame attains high temperatures because of the chemical reactions between the fuel and the oxidizer. The flame above the pool surface radiates necessary heat to vaporize the fuel. The vaporized fuel transports into the flame by diffusion and also by natural convection. The vaporized fuel reacts with the oxidizer that is diffused into the flame from the surroundings. The unburnt carbon appears as soot and radiates energy to the surroundings. Figure 1.4 shows the schematic of pool fires indicating the transport mechanisms. To add the complexity of the pool fire, turbulence significantly affects the pool flames. Radiative properties like flame emissivity, optical thickness, soot volume fraction depend

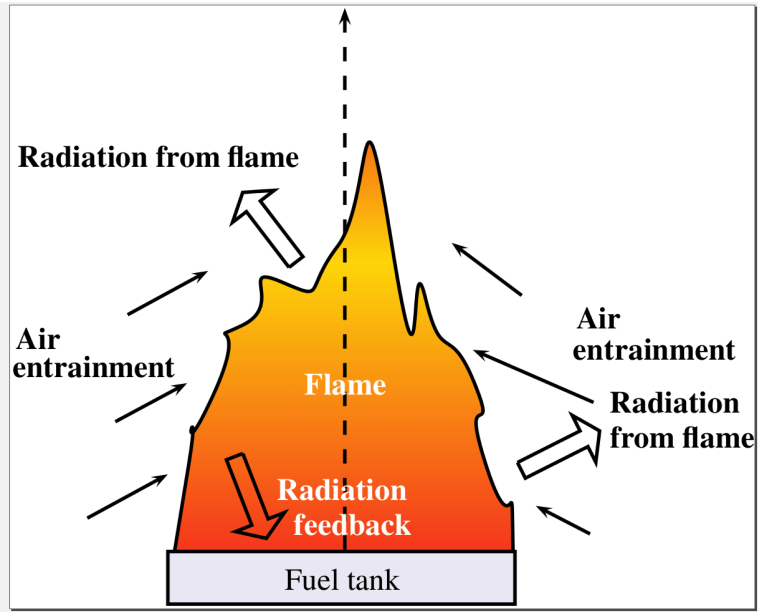

Fig. 1.4 Schematic of pool fires indicating the transport mechanisms

on temperature, wavelength and density. The distribution of these parameters is not uniform in the pool fire. Hence, it is almost impossible to obtain an analytical solution for all of these parameters. Table 1.1 shows the different mechanisms at various species in the open pool fire. The pool surface receives energy from the flame by convection and radiation. Babrauskas (1983) classified the flames basing on the dominant mode of heat transfer. Table 1.2 shows the classification of the pool fire. Optical thickness of a flame determines the opacity of the pool fire, *i.e.,* how much of the light can travel through the flame.

1.4.2 Radiation in Open Pool Fires

The combustion products like carbon dioxide and water vapor were found to be significant emitters and absorbers of radiant energy. The energy emitted from flames depends not only on the gaseous emission but also arises from the heated carbon particles (soot), formed within the flame (Siegel and Howell, 2002). The study of energy transfer through media that can absorb, emit and scatter radiation has received increased attention in the past five decades. In many engineering applications, the interaction of thermal radiation with radiatively participating medium must be accounted for.

The main challenges for the study of the radiation in participating media like sooty pool fire, as detailed by Siegel and Howell (2002), are:

- Firstly, with a participating medium present, absorption, emission, and scattering of energy occur not only at system boundaries, but at all locations within the medium. A complete solution of the energy exchange problem requires the knowledge of the

temperature, radiation intensity, and physical properties at every point within the medium. The mathematics describing the radiative situation is inherently complex.

- A second difficulty is that spectral effects are often much more pronounced in gases than for solid surfaces and a detailed spectrally dependent analysis may be required.
- In obtaining a solution to the equation of transfer, the constant of integration introduces the intensity at the origin of the radiation path being considered. Because the origin is usually at the boundary of the radiating medium, the radiation at the boundaries is coupled into the radiation distribution within the medium.

These challenges almost make it impossible to model the pool fire completely. The factors affecting thermal radiation in pool fire can be listed as: Absorption, emission, scattering, wavelength. An assumption is made for practical application and to reduce the complexity in calculations that diffusion flames radiate a fixed fraction of the released energy, usually assumed as 30%. Figure 1.5 shows the radiative fraction for different pool fires. Radiative

Table 1.1 Various mechanisms in open pool fires

Species	**Transport mechanism**	**Zone of interest**	**Relevant parameters**
Fuel	Diffusion Natural convection	Pool surface	Mass loss rate of fuel Chemical reaction Energy release Soot production
Air	Natural convection	Edge of the flame	Air entrainment
Products	Natural convection	Flame	Heat release
Energy	Diffusion Natural convection Radiation	Everywhere	Temperature distribution Radiative feed back Heat loss

Table 1.2 Classification of pool fires (Babrauskas, 1983)

SI No.	**Pool diameter D (m)**	**Burning mode**
1	< 0.05	Convective, laminar
2	0.05 to 0.2	Convective, turbulent
3	0.2 to 1.0	Radiative, optically thin
4	> 1.0	Radiative, optically thick

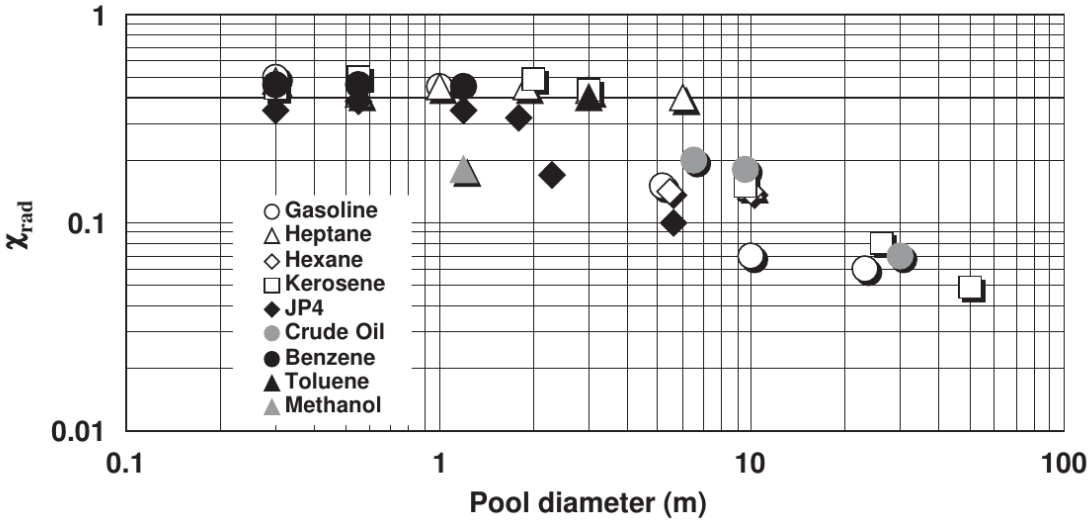

Fig. 1.5 Radiative fraction of different fuels (Tewarson, 2004)

fraction is denoted by χ_{rad} in Fig. 1.5. It is observed that the radiative fraction for most of the hydrocarbon fuels is 0.3 for diameters less than 1 m.

1.5 Heat Flux on to a Package

Heat flux on to the thermal package that is engulfed in a pool fire is very important. The direct measurement of heat flux on to the package engulfed in a pool fire is not possible. Hence, the heat flux is inferred from the measured subsurface temperature. In direct heat transfer problems, the temperature distributions are to be computed while the heat flux or temperature histories at the surface of a solid are known as functions of time. However, in inverse heat conduction problem (IHCP), the surface heat flux and temperature measurements must be determined from transient temperature measurements at one or more interior locations. In simple terms, boundary conditions are known for classical direct problems while in inverse problems, boundary conditions are to be estimated. A problem becomes inverse heat conduction problem, because of several reasons. One of the reasons may be the location of interest is inaccessible for conventional measuring instruments. One such example is the measurement of heat flux on to thermal package engulfed in fire. The package's surface is inaccessible for measurement because of the engulfing flame.

1.5.1 Inverse Heat Conduction Problem

The aim of IHCP codes is to determine unknowns such as thermal conditions, unknown thermo-physical properties from the temperature history and distribution of the sample. Consider a slab of thickness, L is exposed to an unknown heat flux, $\dot{q}''(t)$ as shown in Fig. 1.6. The transient temperature of the slab at a distance of x_1 is measured. The aim of

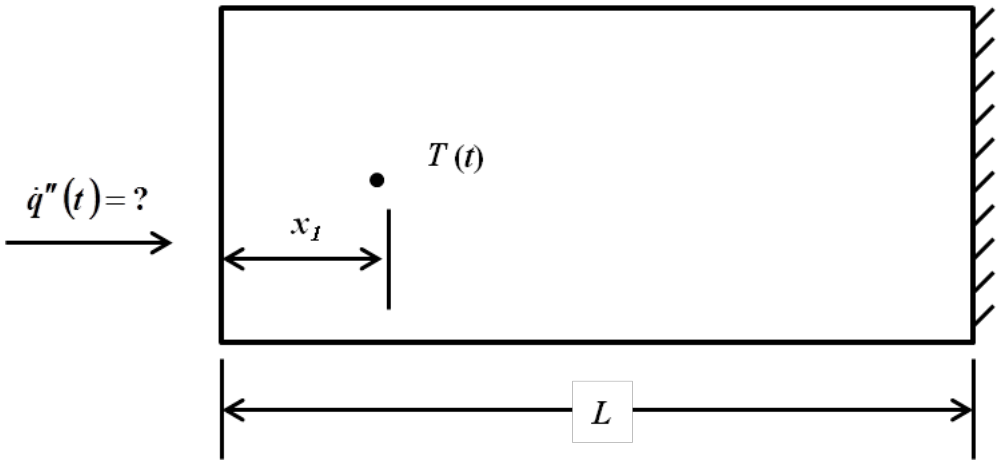

Fig. 1.6 Heat transfer to a slab from an unknown source

inverse heat conduction problem is the estimation $\dot{q}''(t)$ at each time step. This problem is difficult because of its extreme sensitivity to the measurement errors. Smaller time steps frequently introduces instabilities in the solution. Larger time steps would deviate from the actual solution. Hence, the code should be able to work even at some moderate small time steps while maintaining the stability. The problem becomes non-linear if the thermal properties are functions of temperature. Inverse heat codes like Sandia One-Dimensional Direct and Inverse Thermal (SODDIT), Inverse Heat Conduction Problem-1D (IHCP-1D), Container Analysis Fire Environment (CAFE) are generated to solve this kind of problems.

1.5.2 IHCP-1D

The code, IHCP-1D is developed by Beck Engineers in 2006 (Beck, 2012). This code is capable of solving IHCP that involves the estimation of surface heat flux history for an object by utilizing measured subsurface temperature history. IHCP-1D provides solution for planar, cylindrical and spherical geometries. The heat fluxes are estimated from the known temperature history. The temperature history at the known location is estimated using the estimated heat fluxes. The estimated heat fluxes are modified till the estimated temperatures reach the known temperature.

1.6 Numerical Codes to Solve Open Pool Fire

Numerical simulation of fire is becoming increasingly important due to the inherent difficulties associated with experiments, particularly for large size pool fires. The accuracy of the simulation is highly dependent on the inputs like grid size of the numerical grid, number of solid angles, domain size and model coefficients. Apart from this, accuracy also depends on the kind of model incorporated for tracking the species of combustion.

Three approaches were developed to simulate pool fires. All of these three approaches are three dimensional processes marching with time. They are briefly described below:

1. **Zone Model**: This approach is used for compartment fires. The compartment is divided into a finite number of isothermal volumes and surface area zones. Mass and energy balances are then performed for each zone. Simulation of detailed distribution of the species is not possible in this model.

2. **Reynolds-Averaged form of the Navier-Stokes Equations (RANS) Model**: These approaches are developed as a time-averaged approximation to the fluid dynamics conservation equations. The limitation of this approach is the averaging procedure.

3. **Large Eddy Simulation Model**: This model determines the burning rate of the pool fire and controls the spread of smoke and hot gases. Fire dynamics simulator uses LES for solving the pool fire.

Fire Dynamics Simulator (FDS) is a computational fluid dynamics (CFD) model of fire-driven fluid flow (McGrattan *et al.*, 2007). FDS can only handle Cartesian coordinate system. Hence, all the circular shapes in the simulations are generated by small cubes.

1.7 Fire Safety Distances

Fire accidents that carry huge loss with them have increased in the previous two decades than at any time in the history. Hence, there is a need for understanding the safety distances from different fires with different fuels. Knowledge of the radiative environment of potential fire scenarios is very helpful for planning firefighting strategies, that is, it allows a determination of whether or not a particular fire can be approached; if so, how closely it can be approached by personnel and equipment; and therefore what equipment and strategy should be employed in an emergency response plan (Croce and Mudan, 1997).

1.8 Objective of the Present Work

Lack of proper knowledge about the pool fires, motivated this work. The objectives of the present work are chosen to be:

Pool fires

To study the influence of pool diameter on mass burning rate, temperature, radiative fraction, heat flux and gas velocity. To study the variation of flame emissivity with the height of the flame of diesel as the fuel. To relax few simplistic assumptions that were

made in fire safety distance calculations. The model proposed in this study is easy to use and one can easily calculate the fire safety distance for a given fire scenario.

Thermal casks

To study the influence of blockage on the heat release rate of the pool fire. To quantify the convective and radiative heat transfer from fire to a thermal cask for different blockages.

Numerical simulations

To present a more simple numerical model for the simulation of thermal tests that avoids the coupling of conduction and fire codes and thereby reducing the computational costs and time. To study sensitivity analysis on various parameters in Fire Dynamics Simulator.

1.9 Organization of the Report

This report presents the study carried out to optimize the thermal tests for transportation packages. This report consists of seven chapters and is organized as follows:

Present chapter provides an overview of the open pool fires and the challenges in the fire research. The various parameters that involve in this area are briefly described.

Second chapter is a comprehensive literature review on open pool fires in view of thermal tests. This review explains the various instruments to measure some of key thermal properties and the problems encountered during the measurements. Conventional methods to measure and the proposed relations for some of the parameters are discussed.

Third chapter consists of the various experiments conducted to measure the radiative properties of pool fires. Influence of pool diameter on mass burning rate and flame emissivity are reported. The temperature and emissive power distributions of open pool fires are provided in this chapter.

Fourth chapter describes the methodology to measure the fire safety distances using infrared camera. The fire safety distances of different pool fires are provided.

Fifth chapter presents the study of a small lumped body engulfed in pool fires. Gas velocity for diesel pool fires of different sizes is presented. The details of partitioning the heat flux on to the body into convection and radiation components are presented.

Sixth chapter provides the experimental study conducted on casks engulfed in pool fires. A new methodology is introduced in this chapter to predict the temperature of a cask engulfed in a pool fire. The details of the numerical results and their comparison with the experimental results are provided in this chapter.

Seventh chapter describes the various sensitivity analysis for the FDS simulations of diesel pool fires. A comparison between the experimental and FDS results is provided.

Eighth chapter concludes this report with a summary of the outcome of this work. The future scope of the present work is presented.

CHAPTER 2

Literature Review

2.1 General

Radioactive materials comprise one of the United Nations classifications of dangerous goods and, as such, must be packaged to minimize the health risk to transport workers and members of the public and damages to public properties (Burgess and Fry, 1990). The packaging requirements are defined by the International Atomic Energy Agency (IAEA) in the Transport Regulations which are widely adopted as national regulations. All such regulations include tests to demonstrate that no undue hazard should result from a transport accident. The hazards addressed by the tests are release of radioactive contents, loss of shielding resulting in increased external radiation, and geometry or other changes leading to criticality and unacceptable radiation levels and/or heat output. Transport accidents can involve impact, fire and immersion in water in combinations deserving consideration of the sequential damage. For example, a crash is often followed by a fire.

Transportation packages containing radioactive materials have to undergo open pool fire tests before they are certified as per the transport regulations of International Atomic Energy Agency (IAEA). Transport regulations specified by IAEA, the requirements for thermal test as mentioned in Para-728 states (IAEA, 2005): "*Exposure of a specimen for a period of 30 minutes to a thermal environment which provides a heat flux at least equivalent to that of a hydrocarbon fuel/air fire in sufficiently quiescent ambient conditions to give a minimum average flame emissivity coefficient of 0.9 and an average temperature*

of at least 800 °C, fully engulfing the specimen, with a surface absorptivity coefficient of 0.8 or that value which the package may be demonstrated to possess if exposed to the fire specified."

These regulations do not provide any information regarding the pool size. This is an important parameter, as the flame temperature depends on the pool size. As the most transportation vehicles are diesel run, diesel is involved in the accidents of transportation packages. Knowledge of thermal properties of pool fires is very essential for optimizing thermal tests.

2.2 Thermal Properties of Pool Fire

Any kind of measurement in pool fires is difficult because of the high operating temperatures ($\sim$ 800 °C), low velocities ($\sim$ 2 m/s), multi-modes of heat transfer and active chemical reactions. Soot deteriorates the readings as they deposit on the measuring instruments. Hence, the conventional methodologies are not suitable in fire research. All instruments should be rugged enough to withstand high operating temperatures but accurate enough to capture the minute details. In the following sections, each thermal property is considered with the measuring techniques established in the literature.

2.2.1 Mass Burning Rate

Burning rate is defined as the mass of fuel consumed per unit area per unit time (Quintiere, 1998). The fuel can be solid, liquid or gas. In some cases, amount of the fuel consumed may be different to amount of fuel vaporization (mass loss rate). One such example is large structural fire, where structure vaporizes not necessarily interacting with the oxygen. In this work, these two distinctions are considered synonymous. The mass burning rate of the fuel, $\dot{m}''$ is usually expressed in gm/m^2.s or in kg/m^2.s. Mass burning rate can be measured using a weighing machine or it can be measured by tracking the rate at which the level of the fuel in the tank is decreasing. All the instrumentations are to be insulated properly due to the high temperatures involved. Figure 2.1 shows the mass burning rate of a gasoline pool fire as a function of time (Chatris *et al.*, 2001).

In order to burn a fuel, the fuel surface must be at least the flash point temperature. Once the ignition starts, the surface temperature increases to its boiling point. During this period (I), the fire spreads over the entire pool surface and then progressively increases in size. The duration identified as (I) in Fig. 2.1 is called a transitory period, which corresponds to the fire spread over the surface and the development of the fire. Fuel burns at a constant rate after the transitory period. The time period during which fuel burns at a constant rate is called stationary period, identified as (II) in Fig. 2.1. Pool fire is fully developed in (II). Region (III) shows the extinguishing of fire.

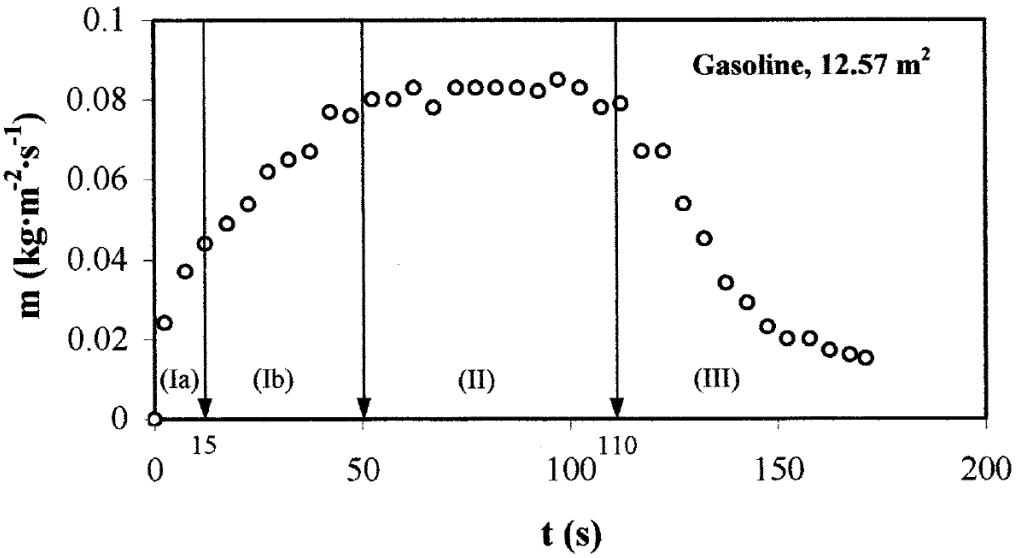

Fig. 2.1 Mass burning rate as a function of time (Chatris *et al.*, 2001)

Blinov and Khudyakov (1961) had collected and generalized the results of fifteen years of experimental and theoretical studies dealing on the physics of the combustion of liquids in tanks. They reported different pool fire parameters of different fuels like: the mass burning rates, shape and dimensions of the flame, pulsations, temperature, radiation and various combustion regimes. They observed that there is a rapid decrease in the mass burning rate with the increase in diameter ($D < 0.1$ m) and then increases with diameter and finally reaches a limit. There is no great variation in mass burning rates for D between 1 m and 22.9 m (Blinov and Khudyakov, 1961). They examined the temperature distribution in burning liquids. Parag and Raghavan (2009) studied the burning rates of ethanol and ethanol blended fuels. It is observed that the mass burning rate increases with the increase in the gasoline content and decreases with the increases in the diesel content. The high volatility of gasoline increases the mass burning rate.

Babrauskas (1983) observed that mass burning rate increased with the increase in diameter up to 2 m for gasoline pool fires. However, for diameters greater than 2 m, mass burning rates were observed to be reasonably constant (Fig. 2.2). Chatris *et al.* (2001) also measured mass burning rates for gasoline and diesel oil pool fires with diameters 1.5 m, 3 m and 4 m. For the two fuels studied, the increase in burning rate as a function of pool diameter approaches a constant burning rate for pool diameters about 3-4 m.

2.2.2 Heat Release Rate

Heat release rate describes the capacity of the pool fire quantitatively "How big is the fire?" This is so important that it has been described as the single most important variable

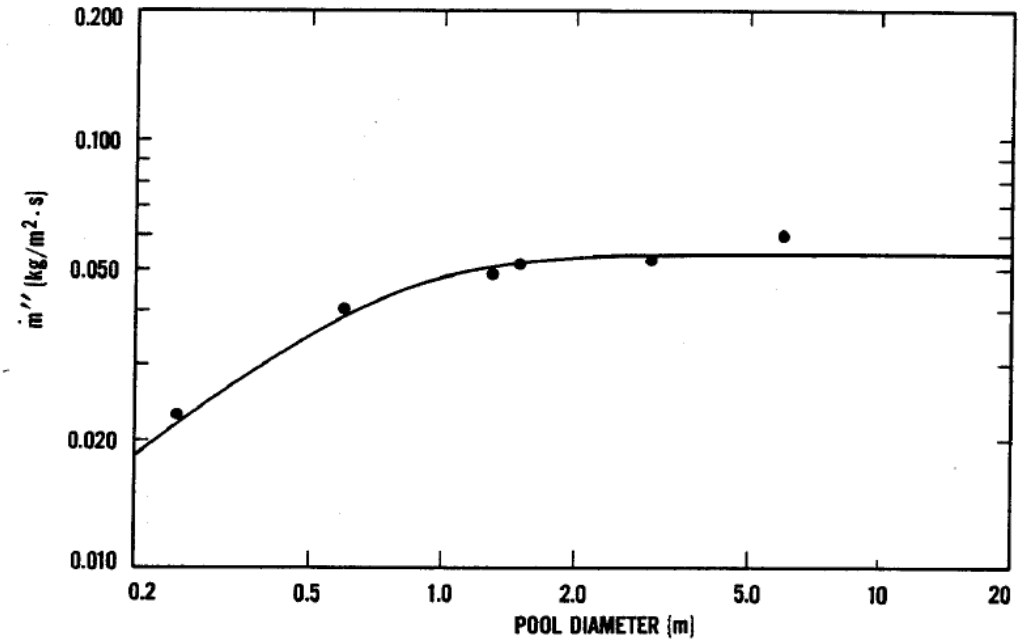

Fig. 2.2 Mass burning rate as a function of diameter for gasoline pool fires (Babrauskas, 1983)

in fire hazard (Babrauskas and Peacock, 1992). Heat release rate is defined as the rate at which the combustion reactions produce heat, usually expressed in kW. Mass burning rate and heat release rate are related by a constant as:

$$HRR = \dot{m}'' A \Delta H_c \tag{2.1}$$

where ΔH_c is the effective heat of combustion (kJ/kg) and A is the pool surface area. ΔH_c of a fuel can be determined by theory or by testing (SFPE, 2008).

2.2.3 Flame Emissivity

The radiation from the flame to the exterior is from hot combustion products that form the flame. The capacity of emission depends on the matter that is burnt and its thickness. Hence, the flame emissivity is the combination of the emissivity of the combustion products and species concentrations. If not impossible, it is difficult to calculate flame emissivity from the individual species, though there are tables to evaluate the emissivity of the combustion gases of a fire (Hottel and Sarofim, 1967). Several investigators have reported studies on pool fires. Rashbash *et al.* (1956) reported the results of a series of pool fire experiments conducted using different fuels with a pool diameter of 0.3 m. Alcohol, petrol, benzole and kerosene were studied in these experiments. They reported the measurements of temperature, mass burning rate, shape of the flame, volume of the flame, upward velocity of the flame and flame emissivity. In this study, the flame emissivities of

alcohol, petrol, kerosene and benzene were found to be 0.066, 0.36, 0.37 and 0.7 respectively. Later, Qian and Saito (1995) and Qian (1995) also measured the flame emissivities of hexane pool fires for four different diameters (0.05 m, 0.09 m, 0.14 m and 0.20 m) using an infrared camera. In this method, emissivity of the flame ε_f was determined by comparing the thermal image of a pool fire with target plates of known emissivities. Their results show that flame emissivity increases with the increase in pool diameter.

Agueda *et al.* (2006) determined the emissivity of the forest fire using the methodology proposed by Qian and Saito (1995). Heated sheets were used to simulate the radiation of blackbodies at different temperatures (300 °C and 400 °C) and the emissivity was computed by means of radiation signal captured by an infrared camera. Dupuy *et al.* (2007) also used a similar technique and studied the emissivity variation at different heights in a flame for a cylindrical forest fuel burner. This establishes that this method is employed extensively for the measurement of flame emissivity in fires burning above both in liquid and solid fuels. Cuchi *et al.* (2003) proposed a similar methodology for the determination of flame emissivity in hydrocarbon pool fires using an infrared camera. They conducted experiments on gasoline and diesel oil pool fires with diameters of 0.13 m, 0.18 m and 0.5 m. From this experimental data, they extrapolated the results to a pool diameter of 1 m and inferred that the emissivity would be close to one (less than one). However, this is in contrast with the conclusions made by Chatris *et al.* (2001) who stated that the data from small-scale fires cannot be extrapolated to larger-scale pool fires.

2.2.4 Flame Temperature

Temperature distribution of a pool fire is essential in estimating the heat flux on a given target. Over the decades, the temperature distribution of a pool fire has been measured using simple high temperature thermocouples without employing any corrections. McCaffrey (1979) measured the centerline temperature of natural gas flame produced by a porous refractory burner using k-type thermocouples without accounting for any errors. His data shows the independency of centerline temperature with different heat inputs. Observing his experimental data, flame was divided into three regions namely flame, intermittent and plume regions. Based on his experimental data, different correlations for centerline temperature distribution with height in each region are given.

Koseki (1989) reported the centerline temperature for heptane pool fire with different diameters and maximum temperature in the flame for gasoline, kerosene and heptane pool fires. In contrast to previous conclusions in McCaffrey (1979), Koseki found that the flame temperature increased with the increase in the diameter for heptane pool fires. Hayasaka *et al.* (1992) conducted pool fire experiments on 4.85 cm diameter cylinder with heptane, kerosene and methanol as test fuels. They measured the center line temperature

distribution using thermocouples and also using thermography method. From their observation, they argue that McCaffrey's model is valid only for low-sooting gas but not for liquid pool fires. Boundary values for liquid fuels depend on the fuel properties because of evaporation and decomposition regions in the bottom of flames or near the fuel surface (Hayasaka, 1996, Schneider and Kent, 1989).

Several authors have reported temperature measurements in fires using thermocouples (Schneider and Kent, 1989, Montes *et al.*, 2009). Thermocouple measurements are subjected to a thermal lag during fire growth, but the main problem is a steady-state error induced by radiant heat transfer at the thermocouple surface (Francis and Yau, 2004, Luo, 1997). For temperature measurement using a thermocouple, the radiation error of the measured temperature is the result of receiving/emitting radiation from/to the environment. Francis and Yau (2004) documented the sources of error and the effect of thermocouple diameter on temperature readings. By taking temperature measurements with different sizes of thermocouple beads and plotting the results against thermocouple diameter, the steady state error is minimized by extrapolation back to the abscissa. Silvani and Morandini (2008) used a simple procedure to correct the temperature values measured with the thermocouples.

2.2.5 Infrared Thermography in Fire Research

Infrared camera has been extensively used in fire research for different purposes. An infrared camera transforms the incident radiation into temperature readings. Some parameters like emissivity of the emitting body, atmospheric temperature between camera and object are to be necessarily introduced during post-processing the thermal images. Hayasaka *et al.* (1992) introduced a method to employ high-speed thermography to measure the radiative heat flux on a target from kerosene pool flames of 2.7 m square tank. Figure 2.3 shows the experimental arrangement for measuring radiation from pool fires. Figure 2.4 shows the thermography measurement from the pool fire. The infrared camera captures the temperature from an imaginary wall. Thermography gives the apparent temperature distribution of the flame. By assuming the flame emissivity to be unity, they converted the temperature distribution images from thermography to mean radiance distribution. From this mean radiance distribution, the irradiance on to a surface at some distance from the flame was estimated and verified with the radiometer measurements.

Recently, Chun *et al.* (2009) estimated the surface emissive power of different pool fires using thermography. Muñoz *et al.* (2007) estimated the emissive power of pool fires for different diameters using thermographic camera with gasoline and diesel as fuels. Pool sizes in their study ranged from 1.5 m to 6 m. They measured the fraction of contribution of luminous and non-luminous zones to the total emissive power of the flame. In all of

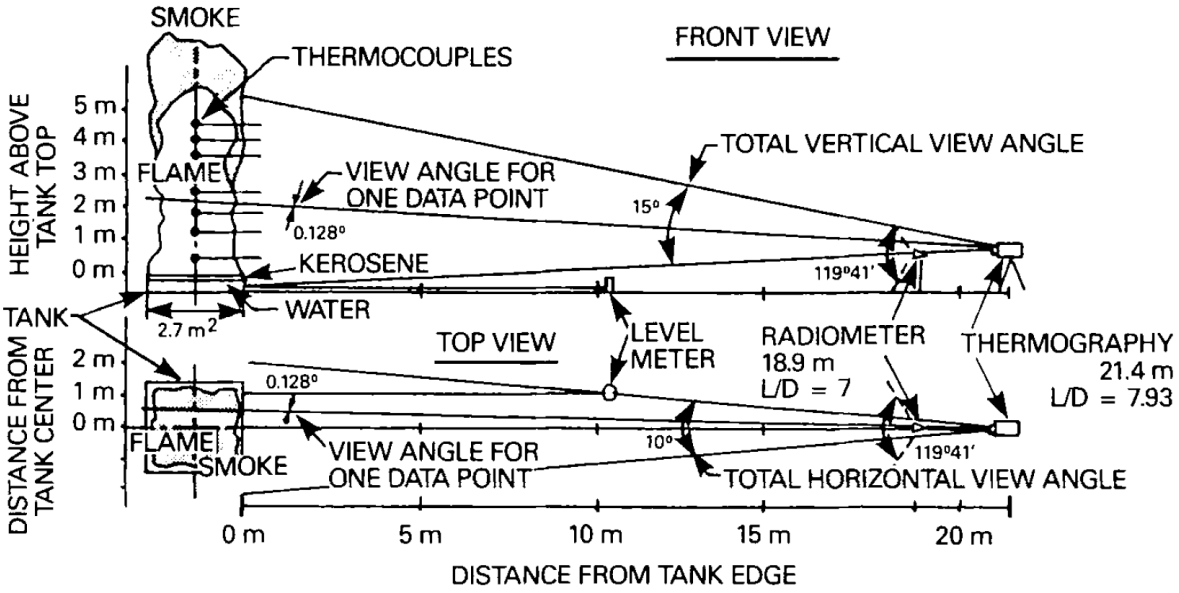

Fig. 2.3 Experimental arrangement for measuring radiation from 2.7 m^2 pool (Hayasaka *et al.*, 1992)

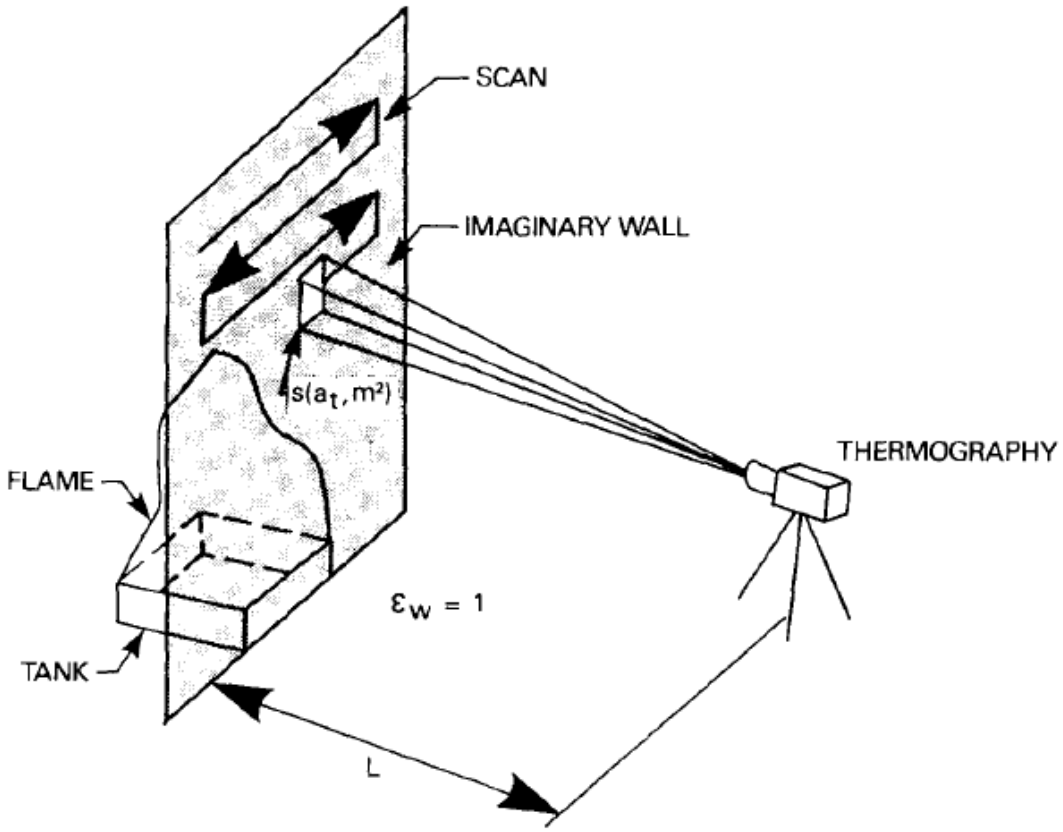

Fig. 2.4 Thermography measurement (Hayasaka *et al.*, 1992)

their studies, the flame emissivity was assumed to be unity. The value of radiative fraction was determined from the thermal flux measured with radiometer.

The flame emissivity cannot be assumed as unity for small scale pool fires (diameters less than 1 m). Since 1995, few methodologies are proposed to measure the flame emissivity using infrared camera (Qian and Saito, 1995, Cuchi *et al.*, 2003, Agueda *et al.*, 2006, Dupuy *et al.*, 2007). All these methodologies share a common principle- the transmissivity of a flame can be determined by measuring the radiation from a known source through the flame. Flame emissivity is computed from transmissivity by neglecting the reflectivity of the flame. Each thermal camera works in a range of wavelength. So, the emissivity obtained from thermal camera is an average flame emissivity over these wavelengths. Though the flame emissivity is a mixture of combustion products that radiate at different wave lengths, the results show that this average flame emissivity is able to capture the flame temperature and irradiance from the flame accurately. If the flame emissivity is measured, then the representative two-dimensional temperature and emissive power distributions of a pool fire can be computed from the infrared thermography.

Arakawa *et al.* (1993) and Qian *et al.* (1994) used the automated infrared thermography to measure the pyrolysis front along vertically oriented flat and corner walls. Through this infrared thermography technique, the limitations of conventional thermocouples can be avoided. They could capture the two-dimensional temporal temperature distribution of the wall fires. More recently, Akafuah *et al.* (2010) used infrared thermography for the visualization and characterization technique for liquid spray. Infrared thermography has been extensively used by various authors, as it can provide more information by overcoming the limitations of conventional thermocouples or video cameras.

2.2.6 Heat Flux

Heat flux is an important parameter in fire research. The heat fluxes in fire are very high and can go up to 100 kW/m^2 in a 1.4 MW pool fire. These high fluxes in a sooty environment makes it challenging to measure. Gardon introduced Gardon gauge to measure the intensity of thermal radiation in the range of 4.2 kW/m^2 to 4,190 kW/m^2 (Gardon, 1953). This gauge consists of a copper cylinder with a thin constantan foil, connected to a copper wire, on the top. This copper wire and the copper cylinder forms a differential thermocouple (Kuo and Kulkarni, 1991). Figure 2.5 shows a Gardon gauge. Two probes are provided for the circulation of cooling water. The working principle of the Gardon gauge is to infer the radiation heat flux by measuring the temperature difference between the center and the edge of a thin metal film (Cumber, 2011).

A similar instrument, Schmidt Boelter gauge is developed for measuring radiative incident heat flux. Schmidt Boelter gauge works under the principle of producing voltage

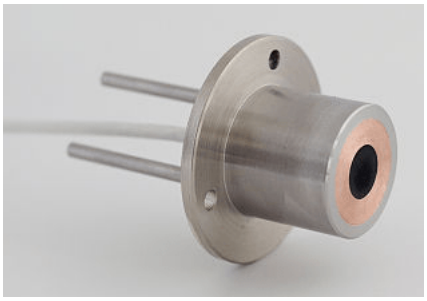

Fig. 2.5 Gardon gauge

corresponding to temperature difference across a thin thermal resistance layer situated at the sensing surface. Both the gauges operate without any external power source and needed water cooling to protect the sensors from high temperatures (Cumber, 2011). Lam and Weckman (2009) compared the steady state responses of four heat flux gauges: Schmidt Boelter, Gardon, Directional flame thermometer and hemispherical heat gauge under various radiative and convective heating conditions. These commercially available transducers have a fast thermal response and are subjected to rigorous and accurate calibration procedure (Silvani and Morandini, 2008). However, the main drawback with these sensors is the need of water supply to the sensor. In several applications like, inside combustion chamber, furnaces and pool fires the supply of water, if not impossible, very difficult due to the limitation of the access and high temperatures.

The measurement of heat flux at high temperature and in harsh environments remains a great challenge (Seo *et al.*, 2011). In 2007, Ingason and Wickström showed the capability of a plate thermometer in measuring the incident radiant heat flux as an alternative to water cooled heat flux sensors like Schmidt Boelter gage and Gardon gage (Ingason and Wickström, 2007). A plate thermometer consists of a 10 mm $\times$ 10 mm plate acting as a sensor. This newly introduced sensor is easy to fabricate and does not need water supply for cooling. However, plate thermometers are sensitive to convection and radiation in a similar way as a real specimen. Hence, the results using plate thermometer yield the effective exposure temperature when exposed to environment involving both convection and radiation but not the radiation alone (Bystrom *et al.*, 1988, Wickström *et al.*, 2011).

2.2.7 Radiative Fraction

Radiative fraction (χ_r) is defined as the ratio of the energy radiated to the surroundings to the idealized combustion heat release. Radiative fraction is given by:

$$\chi_r = \frac{Q_r}{HRR} \tag{2.2}$$

where Q_r (kW) is the radiative heat loss to the surroundings, HRR is the heat release rate of the fuel. Hamins *et al.* (1995) measured χ_r for pool fires of 4.6 cm, 7.1 cm and

30 cm diameter pool fires with different alcoholic and non-alcoholic fuels. χ_r is measured from the heat flux measured at a single location and at multiple locations. Comparing the two results, a new corrected correlation is proposed for computing radiative fraction from heat flux measured at a single location. They concluded that χ_r is a weak function of pool size. Buch *et al.* (1997) measured the steady-state mass burning rate and radiative flux profiles to the surroundings for different pool fire fuels (burning silicone fuels, methanol, ethanol, acetone, heptane and toluene) with diameters ranging from 0.1 m to 1.0 m. The radiative flux was measured in the radial (14 points) and a vertical (18 point) planes. Their experimental data shows that the radiative flux drops off quickly in the radial direction away from the fire. However, the radiative flux obtains maxima at some intermediate distance along the vertical axis. The lower radiative fluxes are associated with the slower burning fuels and the relatively non-luminous fire plumes. From the heat flux data, χ_r was computed.

For hydrocarbon pool fires, χ_r increases from approximately from 0.3 to 0.45 as the pool diameter increases from 0.1 m to 0.6 m. However, for alcohols χ_r remained nearly constant with the pool diameter. A reduction in χ_r for the slower burning fluids was also found. Hamins *et al.* (1995) made an attempt to correlate radiative fraction as a function of fuel mass flux for different pool diameters for several fuels. Yang *et al.* (1994) examined the effect of pool size on χ_r and combustion efficiency for heptane and kerosene fuels, with an assumption of cylindrical flame shape. They found that:

$$\begin{array}{rcll} \chi_r & \approx & \text{constant} & \text{for } 0.1 \text{ m} < D < 1 \text{ m} \\ & \propto & \frac{1}{\sqrt{D}} & \text{for } D > 1 \text{ m} \end{array} \tag{2.3}$$

By applying a simple energy balance on a pool fire (which is assumed cylindrical in shape), Moorhouse and Pritchard (1982) derived an equation for χ_r as follows:

$$\chi_r = \frac{E}{HRR}\left(1 + \frac{4f_h}{D}\right) \tag{2.4}$$

where E is the emissive power of the flame and f_h is the height of the flame.

2.2.8 Flame Velocity

The knowledge of the velocity of the flame is essential for computing the convective heat transfer coefficient. Blanchat *et al.* (2009) studied the contribution of radiation heat flux from a 2 m diameter methanol pool fire to a thermal cask ($B = 19\%$). Free-stream gas velocity was derived from Particle Image Velocimetry (PIV). The convective heat transfer was estimated using this velocity and the cask surface temperature. This study revealed that there was a significant contribution by the convection varying from 33% of the total heat transfer (37.5 kW/m^2) in thermal tests. Nakos and Keltner (1989) reported

a convective component of 10% to 20% of total for a blockage of 5.5%. Measurement of the velocity in pool fires is difficult because of its low value (∼1 m/s) and the high operating temperatures (∼ 800 °C).

Bi-directional probe is extensively used to measure the velocity of the flames (Logenbaugh *et al.*, 1990, McCaffrey and Heskestad, 1976a, Schneider and Kent, 1989). The Bi-directional probe was first introduced by Heskestad in 1974 and closely examined by McCaffrey and Heskestad in 1976 (McCaffrey and Heskestad, 1976a). The velocities are in the range of 4.8 m/s to 9.5 m/s for a JP-4 pool fire of size 9 m × 18 m (Schneider and Kent, 1989) and 3.4 m/s for a pool fire of 6 m × 6 m (Logenbaugh *et al.*, 1990). Hence, the bi-directional probe is adopted for measuring the flame velocity in the present study. These measurements are essential in estimating the convective heat transfer.

2.2.9 Puffing Frequency

Puffing frequency is defined as the periodic oscillatory motion close to the origin of pool fires (Cetegen and Ahmed, 1993). Rashbash *et al.* (1956) studied the flame characteristics for several hydrocarbon pool fires. Several authors reported the puffing frequency of different pool fires (Brötz *et al.*, 1983, Sibulkin and Hansen, 1975, Byram and Nelson, 1970, Portscht, 1975). Cetegen and Ahmed (1993) reported a summary of puffing frequencies as a function of burner diameter Fig. 2.6. Figure 2.6 shows that the solid fuels, liquid fuels and gaseous fuels show the same trend for different pool sizes.

2.3 Transportation Package

The transportation package is generally idealized as a circular cask filled with an insulating material. The major parameters considered for thermal testing of a cask are size of the pool fire, fuel used, size of the cask, location of the cask in the pool fire and orientation of the cask. Conventionally, heat flux on to this cask from the fire is predicted using codes like Sandia One-Dimensional Direct and Inverse Thermal (SODDIT), Inverse Heat Conduction Problem-1D (IHCP-1D). These codes work on the principle of inverse heat conduction problem. The subsurface temperature of the cask engulfed in a fire is used as input to these codes. Ali *et al.* (2004) carried out a transient thermal analysis of transportation packages to determine the temperature distribution under normal and accident conditions.

Solving inverse heat conduction problem (IHCP) is much more difficult than solving a direct heat transfer problem. Since 1960, there has been a lot of investigation in solving IHCP. Stolz (1960) is one of the pioneers in addressing the calculation of heat transfer rates during quenching of bodies of simple finite shapes. Beck (1962) developed basic concepts that permitted much smaller time steps than the Stolz method. Several authors

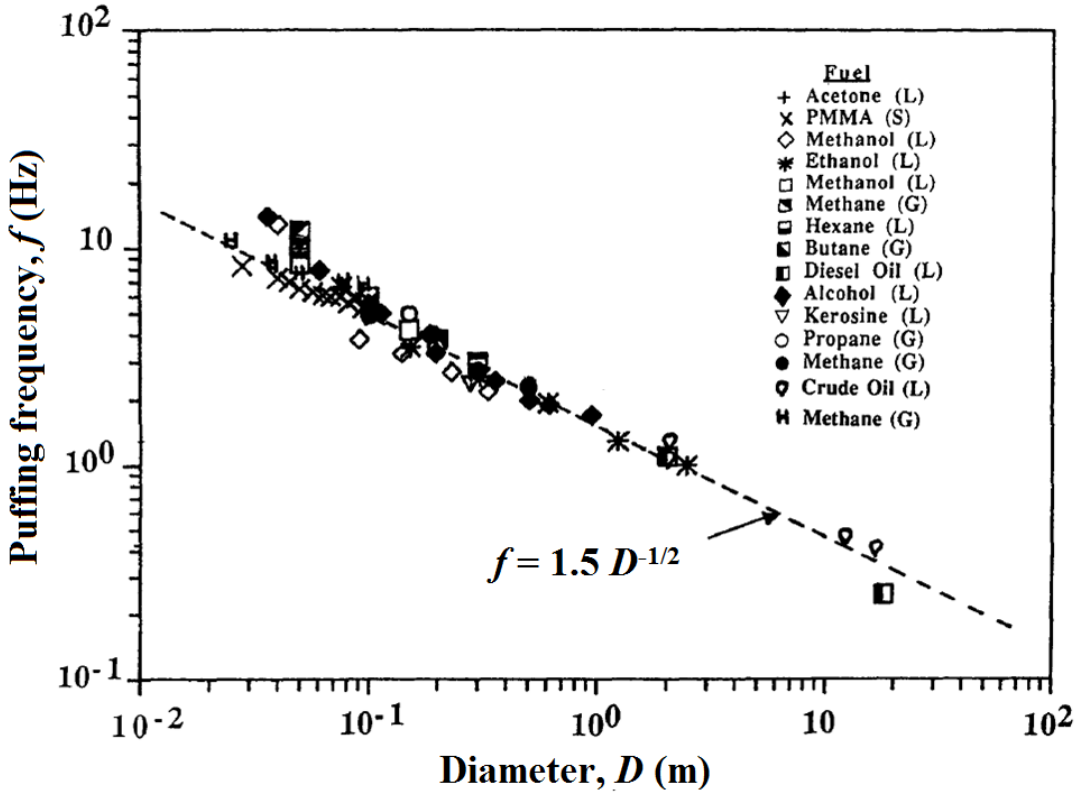

Fig. 2.6 Puffing frequency of pool fires as a function of burner diameter (Cetegen and Ahmed, 1993)

(Imber, 1973, Mulholland *et al.*, 1975, Williams and Curry, 1977) had worked on IHCP for different program applications.

Logenbaugh *et al.* (1990) studied the thermal response of a cask of diameter 0.46 m in a pool fire of 1.8 m diameter. The cask was oriented vertically in a pool fire. The test duration was 100 minutes. The temperatures of the cask and the insulating material were reported. Bainbridge and Keltner (1988) conducted thermal test in a 9.1 m × 18.3 m pool fueled with JP-4 aviation fuel. A thermal cask of 1.43 m in diameter and 6.4 m in length is simulated as the thermal transportation package. The cask was oriented horizontally in the pool fire. Kramer *et al.* (2003) estimated the heat transfer to a cask of 1.2 m diameter in a JP-8 pool fire of size 7.16 m diameter. The cask was oriented horizontally in the pool fire. The temperatures of the cask and the insulating material were reported. In these tests, the heat flux was predicted using an inverse heat conduction SODDIT code. The maximum estimated heat flux on to a cask is 90 kW/m^2 for a 1.8 m diameter pool fire, 70 kW/m^2 for a 6 m × 6 m pool fire, 130 kW/m^2 for a 9.1 m × 18.3 m pool and 150 kW/m^2 for a 7.16 m diameter pool fire. These experimental results demonstrate that the size of the pool fire has significant influence on the temperature and heat flux

distributions of the cask (Logenbaugh *et al.*, 1990, Koseki *et al.*, 1996, Bainbridge and Keltner, 1988, Kramer *et al.*, 2003).

2.3.1 Heat Flux to a Transportation Package

Several methods are proposed to determine the heat flux in thermal tests with different assumptions. Some of these assumptions are too simple to simulate the realistic fire scenario. These models are continuously developed over the decades. Tunc and Venart (1984) proposed a methodology to determine the incident radiation from an engulfing pool fire to a horizontal cylinder. The simplistic assumption of cylindrical flame shape was avoided. Flame shape was characterized by axi-symmetric flame contours obtained from actual photographs. Cuchi and Casal (1998) developed this methodology by taking into account the variation of flame temperature with time for a cask of blockage ratio (B) greater than 35%. Blockage ratio is defined as the ratio of the projected surface area of the cask in fire to the cross-sectional area of the pool. In both of these methodologies, the convective heat transfer from the flame to the cask was neglected. These models under-predicted the temperatures of the cask in comparison with the experimental results. This suggests that the convective heat transfer between the cask and the flame is important. Ojha *et al.* (2012) employed natural convection with a heat transfer coefficient of 15 W/m^2.K. However, the assumption of natural convection is not valid for a cask engulfed in pool fires without the quantification of Gr/Re^2. The general criterion for the free convection to be dominant over forced convection is $Gr/Re^2 > 1$ (Bejan, 1993). The assumption of neglecting convection can only be validated with a proper estimation of convective heat flux in thermal tests.

2.3.2 Influence of Package on Heat Release Rate

The presence of a cask in a pool fire may change the fire scenario and also the heat release rate. Ciro *et al.* (2006) conducted 0.3 m Jet-A pool fire with and without engulfing cooled and un-cooled cylindrical containers ($B = 14.5\%$). There was no significant change in the heat release rate. It shows that the thermal feedback to the pool from the fire and heat release in the flame were similar in all these cases. However, for a higher blockage ratio ($B = 28.3\%$), the heat release rate is found to be lower than that of without blockage (Cuchi *et al.*, 1996). Mass burning rates are measured for the range of blockages covered in the present study in order to reaffirm the influence of blockage on heat release rate of the pool fire.

One another difficulty, from measuring perspective in hydrocarbon pool fires, is heat flux measurement due to the high temperatures, the sooty and chemically reactive environment (Nakos, 2010). Most of the commercially available sensors like Schmidt Boelter gages are water-cooled and make them impractical to adapt for fire environment. Though these

sensors can work well with proper channeling of water, the deposition of the soot on the sensing element or on the transparent sapphire window deteriorate these measurements. Plate thermometer (PT) is reasonably effective in overcoming all these shortcomings of the commercially available heat flux sensors. The plate thermometer (PT) was developed by Wickström in 1980s for controlling fire resistance furnaces to get harmonized test results (Wickström, 1994). This was intended to measure the temperature. In 2007, Ingason and Wickström showed the capability of a plate thermometer in measuring the incident radiant heat flux as an alternative to water cooled heat flux sensors like Schmidt Boelter gage and Gardon gage (Ingason and Wickström, 2007). Unlike a finest thermocouple which is insensitive to radiation, the plate thermometers are sensitive to convection and radiation in a similar way as a real specimen. Hence, the results using plate thermometer yield the effective exposure temperature when exposed to environment involving both convection and radiation which is the case in pool fire.

Bystrom *et al.* (1988) studied the use of plate thermometers to estimate the fire developments. All these tests were performed under controlled conditions using cone calorimeter. Hence, one of the focus of the present study is to show the ability of using the plate thermometer measurements to represent a pool fire. Further details of the working principle of the plate thermometer and the concept of Adiabatic surface temperature (AST) are given in Wickström (1994), Bystrom *et al.* (1988) and Wickström *et al.* (2011).

Literature review suggests that there could be a great influence of pool size on the temperature and heat flux of a cask engulfed in pool fire. Also there is limited information in quantification of neglecting the convective heat transfer in simulating thermal tests for $B < 14\%$. Conventionally, the simulation of thermal tests involves the coupling of conduction code with fire modeling at every time step. The boundary condition obtained from the fire in a fire model at a given instant is given as an input to the conduction model to predict the surface temperature of the cask. This predicted surface temperature is given in the fire model and allow the flame temperature to change at the surface of cask. This approach needs the coupling of fire and conduction codes. These coupled codes are expensive in terms of time and cost.

2.4 Fire Safety Distances

Fire safety distance (FSD) is of greater interest in view of the safety of fire fighters, safe distance for building constructions and also in emergency evacuation of people. Fire safety distance is defined as that at which the thermal radiation flux is equal to some prescribed level. This level depends on what is to be conserved or protected (Atallah and Allan, 1971). The estimation of radiation flux from fires is very crucial and this provides a basis for establishing the safe zones for fire fighters and structures. Numerous methodologies,

from a very simplistic to complex models, are proposed in measuring the thermal radiation from fire and hence estimated the fire safety distances (Atallah and Allan, 1971, Zarate *et al.*, 2008, Billaud and Consalvi, 2001, Butler and Cohen, 1988, Hayasaka *et al.*, 1992). In some of these models, the assumptions made are: representation of flame by a single temperature, simple flame shape representation (like cylinder), radiation from non-visible zones of the fire plume is not accounted, assumptions made in computing the flame height etc.

Atallah and Allan (1971) studied each individual parameter that affects the calculation of safety distances. The parameters studied were: atmospheric transmissivity, view factor, flame height, burning rate of the pool fires, flame temperature, flame shape, soot cloud, luminous flame height, flame pulsation, geometric view factor and wind effects. The authors concluded that some of the assumptions made in computing the safety distances are too simplistic and they are to be refined to get accurate results.

Zarate *et al.* (2008) estimated the thermal radiation emitted by the flame front of a wildland fire using the solid flame model together with the view factor calculations. Some of the assumptions made in solid flame model are: the shape of the flame is either cuboid or cylindrical and the flame temperature is 1200 K. Billaud and Consalvi (2001) proposed a methodology based on the solid flame model and a Monte Carlo method for the estimation of the radiant heat flux and safety distances from wildland fires. The flame is considered as a black surface with a temperature of 1200 K resulting in a heat flux of 118 kW/m^2.

Several authors represented the complete flame by a single representative temperature. Butler and Cohen (1988) approximated the flame as a flat sheet of given height and width with a uniform temperature of 1200 K and a uniform emissivity of one. As the understanding of the radiation increased, few other authors introduced view factor in computing the fire safety distances. But, in most of the studies, the emissivity of the flame is taken as unity, which is not a reasonable assumption. The radiation from the flame is dependent on its emissivity. To add to the complexity, emissivity varies throughout the flame and also is dependent on the wavelength and diameter of the pool fire. Hayasaka *et al.* (1992) used infrared camera technique to measure the irradiance at a distance of 5 times the length of the pool. The pool size used in their study was 2.7 m^2.

2.5 Modeling of Open Pool Fires

Emori and Saito (1983) explained the scaling laws for pool and crib fires and correlated them to experiments. They successfully explained the procedure to interpret and scale the results of model experiments to full size fires. From the experimental results and the scaling laws, they concluded that the irradiance measured at corresponding points in pool fires does not depend on the size of the pan for pool fires, but it is proportional

to the square root of the length for crib fires. Saito and Emori (1980) showed that the scaling laws of a pool fire are applicable in the range of diameters 1.2 m and 30 m. Jolly and Saito (1992) explained different scale modeling schemes of pool and crib fires. The complexities and the limitation of the numerical models were discussed with suggestions for future work of developing numerical models based on experiments results.

2.6 Fire Dynamics Simulator (FDS)

Numerical simulation of fire is becoming increasingly important due to the inherent difficulties associated with experiments, particularly for large size pool fires. Fire dynamics simulator (FDS) is a CFD model of fire-driven fluid flow like pool fires. FDS solves numerically a form of the Navier-Stokes equations appropriate for low-speed flows (Mach number less than 0.3) with an emphasis on smoke and heat transport from fires (McGrattan *et al.*, 2007). Turbulence is treated with large eddy simulation model. It is observed that FDS can deliver accurate predictions for mean values of temperature and axial distributions (Hostikka *et al.*, 2003, Xin *et al.*, 2005, Wen *et al.*, 2007, Xin *et al.*, 2008, Lin *et al.*, 2010). However, these validations are limited to non-blended hydrocarbon pool fires.

Xin *et al.* (2005) studied the methane diffusion flame of 7.1 cm burner and helium plume of 7.3 cm burner size to check the applicability of mixture fraction based combustion model employed in FDS to the real life fire scenario. They observed that FDS can qualitatively capture instantaneous fire structures and quantitatively reproduce the averaged scalars and velocities. Hostikka *et al.* (2003) studied large eddy simulation of the methane pools of various diameters ranging from 0.1 m to 1.0 m. He observed that the radiative fraction obtained from different models is almost the same for methane burners. The model employed in FDS is able to provide correct qualitative dependence between the pool size and the burning rate and is capable of capturing the dynamical differences of flames ranging from the small burner to the scale close to the compartment fires.

Wen *et al.* (2007) carried out validation of 0.305 m methanol pool fire with finest grid resolution which provided closest results. They concluded that FDS can deliver accurate predictions for mean values of temperature and axial velocity distributions. Lin *et al.* (2010) investigated the grid dependence, solid angle dependence and radiation model on radiative characteristics of 0.1 m, 0.14 m, 0.3 m and 0.38 m heptane pool fire. They concluded that the variation among the results using gray band model, six band model and nine band model is merely 3% and also with gray band model the saving in computation time is more than 300% as shown in Fig. 2.7. Solid angle above 500 and the dimensionless grid size above 13 is fairly capable of mimicking the actual fire scenario. However, these observations are limited to small size pool fires.

Lin *et al.* (2010) studied the influence of solid angle and grid resolution on radiative heat flux distribution by changing the solid angle from 100 to 1000 and grid resolution from 6 cm to 1.72 cm as shown in Fig. 2.8. It was observed that at solid angles above 500, results are almost same. Hence, for further analysis solid angle of 500 was fixed. Figure 2.9 shows the influence of grid size on the radiative heat flux distribution for a heptane pool fire. Beyond a grid resolution of 2.55 cm, radiative heat flux prediction is independent of grid size. Hence, grid resolution of 1.93 cm was selected for the further analysis. However, these observations are limited to heptane pool fires but not to blended fuels like gasoline or diesel. Hence, there is a need for the sensitivity analysis for large size pool fire before actual validation.

Xin *et al.* (2008) simulated 1 m diameter methane pool using FDS. The influence of the domain size was studied by changing the domain size as shown in Fig. 2.10. The effect on the velocity predicted at various heights was observed and concluded that the influence of the domain size on FDS output is nil. FDS in conjunction with a mixture-fraction based combustion model can qualitatively and quantitatively reproduce the velocity field of a 1 m methane pool fire and puffing cycle period can be accurately calculated using FDS.

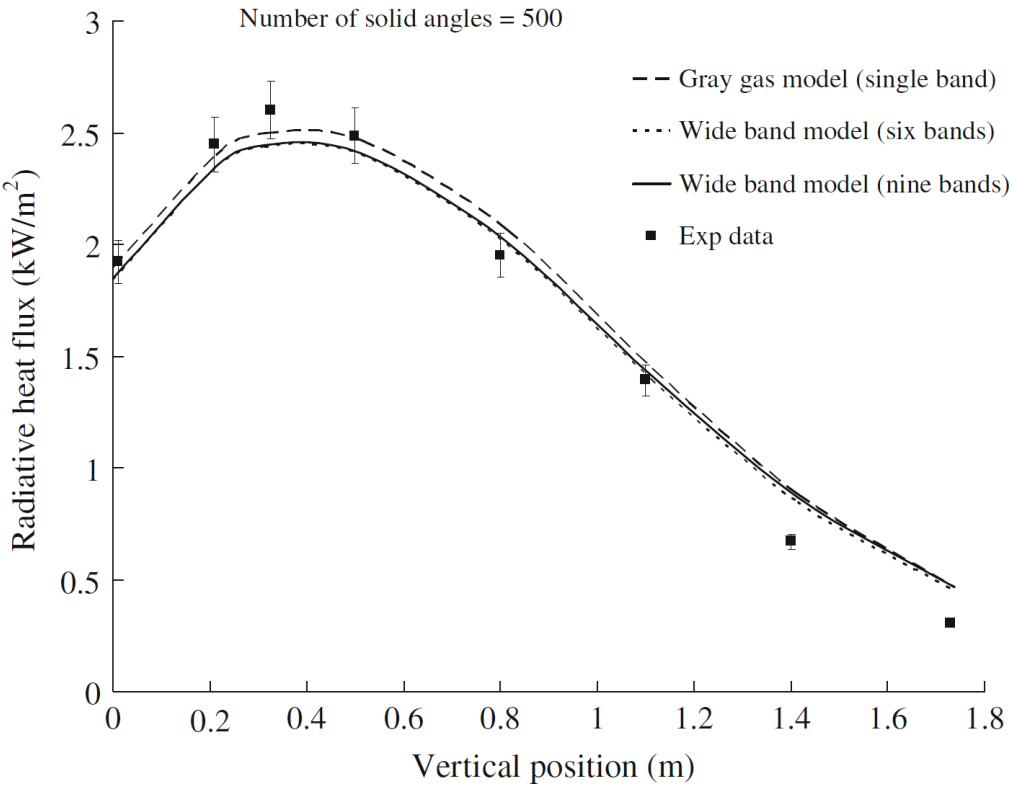

Fig. 2.7 Influence of different radiation models on predicted radiative heat flux (Lin *et al.*, 2010)

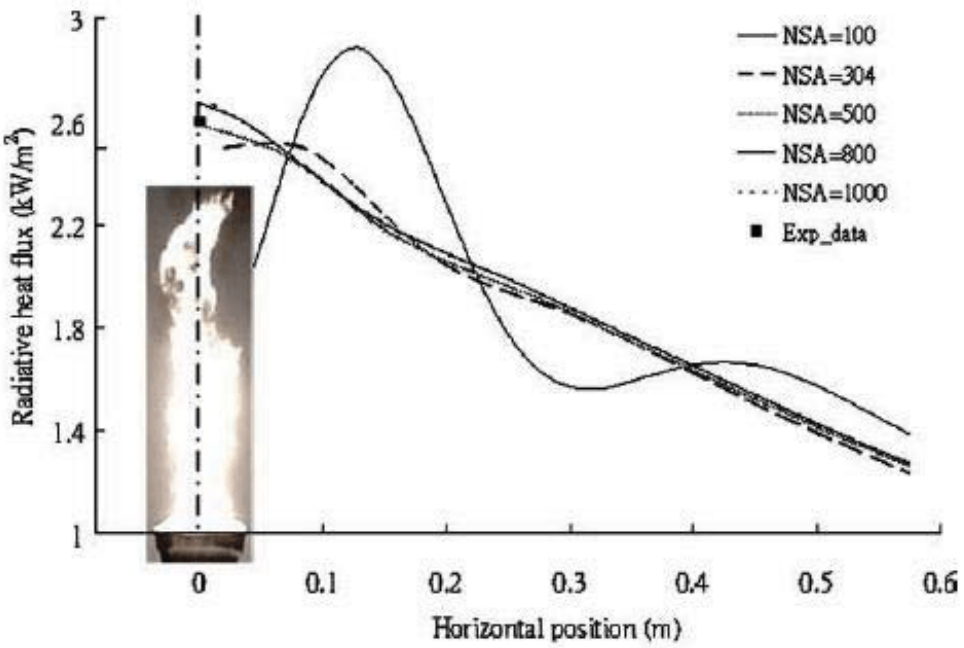

Fig. 2.8 Influence of number solid angles (NSA) on radiative heat flux for a 20 cm heptane pool fire (Lin *et al.*, 2010)

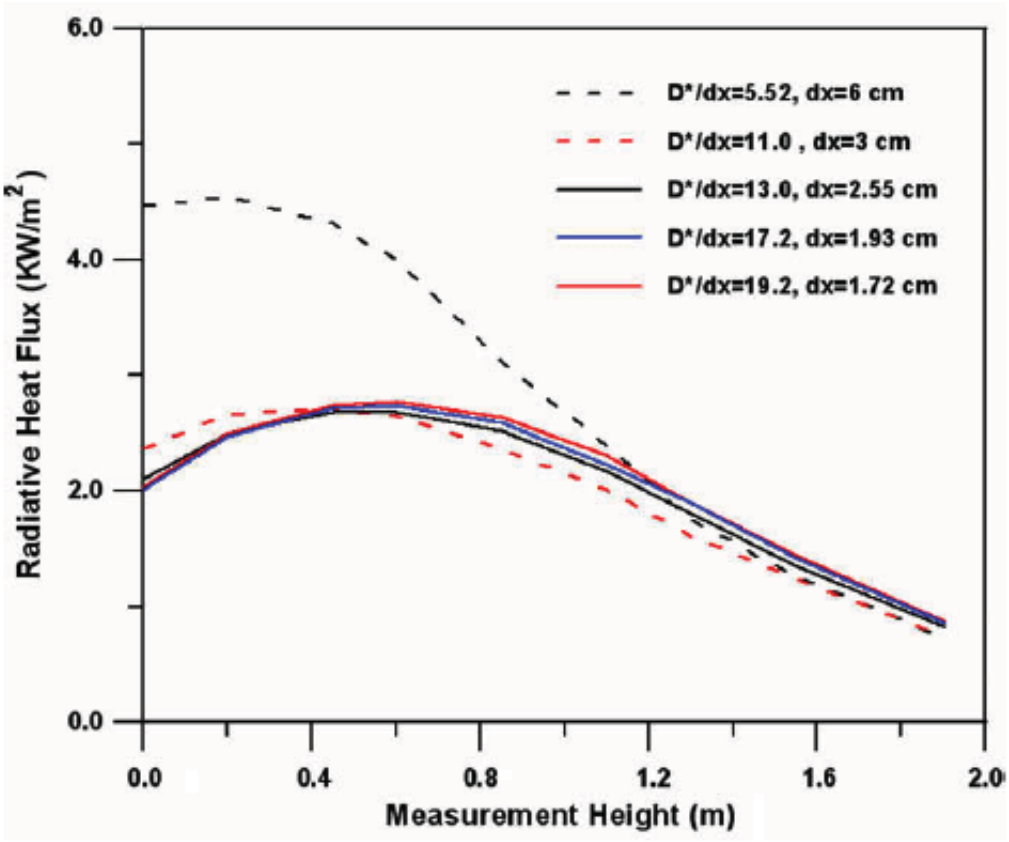

Fig. 2.9 Influence of grid size on radiative heat flux for a 20 cm heptane pool fire (Lin *et al.*, 2010)

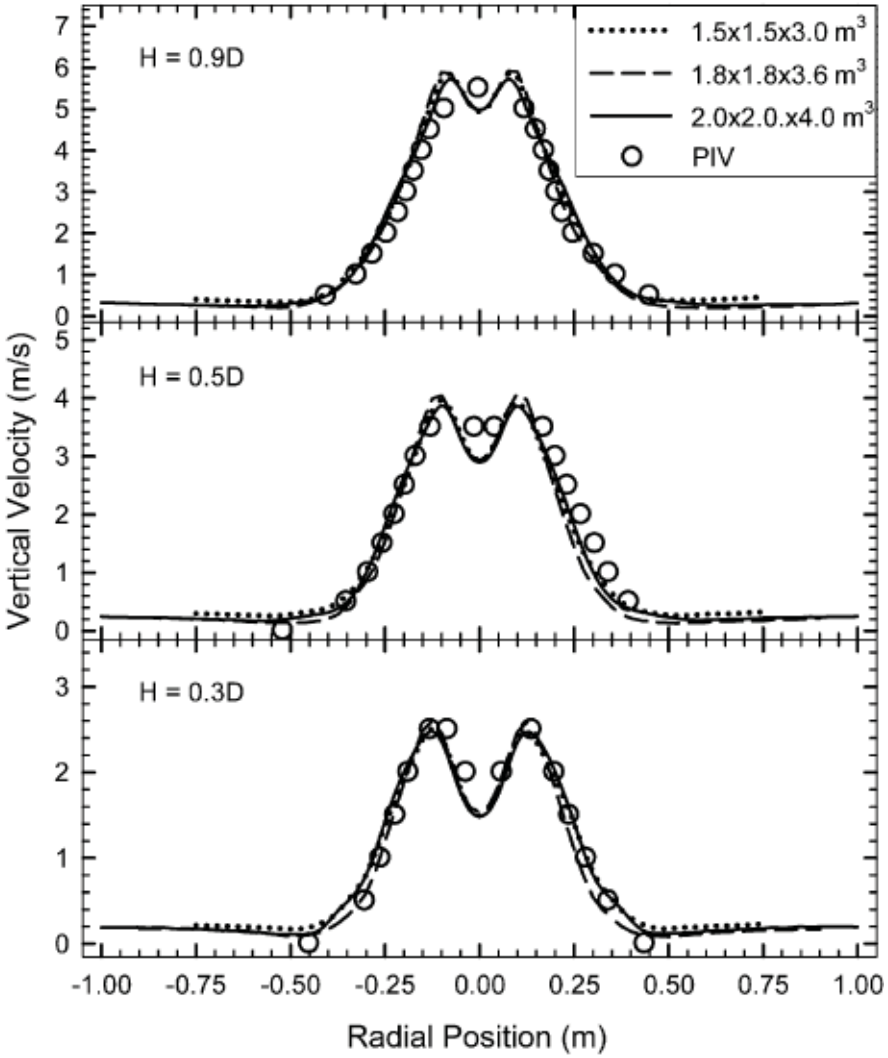

Fig. 2.10 Influence of domain size on radial velocities predicted at various heights (Xin *et al.*, 2005)

Ma and Quintiere (2003) reviewed the correlations for fire plumes to check the applicability of FDS in simulating fire plumes. FDS code has been tested for unconfined fires of different sizes, based on the dimensionless heat release rate in the range of 0.1 to 100. They found that the optimum resolution of a pool fire simulation is around 0.05. Prediction of flame heights was found to fit well with other flame height correlations. They concluded that reliable results can be produced for flame height with a simulation grid size approximately one twentieth of the fire characteristic length. Zhang *et al.* (2009) concluded the mean velocity and temperature near the floor and ceiling are over predicted by FDS because of the constant Smagorinsky constant.

2.7 Studies on Peroxides

Schälike *et al.* (2012) studied the flame heights of di-tert-butyl peroxide (DTBP) pool fires. It was observed that the non-dimensional flame height of DTBP pool fires was two times higher compared to hydrocarbon pool fires. Hence, the regular flame height correlations (like Thomas and Fay correlations) fail to predict flame heights in case of DTBP pool fires. Similar observations were found for tert-butyl peroxybenzoate (TBPB) and tert-butyl peroxy-2-ethylhexanoate (TBPEH) (Mishra, 2010). New Froude number correlations were proposed for DTBP (Schälike *et al.*, 2012). Mishra and Wehrstedt (2012) studied the mass burning rates of organic peroxides collected from various reports. Organic peroxides showed a different trend as opposed to hydrocarbon fuels like kerosene. The mass burning rate of hydrocarbon pool fires increases with the increase in diameter up to a certain diameter and subsequently it remains constant. The mass burning rate of organic peroxide pool fires are diameter independent and makes them turbulent right from the smallest possible diameter. Mishra and Wehrstedt (2011) carried out some CFD simulations to predict the flame temperatures. The temporal and spatial averaged thermograms were compared the CFD simulations. This comparison brings importance of the development of numerical methods for organic peroxide fuels. Chun *et al.* (2009) conducted experimental and numerical investigation on di-tert-butyl peroxide (DTBP) pool fires. Attempts are being made in simulating the organic peroxide pool fires using Ansys CFX code (Chun *et al.*, 2009, Mishra and Wehrstedt, 2011). These results show that the CFD simulations for organic peroxides are not capable enough to capture the flame physics as accurately as they do for hydrocarbon pool fires (Mishra and Wehrstedt, 2011).

2.8 Voids in the Literature

The following summary can be extracted from the above literature review:

1. Several experimental studies are reported on open pool fires. However, there is no comprehensive information on the influence of diameter on mass burning rate, flame temperature, flame emissivity and radiative fraction for diesel pool fires.

2. There could be a great influence of the pool size on the temperature and heat flux of a cask engulfed in a pool fire. Also, there is limited information in quantification of neglecting the convective heat transfer in simulating thermal tests for $B < 14.4\%$.

3. Conventionally, the simulation of thermal tests involves the coupling of conduction code with fire modeling at every time step. These coupled codes are expensive in terms of time and cost. Hence, there is a need to decouple the conduction problem with the modeling of fire.

4. Many simplistic assumptions are made in fire safety distance calculations. Hence, there is a need to relax some of these assumptions.

These voids in the literature motivated for further research in the area of pool fires and resulted in the present work.

2.9 Objectives of the Present Work

The objectives of the present work are chosen to be:

Pool fires

To study the influence of pool diameter on mass burning rate, temperature, radiative fraction, heat flux and gas velocity. To study the variation of flame emissivity with the height of the flame of diesel as the fuel. To relax few simplistic assumptions that were made in fire safety distance calculations. The model proposed in this study is easy to use and one can easily calculate the fire safety distance for a given fire scenario.

Thermal casks

To study the influence of blockage on the heat release rate of the pool fire. To quantify the convective and radiative heat transfer from fire to a thermal cask for different blockages.

Numerical simulations

To present a more simple numerical model for the simulation of thermal tests that avoids the coupling of conduction and fire codes and thereby reducing the computational costs and time. To study sensitivity analysis on various parameters in Fire Dynamics Simulator.

2.10 Experimental Parameters of the Present Work

In view the objective explained above, the present work considered following parameters:

Fuels - diesel, gasoline, hexane

Pool diameters - from 0.3 m to 1.0 m for circular pool fires and a 4 m $\times$ 4 m square diesel pool fire (0.057 MW to 41.4 MW)

Blockages ratio - in the range of $0.8 < B < 14.4\%$.

CHAPTER 3

Characterization of Open Pool Fires

3.1 Introduction

The study of parameters like mass burning rate, flame emissivity is essential in order to understand the amount of heat flux contributed from the flames. Literature review (Section 2.2) suggests that the limited information is available on the variation of flame emissivity with diameter (especially for pool diameters less than 1 m). This chapter describes various experiments conducted to measure the mass burning rate and the flame emissivity of pool fires in the following order:

- Measurement of mass burning rate
- Inference of flame emissivity from the measured mass burning rate
- Inferring of flame emissivity using infrared camera
- Measurement of flame emissivity at different locations along the axis of pool fire.

3.2 Experimental Setup

The experimental setup consists of mild steel circular pans of 2 mm thick and 15 cm height. To avoid boiling of water at high temperatures, the pans are filled only with the fuel, that is, without water at the base. Diesel, gasoline and hexane are considered as fuels. The properties of the fuel are given in Table 3.1. $\dot{m}''_{\infty}$ in Table 3.1 is the mass

burning rate of large pool fires, *i.e.,* for pool diameter greater than 4 m. Pool diameters of 0.3 m to 1.0 m are studied. Due to the high boiling point of diesel, a small amount of gasoline is used to ignite diesel pool fires. All the transient measurements are started before the ignition of the fuel.

Table 3.1 Physical properties of different pool fires

Fuel	Boiling point (°C) (SFPE, 2008)	Mass burning rate of large pool fire $\dot{m}''_{\infty}$ (gm/m^2.s)
Diesel	250	57.0 (Chatris *et al.*, 2001)
Gasoline	155	77.0 (Chatris *et al.*, 2001)
Hexane	68	97.5 (Koseki, 1989)

3.3 Mass Burning Rate

A 250 kg platform type weighing scale is used for measuring mass burning rate of the pool fires (Fig. 3.1). Mass burning rate increases with time and reaches steady state. After ignition, the fire spreads over the entire pool surface and then progressively increases in size and burns steadily. The former duration is called a transitory period, which corresponds to the fire spread over the surface and the development of the fire (Chatris *et al.*, 2001). The transitory period increases with the increase in the diameter because of the increase in the surface area. A similar trend is seen for all other fuels.

Fuel burns at a constant rate after the transitory period. The time period during which fuel burns at a constant rate is called stationary period (Chatris *et al.*, 2001). Pool fire, in this stationary period, is fully developed. Time averaged data of the mass burning rates per unit area (in gm/m^2.s) during this stationary period is given in Fig. 3.2. It is observed for all the fuels that as the diameter increases, the mass burning rate increases. Babrauskas (1983) reports a similar trend for LNG pool fires. Figure 3.2 shows the comparison of the measured mass burning rates with those reported in the literature.

Cong *et al.* (2009) reported a value of 19.9 gm/m^2.s for diesel pool fire of diameter 0.3 m. In this study it is found to be 17 gm/m^2.s. This difference in mass burning rate may be attributed to the environmental conditions. For gasoline pool fire of 0.3 m diameter, Babrauskas reported mass burning rate as 25 gm/m^2.s, and in this study it is found to be 29 gm/m^2.s. Mass burning rate for 0.64 cm is reported as 49 gm/m^2.s (Emori and Saito, 1983) which is in line with the experimental results shown in Fig. 3.2. Wind plays a vital role on the measurement of mass burning rate. Moreover, there can be a difference in the composition of diesel and gasoline.

Fig. 3.1 Experimental setup of 0.3 m pool fire with weighing machine

3.4 Methodology 1: Inference of Flame Emissivity from Mass Burning Rate

In sooty diffusion flames for most of the hydrocarbons, dominant part of radiation energy is emitted by the soot particles. Presence of soot also plays a dominant role in radiation energy transport. This can be appreciated by the following equation:

$$\varepsilon_t = \varepsilon_{soot} + \varepsilon_{gas} - \varepsilon_{soot}\varepsilon_{gas} \tag{3.1}$$

where ε_t is the total emissivity, ε_{soot} is the soot emissivity and ε_{gas} is the gas emissivity. The diffusion flames are luminous in nature. The luminosity is derived from the illumination provided by the soot. The gas emissivity is lower compared to soot emissivity. Hence, it is believed that the emissivity of the hydrocarbon pool fires is contributed by soot alone.

Figure 3.3 shows the energy balance at the fuel surface. Babrauskas (1983) applied conservation of energy for the liquid surface as given below:

$$\dot{m}''\Delta h_g = \dot{q}''_{rad} + \dot{q}''_{conv} + \dot{q}''_{rr} + \dot{q}''_{loss} \tag{3.2}$$

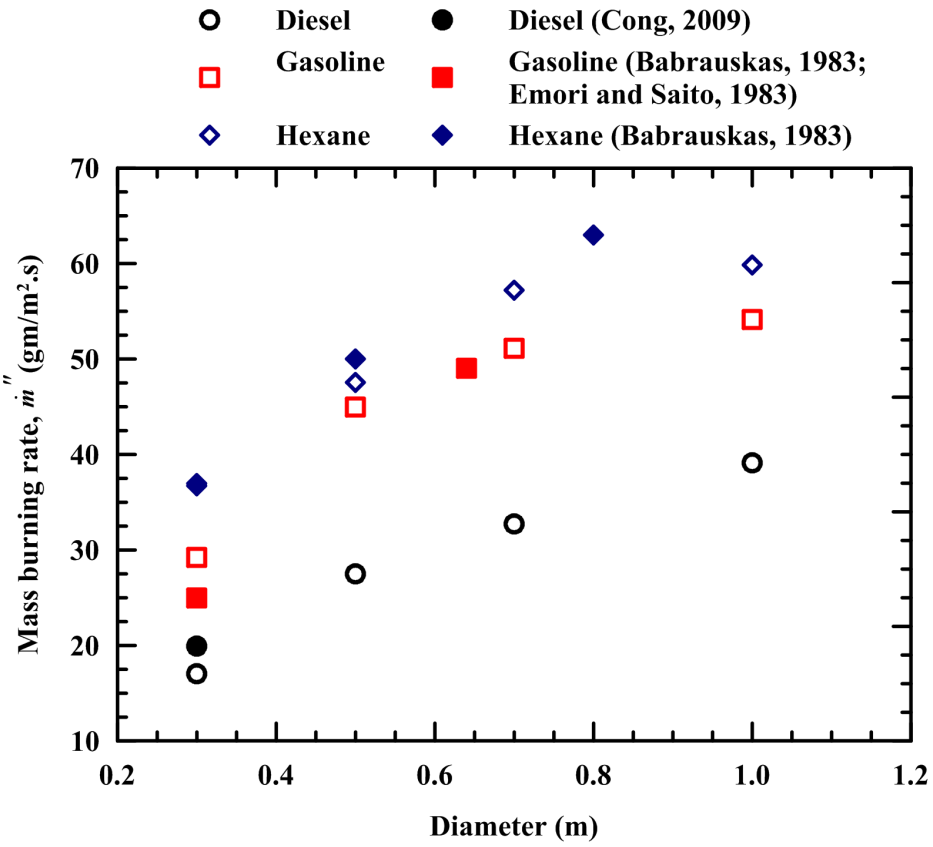

Fig. 3.2 Time averaged mass burning rate of different pool fires

where $\dot{m}''$ is the mass loss rate per unit area (assumed identical to the burning rate), Δh_g is the total heat of gasification, $\dot{q}''_{rad}$ is the radiant flux absorbed by the pool (given as $\sigma \varepsilon_f T_f^4$), $\dot{q}''_{conv}$ is the heat received by convection, $\dot{q}''_{rr}$ is the re-radiant heat loss due to the surface of the pool being at an elevated temperature and $\dot{q}''_{loss}$is the wall conduction losses and unsteady terms. Wall conduction losses ($\dot{q}''_{loss}$) and re-radiant heat losses ($\dot{q}''_{rr}$) are usually small and hence neglected. In the radiatively dominant pool fires (large diameters), heat received by convection ($\dot{q}''_{conv}$) can be neglected. Therefore, Eq. (3.2) takes the form:

$$\dot{m}'' = \frac{\dot{q}''_{rad}}{\Delta h_g} = \frac{\sigma \varepsilon_f T_f^4}{\Delta h_g} \tag{3.3}$$

Flame emissivity is given as (Modest, 2003),

$$\varepsilon_f = 1 - e^{-\kappa \beta D} \tag{3.4}$$

where κ is the absorption extinction coefficient and β is the mean bean length corrector. Substituting Eq. (3.4) in Eq. (3.3)

$$\dot{m}'' = \frac{\sigma \left(1 - e^{-\kappa \beta D}\right) T_f^4}{\Delta h_g} \tag{3.5}$$

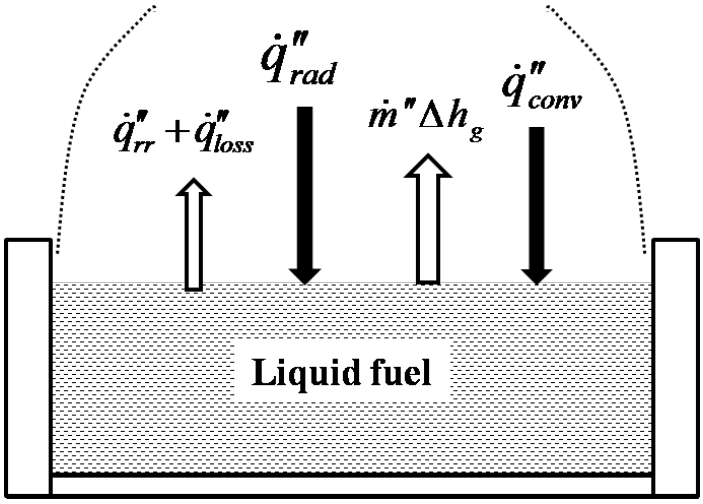

Fig. 3.3 Energy balance at the pool surface

Mass burning rate, $\dot{m}''$ becomes $\dot{m}''_\infty$ for larger diameter pool fires ($D \to \infty$). Also, as $D \to \infty$, the flame emissivity, $\varepsilon_f \to 1$, *i.e.*,

$$\dot{m}''_\infty = \frac{\sigma T_f^4}{\Delta h_g} \tag{3.6}$$

Combining Eqs. (3.4) to (3.6)

$$\varepsilon_f = 1 - e^{-\kappa\beta D} = \frac{\dot{m}''}{\dot{m}''_\infty} \tag{3.7}$$

The $\dot{m}''_\infty$ of different pool fires is given in Table 3.1. Flame emissivity of a given pool fire can be found from Eq. (3.7) provided the mass burning rate of the pool fire is known. Flame emissivity for different pool fires (0.3 m, 0.5 m, 0.7 m and 1.0 m diameters) is inferred from Fig. 3.2 by using Eq. (3.7). Figure 3.4 shows the flame emissivity of different pool fires.

3.5 Inference of Emissivity using Infrared (IR) Camera

Thermal cameras are used to measure the temperature of the flame. These instruments require the knowledge of emissivity of the object to generate the radiometric image of the object. Hence, flame emissivity can be measured along the camera view. Since, the flame emissivity inferred on the basis of mass burning rate (Section 3.4) is an average flame emissivity. Flame emissivity is measured along the height of the pool using IR camera. This variation would give the information on the limits of the emissivity variation in the flame. Two methodologies are employed to measure the flame emissivity using IR camera to cross-validate the results:

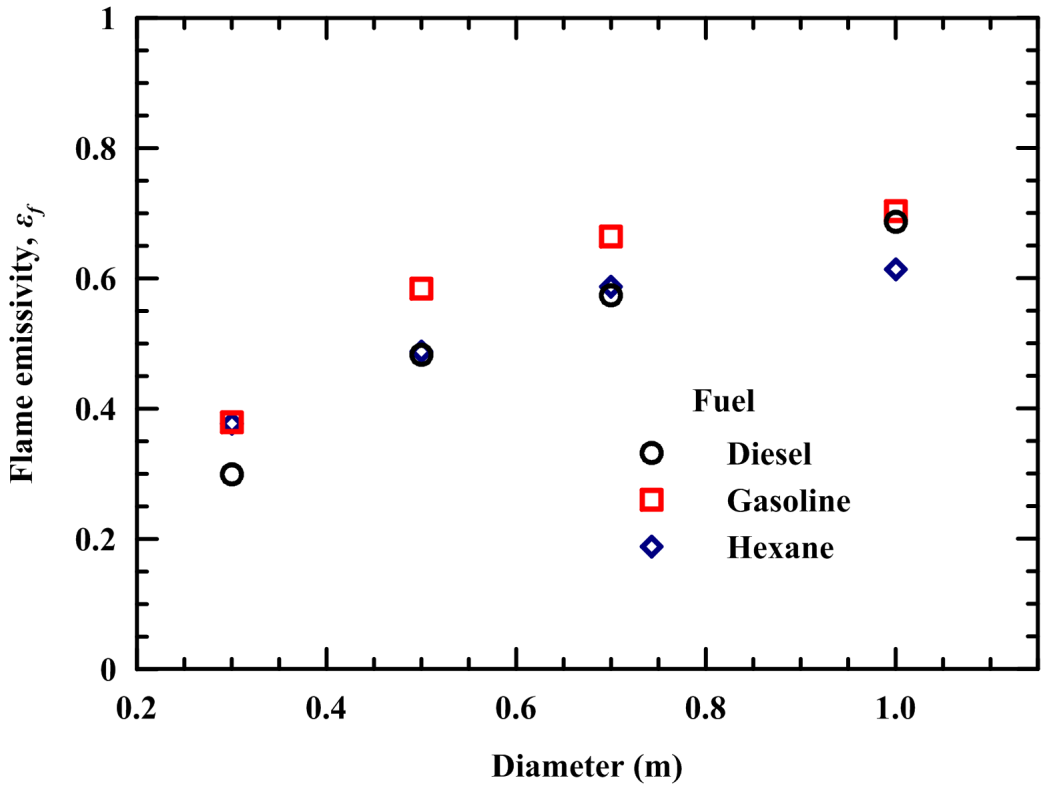

Fig. 3.4 Flame emissivity inferred from mass burning rate

1. **Methodology 2:** Emissivity measurement by observing the flame with reference to a reference body using an infrared camera

2. **Methodology 3:** Emissivity measurement by observing the flame with reference to an electrically heated reference body using infrared camera

Cuchi *et al.* (1997) and Qian and Saito (1995) reported the emissivity measurement method using methodology I and II respectively. Since the reflectivity of the flame is nearly equal to zero, flame emissivity is determined by measuring the flame transmissivity. This is done by taking a reference body of known emissivity as reference. These methodologies are discussed after a brief introduction about the infrared cameras used in this work.

3.5.1 Thermal Camera

The radiation from pool fires is mainly due to the emission from carbon dioxide and water vapor. The significant absorption (or emission) band(s) for carbon dioxide is ∼15 μm and for water vapor are 6 μm and 17 μm. However, the atmospheric window is in the range of 8 μm to 13 μm, *i.e.,* the atmosphere allows radiation in this spectrum only Modest (2003). Hence, the radiation captured from the flames is in the range of 8 μm to 13 μm. Thermoteknix make VisIR® Ti 200 and Flir Systems make ThermaCam™ SC640 cameras

are chosen for this work. The spectral range of IR cameras is 7.5 μm to 13 μm. Details of these cameras are given in Table 3.2. The infrared camera transforms the incident radiation into temperature readings, therefore a few parameters like emissivity of the emitting body, atmospheric temperature between camera and object must be introduced during post-processing of the thermal images. Typically 20 images are time-averaged for the analysis in this study.

Table 3.2 Specifications of uncooled thermal cameras

Camera	Pixel resolution	Field of view	Temperature range	Accuracy	fpm
VisIR Ti200 ThermaCam SC640	320 × 240	25 × 19	-20 °C to 1200 °C	±2% of range	12
	640 × 480	24 × 18	−20 °C to 1500 °C	±2% of range	3

3.6 Methodology 2: Inference of Flame Emissivity with Reference to a Body

The flame emissivity is determined by measuring the flame transmissivity by using a square shaped stainless steel plate which acts as a reference body. This reference body gets heated up because of the radiation from the flame which in turn emits thermal radiation. The surface of the plate is painted with Tempil make high temperature paint, pyromark series 2500. The emissivity of the pyromark painted surface is found to be between 0.85± 0.05 for a temperature range of 100 °C to 400 °C (Nakos, 2005, Logenbaugh *et al.*, 1990). The size of the reference body is so chosen that the outer limits of the body are always inside the pool as seen through the pool fire. Sizes of the stainless steel plates used for pools with different diameters are given in Table 3.3. Thermoteknix make VisIR Ti 200 camera is used in this methodology.

Thermal images are captured with the infrared camera placed in three different positions namely:

- position 1: Image of the reference body without flame at an angle less than 45 ° normal to the reference body
- position 2: Image of the reference body viewing through the flame (normal to reference body)
- position 3: Image of the flame alone (by removing the reference body from position 2)

Table 3.3 Dimensions of reference bodies used for pool fires with different diameters

SI no.	Pool diameter, D (m)	Dimensions of reference body (mm)		
		Width, w	Height, h	Thickness
1	0.10	25	25	0.5
2	0.13	25	25	0.5
3	0.20	50	50	1.0
4	0.30	50	50	1.0
5	0.34	50	50	1.0
6	0.50	100	100	1.0
7	0.70	100	100	1.0
8	1.00	120	120	1.0

Fig. 3.5 shows the schematic view of the three different positions of the infrared camera. Figure 3.6 shows the typical images taken by infrared camera from these three positions for a diesel pool fire of diameter 0.5 m.

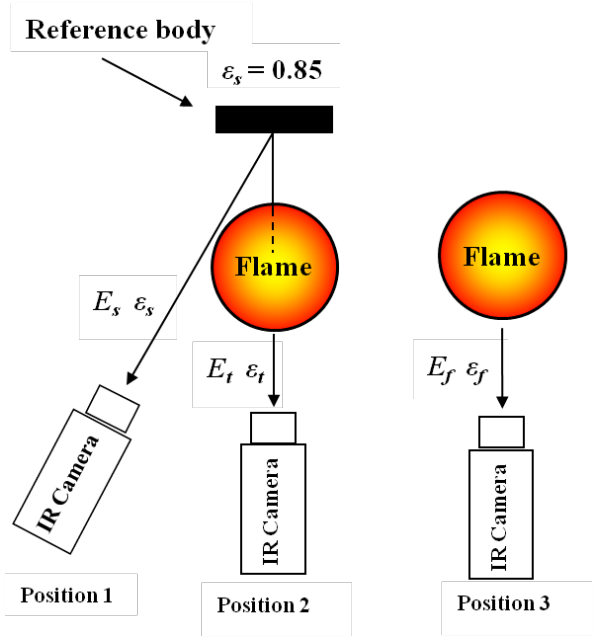

Fig. 3.5 Schematic of the three positions of infrared camera in methodology 2

3.6.1 Mathematical Modeling Involved in Methodology 2

The following analysis is aimed to determine the emissivity of the flame and is based on the theory outlined by Cuchi *et al.* (2003). The emissivity of the reference body is assumed to be 0.85 and it is assumed that the medium or ambient (air) is not participating in transferring heat in any fashion. By introducing reference body emissivity ($\varepsilon_s = 0.85$),

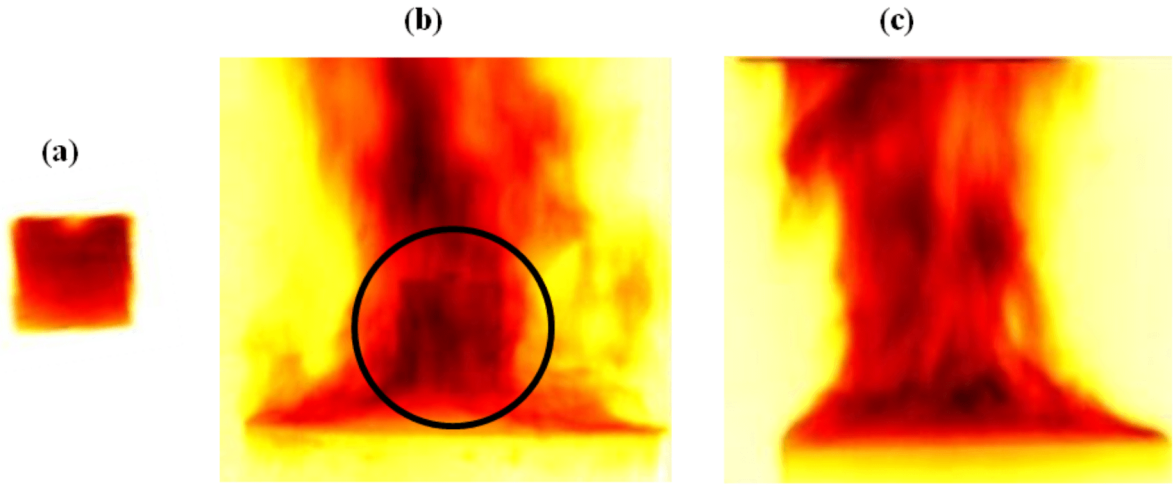

Fig. 3.6 Single set of thermal images of 0.5 m diesel pool fire: (a) magnified image taken from position 1, (b) image taken from position 2 (reference body is encircled), (c) image taken from position 3

temperature of the reference body (T_s) can be measured with infrared camera placed at position 1. According to Stefan-Boltzmann's law, the emissive power of radiation emitted by the reference body (E_s) can be written as

$$E_s = \sigma \varepsilon_s T_s^4 \tag{3.8}$$

Now, the infrared camera is shifted to position 2. The thermal radiation captured by infrared camera located in this position, is the radiation emitted by the flame (E_f) along with the radiation emitted by the reference body which has traveled (transmitted) through the flame, *i.e.*,

$$E_t = E_f + \tau_f E_s \tag{3.9}$$

where E_t is the intensity of the radiation captured by infrared camera from position 2. If the flame reflection is assumed to be zero, then

$$\tau_f = 1 - \varepsilon_f \tag{3.10}$$

The emissive power of radiation captured by the camera in position 2 can also be written as:

$$E_t = \sigma \varepsilon_t T_t^4 \tag{3.11}$$

where T_t is the flame temperature combined with reference body temperature and ε_t is the flame emissivity combined with reference body emissivity. The thermal radiation from the flame (E_f) alone is captured by infrared camera placed at position 3. This radiation is equal to:

$$E_f = \sigma \varepsilon_f T_f^4 \tag{3.12}$$

By introducing Eqs. (3.8) and (3.10) to (3.12) into Eq. (3.9), a function that depends on emissivities is obtained as:

$$f(\varepsilon) = \varepsilon_f T_f^4 + (1 - \varepsilon_f)\,\varepsilon_s T_s^4 - \varepsilon_t T_t^4 \tag{3.13}$$

In Eq. (3.13), ε_s and T_s are known. Hence, the resolution of Eq. (3.13) requires the knowledge of two parameters: ε_f and ε_t, while the other two unknowns, T_f and T_t depend on the emissivities ε_f and ε_t respectively. To find this dependency, an analysis of the thermographic images is carried out by changing the emissivities ε_f and ε_t. The function that best fits the dependency of the temperature on emissivity which must be a characteristic function of the infrared camera is taken as:

$$T = a\varepsilon^b \tag{3.14}$$

where a and b are two constants. Fig. 3.7 shows these dependencies for a diesel oil pool fire of diameter 0.5 m. The best fit exponential relations for these dependencies are also shown. Introducing Eq. (3.14) into Eq. (3.13):

$$f(\varepsilon) = \varepsilon_f \left(a_f \varepsilon_f^{b_f}\right)^4 + (1 - \varepsilon_f)\,\varepsilon_s T_s^4 - \varepsilon_t \left(a_t \varepsilon_t^{b_t}\right)^4 \tag{3.15}$$

There are two unknowns in the Eq. (3.15) namely ε_f and ε_t. Flame emissivity (ε_f) can

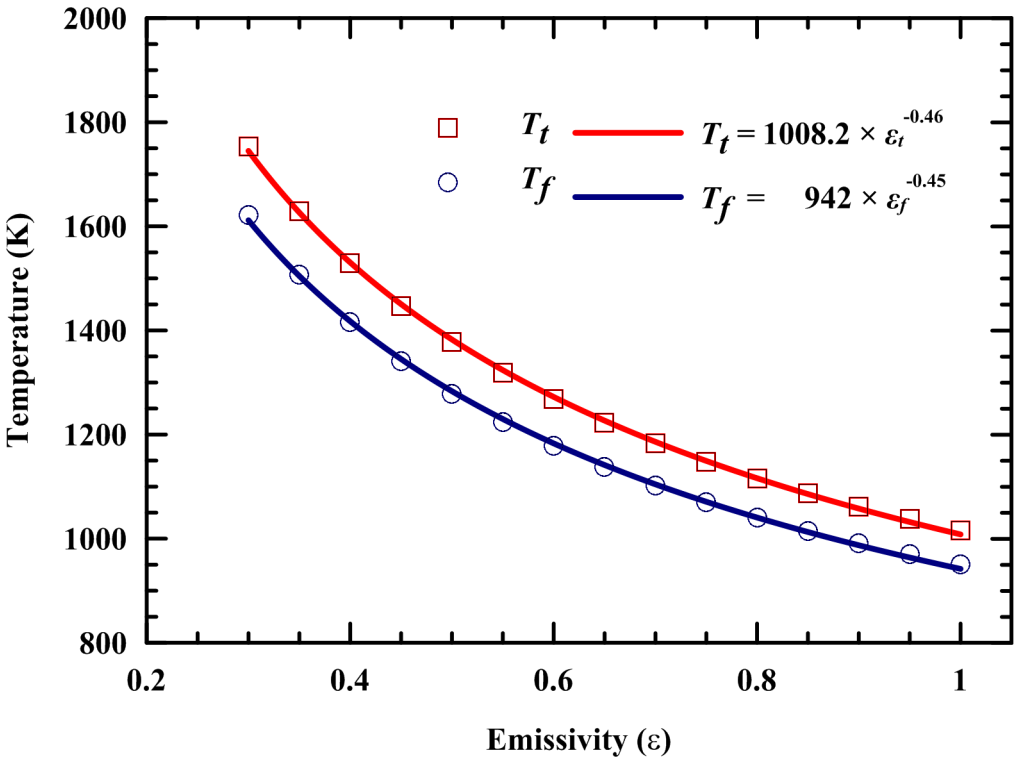

Fig. 3.7 Dependency of temperature on emissivity for diesel pool fire of 0.5 m diameter

be determined by choosing a suitable value of ε_t with proper reasoning. The following considerations are taken into account while choosing the value of ε_t (Cuchi *et al.*, 1997):

- It is logical to assume that the flame emissivity will always be lower than the reference body emissivity at least for the cases studied
- The emissivity at position 2, ε_t, must be greater than emissivity of flame and the emissivity of reference body seen through the flame (if not the case, then $\varepsilon_t = \varepsilon_f$)

Fig. 3.8 shows the variation of $f(\varepsilon)$ for a diesel pool fire with a diameter of 0.5 m. It is observed that these conditions are met for ε_t greater than 0.80 and less than 0.95. It is assumed that the combined emissivity (ε_t) as 0.85. This results in a flame emissivity (ε_f) of 0.63 for the set of data shown in Fig. 3.8. Sensitivity of flame emissivity (ε_f) for ε_t varying from 0.8 to 0.95 is detailed in Section 3.11.

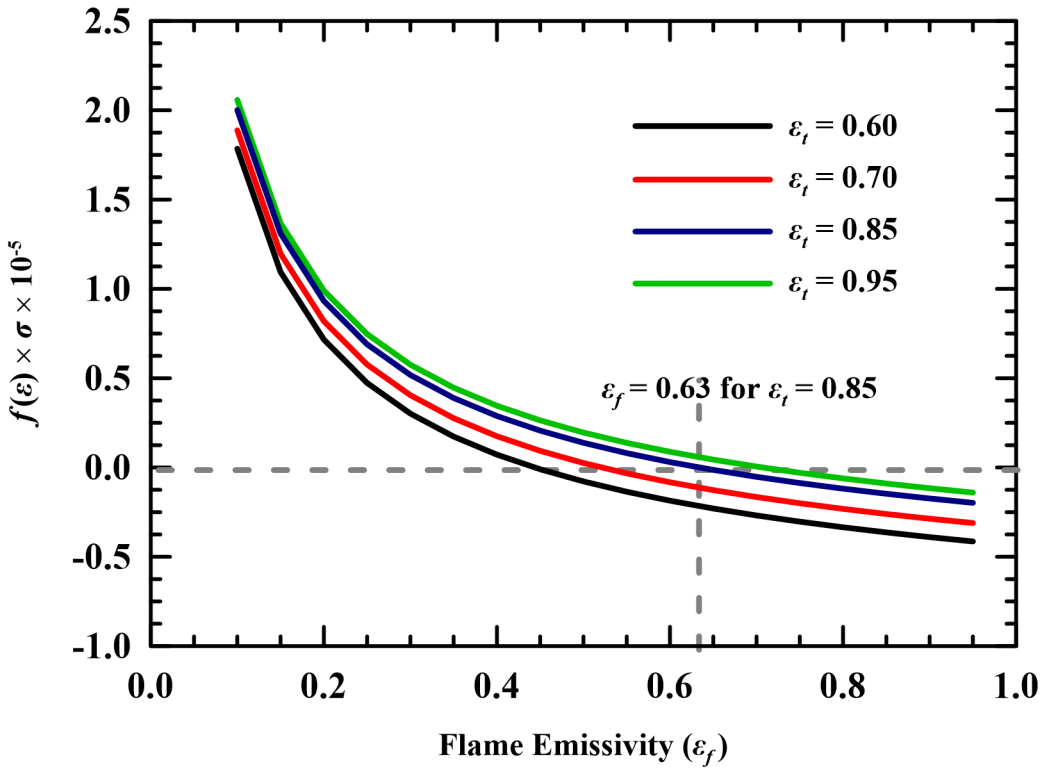

Fig. 3.8 Dependency of temperature and $f(\varepsilon)$ on emissivity for diesel pool fire of 0.5 m diameter

3.6.2 Flame Emissivity of Pool Fires at $Y/D = 0.25$

Experiments are conducted to measure the emissivity of diesel and gasoline pool fires using methodology 2 at a height of $Y/D = 0.25$. Figure 3.9 shows the variation of emissivity of the pool fires with diameter. Flame emissivity increases with the increase in diameter of

the pool fire. This suggests that the radiative fraction of the total heat content increases with the increase in diameter. Flame volume may be visualized as a combination of a number of two-dimensional plain layers. The radiant energy of the reference body passing through the flame is attenuated because of these participating flame layers. As the diameter of the flame increases, the number of the layers that obstruct the reference body radiation while it is passing through the flame increases. Hence, the transmissivity decreases with the increase in diameter. From Eq. (3.4), flame emissivity increases with the increase in diameter, as the transmissivity decreases. In all the measurements using methodology 2, ε_t is taken as 0.85.

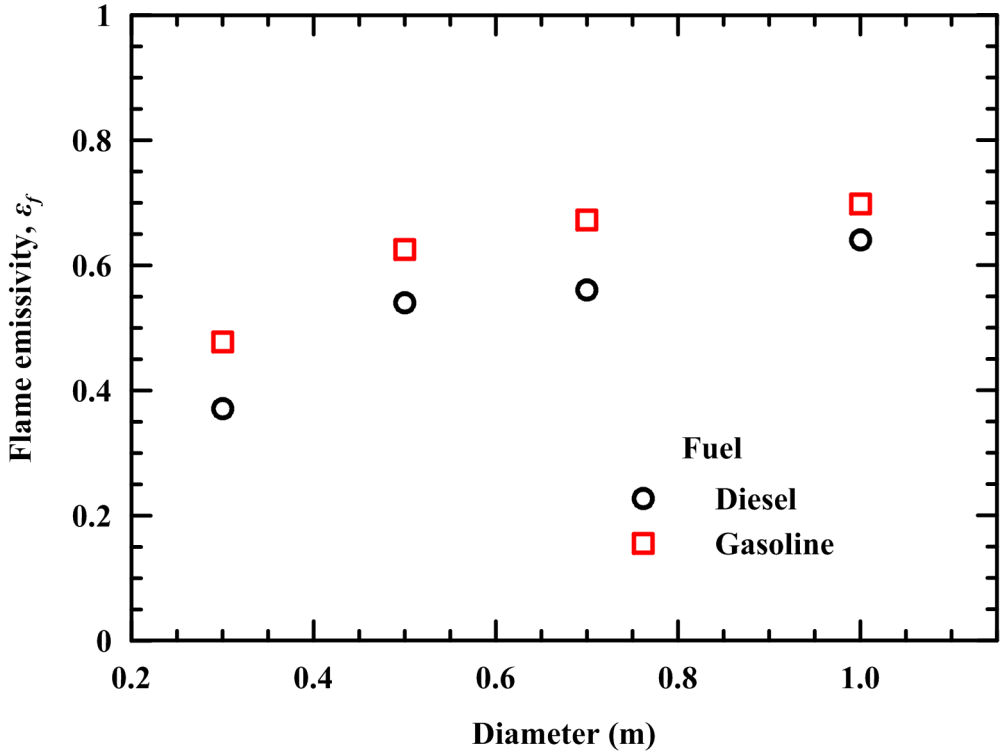

Fig. 3.9 Flame emissivity inferred using IR camera, methodology 2

3.6.3 Sensitivity of ε_f on ε_t

In all the measurements using infrared thermography in methodology 2, ε_t is taken as 0.85. Sensitivity of the flame emissivity (ε_f) for ε_t varying from 0.8 to 0.9 is shown in Table 3.4. The emissivity values shown in Table 3.4 are the values inferred at the bottom plate of gasoline pool fires. For diameters from 0.3 m to 1.0 m, the variation of flame emissivity is not more than 6% for different combined emissivities (ε_t = 0.8 to 0.9).

Table 3.4 Sensitivity of ε_f with the variation of ε_t at the bottom plate for gasoline pool fire

		Flame emissivity, ε_f		
SI no.	**Diameter, D (m)**	$\varepsilon_t = 0.80$	$\varepsilon_t = 0.85$	$\varepsilon_t = 0.90$
1	0.3	0.54	0.57	0.60
2	0.5	0.58	0.62	0.65
3	0.7	0.68	0.72	0.76
4	1.0	0.71	0.75	0.79

3.7 Methodology 3: Inference of Flame Emissivity with Reference to an Electrically Heated Body

In order to validate the measurements of emissivity using methodology 2 (Section 3.6.2), flame emissivity is inferred using a different methodology. The methodology used to determine the flame emissivity is based on the calculation of flame transmissivity using an infrared camera with reference to an electrically heated body (Qian and Saito, 1995). Heater plates are used as reference bodies for reference to obtain the transmissivity of the flame. These heaters are made of 0.06 mm thick stainless steel foil. Two heater plates of 80 mm × 150 mm for 0.3 diameter pool fire and 28 mm × 125 mm for 0.5 m and 0.7 m diameter pool fire are used. The heater plate is clamped tightly and stretched between two copper bus bars. Approximately 5 mm of the foil on either side is sandwiched in the bus bars to ensure firm grip. The heater plate assembly is as shown in Fig. 3.10. The lateral conduction is negligible because of the thinness of foil. Unlike the methodology 2, the size of the plate is limited by the power supply but not by the pool diameter. This is because the plate is maintained at a constant temperature by electrically heating but not by radiation from pool fire. The surface of heater element is painted using a thin coat of pyromark paint, which makes the emissivity of the surface as 0.85.

The camera used in this method is Flir Systems make ThermaCam™ SC640. One of the outputs given by the camera is object signal. This object signal (OS) is an internal parameter proportional to the radiation captured instead of a temperature value. This output parameter can be used for comparative radiation measurements within the same measurement range for the same camera, while the emissivity of the studied object must be actually known when working with temperatures.

Emissivity is computed considering the radiant intensity (*i.e.,* object signal) of both the flame and the heated sheets. Images are taken with infrared camera in four different steps. The body is placed right behind the flame, in line with camera (Fig. 3.11). The body is heated up to 300 °C using a DC power supply and then the flame is ignited.

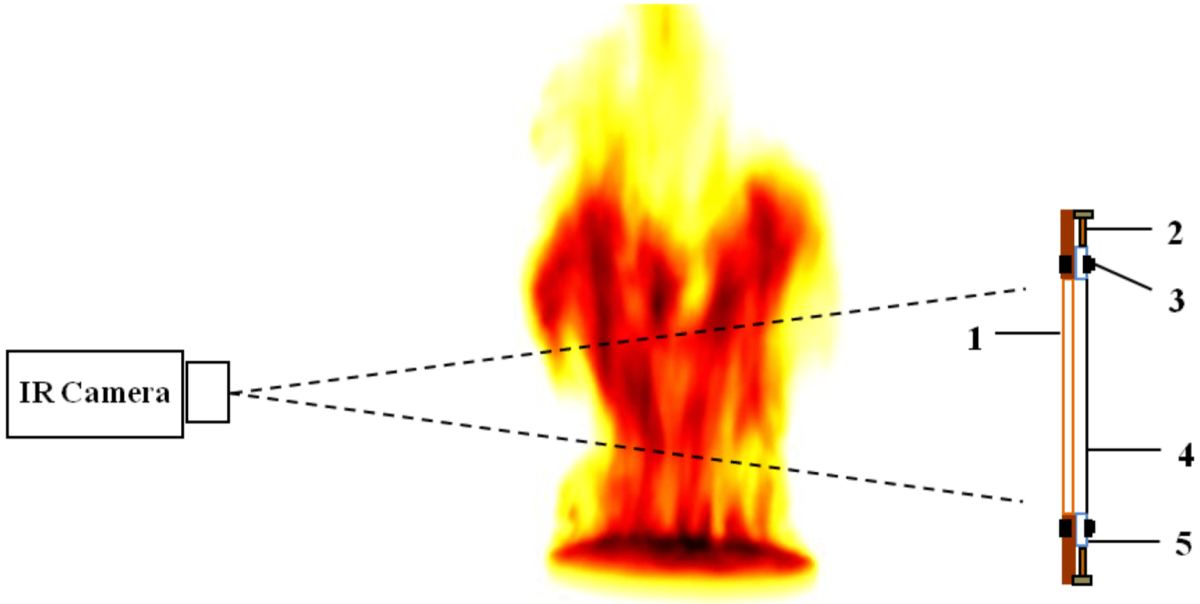

Fig. 3.10 Schematic of flame emissivity measurement with reference to an electrically heated body: 1. Stainless steel foil, 2. stretching screw, 3. clamping screw, 4. frame, 5. copper bus bar

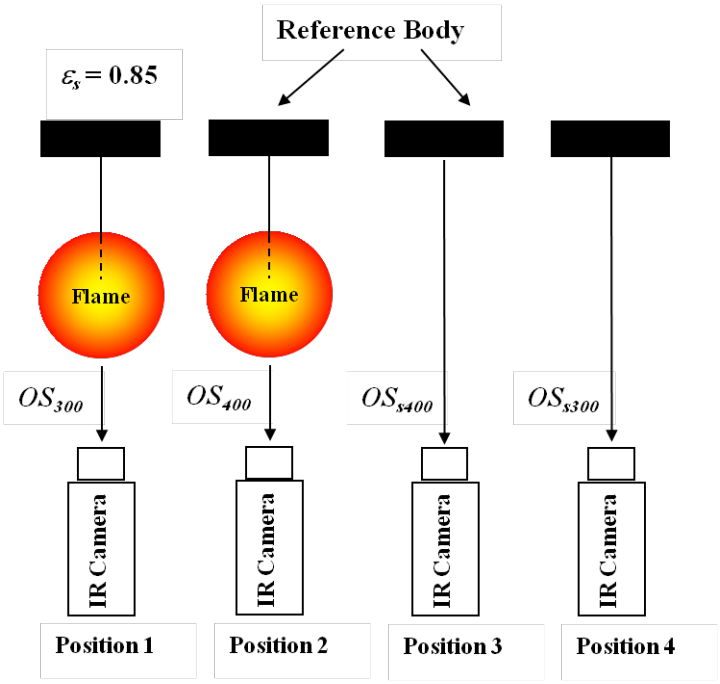

Fig. 3.11 Schematic view of different positions of infrared camera and the heated body assembly in methodology 3

After 3 minutes, the images of the body through the flame are captured. The object signal camera in this position is the combination of the radiant intensity of flame and the radiant intensity of the body when seen through the flame:

$$OS_{300} \propto (I_f + \tau_f I_{s300}) \tag{3.16}$$

where I_f is the radiant intensity of the flame, τ_f is the transmissivity, I_{s300} is the radiant intensity of the heated body at 300 °C. The temperature of the heated body is increased to 400 °C. The second set of data is captured in this position. The object signal captured by the camera in this position is given by:

$$OS_{400} \propto (I_f + \tau_f I_{s400}) \tag{3.17}$$

The third set of data is captured by putting out the flame (body alone at 400 °C). The radiation intensity of the body at 400 °C captured by the camera is:

$$OS_{s400} \propto I_{s400} \tag{3.18}$$

The temperature of the body is reduced to 300 °C. In this position of the camera (flame is off), the fourth set of data is collected. The radiant intensity of the body at 300 °C captured by the camera in this position is:

$$OS_{s300} \propto I_{s300} \tag{3.19}$$

The emissivity of the flame is computed by considering the radiant intensity of both the flame and the heated sheets. Using Eqs. (3.16) to (3.19), the emissivity of the flame in terms of object signal can be written as:

$$\varepsilon_f = \alpha_f = 1 - \tau_f = 1 - \frac{OS_{400} - OS_{300}}{OS_{s400} - OS_{s300}} \tag{3.20}$$

where OS_{400} and OS_{300} correspond to the combined radiant intensity of the flame and body. The radiant intensities of the corresponding heated sheets alone are named as OS_{s400} and OS_{s300}.

3.8 Comparison of Flame Emissivities Inferred using Methodologies 2 and 3

Emissivity of a pool fire measured by observing flame with reference to a body using infrared camera is compared with a method involving infrared camera with reference to an electrically heated body for diesel pool of diameters 0.3 m, 0.5 m and 0.7 m. The position of the body in both the methods is located at a height of 0.25 times the diameter

(Y/D = 0.25) of the pool fire. Figure 3.12 shows that the measured emissivities from both the methods are comparable to each other. The percentage deviation of the flame emissivity measured using methodology 2 from that measured using methodology 3 is 10% for 0.3 m, but for 0.5 m and 0.7 m the percentage deviation is less than 5%. In methodology 2, the body is heated up by the radiation from the flame, where as in methodology 3, the body is electrically heated up. But the measured flame emissivities are independent of the methodology employed (Fig. 3.12).

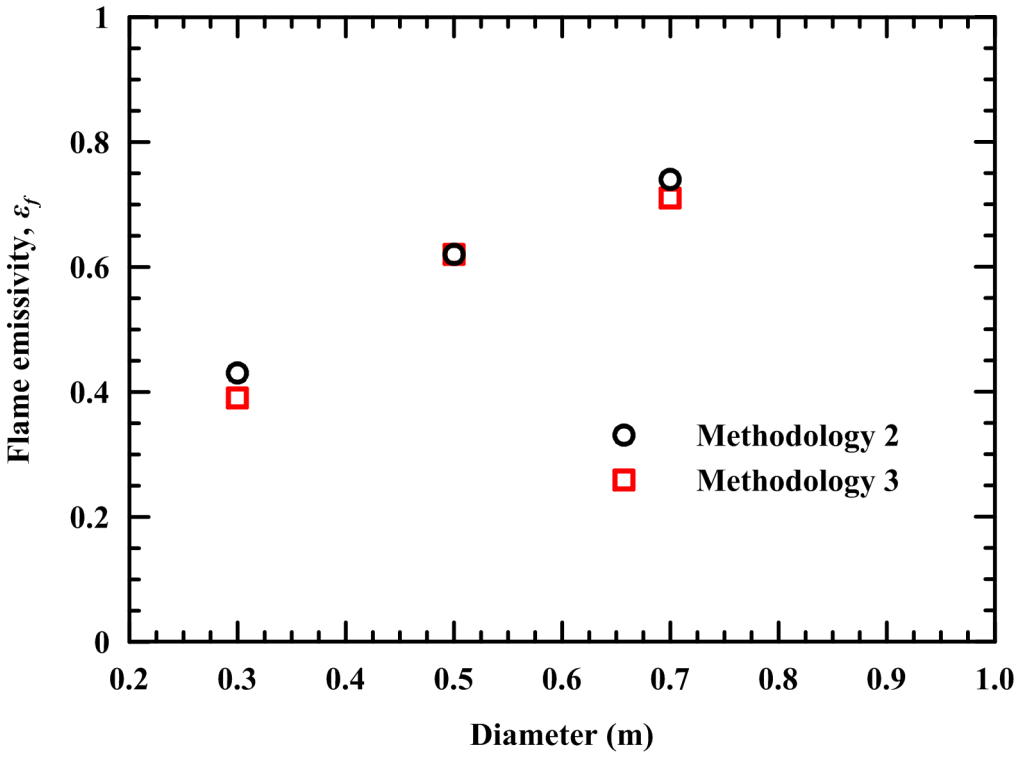

Fig. 3.12 Comparison of flame emissivity measured using methodologies 2 and 3

3.9 Variation of Emissivity with Height for Different Pool Diameters

Flame emissivity variation along the axis is measured using IR camera with reference to a body (methodology 2). Multiple plates along the vertical axis are used as reference bodies. The sizes and the position of the plates used are given in Table 3.5 and Fig. 3.13. The results obtained for diesel pool fires of diameters 0.3 m, 0.5 m, 0.7 m and 1.0 m are shown in Fig. 3.14.

Emissivity at the tip of the flame is 25% less than the emissivity observed at the base of the pool. This may be because of the decrease in the flame thickness (decrease in the

Table 3.5 Sizes and positions of multiple plates

	Plate size (cm)		Position of plate (cm)					
D (m)	Width, w	Height, h	Y_1	Y_2	Y_3	Y_4	Y_5	Y_6
0.3	5.5	5.5	9.3	15.7	22.1	28.6	35.5	-
0.5	5.5	5.5	10.7	21.7	30.9	40.1	48.2	57.3
0.7	5.0	4.5	13.9	24.1	33.1	41.2	49.5	-
1.0	7.5	8.0	21.0	31.7	43.4	-	-	-

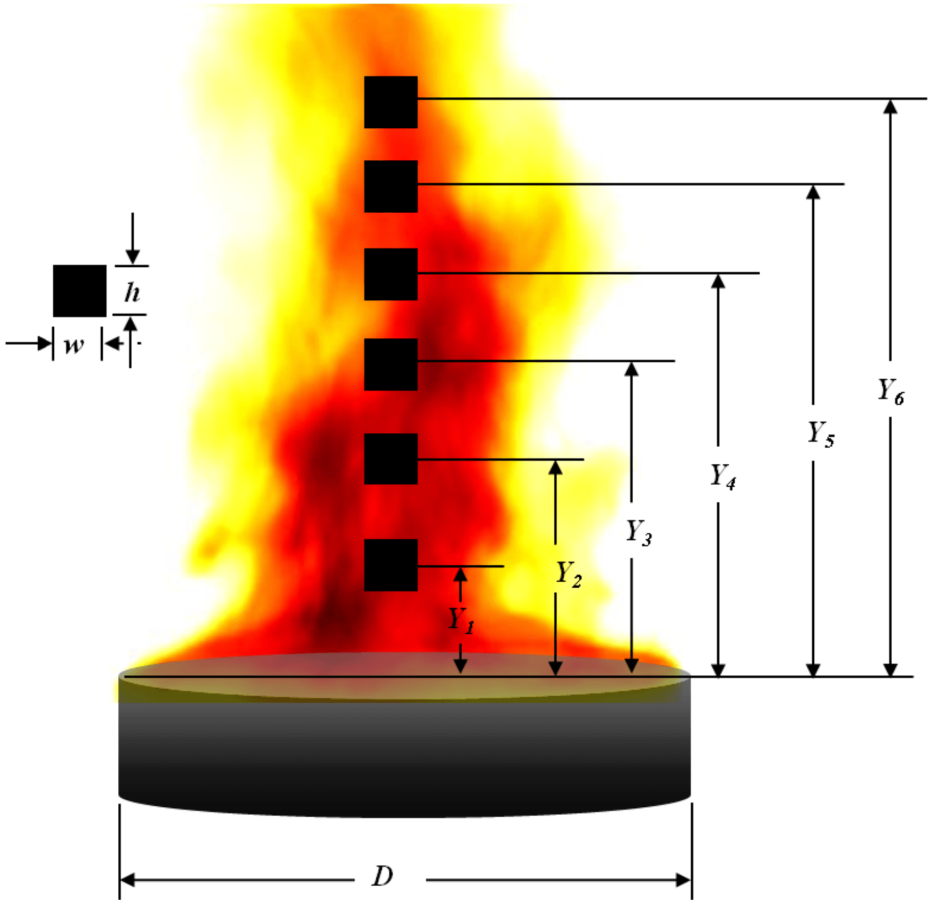

Fig. 3.13 Illustration of the arrangement of multiple plates

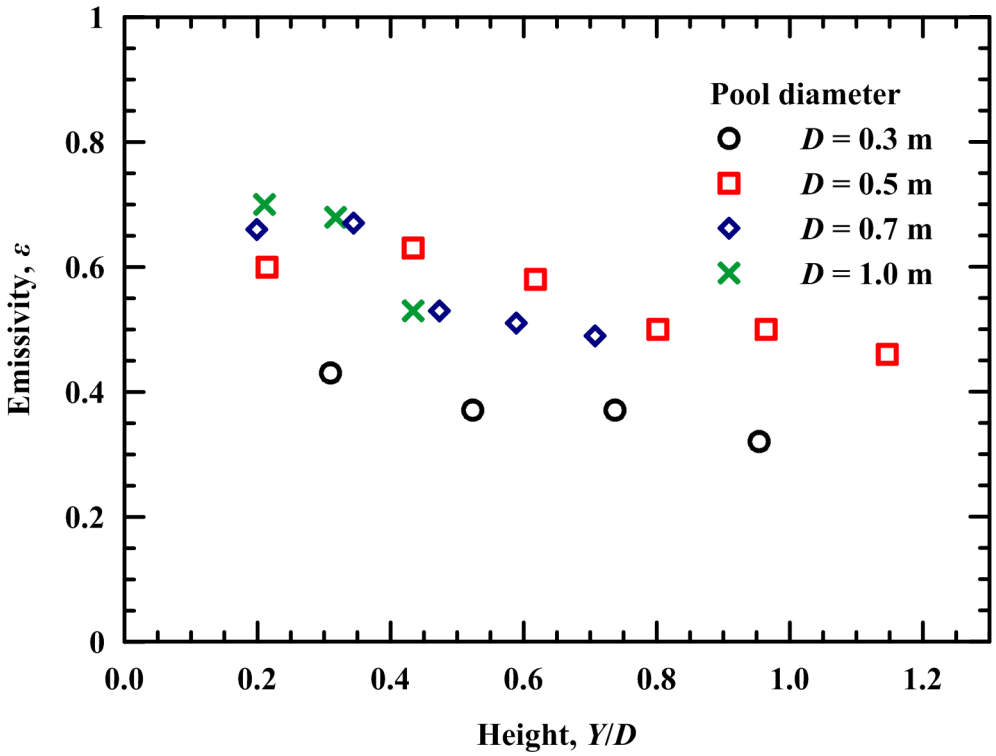

Fig. 3.14 Variation of emissivity along the height of diesel pool fires

number of participating flame layers) as one moves along the vertical axis from the pool base.

To get the overall flame emissivity of the flame, the emissivity values from the five locations (five plates) are averaged for each pool fire. Figure 3.15 shows that the average flame emissivity measured using infrared thermography and the flame emissivity inferred from mass burning rate are comparable. This establishes the methodology of measuring the flame emissivity. Hence, for all the remaining experiments, flame emissivity is measured on the basis of mass burning rate (methodology 1) is employed.

3.10 Optical Thickness

The mean optical thickness ($\kappa\beta$) can be obtained from Eq. (3.4) using Fig. 3.4. For diesel pool fires, $\kappa\beta$ is found to be 1.16 m^{-1}, which is in-line with Rew *et al.* (1997) whose value is 1.3 m^{-1}. The mean optical thickness for gasoline pool fire is found to be 1.52 m^{-1} and for hexane pool fire 1.1 m^{-1}.

3.11 Uncertainty Analysis

The uncertainty in the measurement of the mass burning rate is around 2% - 9%. However, the uncertainty in the measurement of $\dot{m}''_{\infty}$ cannot be quantified because this value is taken

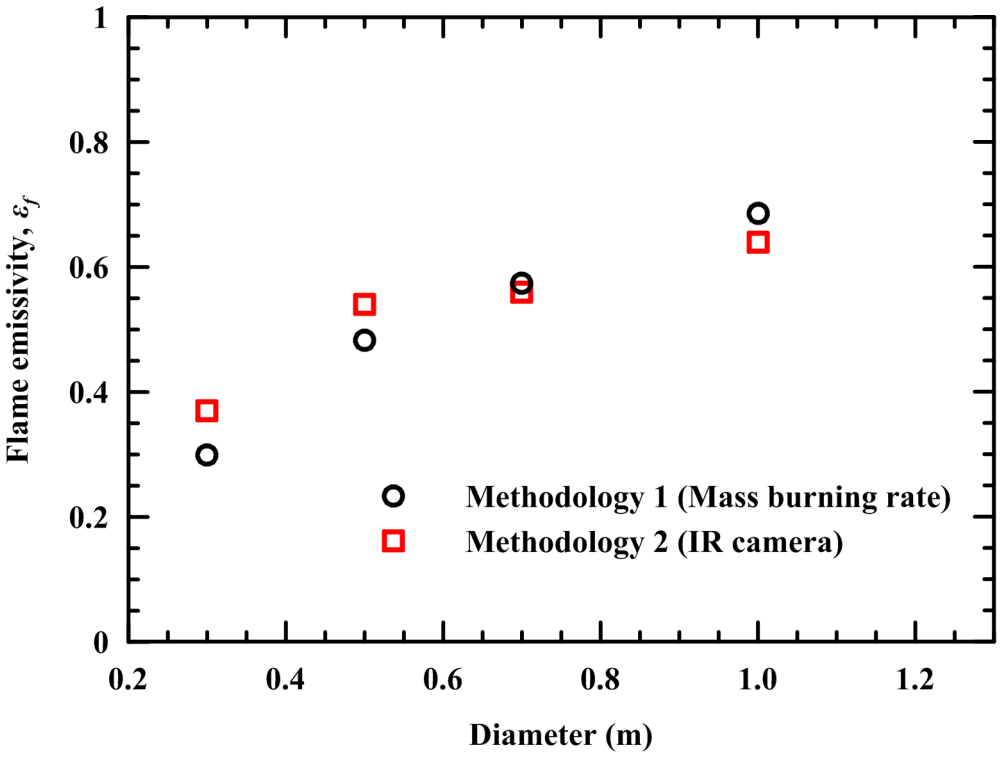

Fig. 3.15 Comparison of emissivity values inferred using mass burning rate and thermography

from the literature.The repeatability in the measurement of mass burning rate for the various experiments conducted is within 3%. The uncertainty in the measurement of the flame emissivity is around 10%. One of the sources of uncertainty in the measurement of emissivity is the presence of atmospheric wind. As these are open pool fire experiments, there is no control on the atmospheric wind. Experiments are conducted at around 6.30 AM to 8.00 AM in order to keep the wind velocity lower than 2 m/s. The base length is large for larger diameter pool fires and the dense flame is spread over to larger areas and hence the reference body seen through the flame covers reasonably uniform emissivity area. But, for smaller diameter pool fires, reference body seen through the flame involves non-uniform emissivity area. Hence, the uncertainty in the measurement of emissivity for larger diameter pool fires (0.7 m and 1.0 m) is around 5%. However, the uncertainty in the measurement of emissivity for smaller diameter pool fire (0.3 m) is around 10%. A variation of 10% in the emissivity value only resulted 5% deviation in temperature. The repeatability in the flame emissivity measurement for the various experiments conducted is within 2%.

3.12 Temperature Distributions of Diesel Pool Fires

Since the flame is gaseous and taking into account that flame's emissivity varies with position, the temperature obtained from the IR camera does not represent the true flame temperature. However, if the distance between the camera and the flame is large enough, the fire can be replaced by an imaginary wall (placed in front of the pool), which shows the apparent temperature distribution obtained by the thermographic camera (Chun *et al.*, 2009, Hayasaka *et al.*, 1992, Muñoz *et al.*, 2004, 2007). Average flame emissivity values are used to obtain the temperature distribution of the open pool fires from the thermal images. In each set of experiments, thermal images of the flame are captured using a thermal camera (VisIR Ti200) at a rate of 12 fpm.

Using emissivity values measured on the basis of mass burning rate (Fig. 3.4), these thermal images are converted to corresponding temperature contour plots. For each diameter around 20 to 40 temperature plots are averaged. Figures 3.16 and 3.17 show these temperature distributions for diesel pool fires of 0.3 m, 0.5 m, 0.7 m and 1.0 m diameters. The origin in all these figures is chosen at the center of the base of the pool. The horizontal and the vertical axis are non-dimensionalized by dividing the axis with diameter of the pool fire. Peak values are observed at Y/D = 0.1 (X/D varies -0.2 to 0.2) and along the centerline of the pool for all the diameters that are considered. The temperature and emissive power distributions of gasoline and hexane pool fires are details in Appendix A.

The temperature variations along the height of the pool on different vertical lines namely, X/D = -0.25, -0.125, 0, 0.125 and 0.25 are shown in Figs. 3.18 and 3.19 for all the diameters that are considered in this study. As discussed earlier, there is a peak at Y/D = 0.1 and then the temperature falls along the height of the pool. The highest values are due to the hot burnt and unburnt gases. As the burnt and unburnt gases move up due to the buoyancy force, they get cooled by mixing up with ambient air. Hence, there is a decrease in temperature values as the particles move up from the base of the pool fire.

The peak temperature varies from 1100 K (for 0.3 m diameter) to 1200 K (for 1.0 m diameter). The temperature variations along the horizontal lines at different heights from the pool base namely, Y/D = 0.1, 0.5, 1.0, 1.5, 2.0, are shown in Figs. 3.20 and 3.21. At Y/D = 0.1, the temperature measurements are higher than the temperatures at other heights. Moreover, the highest temperature is measured at X/D = 0 and at height Y/D = 0.1. The temperature values decreases with the height.

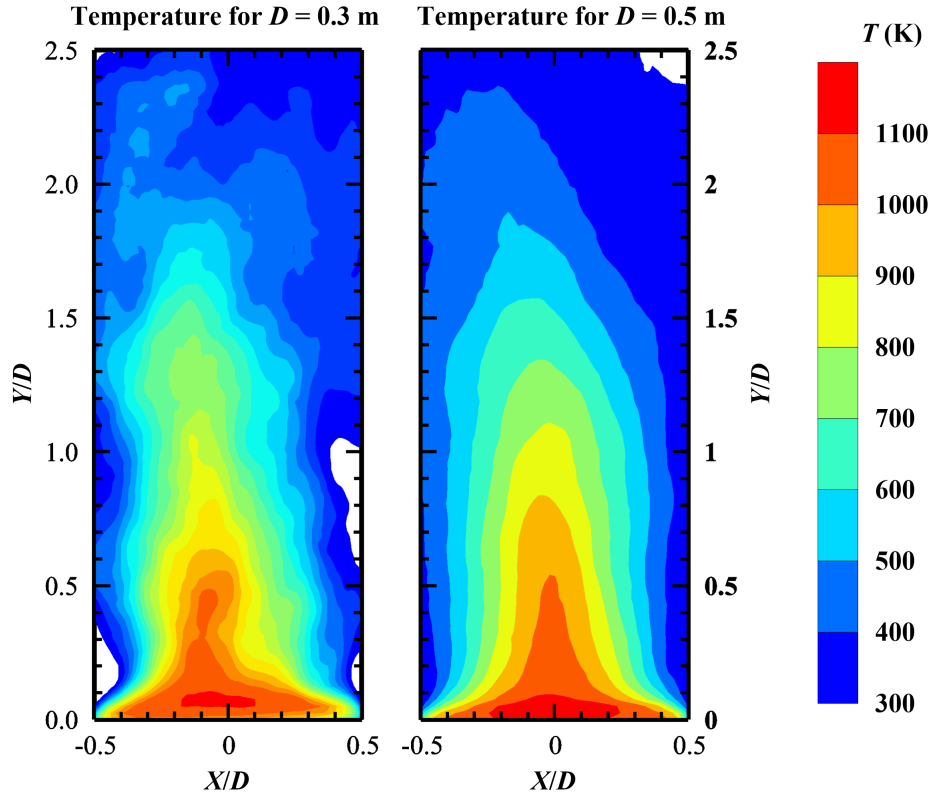

Fig. 3.16 Temperature contour of 0.3 m and 0.5 m diesel pool fire

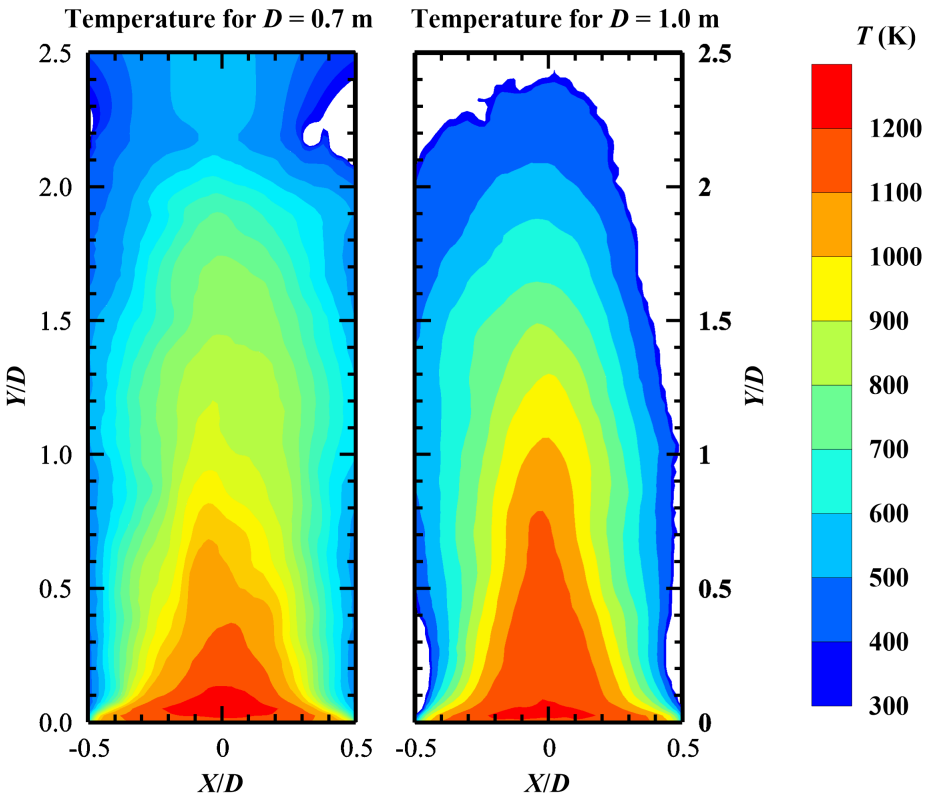

Fig. 3.17 Temperature contour of 0.7 m and 1.0 m diesel pool fire

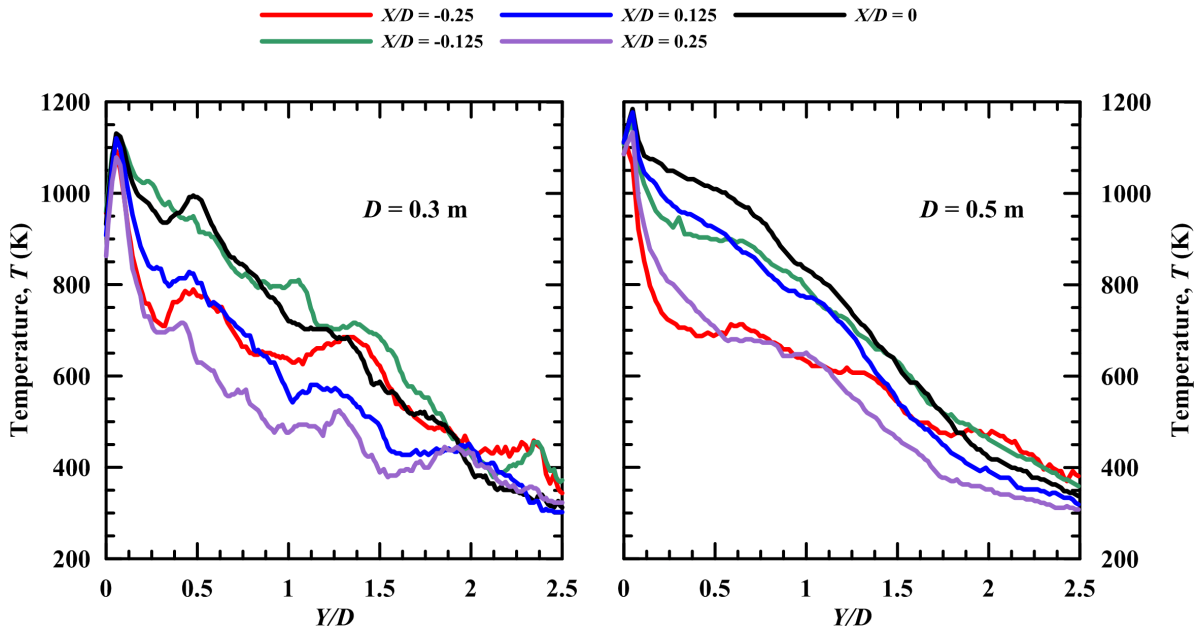

Fig. 3.18 Temperature variations along the height of 0.3 m and 0.5 m diesel pool fire

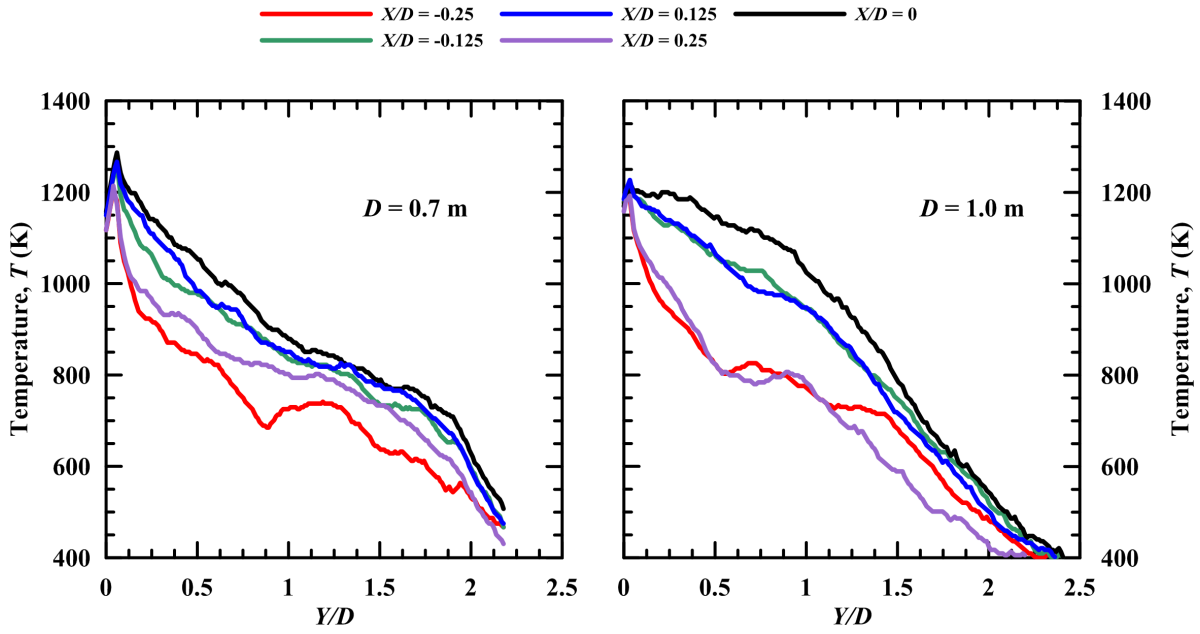

Fig. 3.19 Temperature variations along the height of 0.7 m and 1.0 m diesel pool fire

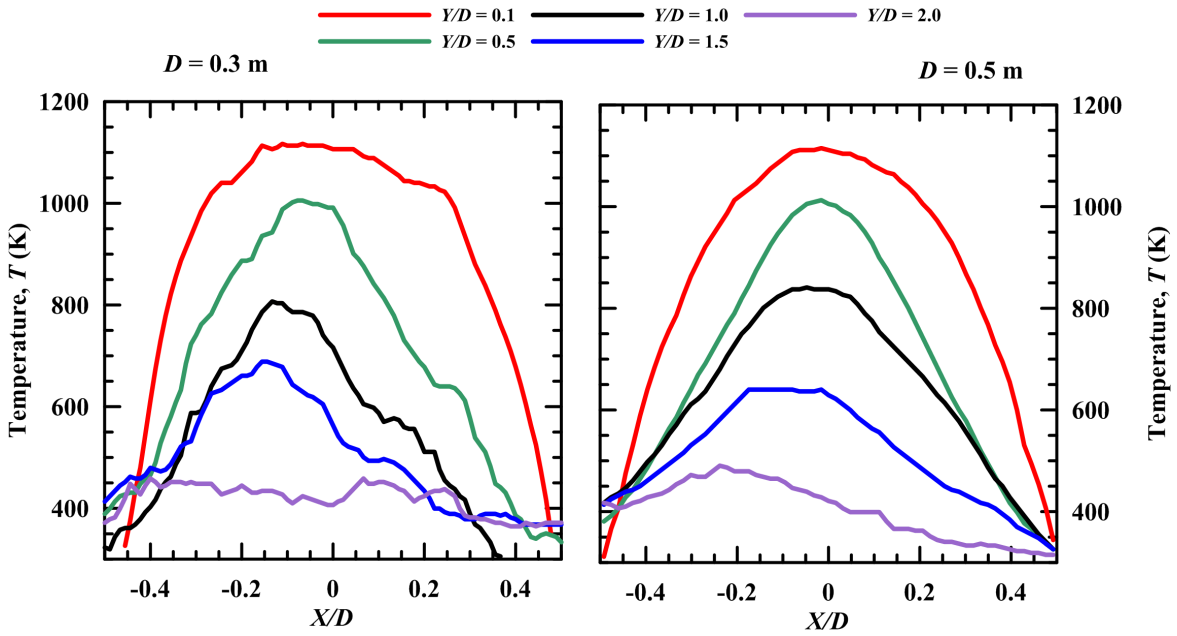

Fig. 3.20 Temperature variations at different heights of 0.3 m and 0.5 m diesel pool fires

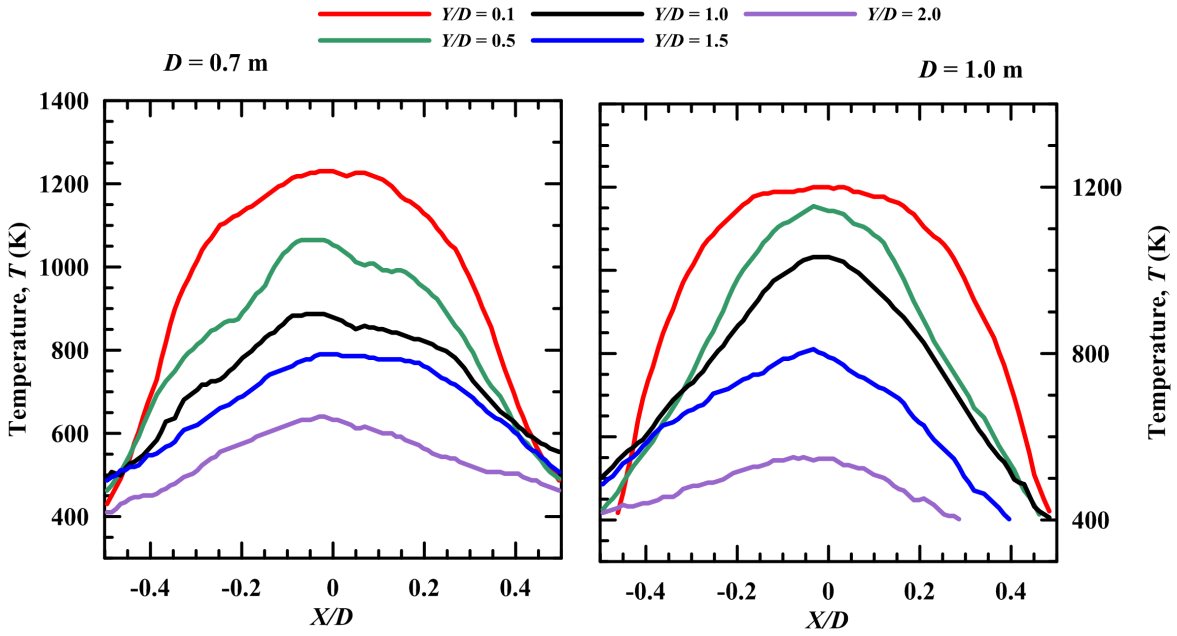

Fig. 3.21 Temperature variations at different heights of 0.7 m and 1.0 m diesel pool fire

3.12.1 Validation of Thermal Camera Temperature Measurements

Flame temperature is measured at several locations using K-type thermocouples along the axis of 0.3 m pool fire. A set of 20 sheathed K-type thermocouples are placed along the centerline of the pool axis. Each thermocouple is separated from the other by 2.5 cm. The experimental set up is shown in Fig. 3.22. All the thermocouples are connected to the computer via data logger. Though the temperature data from the thermocouples are being used extensively in the literature, these readings are not the representation of the true gas temperature (Luo, 1997, Francis and Yau, 2004). An estimation of error can be derived from an energy balance equation on the thermocouple junction. The difference in between the true gas and the thermocouple junction is given by (Luo, 1997, Silvani and Morandini, 2008):

$$T_f - T_{TC} = \frac{\varepsilon_{TC}\sigma\left(1-\varepsilon_f\right)T_f^4}{h_{TC} + 4\varepsilon_{TC}\sigma T_f^3} \tag{3.21}$$

where h_{TC} is the convective heat coefficient. h_{TC} can be obtained from Nusselt number correlation (Incropera and DeWitt, 2002) by assuming the thermocouple junction as a cylinder and is given by:

$$h_{TC} = \frac{k_f}{d_{TC}}\left(0.43 + 0.53\ \mathrm{Re}^{0.5}\ \mathrm{Pr}^{0.31}\right) \tag{3.22}$$

where d_{TC} is the diameter of the thermocouple (1.5 mm). For velocity of the gas is taken as 2 m/s for calculating Reynolds number. Figure 3.23 shows the centerline temperature distributions from thermocouples (after correction) and thermal images for pool fires of diameter 0.3 m. This shows a good agreement in the temperature values inferred from thermal images.

Fig. 3.24 shows the centerline temperature distribution of the pool fires of present work and the centerline temperature distributions reported by McCaffrey (1979). McCaffrey measured the centerline temperature distributions of natural gas for different heat release rates. The size of the burner used to produce purely buoyant diffusion flame was 0.3 m square. By varying the gas flow rates, he achieved different fire sizes or heat release rates. $Y/Q^{2/5}$ is represented along the abscissa in Fig. 3.24. Heat release rate (Q) for a given pool fire is given by (Babrauskas, 1983):

$$Q = \eta\, \dot{m}'' A \Delta H_c \tag{3.23}$$

where η is the efficiency of combustion, A is the pool surface area and H_c is the effective heat of combustion. In this study, η is assumed to be unity and H_c is taken as 47 MJ/kg (Akers *et al.*, 2006). Figure 3.24 suggests that the temperature distribution of diesel pool

Fig. 3.22 Experimental arrangement of thermocouples

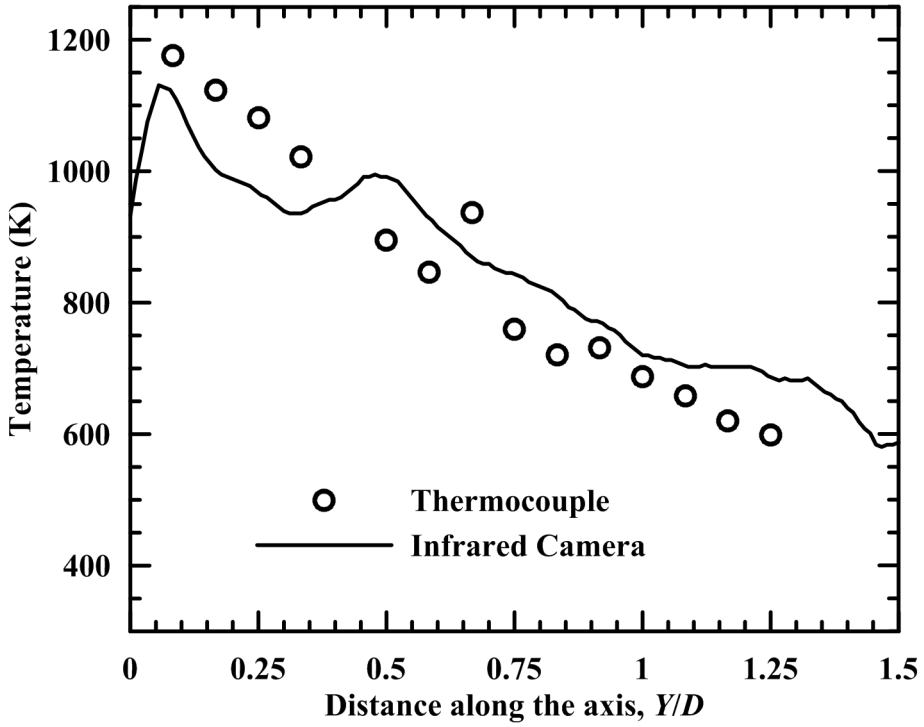

Fig. 3.23 Centerline temperature distribution for 0.3 m diesel pool fire

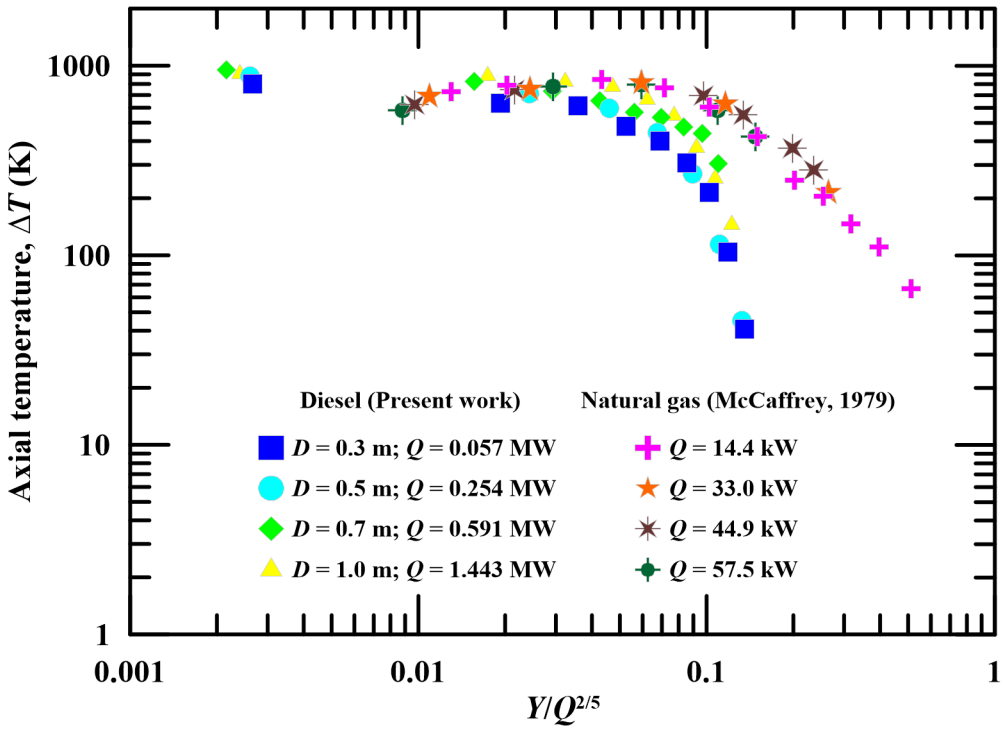

Fig. 3.24 Comparison of centerline temperatures of the present work with McCaffrey's data (McCaffrey, 1979)

fire qualitatively matches with that reported by McCaffrey (1979). In both the cases, the centerline temperature increases with the increase in heat release rate (mass burning rate). However, substantial quantitative differences between the present results and McCaffrey's data exist. These differences may be attributed to the soot existing in the diesel pool fires. The flame height for natural gas ($3D$) is higher than diesel ($2.5D$) and hence there is a considerable change in the temperatures for diesel and natural gas pool fires at higher heights. Similar observations are reported by Koseki (1989).

3.13 Emissive Power Distributions of Diesel Fires

The apparent temperature at each pixel on the thermographic image, can be transformed to emissive power using the relationship

$$E_{ij} = \sigma \varepsilon_f T_{ij}^4 \tag{3.24}$$

where T_ij is the temperature (K) of a pixel element, i and j indicate the position/location in the thermographic image, E_{ij} is the emissive power (kW/m^2) at that location. Surface emissive power distributions are calculated for diesel pool fires of diameters 0.3 m, 0.5 m, 0.7 m and 1.0 m (shown in Figs. 3.25 and 3.26). A point on this imaginary wall does not necessarily represent the real emissive power of the flame behind this imaginary wall, but the approximation is accurate enough for the emissive power distribution of the flame to

be analyzed (Muñoz *et al.*, 2004). The emissive power variations along the height of the pool on different vertical lines namely, X/D = -0.25, -0.125, 0, 0.125 and 0.25 are shown in the Figs. 3.27 and 3.28 for all the diameters that are considered in this study. There is a peak at Y/D = 0.1 and then the heat flux falls along the height of the pool. The emissive power variations along the horizontal lines at different heights from the pool base namely, Y/D = 0.1, 0.5, 1.0, 1.5 and 2.0, are shown in Figs. 3.29 and 3.30. At Y/D = 0.1, the emissive power measurements are higher than the emissive power measurements at other heights. The emissive power distributions of gasoline and hexane pool fires are details in Appendix A.

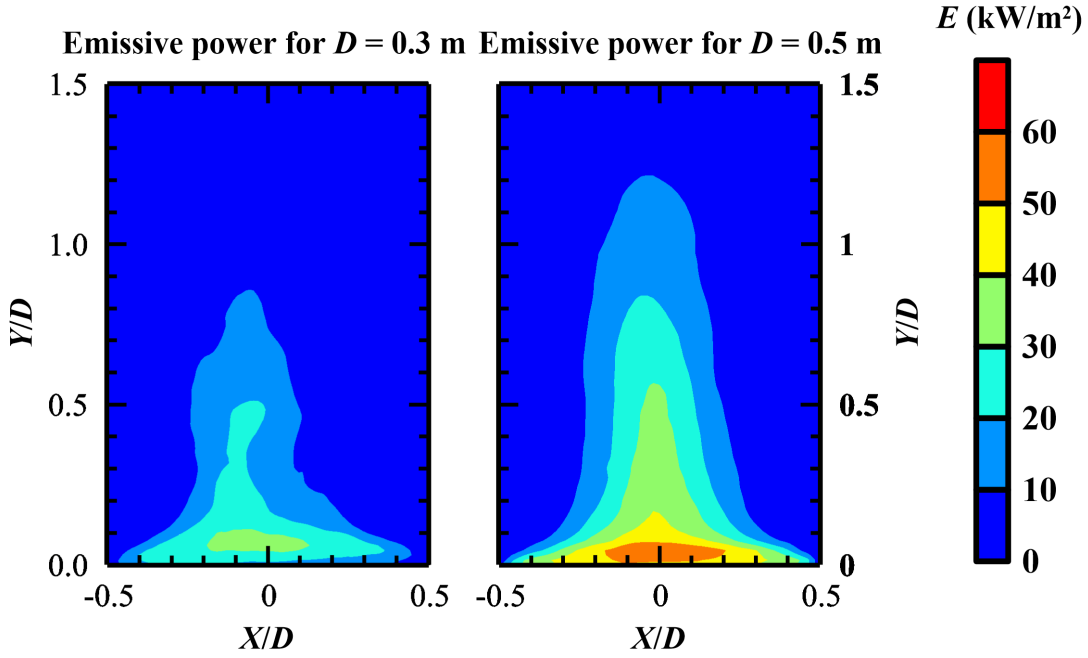

Fig. 3.25 Emissive power distribution of 0.3 m and 0.5 m diesel pool fire

3.14 Heat Flux Measurements at a Distance

Flame volume may be visualized as a combination of number of two-dimensional plain layers. A two-dimensional radiometric image can only give information of the radiation coming from all of these two-dimensional plain layers cumulatively, but not individually. The radiation from the extreme end layer (farthest layer from the camera) of the flame has to penetrate all the other flame layers in order to be perceived by the camera, whereas the radiation from the layer which is nearer to the camera can directly be perceived by the camera. Hence, the radiometric image is the representation of the equivalent energy release from the flame volume as if the whole energy is released from a vertical two-dimensional plain which is placed at the center of the pool. Therefore the heat flux calculated at a distance from the radiometric image must be equivalent to that measured

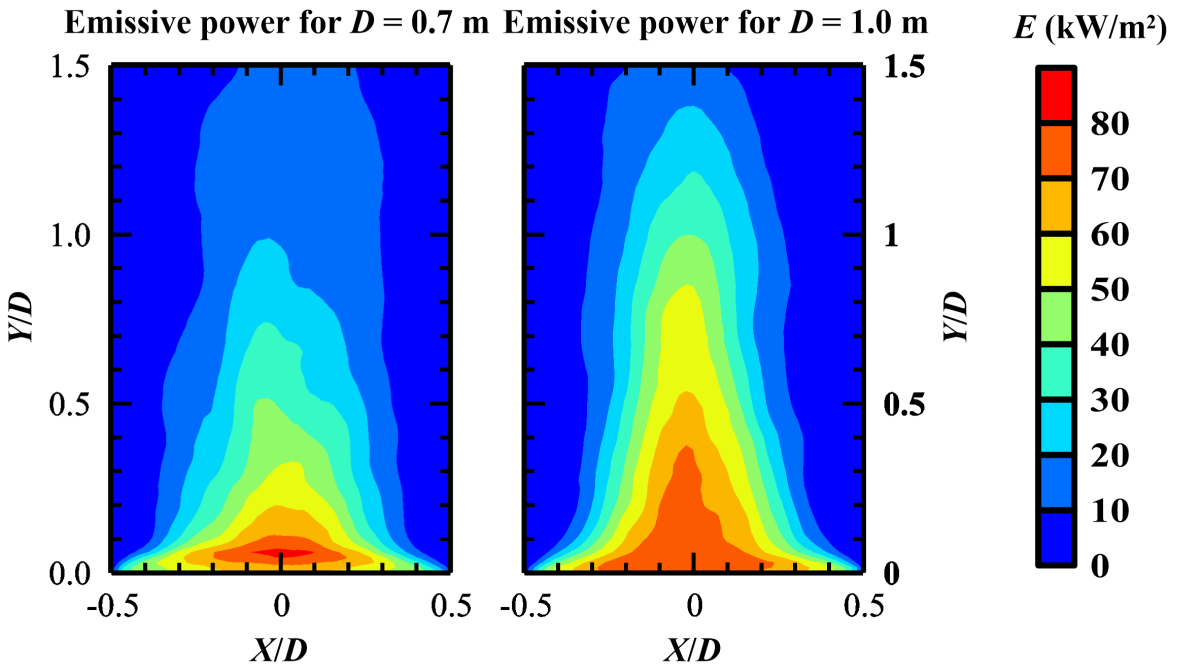

Fig. 3.26 Emissive power distribution of 0.7 m and 1.0 m diesel pool fire

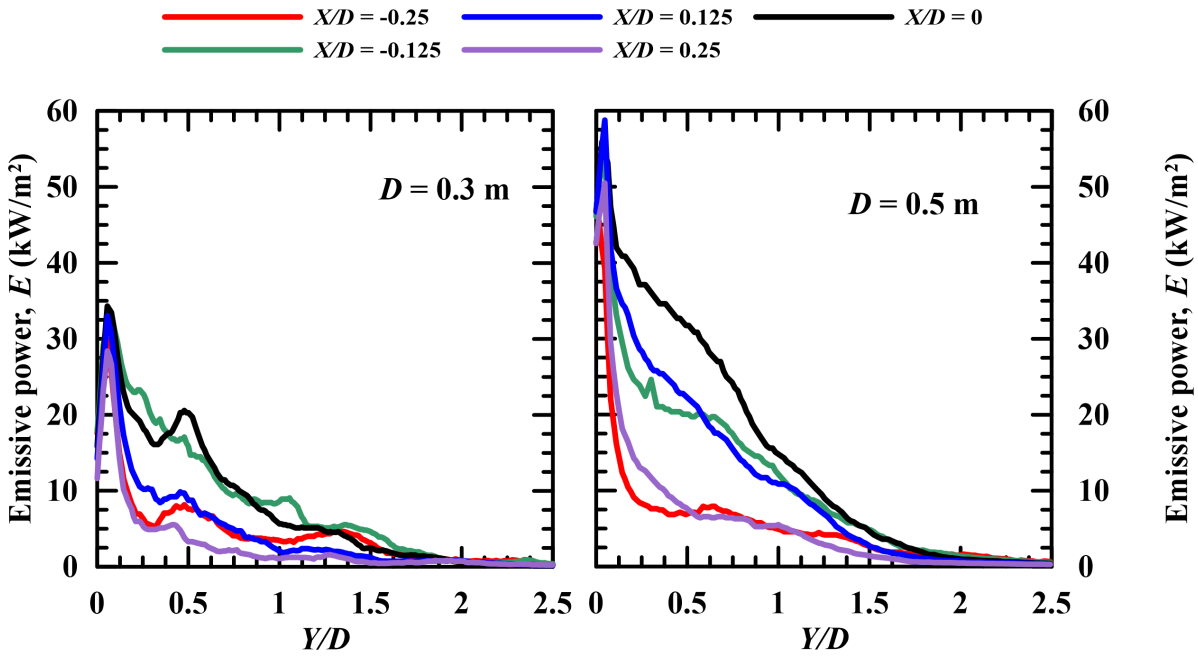

Fig. 3.27 Emissive power variations along the height of 0.3 m and 0.5 m diesel pool fire

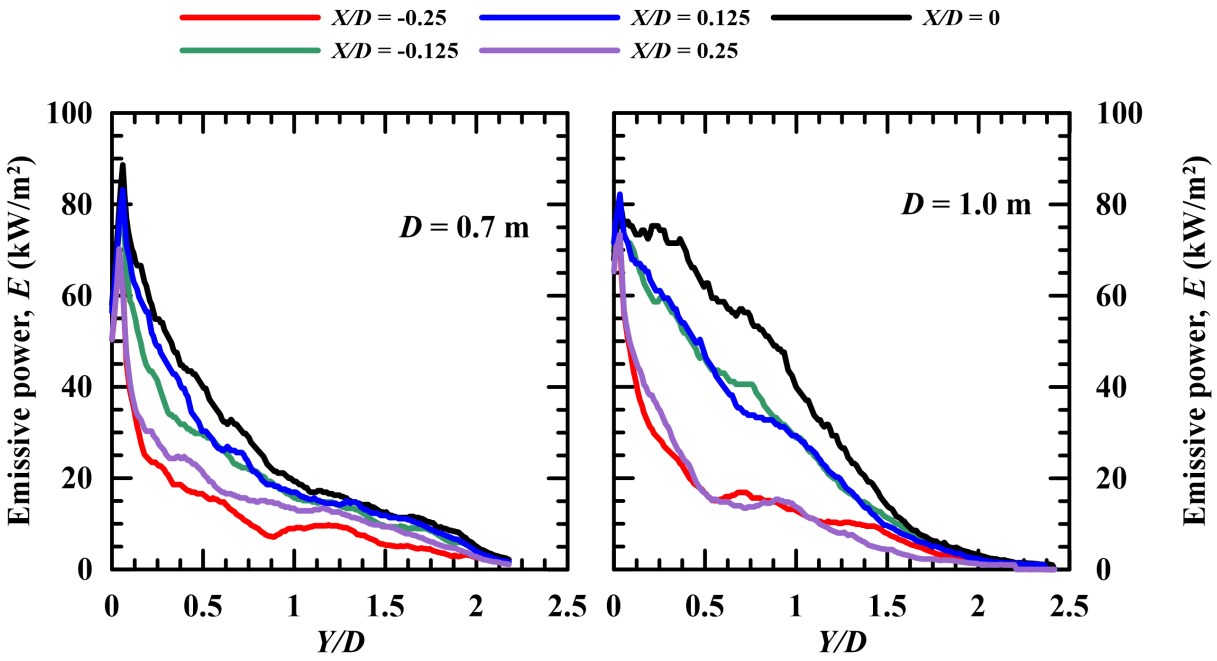

Fig. 3.28 Emissive power variations along the height of 0.7 m and 1.0 m diesel pool fire

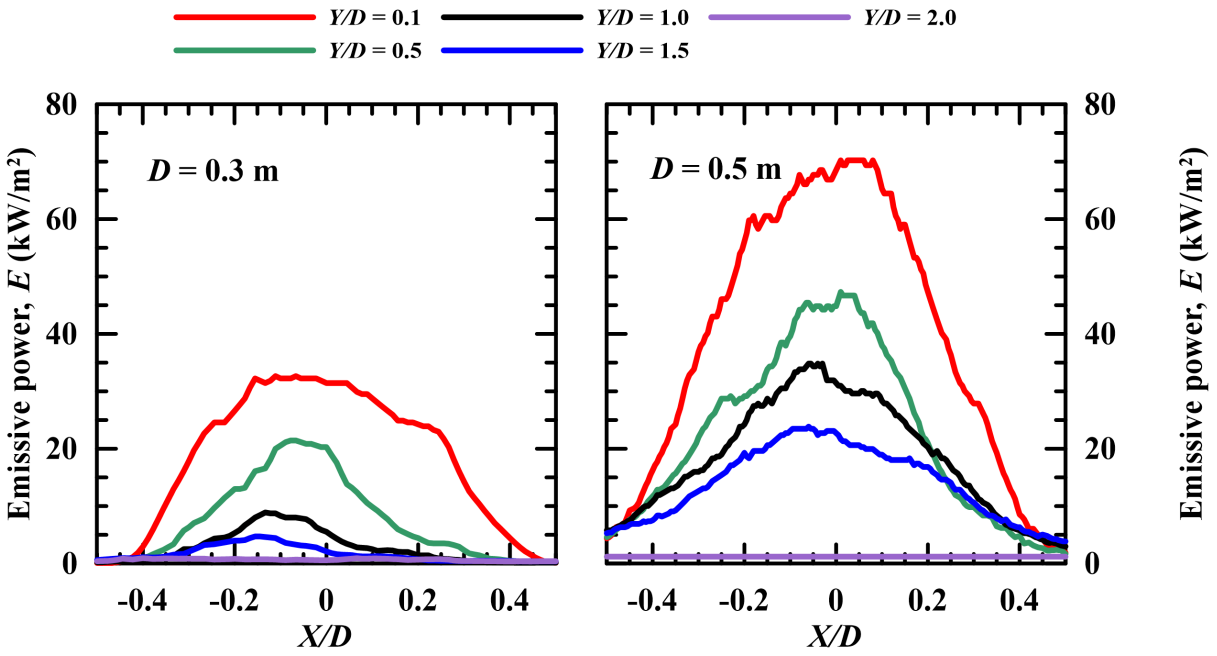

Fig. 3.29 Emissive power variations along the height of 0.3 m diesel pool fire

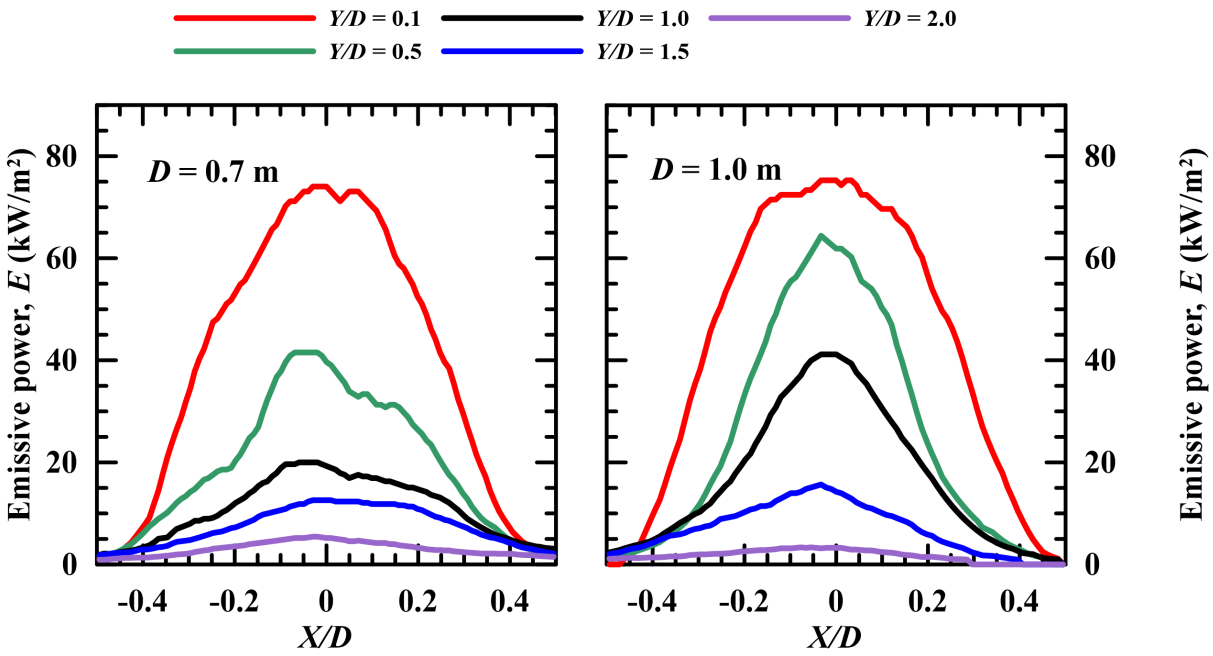

Fig. 3.30 Emissive power variations along the height of 0. m diesel pool fire

from the flame by the heat flux sensor at the same location. Emissive power at a pixel in the radiometric image in Eq. (3.24). The heat flux passing through an area, A_2 from the pixel A_1 is (Fig. 3.31)

$$q''_{1-2} = \frac{F_{1-2} A_1 E_1}{A_2} \tag{3.25}$$

View factor, F_{1-2} is involved in the calculation procedure of heat flux at a distance from the radiometric image. Consider two parallel rectangles of area A_1 and A_2 separated by a distance of z m as shown in Fig. 3.31. The view factor as seen from A_1 to A_2 is given as (Howell, 2008):

$$f_{1-2} = \frac{1}{(x_2 - x_1)(y_2 - y_1)} \sum_{l=1}^{2} \sum_{k=1}^{2} \sum_{j=1}^{2} \sum_{i=1}^{2} (-1)^{(i+j+k+l)} G\left(x_i, y_j, \eta_k, \xi_l\right) \tag{3.26}$$

$$G = \frac{1}{2\pi} \begin{bmatrix} (y-\eta)\left[(x-\xi)^2 + z^2\right]^{1/2} \tan^{-1}\left\{\frac{y-\eta}{[(x-\xi)^2+z^2]^{1/2}}\right\} \\ +(x-\xi)\left[(y-\eta)^2 + z^2\right]^{1/2} \tan^{-1}\left\{\frac{y-\xi}{[(y-\eta)^2+z^2]^{1/2}}\right\} \\ -\frac{z^2}{2} \ln\left[(x-\xi)^2 + (y-\eta)^2 + z^2\right] \end{bmatrix} \tag{3.27}$$

The assumption made in deriving view factor is that the distance z is far greater than the sides of the rectangles considered. f_{1-2} is different to F_{1-2}, as the earlier represents the view factor between two rectangular surfaces, but the latter represents the view factor between apparent two dimensional pixel to a rectangular surface. From previous experiments, it is found that F_{1-2} is four time larger than f_{1-2} for all the diameters used in

this work. Using Eq. (3.24) and Eq. (3.25) in Eq. (3.26), the heat flux passing through an area, A_2 from the pixel A_1 of pool fire can be calculated. Therefore, the net heat flux passing through an area, A_2 from the flame represented by n pixels is:

$$\dot{q}''_{f-A_2} = \sum_{i=1}^{n} \frac{(F_{i-2} A_1 E_{ij})}{A_2} \tag{3.28}$$

3.14.1 Validation of Heat Flux

Experiments are conducted on a diesel pool fire of 0.3 m diameter using Schmidt Boelter gauge (radiometer). The heat flux gauge is traversed along the vertical axis from a distance of 0.3 m from the pool center (Fig. 3.32. At each position, measurements are made for a period of 30 seconds to get time averaged heat flux at that location. Figure 3.33 shows the comparison of heat flux measurements at $Z/D = 1$ with heat flux transducer and camera for 0.3 m diameter pool fire. There is a reasonably good agreement between the computed results using Eq. (3.28) and measurements using heat flux gauge. A similar experiment on gasoline pool fire is also conducted on gasoline pool fire Appendix A. It is found that the heat flux measurements using infrared camera are compared well with the Schmidt Boelter gauge.

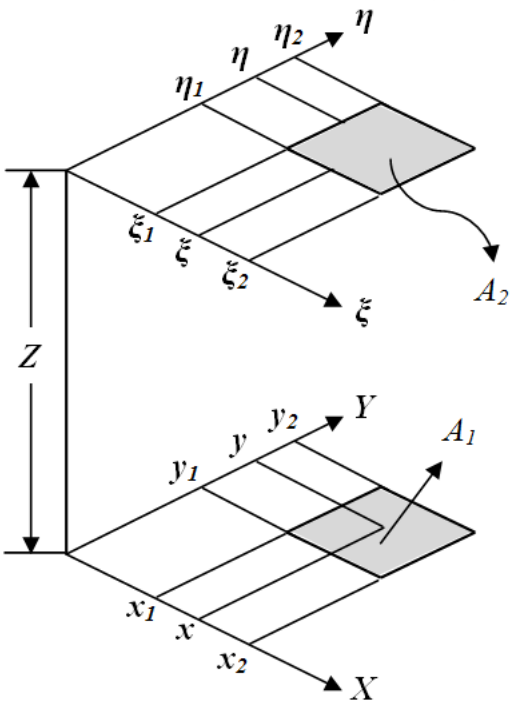

Fig. 3.31 Schematic of rectangle-rectangle in a parallel plane for finding the view factor (Howell, 2008)

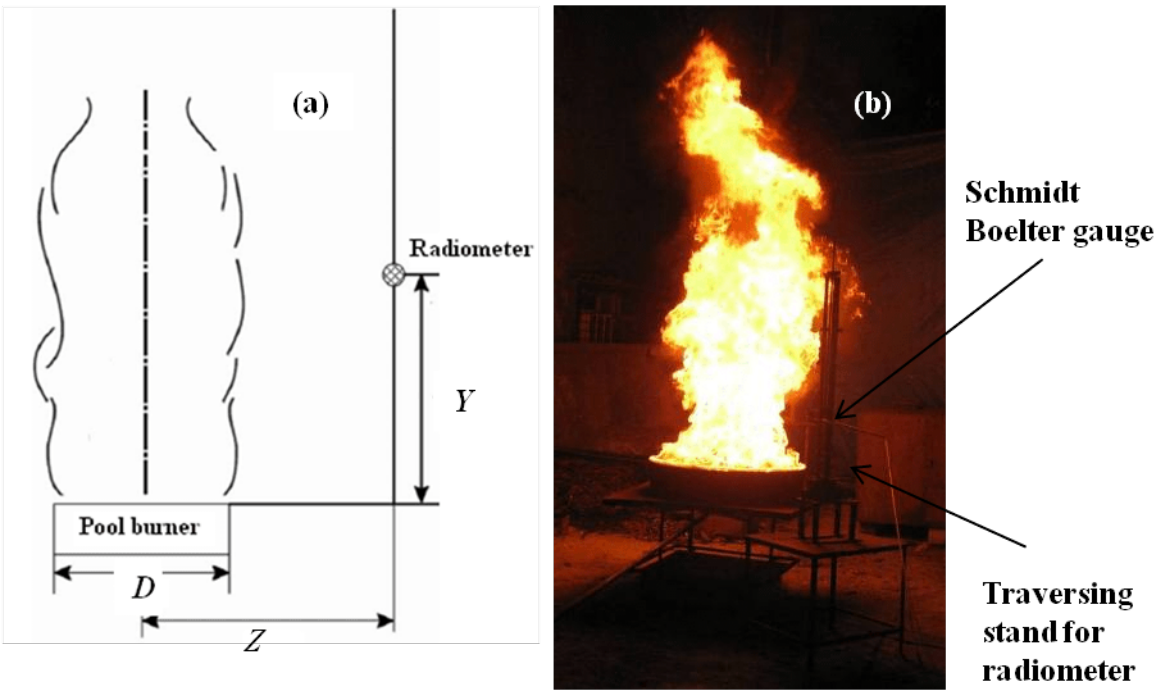

Fig. 3.32 Heat flux measurements using Schmidt Boelter gauge:
(a) Schematic view, (b) Experimental setup for 1 m pool fire

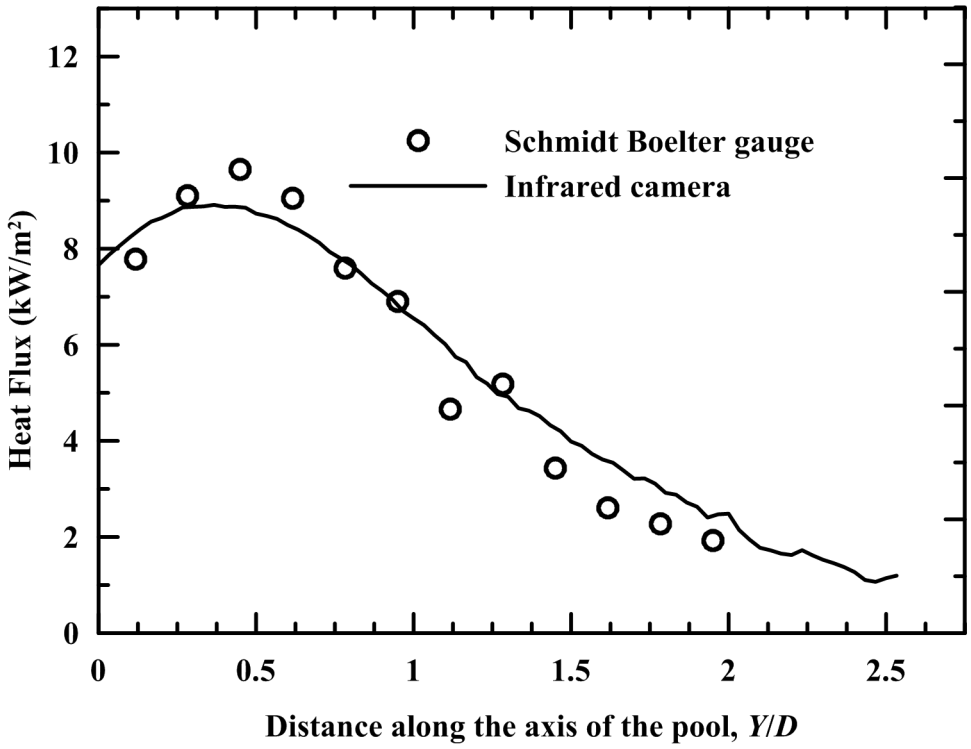

Fig. 3.33 Comparison of heat flux measurements at $Z/D = 1$ with sensor and infrared camera for diesel fire of 0.3 m pool diameter

3.14.2 Heat Flux at $Z/D = 1$

Figure 3.34 shows the heat flux measurements of 03 m, 0.5 m, 0.7 m and 1.0 m at a distance of $Z/D = 1$. It is observed that the heat flux values increase with the increase in the pool diameter. Maximum heat flux is obtained at different heights for different diameters. This peak is shifted towards the top from $Y/D = 0.37$ for 0.3 m diameter to $Y/D = 0.53$ for diameter 1.0 m. The maximum heat flux value varies from 9.8 kW/m^2 (for 0.3 m diameter) to 33 kW/m^2 (for 1.0 m diameter).

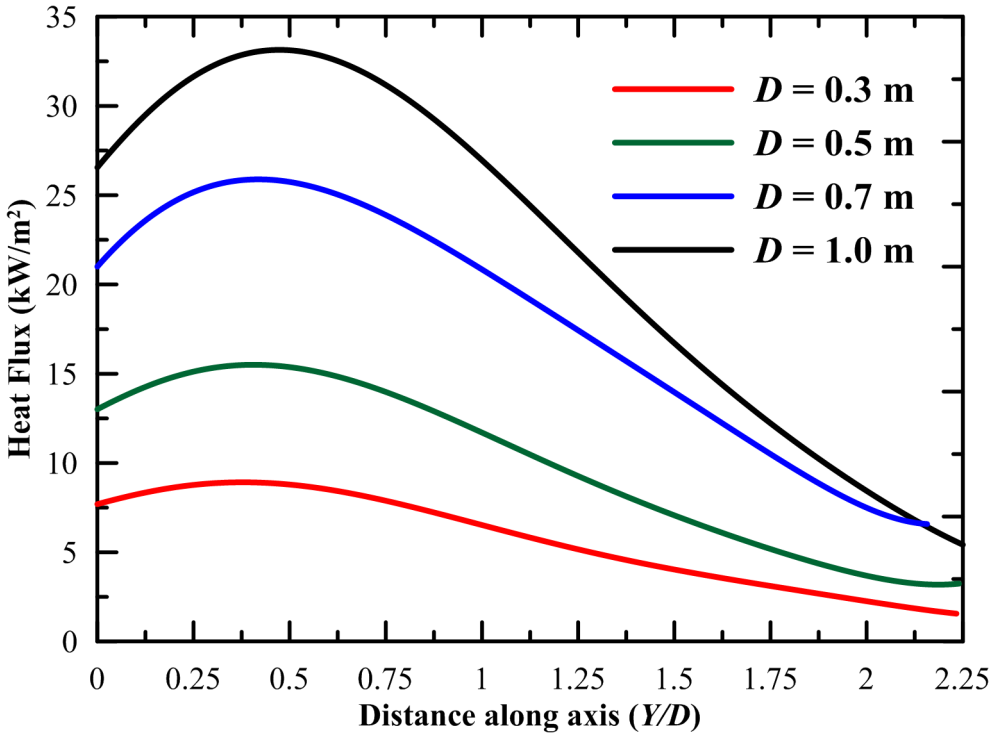

Fig. 3.34 Heat flux variation with Y/D at $Z/D = 1$ for diesel pool fires

3.14.3 Radiative Fraction

Radiative fraction (χ_r) is defined as the ratio of the energy radiated to the surroundings to the idealized combustion heat release. Radiative fraction is given by:

$$\chi_r = \frac{Q_r}{HRR} \tag{3.29}$$

where Q_r (kW) is the radiative heat loss to the surroundings, HRR'' is the heat release rate.

Due to the difficulties involved in measuring the distribution of the radiant flux over a surface surrounding the fire, many estimates of radiative heat loss fraction reported in the literature rely on a single-location measurement and the assumption of isotropy. Heat

flux is measured at a location of R m away from the pool fire. This measured heat flux is then multiplied with the area of the virtual sphere formed with radius R. The center of this virtual sphere is located on the pool surface, at the axis, *i.e.*, at $x = 0$ and $y = 0$. Hence, the radiative heat loss in a single-location measurement is given by:

$$Q_r = 4\pi R^2 \cdot q'' \tag{3.30}$$

where R is the radius of the virtual sphere and q'' is the radiative heat flux at the measured location on the virtual sphere.

Radiative fraction can also calculated using multi-location measurement. It is calculated by integrating the measured vertical ($q''(y)$) and radial ($q''(r)$) distributions of radiative flux using the relation:

$$Q_r = 2\pi \left(\int_{R_0}^{R} r \cdot q''(r)dr + R \cdot q''(y)dy \right) \tag{3.31}$$

where $q''(y)$ is the heat flux measured at a distance R from the pool center and along the vertical axis, $q''(r)$ is the heat flux measured along the horizontal line at the base of the pool fire Fig. 3.35. Heat flux along the vertical axis has to be measured until the heat flux approaches zero. $q''(y)$ and $q''(r)$ are obtained from Eq. (3.28). The constant G in Eq. (3.26) for $q''(r)$ is given as (Howell, 2008):

$$G = \frac{1}{2\pi} \begin{bmatrix} (y-\eta)\left(x^2+\xi^2\right)^{1.2} \tan^{-1}\left\{\frac{y-\eta}{(x^2+\xi^2)^{1.2}}\right\} \\ -\frac{1}{4}\left[x^2+\xi^2-(y-\eta)^2\right] \ln\left[x^2+\xi^2-(y-\eta)^2\right] \end{bmatrix} \tag{3.32}$$

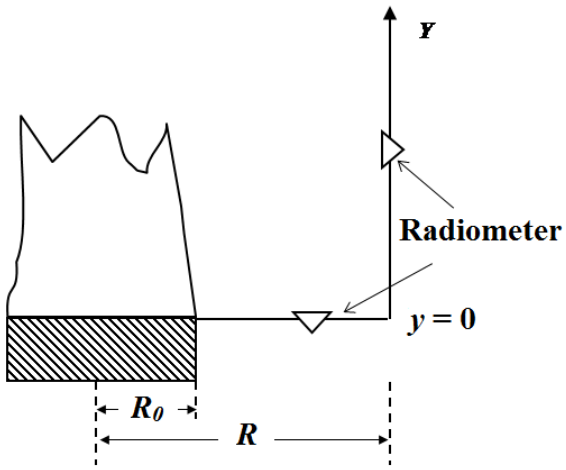

Fig. 3.35 Schematic of radiative fraction calculation

Figure 3.36 shows the variation of radiative fraction for diesel pool fires of diameters 0.3 m, 0.5 m, 0.7 m and 1.0 m. Radiative fraction increases with the increase in diameter

at least for the diameters that are considered in this study. From Fig. 3.36, it is observed that the single-location measurement underpredicted the radiative fraction by 11.8% for 0.3 m diameter. For larger diameters both the single-location measurement and the multi-location measurement gave the same results.

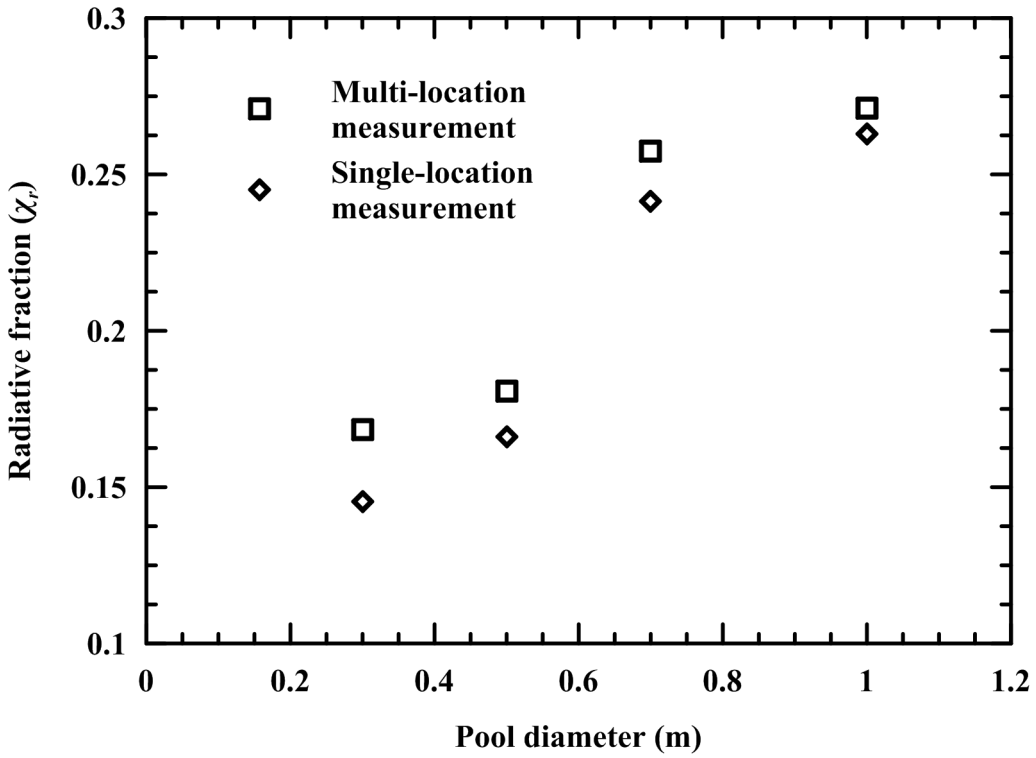

Fig. 3.36 Variation of radiative fraction with the pool diameter for diesel pool fires

3.14.4 Flame Height

Flame height is defined as the average position of the luminous flame (Consalvi *et al.*, 2007). The luminosity of the lower part of the flaming region appears fairly steady, whereas the upper part fluctuates or, in other words, is intermittent. Mean flame height is the height at which the intermittency is 0.5, *i.e.,* the height above which the flame appears half the time. The visual images are taken for diesel pool fires of diameters 0.3 m, 0.5 m, 0.7 m and 1.0 m. The flame height for diesel pool fires is found to be varying from $2.13D$ for smaller pool fire to $2.5D$ for larger pool fire.

3.15 Conclusions

Flame emissivity is an important parameter for characterizing an open pool fire. Flame emissivity is measured using three methodologies namely emissivity measurement by observing flame with reference to a reference body using infrared camera, emissivity measurement using infrared camera with reference to an electrically heated reference body

and inference of emissivity from mass burning rate. Emissivity measured by observing flame with reference to a reference body is corroborated with that measured by using electrically heated body as a reference for diameters 0.3 m, 0.5 m and 0.7 m.

Flame emissivity of pool fires is measured for diesel, gasoline, hexane and kerosene with different pool diameters (0.1 m, 0.13 m, 0.2 m and 0.3 m) at the base of the pool fire (Y/D = 2.5). Flame emissivities are measured by observing flame with reference to a reference body using infrared camera. It is observed that the flame emissivity increases with the pool diameter for all fuels covered in this study. The percentage deviation of emissivities of gasoline when hexane in the range of pool diameters considered is $\pm 10\%$. Both of these fuels are volatile in nature. Kerosene is observed to have higher emissivities where as diesel is observed to have lower emissivities when compared to other fuels. Variation of flame emissivity with the height of the flame along the center of diesel pool fire (0.30 m, 0.50 m, 0.7 m and 1.0 m) is investigated using multiple reference bodies at various heights. Emissivities at the tip of the flame are less than the emissivities at the base of the pool fire.

Mass burning rate is measured for diesel pool fires (0.30 m, 0.50 m, 0.7 m and 1.0 m). Mass burning rates for diesel pool fire increases with the increase in diameter. Estimated emissivities from mass burning rates are comparable with the average values obtained using infrared camera with reference to a reference body. The mean optical for diesel pool fires, $\kappa\beta$ is 1.16 m^{-1}, for gasoline pool fire is 1.52 m^{-1} and for hexane pool fire 1.1 m^{-1}.

Temperature and emissive power distributions of the diesel pool fires for diameters 0.30 m, 0.50 m, 0.7 m and 1.0 m are computed using infrared thermography by employing the emissivity values in the thermal images. It is observed that the maximum temperature lies at the bottom of the flame along the pool central axis and falls with the height.

The radiative fraction measured using single-location measurement underpredicted the values for lower diameters and are comparable for higher diameters with multi-location measurement. The radiation fraction for diesel pool fires vary from 0.17 to 0.27 for pool diameters from 0.3 m to 1.0 m.

CHAPTER 4

Fire Safety Distances for Open Pool Fires

4.1 Introduction

Fire safety distance (FSD) is of greater interest in view of the safety of fire fighters, safe distance for building constructions and also in emergency evacuation of people. Fire safety distance calculations also helps in arranging for the large scale experiments. FSD answers the questions like: the distance at which the controlling system has to be placed, the distance at which the thermal camera has to be placed without burning it out, nearest safe distance for a observer with and without protective clothes. The emissive power distributions that are measured in the previous chapter are utilized to measure the FSD of different pool fires. The objective of this work is to relax few too simplistic assumptions that were made in fire safety distance calculations. The model proposed in this study is easy to use and one can easily calculate the fire safety distance for a given fire scenario. Circular pool fires of diameters 0.5 m, 0.7 m, 1 m and a square pool fire of 4 m length are chosen to study the fire safety distances. Diesel, gasoline and hexane are used as fuels for all the circular pool fires and diesel is used in square pool fire. The temperature profile of the pool fires are measured using an infrared camera. These temperature profiles are used in computing the incident heat flux at different locations from each pool fire.

Table 4.1 Consequences of thermal heat flux on human bodies (Zarate *et al.*, 2008)

Heat flux (kW/m^2)	**Effects on a human body**
1.4	Harmless for persons without any special protection
1.7	Minimum required to cause pain
2.1	Minimum required to cause pain after 60 s
4.0	Causes pain after an exposure of 20 s(first degree burns)
4.7	**Causes pain in 15-20 s and burns after 30 s**
7.0	Maximum tolerable value for firefighters completely covered protected by special Nomex protective clothes
10.0	Certain polymers can ignite
11.7	Thin steel (partly insulated) can lose mechanical integrity
12.6	Wood can ignite after a long exposure; 100% lethality
25.0	Thin steel (insulated) can lose mechanical integrity
37.5	Damage to process equipment and collapse of mechanical structures

4.2 Fire Safety Distance

Fire safety distance is defined as that at which the thermal radiation flux is equal to some prescribed level. This level depends on what is to be conserved or protected (Atallah and Allan, 1971). The estimation of radiation flux from fires is very crucial and this provides a basis for establishing the safe zones for fire fighters and structures. Zarate *et al.* (2008) tabulated, from various sources, the consequences of diverse thermal fluxes and thermal radiation threshold values, as shown in Table 4.1. It shows the consequences of thermal radiation on human bodies. It is identified that a person is safe when he is exposed to heat fluxes less than 1.4 kW/m^2. In this region, no special protection is required for inordinately long time. A person experiences a first degree burn for a heat flux of 4.7 kW/m^2 in 30 s. These two limits are identified in all the measurements in this study.

4.3 Mathematical Modeling

The radiometric image that is obtained from the thermal camera is a two dimensional distribution comprising of number of pixels. The radiometric image is the representation of the equivalent energy release from the flame volume as if the whole energy is released from a vertical two-dimensional plain which is placed at the center of the pool. The thermal energy received by a person who is standing at some distance from the fire is due to contribution from all the pixels of the radiometric image. Emissive power at a pixel in

the radiometric image is given by Stefan-Boltzmann constant:

$$E_1 = \sigma \varepsilon_f T_1^4 \tag{4.1}$$

The heat flux passing through an area, A_2 from the pixel A_1 is

$$q''_{1-2} = \frac{F_{1-2} A_1 E_1}{A_2} \tag{4.2}$$

View factor, F_{1-2} is involved in the calculation procedure of heat flux at a distance from the radiometric image. Consider two parallel rectangles of area A_1 and A_2 separated by a distance of z m as shown in Fig. 5.10. The view factor as seen from A_1 to A_2 is given as Howell (2008):

$$f_{1-2} = \frac{1}{(x_2 - x_1)(y_2 - y_1)} \sum_{l=1}^{2} \sum_{k=1}^{2} \sum_{j=1}^{2} \sum_{i=1}^{2} (-1)^{(i+j+k+l)} G\left(x_i, y_j, \eta_k, \xi_l\right) \tag{4.3}$$

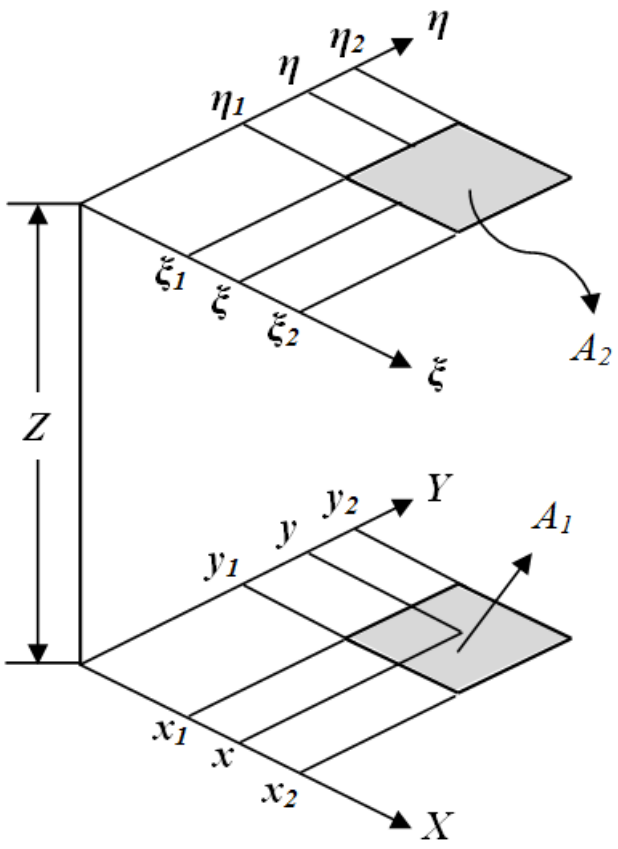

Fig. 4.1 Schematic of rectangle-rectangle in a parallel plane for finding the view factor (Howell, 2008)

$$G = \frac{1}{2\pi}\left[\begin{array}{c} (y-\eta)\left[(x-\xi)^2+z^2\right]^{1/2}\tan^{-1}\left\{\dfrac{y-\eta}{\left[(x-\xi)^2+z^2\right]^{1/2}}\right\} \\ +(x-\xi)\left[(y-\eta)^2+z^2\right]^{1/2}\tan^{-1}\left\{\dfrac{y-\xi}{\left[(y-\eta)^2+z^2\right]^{1/2}}\right\} \\ -\dfrac{z^2}{2}\ln\left[(x-\xi)^2+(y-\eta)^2+z^2\right] \end{array}\right] \tag{4.4}$$

The assumption made in deriving view factor is that the distance z is far greater than the sides of the rectangles considered. f_{1-2} is different to F_{1-2}, as the earlier represents the view factor between two rectangular surfaces, but the latter represents the view factor between apparent two dimensional pixel to a rectangular surface. From previous experiments, it is found that F_{1-2} is four times larger than f_{1-2} for all the diameters used in this work. Using Eq. (4.1) and Eq. (4.2) in Eq. (4.3), the heat flux passing through an area, A_2 from the pixel A_1 of pool fire can be calculated. Therefore, the net heat flux passing through an area, A_2 from the flame represented by n pixels is:

$$\dot{q}''_{f-A_2} = \sum_{i=1}^{n} \frac{(F_{i-2}A_1E_i)}{A_2} \tag{4.5}$$

The net heat flux from the flame is measured by moving the position of A_2 away from the axis of the pool and also moving along the height of the pool fire.

4.4 Experimental Setup

Open pool fire experiments are conducted for different pool sizes and different fuels. Circular pool fires of diameters 0.5 m, 0.7 m, 1 m with diesel, gasoline and hexane as fuels. The pans are made up of 2 mm thick mild steel and of 15 cm in height. Fuel is filled into the pans to a height of 10 cm. The wind velocity is less than 2 m/s during all the pool fire experiments that are conducted. Further details of these circular pool fire experiments are explained in Chapter 3. The fire safety distances are calculated from the temperature and emissive power distributions given in Chapter 3 and Appendix A.

A large square diesel pool fire experiment is conducted at Centre for Fire, Environment and Explosive Safety (CFEES), Delhi in India. This pool is made of brick and cement and of 4 m × 4 m in size. 1000 liters of diesel is filled into the pool above a 75 mm thick layer of water bed. For the square pool fire of 4 m length, the emissivity is considered as 0.94 from mass burning rate calculations Babrauskas (1983). Figure 4.2 shows the visual image of large pool fire experiment. Each experiment is conducted for at least 20 min. Thermal images are captured using VisIR 640, thermal camera. The images are time averaged to get the average temperature distribution of pool fire. The flame temperature distribution is shown in Fig. 4.3. It is observed that a maximum temperature of around

1000 °C at a height of 0.6 m axially. The emissive power distributions are computed using Eq. (4.1). Figure 4.3 shows the emissive power distribution of the large square pool fire. Using Eq. (4.5), the heat fluxes at different locations from the pool fire are calculated. The area, A_2 in Eq. (4.5) is taken 1 cm^2 in all the calculations, *i.e.,*, the heat fluxes mentioned in this study are averaged over an area of 1 cm^2.

4.5 Validation of Heat Flux Measurements

Experiments are conducted on a diesel pool fire of 0.3 m diameter using Schmidt Boelter gauge. The heat flux gauge is traversed along the vertical axis from a distance of 0.3 m from the pool center. In each position measurements are made for a period of 30 seconds to get time averaged heat flux at that location. Figure 4.5 shows the comparison of heat flux measurements at $Z/D = 1$ with heat flux transducer and camera for 0.3 m diameter pool fire. There is a reasonably good agreement between the computed results using Eq. (4.5) and measurements using heat flux gauge. A similar experiment on gasoline pool fire is also conducted on gasoline pool fire. It is found that the heat flux measurements using infrared camera are compared well with the Schmidt Boelter gauge.

Fig. 4.2 Large scale diesel pool fire experiment

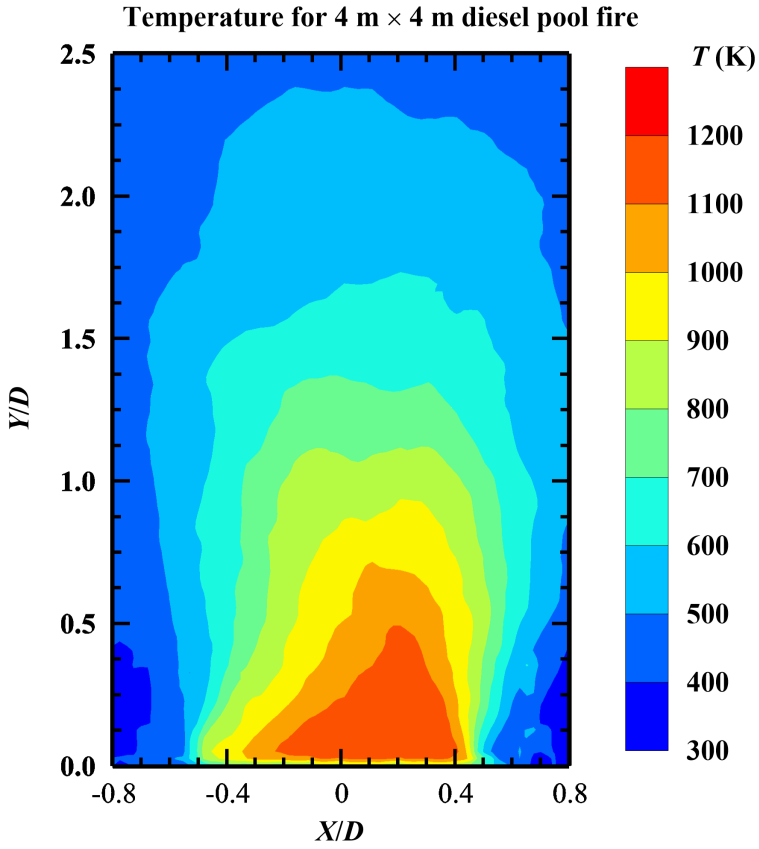

Fig. 4.3 Temperature distribution of a 4 m × 4 m diesel pool fire

4.6 Results and Discussions

The temperature distributions of pool fires are captured using an infrared thermal camera. Experiments are conducted on circular pool fires of diameters 0.5 m, 0.7 m and 1.0 m and a square pool of length 4 m. Figures 4.6 to 4.15 show the irradiance from pool fires of different sizes. The threshold values of 1.4 kW/m^2 (dotted line) and 4.7 kW/m^2 (solid red line) are marked in all the Figs. 4.6 to 4.15. The abscissa represents the distance from the pool center and the ordinate represents the height above the cylinder tip. The abscissa starts from $0.5D$, *i.e.*,, the tip of the mild steel cylinder.

It is observed from the Figs. 4.6 to 4.15, that the irradiance decreases as one moves away from the pool fire and is obvious as the farther the distance, lesser the influence of radiation from the fire. As the distance increases, the view factor from the flame to the object decreases and hence, decreases the radiation. The maximum heat flux is observed at the tip of the pool surface to a height of $1D$. Though the safety zones along the height are shown in this study, care is to be taken while considering the presence of soot and the availability of oxygen. The presence of soot and the availability of oxygen are not

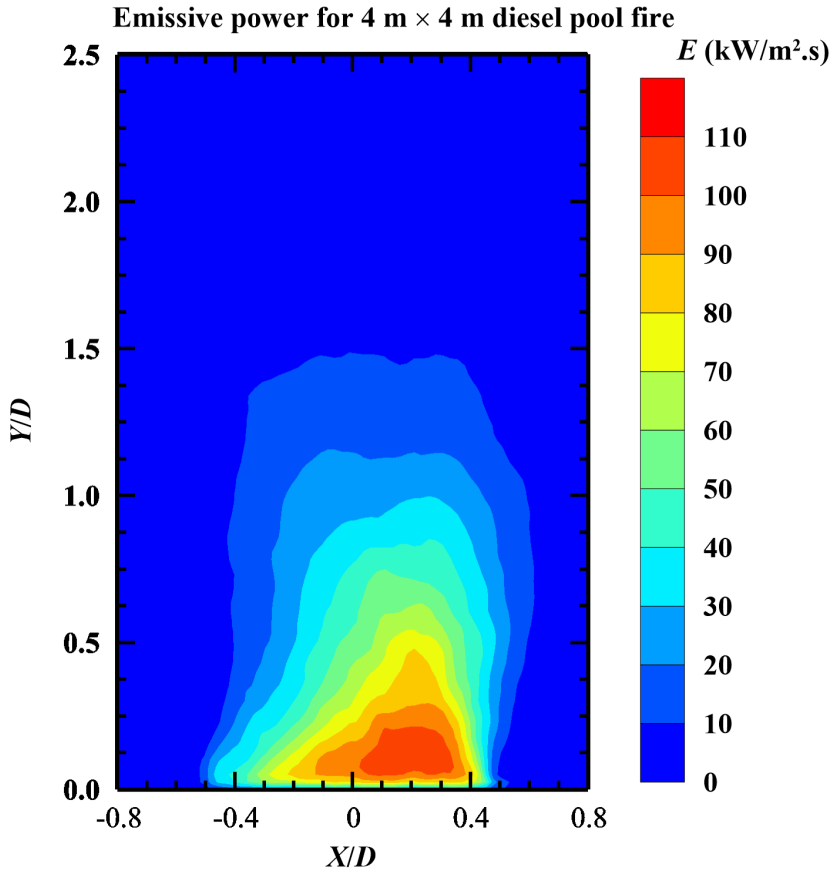

Fig. 4.4 Emissive power distribution of a 4 m × 4 m diesel pool fire

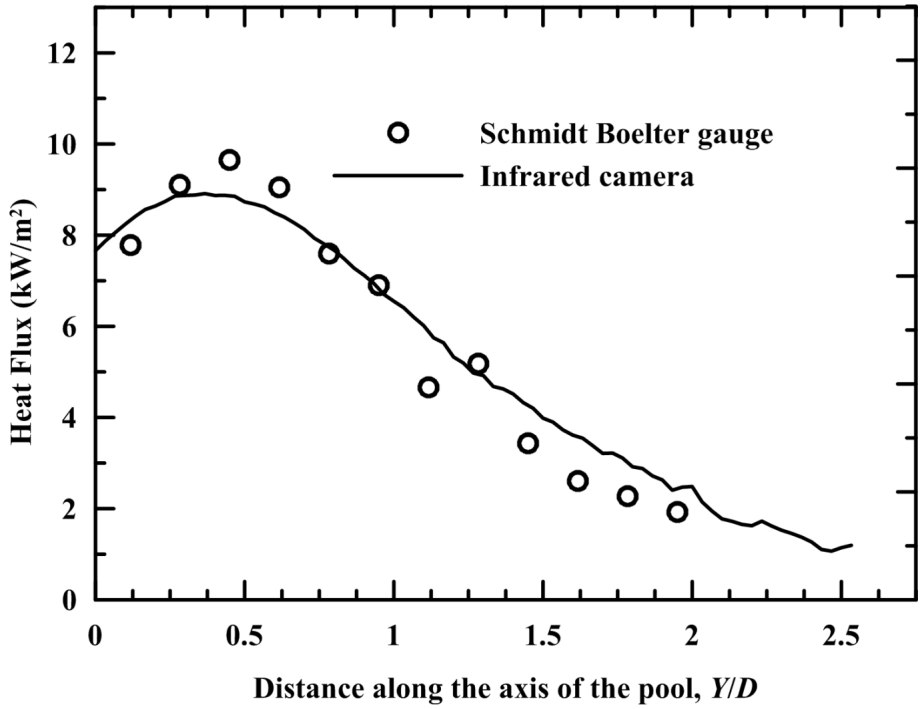

Fig. 4.5 Comparison of heat flux measurements at $Z/D = 1$ with sensor and infrared camera for diesel fire of 0.3 m pool diameter

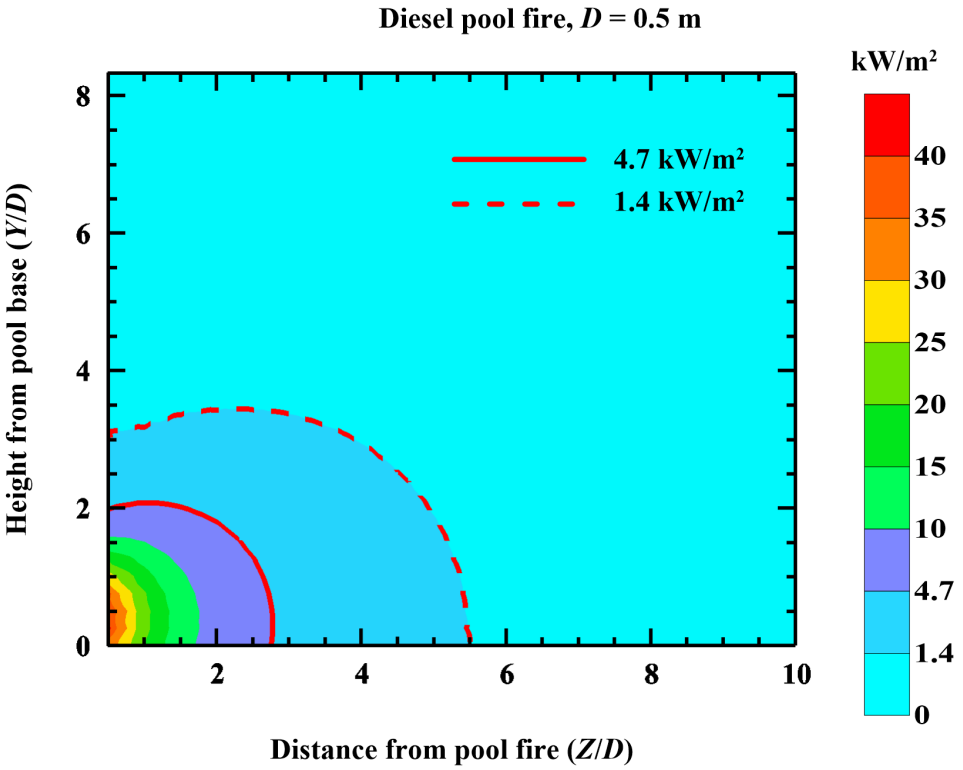

Fig. 4.6 Fire safety distances for a 0.5 m diameter diesel pool fire

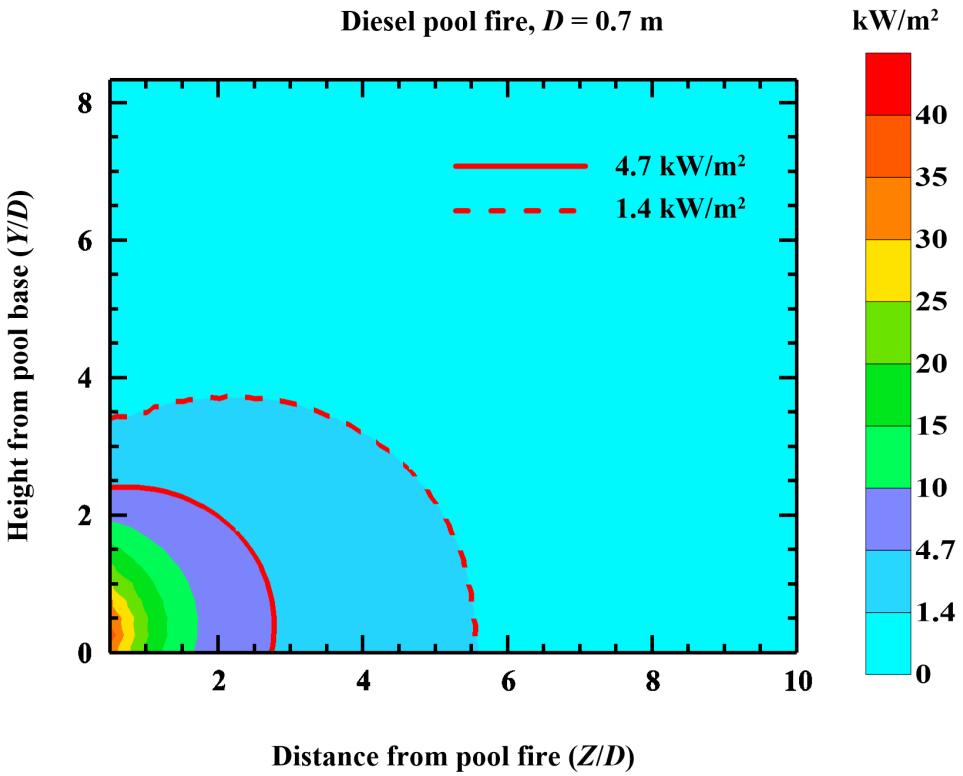

Fig. 4.7 Fire safety distances for a 0.7 m diameter diesel pool fire

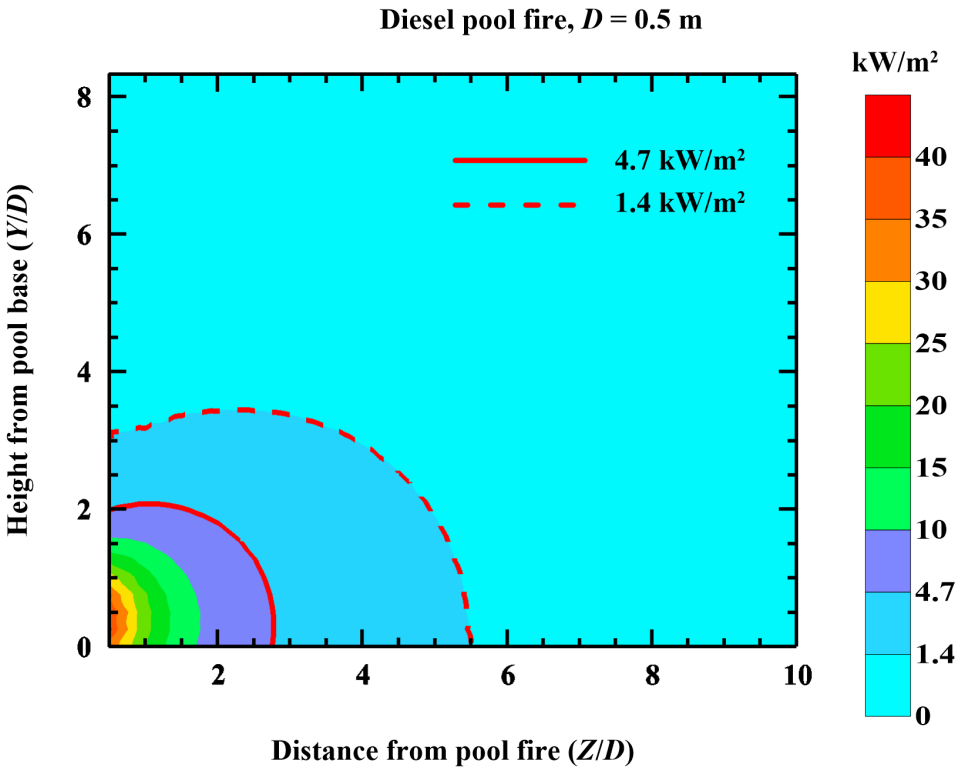

Fig. 4.8 Fire safety distances for a 1.0 m diameter diesel pool fire

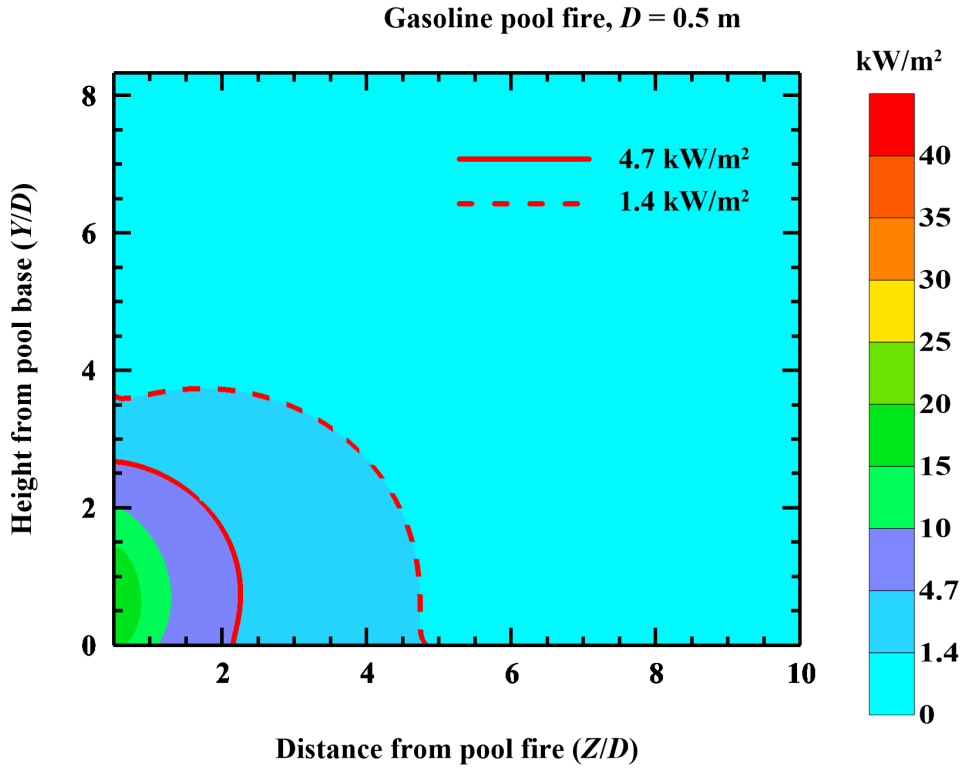

Fig. 4.9 Fire safety distances for a 0.5 m diameter gasoline pool fire

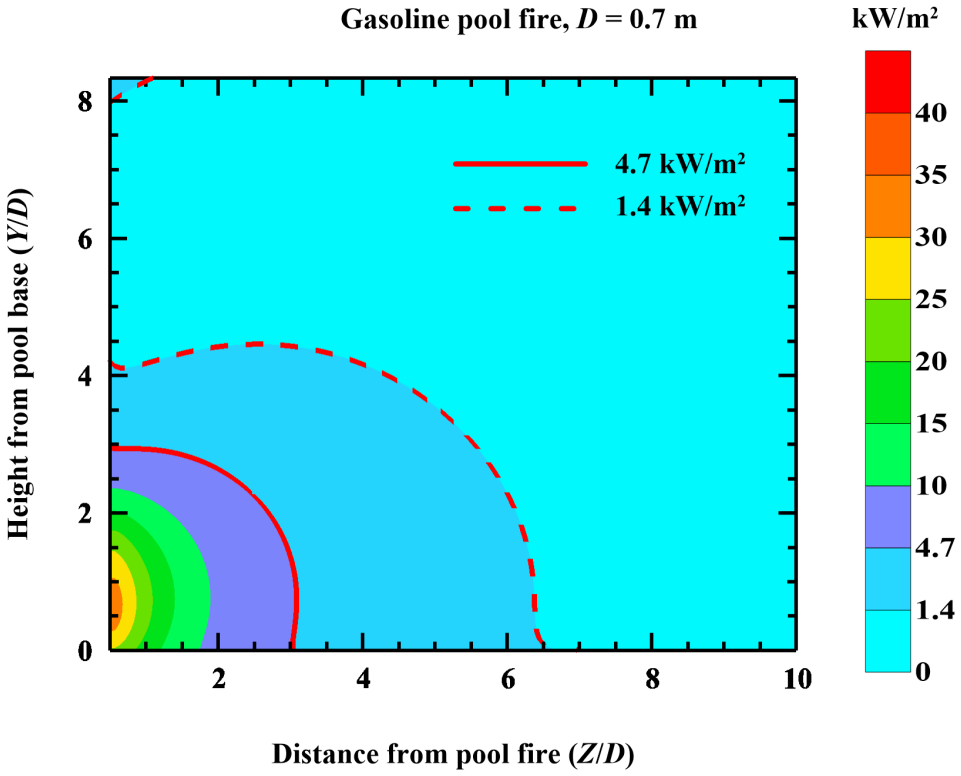

Fig. 4.10 Fire safety distances for a 0.7 m diameter gasoline pool fire

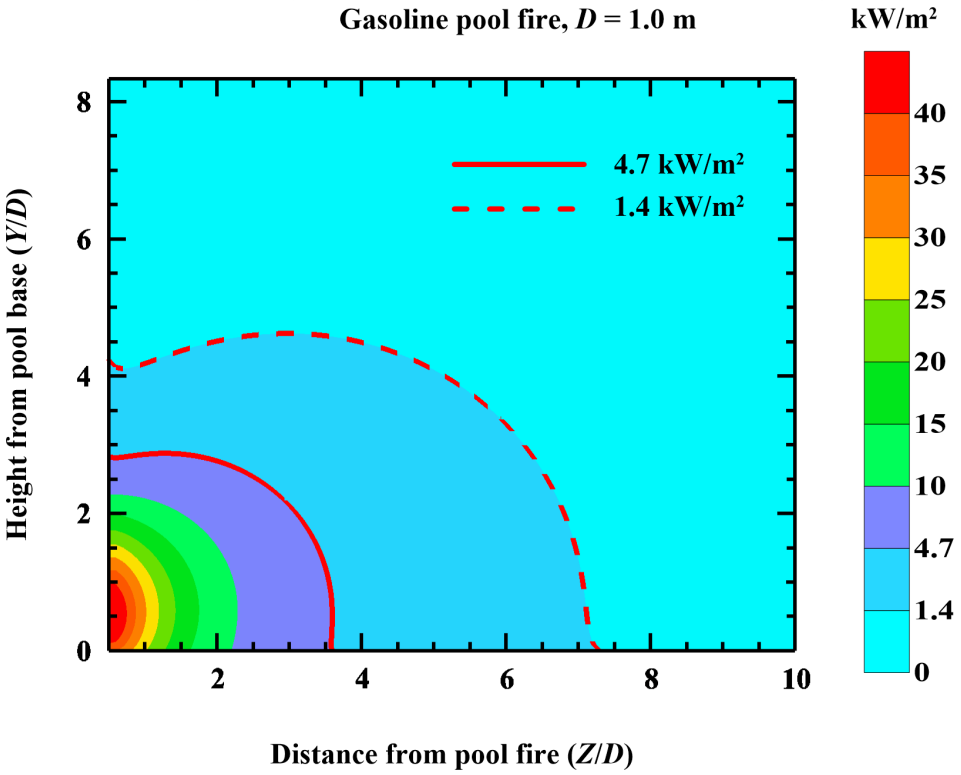

Fig. 4.11 Fire safety distances for a 1.0 m diameter gasoline pool fire

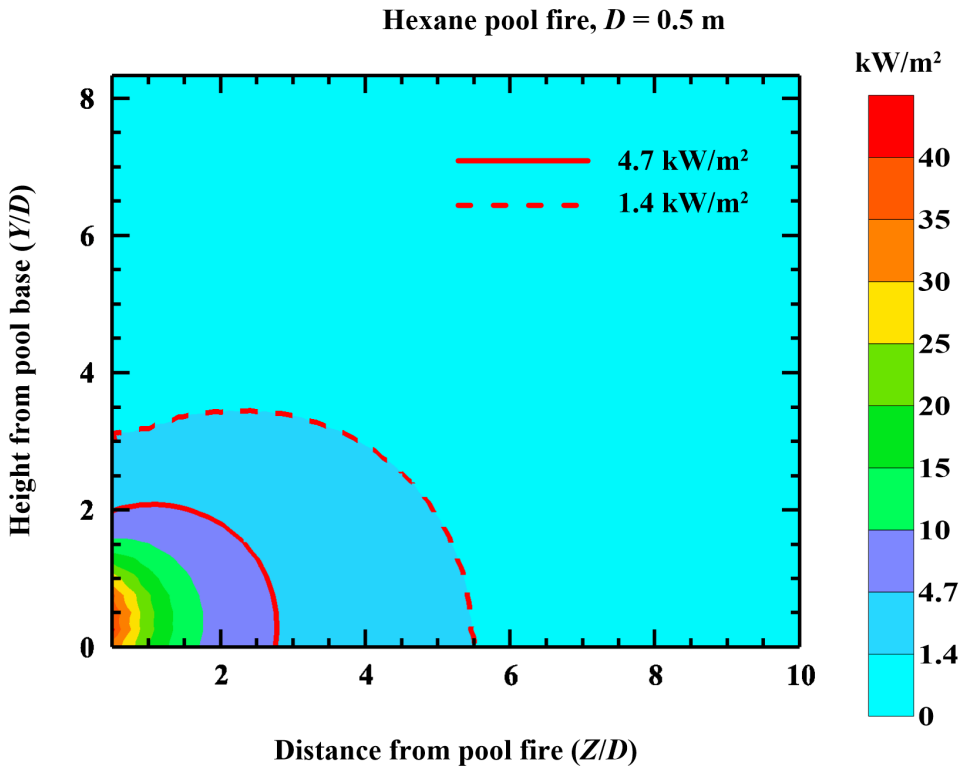

Fig. 4.12 Fire safety distances for a 0.5 m diameter hexane pool fire

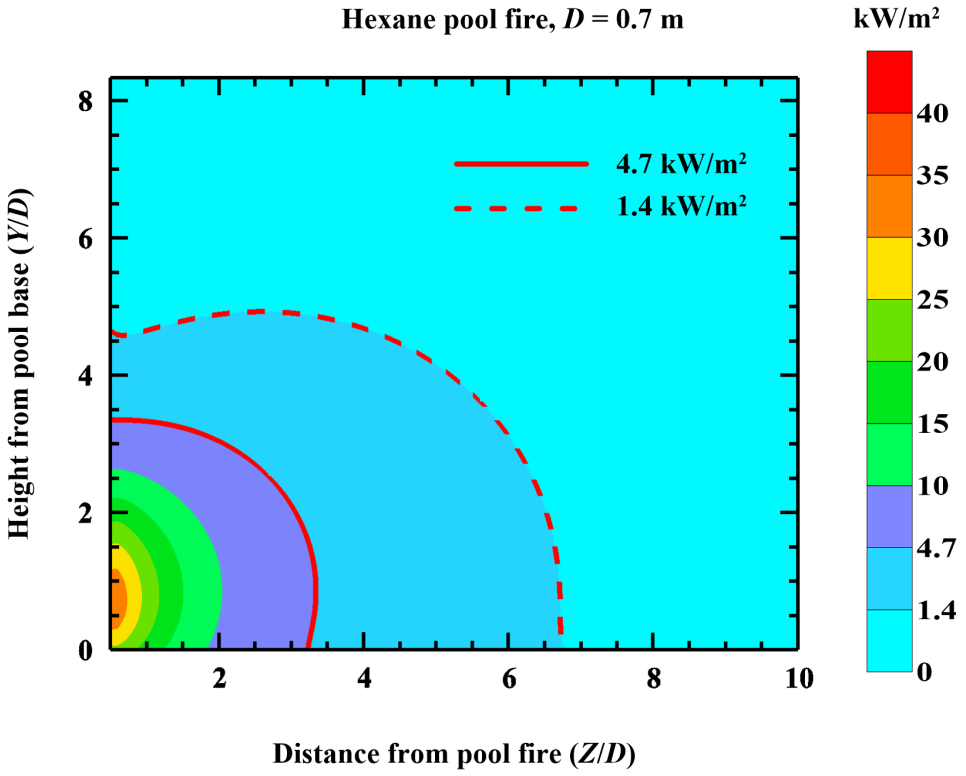

Fig. 4.13 Fire safety distances for a 0.7 m diameter hexane pool fire

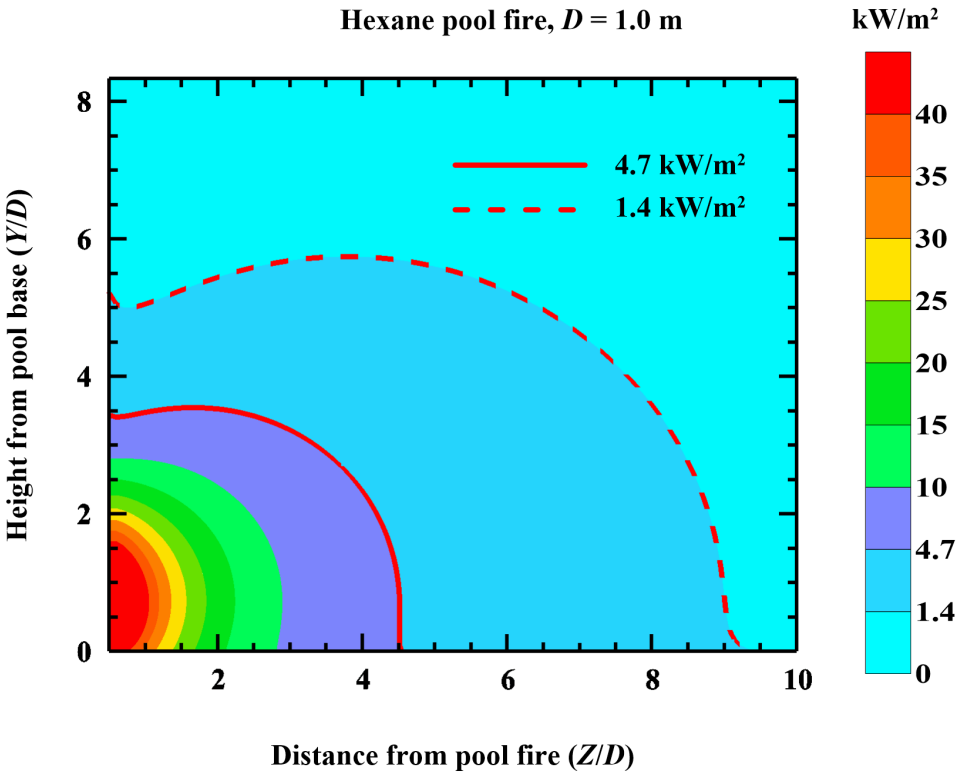

Fig. 4.14 Fire safety distances for a 1.0 m diameter hexane pool fire

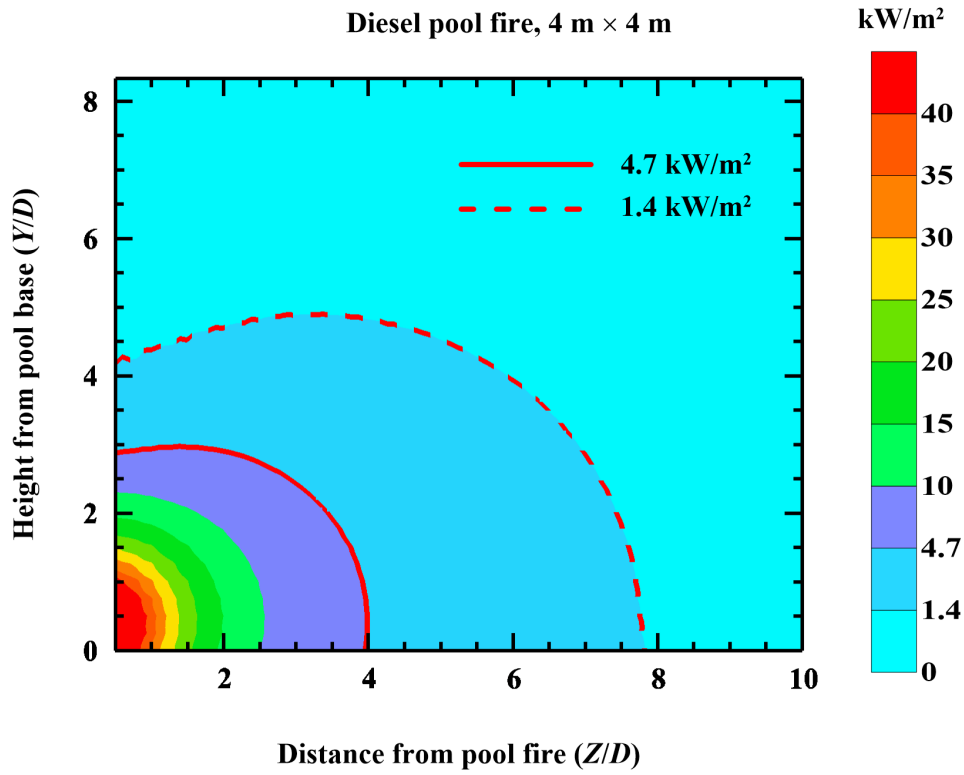

Fig. 4.15 Fire safety distances for a 4 m × 4 m diameter diesel pool fire

Table 4.2 Fire safety distances for different pool fires

	Pool diameter/length, *D*			
Fuel	**0.5 m**	**0.7 m**	**1.0 m**	**4.0 m**
Diesel	$5.5D$	$5.5D$	$5.7D$	$7.8D$
Gasoline	$5.7D$	$6.3D$	$7.1D$	-
Hexane	$4.5D$	$6.7D$	$9.2D$	-

considered in this study while prescribing the fire safety distances and is out of the scope of this work.

Figures 4.6 to 4.8 show the fire safety distances from circular diesel pool fires. For all the circular diesel pool fires, the safety zone, on the ground, is around $5.7D$ away from pool fire. The maximum heat flux received from these pool fires is around 45 kW/m^2. The safety zone in view of height is varying. Figures 4.9 to 4.11 are the computed fire safety distances for gasoline pool fires of diameters 0.5 m, 0.7 m and 1.0 m. For all the circular gasoline pool fires the safety zone, on the ground, is varying from $5D$ to $7D$ away from pool fire. The temperatures and the emissive powers of the gasoline fires are observed to be higher than that of the corresponding diesel pool fires.

Figures 4.12 to 4.14 are the computed fire safety distances for hexane pool fires of diameters 0.5 m, 0.7 m and 1.0 m. For all the circular hexane pool fires the safety zone, on the ground, is varying from $4.5D$ to $9.5D$ away from pool fire. The temperatures and the emissive powers of the hexane fires are observed to be higher than that of the corresponding diesel and gasoline pool fires. For the large square pool fire (Fig. 4.15), the person has to stand at least $8D$ away from pool fire. The maximum heat flux observed is around 75 kW/m^2 at the tip of the pool surface.

Table 4.2 shows the fire safety distances for different pool fires on ground level. It is observed that the hexane fuel is more dangerous than the other fuels that are considered in this study. Table 3.1 shows the boiling point temperatures and the mass burning rates of different pool fires. Boiling point temperature is a property of the fuel and is independent of the pool size, where as the mass burning rate depends on the size. Hexane has a low boiling temperature as compared to diesel and gasoline and hence evaporates even at lower temperatures. Hence, the mass burning rates of hexane are higher than the of the corresponding diesel or gasoline pool fires. This makes more fuel to burn and release more energy at a given instant.

A person with special fire safety protection dress can go nearer to the flame from safety zone, basing on the heat flux rating of the dress. Care must be taken before leaving the safety zone (1.4 kW/m^2). One has to check for any kind of exposure of body due

to wear or tear of the protective equipment. More precautions should be taken in case of high wind velocities. Flame gets tilted because of the wind and hence the person or the instrumentation or the objects may get affected, even if they are in the safety zone. The safety limits prescribed in this work are purely thermal with no consideration of the presence of soot that pollutes the air nor the absence of oxygen that is essential for human beings.

Using these plots, one can decide on the placement of instrumentation or any kind of equipment or sensors. Equipments with low operating temperatures should be kept in the safety zone. Proper insulation is required for all those instruments or equipments that are placed in high heat flux zones.

4.7 Conclusions

Fire safety distances for circular pool fires of 0.5 m, 0.7 m and 1.0 m diameters and a square pool fire of length 4 m are computed using infrared thermal camera. For all the circular pool fires the safety zone to stand or operate is around $5.7D$ for diesel fire, $5D$ to $7D$ for gasoline fire and $4.5D$ to $9.5D$ for hexane fire away from pool fire. The fire safety distance for large pool fire (4 m $\times$ 4 m) is around $8D$ away from pool fire.

CHAPTER 5

Partitioning Convective and Radiative Heat Fluxes Absorbed by a Lumped Body Engulfed in a Diffusion Flame

5.1 Introduction

In the previous chapters, the characterization of diesel pool fire is covered. Next pertinent question that arises is the thermal energy absorbed by the cask engulfed in a diffusion flame. Before undertaking the study of the simulated cask, study of the temperature distribution and thermal energy absorbed by a lumped body is investigated.

In the present study, heat flux absorbed by several lumped bodies that are engulfed in the pool fire are inferred. Diesel open pool fires of 0.5 m, 0.7 m and 1.0 m diameters are considered. Different sizes of brass and stainless steel (SS 304L) rods are used as lumped bodies. K-type thermocouple is embedded into the body to measure the transient temperature distribution of the body. Gas velocity at the location of immersion is measured using bidirectional probe. CFD modeling is carried out using FLUENT to obtain the correlations for circular cylinders in axial flow. The net heat flux absorbed by the body is computed using lumped body approach. Using simple energy balance, the net heat flux is divided into individual heat transfers with respect to the mode and directions of transfer: radiative heat gain, convective heat gain and radiative heat loss. A three dimensional formulation for an axi-symmetric pool fire of a measured flame shape, flame temperature and a gray flame absorption coefficient is employed to predict the temperature of the body engulfed in pool fires using the radiometric pool fire images.

5.2 Experimental Setup

Experiments are conducted on diesel pool fires of 0.5 m, 0.7 m and 1.0 m diameters. Fuel pans are made up of mild steel of 2 mm thick and 15 cm height. These pans are filled with diesel. Small amount of gasoline is used to ignite the diesel. Different sizes of brass and stainless steel (SS 304L) rods that are tabulated in Table 5.1 are used as lumped bodies. As shown in Fig. 5.1, all the bodies are positioned at a height of $0.2D$ axially from the pool surface of diameter, D. A K-type thermocouple is embedded at the center of the each body using screws. The temperature data from the thermocouples is collected through a data acquisition system.

Table 5.1 Sizes of lumped bodies used in pool fires

Pool fire diameter, D (m)	**Material**	**Size of the lumped bodies**	
		Diameter (d)	**Height (h)**
0.5, 0.7 and 1.0	Brass & SS304L	25.4 mm (1.0″)	25.4 mm (1.0″)
			38.1 mm (1.5″)
			50.8 mm (2.0″)
0.5 and 0.7	SS304L	50.8 mm (2.0″)	50.8 mm(2.0″)

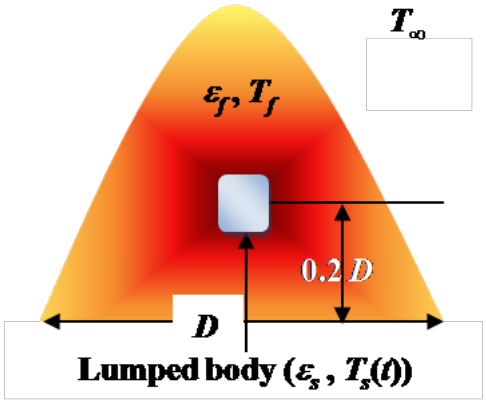

Fig. 5.1 Schematic of a lumped body engulfed in pool fire

5.3 Mathematical Modeling for Measuring Net Heat Flux Using Lumped Capacitance Model

Consider a pool fire of representative temperature, T_f . A lumped body is engulfed in a pool fire of flame emissivity, ε_f as shown in Fig. 5.1. Energy absorbed by the body is due

to the radiation from the flame and due to the convective heat transfer between flame and the body. It is given by:

$$\dot{q}''_{abs} = \varepsilon_s \varepsilon_f F \sigma \left(T_f^4 - (T_s)^4\right) + h\left(T_f - T_s\right) \tag{5.1}$$

where ε_s is the emissivity of the surface of lumped body, ε_f is the flame emissivity, F is the configuration factor from flame to the specimen and h is the convective heat transfer coefficient between the flame and the specimen and $T_s(t)$ is the temperature of the speciment (lumped body) at any instant, t. Heat flux leaving the body is due to the temperature difference between the body and the atmosphere. The specimen interacts with the atmosphere radiatively. It is given by:

$$\dot{q}''_{out} = \varepsilon_s \sigma \left(1 - \varepsilon_f\right)\left(T_s^4 - T_\infty^4\right) \tag{5.2}$$

where T_∞ is ambient temperature. Combining Eqs. (5.1) and (5.2) for the net heat flux into the body:

$$\dot{q}''_{net} = \dot{q}''_{in} - \dot{q}''_{out} \tag{5.3}$$

$$\dot{q}''_{net} = \varepsilon_s \varepsilon_f F \sigma \left(T_f^4 - T_s^4\right) + h\left(T_f - T_s\right) - \varepsilon_s \sigma \left(1 - \varepsilon_f\right)\left(T_s - T_\infty^4\right) \tag{5.4}$$

In Eq. (5.4), T_f is the representative flame temperature and is always higher than the temperature of the specimen. This value is taken from the thermal images given in Section 3.12. An average temperature value is computed for an area of size 4 cm $\times$ 4 cm with $0.2D$ as its center. ε_s is the emissivity of the specimen as given in Incropera and DeWitt (2002). ε_f, the flame emissivity can be obtained from mass burning rate as explained in Section 3.4. Convective heat transfer coefficient (h) can be obtained from Nusselt number and Prandtl number correlations. The only unknown in Eq. (5.4) is configuration factor, F.

If ρ is the density of the material, V is the volume of the body, C_p specific heat capacity and A_s is the surface area of the body exposed to flame, then the heat flux that is being stored in the body is:

$$\dot{q}''_{sto} = \frac{\rho V C_p}{A_s}\frac{dT_s}{dt} \tag{5.5}$$

Equation (5.5) assumes that the bodies engulfed in a pool fire are lumped. This lumped approach is valid for sufficiently small Biot number ≤ 0.1 (Incropera and DeWitt, 2002). Biot number is calculated taking into account the convection and radiation effect from the pool fire to the body. Biot numbers of the sizes of the rods that are shown in Table 5.1 are less than 0.1. The total net energy transferred to the body is stored in the body. Hence, from Eq. (5.5) takes the form:

$$\dot{q}''_{net} = \frac{\rho V C_p}{A_s}\frac{dT_s}{dt} \tag{5.6}$$

Net heat flux can be computed using central difference scheme from Eq. (5.6). Temporal variation of the properties is considered wherever applicable.

Combining Eqs. (5.4) and (5.6) to get the following equation:

$$\frac{\rho V C_p}{A_s}\frac{dT_s}{dt} = \varepsilon_s\varepsilon_f F\sigma\left(T_f^4 - T_s^4\right) + h\left(T_f - T_s\right) - \varepsilon_s\sigma\left(1-\varepsilon_f\right)\left(T_s^4 - T_\infty^4\right) \tag{5.7}$$

Under steady state conditions, net heat flux vanishes, *i.e.,*

$$\varepsilon_s\varepsilon_f F\sigma\left(T_f^4 - T_s^4\right) + h\left(T_f - T_s\right) - \varepsilon_s\sigma\left(1-\varepsilon_f\right)\left(T_s^4 - T_\infty^4\right) = 0 \tag{5.8}$$

$$F = \frac{\varepsilon_s\sigma\left(1-\varepsilon_f\right)\left(T_s^4 - T_\infty^4\right) - h\left(T_f - T_s\right)}{\varepsilon_s\varepsilon_f\sigma\left(T_f^4 - T_s^4\right)} \tag{5.9}$$

where T_s is the temperature of the speciment after reaching steady state. The configuration factor obtained from Eq. (5.9) is used in Eq. (5.4) to get the transient heat flux. In this methodology, the accuracy of the heat flux measurement depends on the accuracy of representing the flame temperature and the accuracy of measuring instruments. The results obtained from Eqs. (5.4) and (5.6) are compared to each other. Equation (5.4) gives the contribution with each individual mode of heat transfer in the energy balance.

5.4 Velocity Measurement at $Y/D = 0.2$

Estimation of heat transfer coefficient makes it necessary to measure the velocity of the flame at the location where the lumped body is located. In this study, velocity is measured at a height of $Y/D = 0.2$ from the pool surface using a bidirectional probe. Bidirectional probe was first introduced by Heskestad in 1974 and closely examined by McCaffrey and Heskestad (1976b). Bidirectional probe is made up of a brass tube of 1 mm thick, 1.5 cm in diameter and 3 cm length with a diaphragm at the center (Fig. 5.2). Two tubes of 6.35 mm diameter are pivoted on either side of the diaphragm as shown in the Fig. 5.3. These two tubes are encased in a mild steel water jacket of 1.91 cm diameter tube. Water is circulated through the water jacket from the front end to the rare to cool the tubes. Furness controls limited make FC012, micro-manometer (accuracy 1%) is used to measure the pressure difference at the end of two pivoted tubes. The measuring tip is aligned with the flame. The upstream tube senses the stagnation pressure and the downstream tap senses a pressure slightly less than static (McCaffrey and Heskestad, 1976b). This differential pressure, dp is converted into velocity using the relation:

$$u = \frac{1}{K}\sqrt{\frac{2dp}{\rho}} \tag{5.10}$$

where u is upstream velocity of combustion products and ρ is the density of the flue

Fig. 5.2 Bidirectional probe

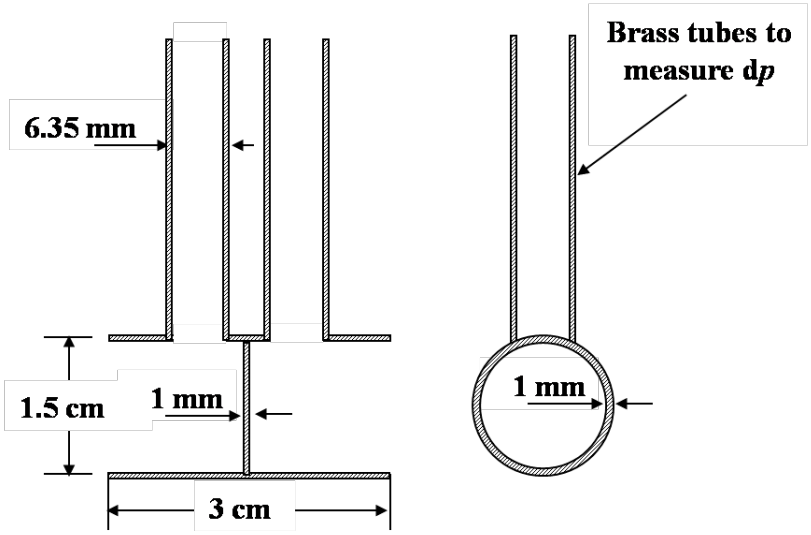

Fig. 5.3 Schematic of bidirectional probe (McCaffrey and Heskestad, 1976b)

gases at flame temperature, dp is in mm of water column. The calibration constant of the probe, K, as suggested by McCaffrey and Heskestad (1976b):
for $40 < \ \mathrm{Re}_d < 3800 \pm 5\%$

$$K = 1.533 - 1.366 \times 10^{-3}\ \mathrm{Re}_d + 1.688 \times 10^{-6}\ \mathrm{Re}_d^2 - 9.706 \times 10^{-10}\ \mathrm{Re}_d^3 + 2.555 \times 10^{-13}\ \mathrm{Re}_d^4 - 2.484 \times 10^{-17}\ \mathrm{Re}_d^5 \tag{5.11}$$

where Re_d is based on the tube diameter. This measured velocity is used for estimating Reynolds number which is essential for the determination of heat transfer coefficient. Table 5.2 shows the velocity of different pool fires. The differential pressure, dp, is very low and hence, the gas velocity is very low. From Table 5.2, it is observed that the velocity increases with the increase of flame diameter. The uncertainty in the velocity measurement is 1%.

Table 5.2 Gas velocity for different pool fires at $Y/D = 0.2$

Pool Diameter, D (m)	Differential pressure, dp (mm of water column)	Velocity, u (m/s)
0.5	0.064	1.53
0.7	0.067	1.57
1.0	0.085	1.79

5.5 Correlations for Nu for the Cylinder in Axial Flow

The measured velocity of the flame using bi-directional probe is used as the boundary condition to estimate the heat transfer coefficient. A two dimensional axi-symmetric numerical domain of 25.4 cm × 25.4 cm is chosen as shown in Fig. 5.4. Grid independency is checked for the different grid sizes and found that the optimal grid size of each cell is 1.27 mm × 1.27 mm. The boundary conditions are: velocity inlet at $x = 0$; outflow at $x = 25.4$ cm; axis at $y = 0$ and adiabatic wall at $y = 25.4$ cm. The cylinder outline is modeled as constant temperature wall at 500 K. In Fig. 5.4, l is the length of the cylinder and d is the diameter of the cylinder.

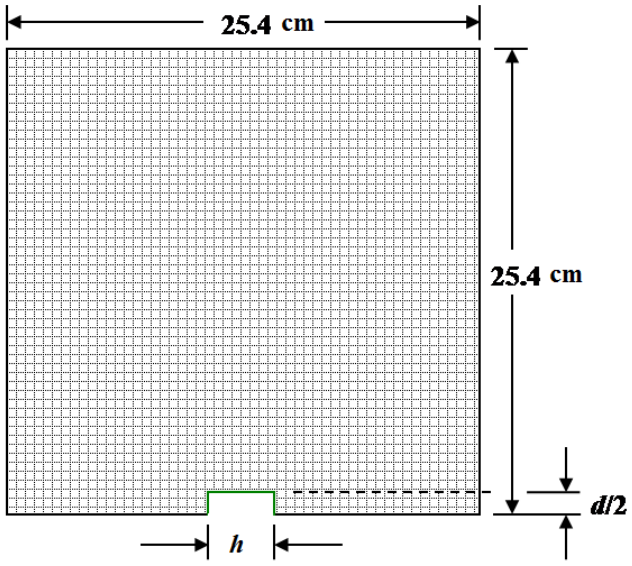

Fig. 5.4 Numerical grid for computations on flow over a cylinder

Reynolds number is varied by varying the inlet velocity. Simulations are carried out and the Nusselt number results are validated with Hadad and Jafarpur (2011) for $h/d = 1$ and 2. Simulated results are within 9% of that reported by Hadad and Jafarpur (2011). The data reported by them is for Reynolds numbers less than 445. Characteristic length (D_e)

in the Reynolds number is defined as the square root of the bathing area of the cylinder.

$$\mathrm{Re} = \frac{uD_e}{\nu} \tag{5.12}$$

where U is the fluid velocity in the vicinity of the body, ν is the kinematic viscosity and the characteristic length, D_e is defined as:

$$D_e = \sqrt{\pi dh + 2\left(\frac{\pi}{4}d^2\right)} \tag{5.13}$$

The numerical results are obtained for Reynolds number ranging from 50 to 4000. A curve fit is obtained for all the three configurations: $h/d = 1$, 1.5 and 2. These relations are as follows:
for $h/d = 1$ and $20 < \mathrm{Re} < 1500$,

$$\mathrm{Nu} = 4.635 + 0.6054\ \mathrm{Re}^{0.5}\ \mathrm{Pr}^{1/3} \tag{5.14}$$

for $h/d = 1.5$ and $20 < \mathrm{Re} < 1500$,

$$\mathrm{Nu} = 7.575 + 0.4331\ \mathrm{Re}^{0.5}\ \mathrm{Pr}^{1/3} \tag{5.15}$$

for $h/d = 2$ and $20 < \mathrm{Re} < 4000$,

$$\mathrm{Nu} = 6.341 + 4.593\ \mathrm{Re}^{0.5}\ \mathrm{Pr}^{1/3} \tag{5.16}$$

These correlations are used in modeling the thermal energy absorbed by cylinder engulfed in a pool fire. The flow field gets complex when a cylinder is engulfed in a pool fire. The velocities given in Table 5.2 and the Nusselt number correlations given in Eqs. (5.14) to (5.16) do not account for the change in the flow field due to the presence of an object in the flow field. Hence, these relations are only approximate and gives an insight about the contribution of the convective heat transfer in a pool fire quantitatively.

5.6 Results and Discussions

5.6.1 Experimental Results

The transient temperature distributions of the lumped bodies in each of the experiment are collected for every second. The transient temperature distribution of bodies engulfed in pool fires are shown in Fig. 5.5. Figure 5.5 suggests that the temperature of the body increases to a certain extent and then becomes steady. Before the ignition, the cask is at atmospheric temperature. It is clearly observed that irrespective of the size or material

of the body, body attained higher temperatures in pools with higher diameter and in a faster rate. Higher diameter pool fires have higher emissivities implying that flame emits more energy radiatively. From Table 5.2, it can be seen that the gas velocity increases with diameter and so the heat transfer coefficient is higher for higher diameter pool fires. This shows that convective heat transfer from the flame to the body engulfed in flame is higher for higher diameter pool fires.

Figures 5.6 to 5.8 show the heat flux distribution on to cylindrical rods engulfed in different pool fires. All the graphs on the left side are of the brass rods and the graphs on the right side are of the stainless steel rods. The total energy observed by the body (black line) is obtained using Eq. (5.6). Net heat flux falling on to the body (dotted line) is computed from Eq. (5.4). Net energy absorbed per unit area is divided into three different components: the radiative heat transfer to the body per unit area (blue line), the convective heat transfer to the body per unit area (red line) and the radiative heat loss to the ambient (green line). All these three components are the three terms on the right hand side of Eq. (5.4) respectively.

The first derivative of temperature in Eq. (5.6) is computed using central difference scheme, taking into account the previous and the next time step. The representative flame temperatures are taken from the thermal images. All the required material properties for brass and stainless steel are taken from Incropera and DeWitt (2002). The energy stored per unit area computed using Eq. (5.6) starts from zero as the fire takes some time to reach steady state. Initially, the body is at lower temperature compared to fire and so the maximum heat transfer. As the temperature of the body rises, the temperature difference between the body and flame decreases causing a decrement in the energy absorbed. It can be seen that as the diameter of the pool increases, the heat transfer or energy stored per unit area also increases.

After a certain time (above 400 s) the temperature value is oscillating around an average value. From this time onwards, the lumped body is assumed to achieve steady state. The configuration factor for each lumped body in all the diameters is obtained using Eq. (5.9) and the temperature data of the corresponding lumped body. All these values are tabulated in Table 5.3. From Table 5.3, it is observed that the F is within the uncertainty limits for different materials. This may be due to the small size of the bodies when compared with the pool fires. F varies with the pool diameter. These configuration factors are used in Eq. (5.4) to get the net heat flux. From Fig. 5.5, comparing temperature distributions of brass with SS 304L, it is observed that SS 304L rods absorbed more heat flux than brass rods by nearly 33%. SS 304L has more volumetric heat capacity than brass material.

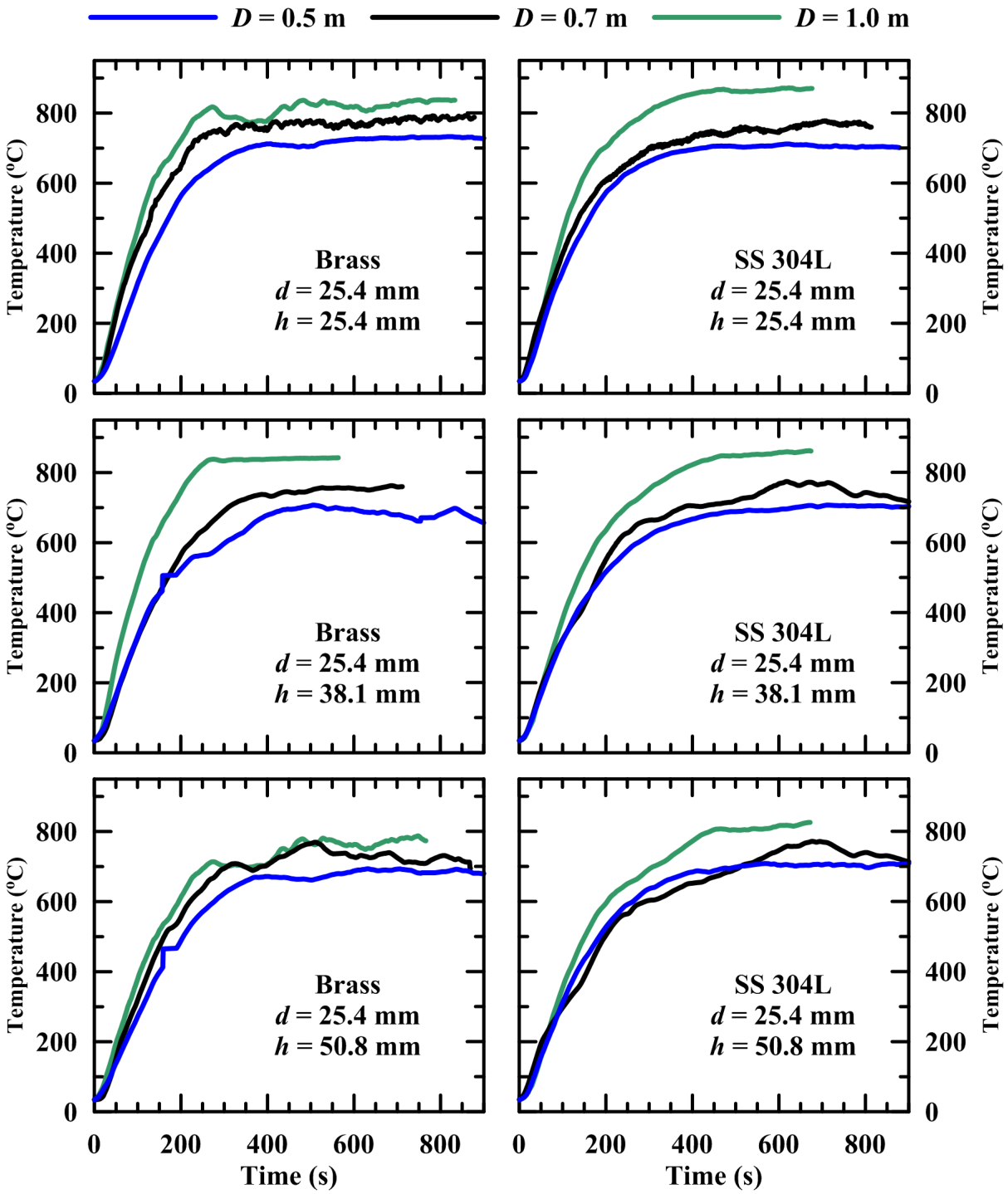

Fig. 5.5 Temperature distribution of different cylinders engulfed in diesel pool fires of different pool diameters

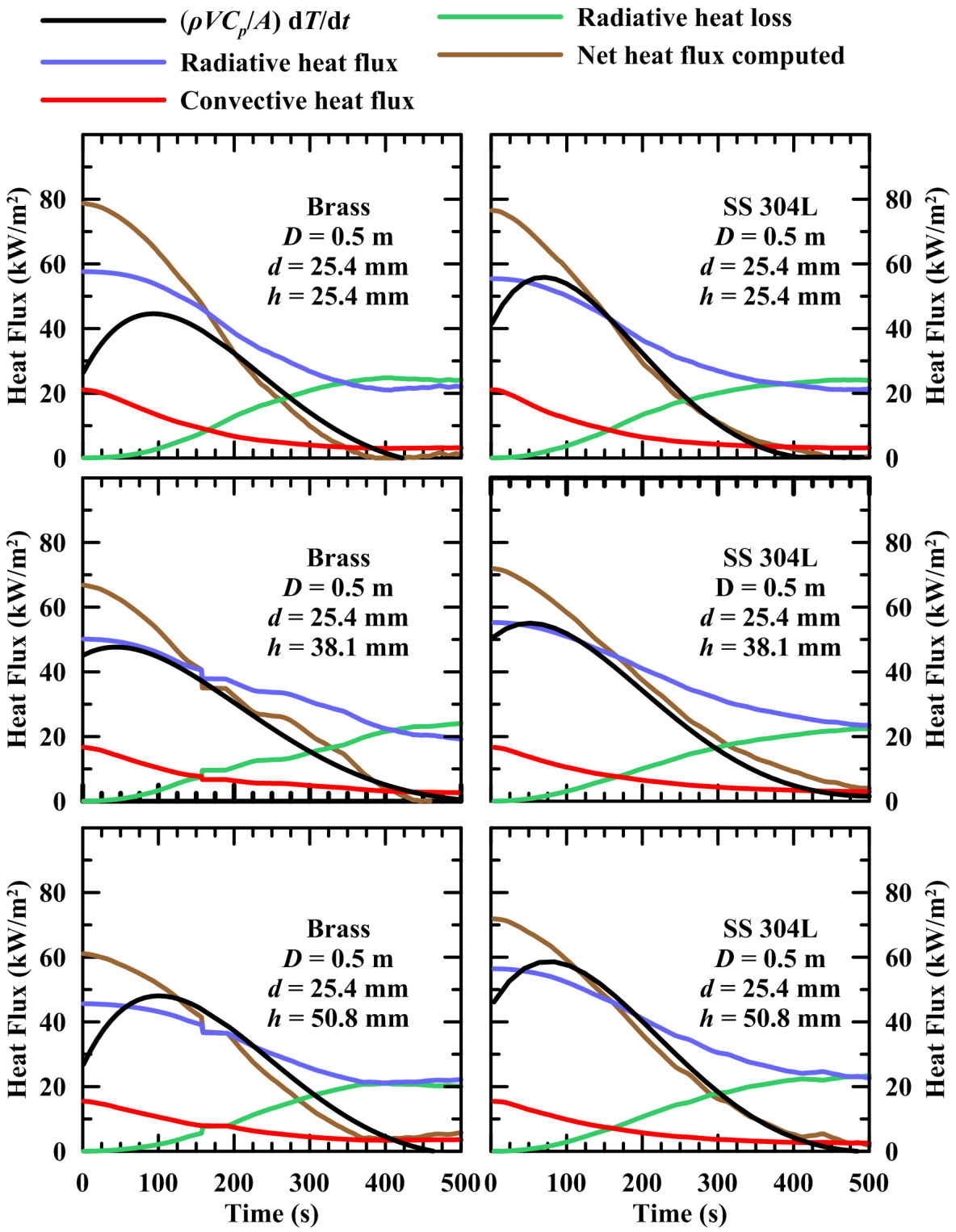

Fig. 5.6 Heat flux distribution of cylinders in a 0.5 m pool fire

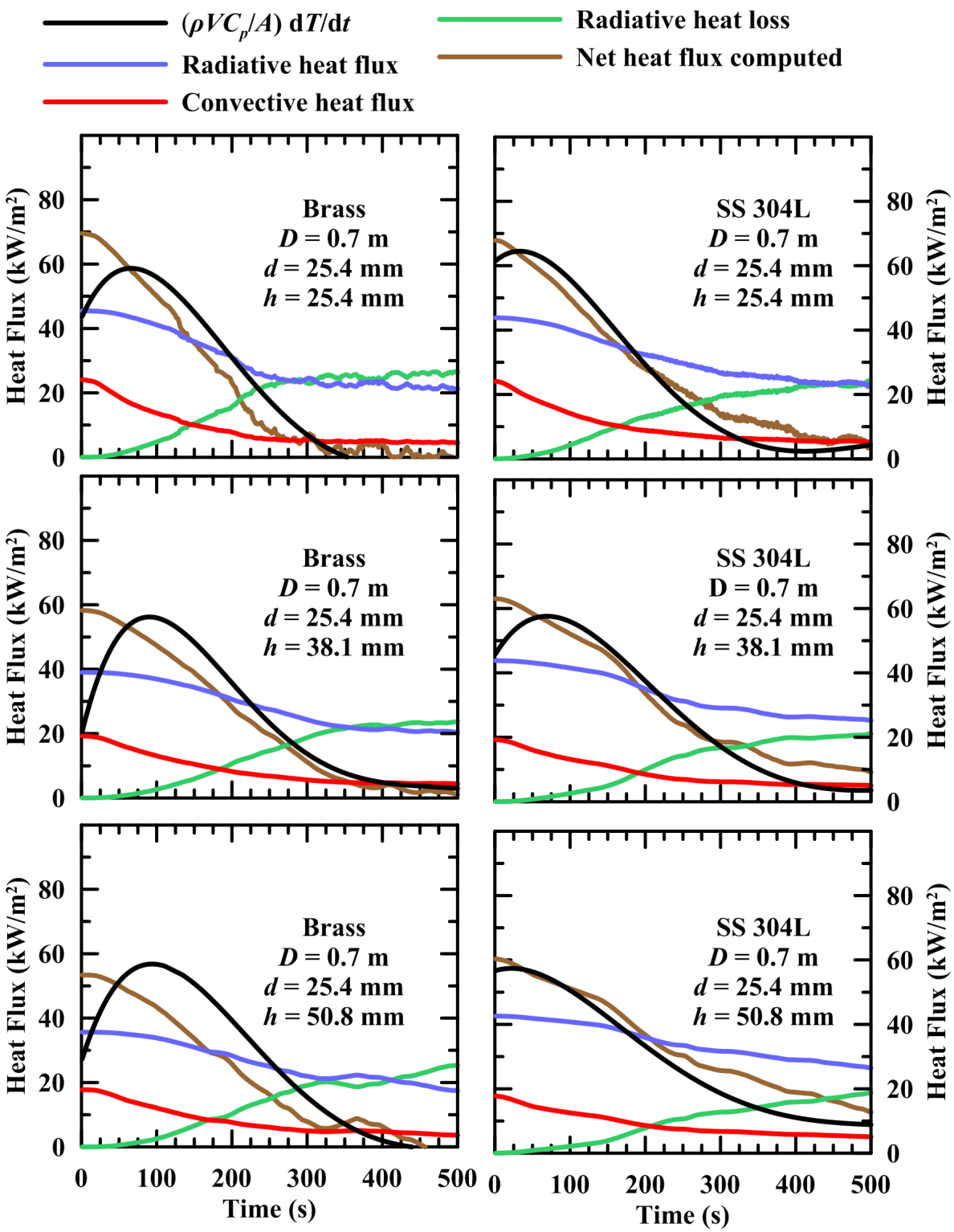

Fig. 5.7 Heat flux distribution of cylinders in a 0.7 m pool fire

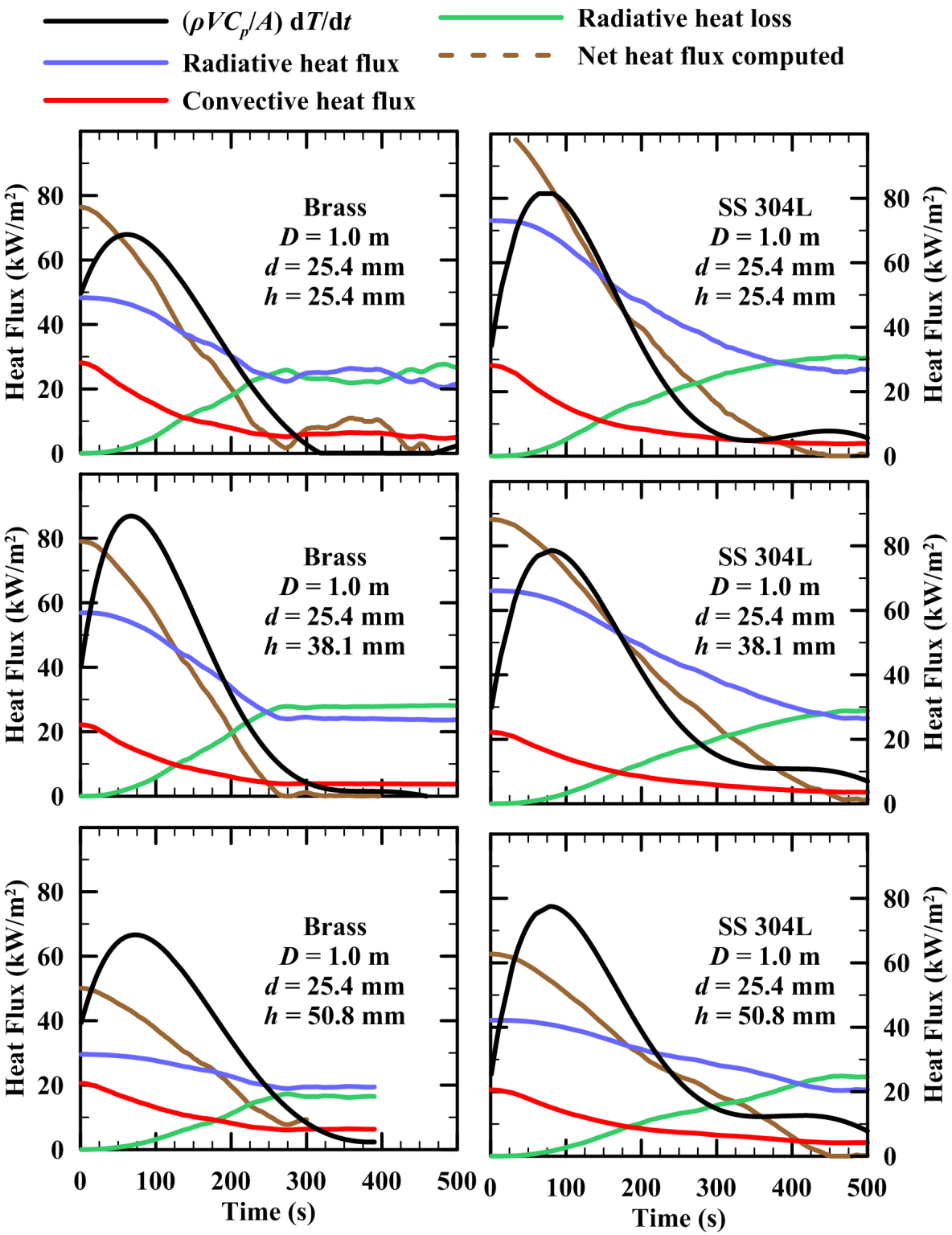

Fig. 5.8 Heat flux distribution of cylinders in a 1.0 m pool fire

Table 5.3 Configuration factors for different bodies in different pool fires

	Size of the body		Configuration factor, F		
Material	d **(mm)**	h **(mm)**	$D = 0.5$ **m**	$D = 0.7$ **m**	$D = 1.0$ **m**
Brass	25.4	25.4	0.77	0.39	0.36
	25.4	38.1	0.67	0.34	0.43
	25.4	50.8	0.61	0.31	0.22
SS 304L	25.4	25.4	0.74	0.38	0.55
	25.4	38.1	0.74	0.38	0.49
	25.4	50.8	0.75	0.37	0.31
	50.8	50.8	0.72	0.72	-

Though the energy computed from Eq. (5.4) is not able to pick up the initial trend, the main advantage of Eq. (5.4) is its ability to differentiate the energy into different components. A body engulfed in a pool fire will experience more energy transfer by radiation than by convection at least for the body sizes considered in this work. This is because of very high temperatures ($> 700\,^{\circ}$C) and low velocity (< 2 m/s). The radiative heat loss from the specimen to the surrounding atmosphere is almost zero during the initial period as the temperature of the specimen is very much comparable to the atmospheric temperature. As the time progresses both the radiative and the convective heat transfers decreased to a certain value whereas the radiative heat loss to atmosphere has increased to a certain value.

5.7 Three Dimensional Formulation for an Axisymmetric Pool Fire

A three dimensional formulation is adapted to predict the temperature of the cylinder engulfed in pool fire. This procedure uses the thermal images of the pool fire captured by thermal camera. These thermal images are the two-dimensional temperature representation of pool fires. Figures 3.16 and 3.17 show the two-dimensional temperature distribution of different diesel pool fires. A simple numerical code is written to convert the two-dimensional thermal images to three-dimensional thermal images. The two-dimensional thermal image is rotated along axis. A three-dimensional numerical grid is made and each control volume is given appropriate temperature obtained by rotating the two-dimensional thermal image. Now, the energy equation is solved for a body in a pool fire to get the temperature distribution of the body with time.

Flame volume may be visualized as a combination of number of two-dimensional plain layers. A two-dimensional radiometric image can only give information of the radiation coming from all of these two-dimensional plain layers cumulatively, but not individually. The radiation from the extreme end layer (farthest layer from the camera) of the flame has to penetrate all the other flame layers in order to be perceived by the camera. However, the radiation from the layer which is nearer to the camera can directly be perceived by the camera. Hence, the radiometric image is the representation of the equivalent energy release from the flame volume as if the whole energy is released from a vertical two-dimensional plain which is placed at the center of the pool. Therefore, the heat flux calculated at a distance from the radiometric image must be equivalent to that measured from the flame by the heat flux sensor at the same location.

Figures 3.18 to 3.21 show the temperature variation along different planes of different pool fires. It is observed that the temperatures on either side of $X/D = 0$ are symmetric. Figure 5.9 shows the flame width from the center of the axis for 0.5 m diesel pool fire. Flame width is obtained by measuring the radial distance from the axis at which the temperature reduces to half that of the temperature at axis. That is, the temperature at flame width is half of the temperature at axis. It is observed that the flame width is symmetric along the axis. Hence, it can be concluded that the flame is axi-symmetric.

Consider a cylinder engulfed in a pool fire. This cylinder receives heat from the flame by radiation and convection. The cylinder loses its heat to the cold atmosphere. The three-dimensional temperature data is divided into control volumes. The net heat flux from the flame to the body is the combination of heat fluxes from each control volume to the body and the heat loss from the body.

5.7.1 Radiative Heat Flux to the Body

The heat transfer to the body from each individual control volume farther from the body is given by the following relation:

$$\dot{q}''_{rad-CV} = \varepsilon_s \sigma \frac{F}{dA} \left(T_f^4 - T_s^4\right) \tag{5.17}$$

where F is the configuration factor from the control volume, dV, to the differential area dA on the body. F is given by (Tunc and Venart, 1984):

$$F = 4\kappa dV \cos\phi \frac{dA}{4\pi s^2} \exp(-\kappa s) \tag{5.18}$$

where dV is the volume of the control volume, κ is the optical thickness of diesel pool fire, s is the distance between the control volume and the surface of the body, ϕ is the inclination of dA with respect to dV. Optical thickness is 1.16 m^{-1} for diesel pool fires (Section 3.10).

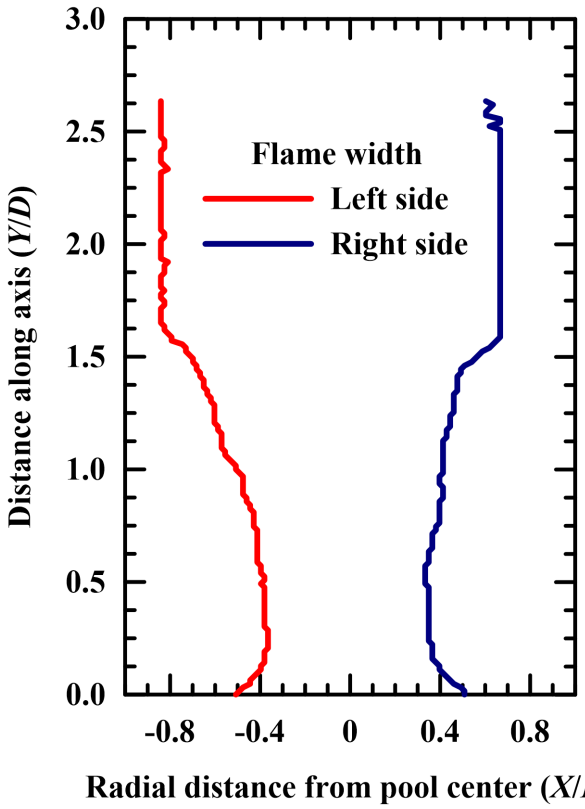

Fig. 5.9 Temperature along the flame width on both sides of the axis for a 0.5 m diesel pool fire

All geometrical variables in Eq. (5.18) can be defined in terms of distances between dA and dV (Tunc and Venart, 1984). dA can be a differential area on the circumference of the body or perpendicular to the axis of the body.

$$\cos\phi = (z - h_1)/s \tag{5.19}$$

where h_1 is the distance between dV and dA along the axis of the pool and s is the distance between dV and dA.

Radiative heat flux from each control volume to the surface of the body is computed using Eq. (5.17). The total radiation received by the body from all the control volumes is given by summation of all the individual heat fluxes, *i.e.,*

$$\dot{q}''_{rad} = \sum_{CV} \dot{q}''_{rad-CV} \tag{5.20}$$

5.7.2 Convective Heat Flux to the Body

The velocity of the flame in the vicinity of the body is measured using bidirectional probe and the details are given above. The heat transfer correlations in Eqs. (5.14) to (5.16)

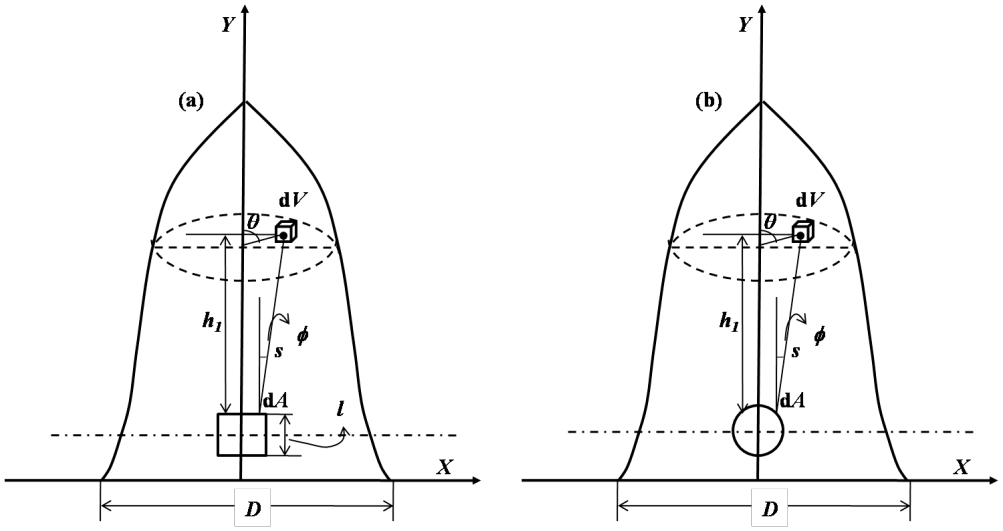

Fig. 5.10 Geometries to find view factor: (a) Normal of dA is along the axis of the pool fire, (b) Normal of dA is perpendicular to the axis of the pool fire

are used in these in these numerical simulations. The convective heat transfer from the flame to the body is given by:

$$\dot{q}''_{conv} = h\left(T_f - T_s\right) \tag{5.21}$$

The average temperature of the control volumes engulfing the body is taken as the flame temperature. For this purpose a region of 4 cm × 4 cm × 4 cm is selected to get the averaged flame temperature. It is observed that the averaged flame temperature value changes by only 6°C for different areas of selection: 4 cm^3 and 6 cm^3 regions. All the properties of flame are taken as that of air at film temperature (average of body temperature and flame temperature averaged within the domain).

5.7.3 Energy Balance

The body loses some of its energy to the ambient. This energy has to be transmitted through the flame. The radiative heat loss to the ambient from the body is given by:

$$\dot{q}''_{loss} = \varepsilon_s \sigma \left(1 - \varepsilon_f\right)\left(T_s^4 - T_\infty^4\right) \tag{5.22}$$

The net energy stored in the body is given by:

$$\dot{q}''_{sto} = \frac{\rho V C_p}{A_s}\frac{dT_s}{dt} \tag{5.23}$$

Combining Eqs. (5.17) and (5.20) to (5.23), the energy balance at the surface of the body leads to:

$$\frac{\rho V C_p}{A_s}\frac{dT_s}{dt} = \sum_{CV}\left[\varepsilon_s\sigma\frac{F}{dA}\left(T_f^4 - T_s^4\right)\right] + h\left(T_f - T_s\right) - \varepsilon_s\sigma\left(1-\varepsilon_f\right)\left(T_s^4 - T_\infty^4\right) \quad (5.24)$$

5.7.4 Algorithm

The only unknown in Eq. (5.24) is the temperature of the specimen at each time step, T_s. The initial condition is:

$$T_s(t=0) = T_\infty \quad (5.25)$$

Equation (5.25) is solved using fourth-order RungeKutta method to get the transient temperature of the body. A time step of one second is chosen after sensitivity analysis. The numerical code is run for different sizes of the cylindrical bodies. Figure 5.11 shows the flow chart for the numerical program. Scilab (version 5.3.3) is used to run the numerical code. Each simulation takes 4 hours on a multi core Xenon processor. The temporal variation in the properties of flame and the cylinder material (brass and SS 304L) are considered. Simulations are run for cylinders of diameter, $d = 25.4$ mm given in Table 5.1. The predicted temperature data is compared with the experimental data.

5.7.5 Three Dimensional Formulation Results

Simulations are performed for cylinders given in Table 5.1. Figure 5.12 show the comparison of the predicted temperatures and the experimental data. It is observed that the temperatures computed numerically from thermal images are underpredicting. The reason may be the change in emissivity of the body due to the soot deposition. The two-dimensional thermal images only capture the cumulative along the depth of the flame.

Also, the thermal images are obtained with one averaged emissivity. The gas emissivity varies with space in pool fires. Probably, the edges would show a different emissivity compared to the readings at the axial location. A body engulfed inside a flame may experience a different heat flux other than what the thermal image reads. Since, the irradiance from the flame is an integrated parameter and the thermal image could able to capture irradiance. Whereas this integrated temperature is not able to replicate the true flame temperatures inside the flame.

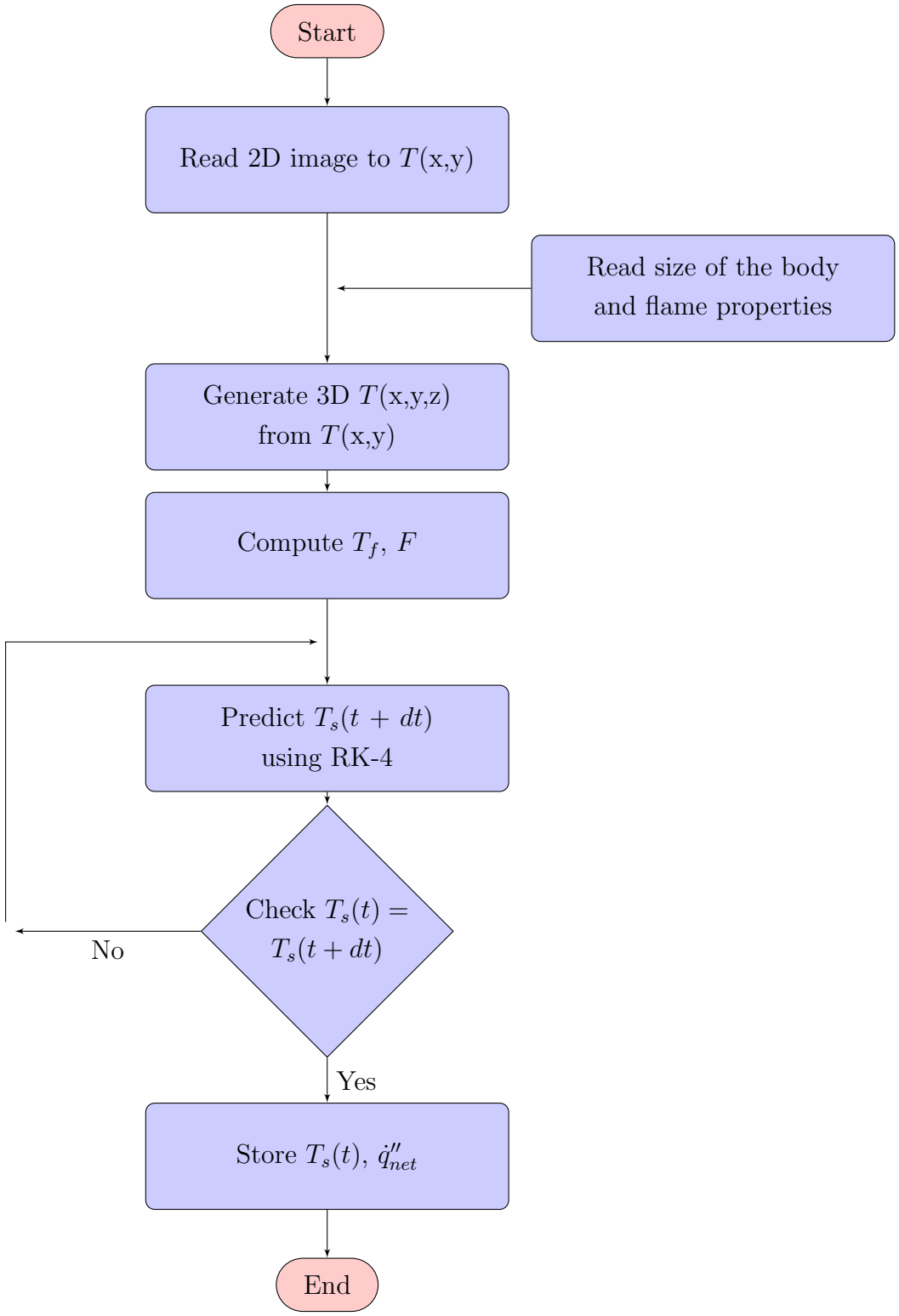

Fig. 5.11 Flow chart to predict the temperature of a body engulfed in a fire

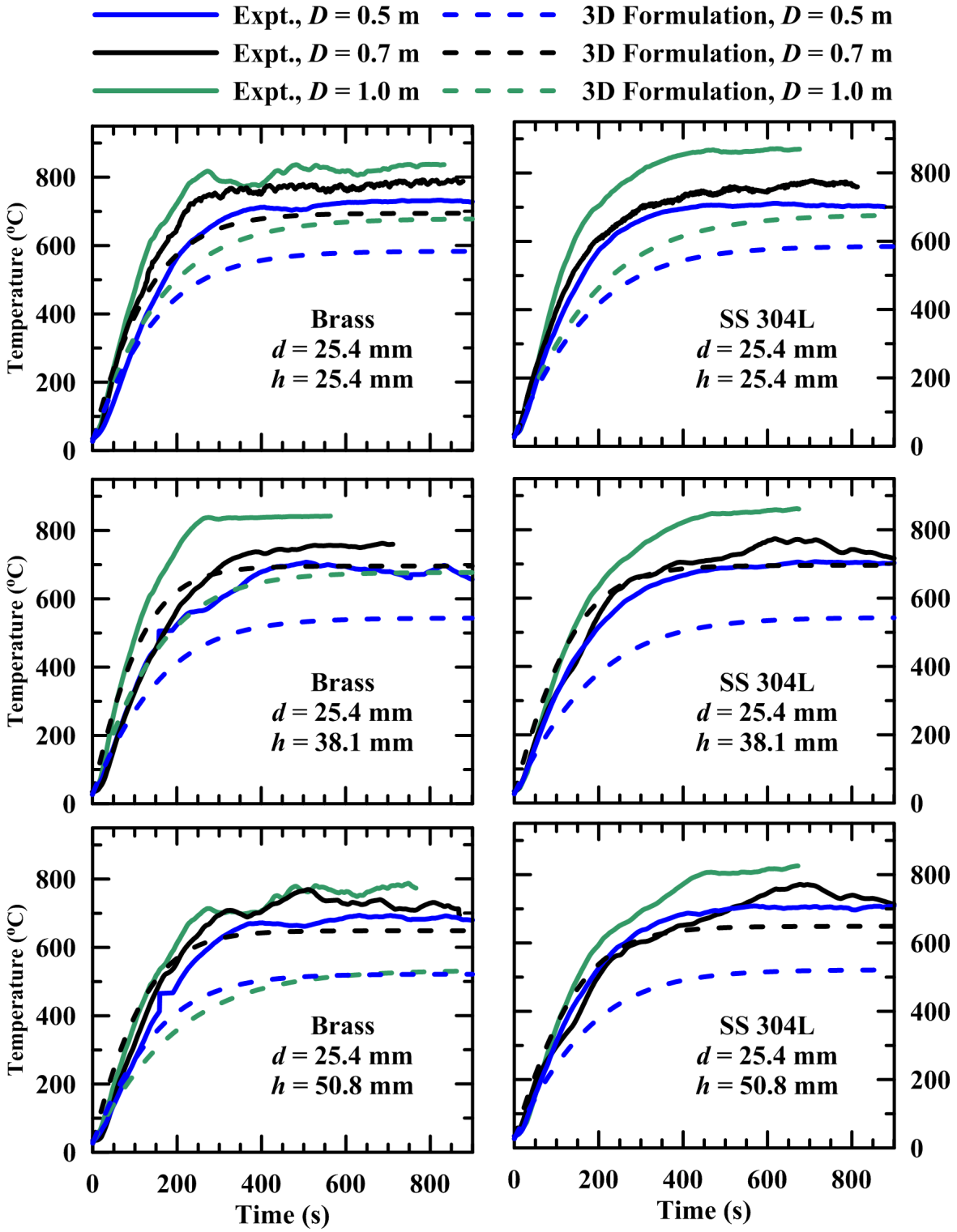

Fig. 5.12 Predicted temperature distribution from three dimensional formulation of an axi-symmetric pool fire

5.8 Conclusions

Using a simple lumped body approach, the net heat flux onto a body engulfed in pool fire can be estimated from the measured temperature distribution. It is possible to differentiate the radiative and convective component of heat transfer by using the computed configuration factor. A body engulfed in a pool fire will experience more energy transfer by radiation than by convection. The energy absorbed by a body increases with the increase in pool diameter. The gas velocity of the flame at $Y/D = 0.2$ for diesel pool fires varies from 1.53 m/s to 1.79 m/s for the range of pool sizes studied. The Nusselt number correlations for longitudinal flow around cylinder are reported for Reynolds number up to 4000.

A numerical code using thermal images is written to predict the temperature of a body engulfed in a pool fire. The temperature values are underpredicted by the numerical simulations. The two-dimensional thermal images are not capable of predicting the temperature inside the flame. Local values of flame emissivity and soot volume fraction are essential to predict the temperature of a body accurately.

CHAPTER 6

Heat Transfer in Casks Engulfed in Open Pool Fires

6.1 Introduction

In the previous chapter, it is absorbed that the radiation is dominant in the pool fire for a lumped body engulfed in pool fire. This chapter investigates the energy absorbed by a cask engulfed in pool fire. Literature review (Section 2.3) suggests that there could be a great influence of pool size on the temperature and heat flux of a cask engulfed in a pool fire. Also, there is limited information in quantifying the convective heat transfer in simulating thermal tests for $B < 14.4\%$. Conventionally, the simulation of thermal tests involves the coupling of conduction code with fire modeling at every time step. These coupled codes are expensive in terms of time and cost. Hence, the present study aims to conduct the following experimental and numerical investigations on pool fires:

- To study the influence of blockage on the heat release rate of diesel circular open pool fire
- To quantify the convective heat transfer from fire to cask for different blockages ($0.8\% < B < 14.4\%$)
- To demonstrate the strength of adiabatic surface temperature (AST) computed using measured plate thermometer temperature as a means to represent the pool fire for different blockages ($0.8\% < B < 14.4\%$)

- To present a more simple numerical model for the simulation of thermal tests that avoids the coupling of conduction and fire codes
- To prescribe the fire of a given pool diameter into a mixed boundary condition (convection and radiation)

Experiments are carried out with vertical and horizontal casks engulfed by diesel pool fires of 0.5 m, 0.7 m and 1.0 m in diameter. The trucks that carry the transportation package are diesel run and hence diesel is chosen as fuel. The casks are made up of stainless steel 304L pipes of different sizes and are filled with insulation. Temperatures are measured at various locations inside the casks and at the center of the insulation. IHCP-1D code is applied to estimate the incident heat flux on to the casks. AST computed using the measured plate thermometer temperature is used for the numerical analysis to estimate the cask surface temperatures and the heat flux experienced by the casks engulfed in a pool fire.

6.2 Casks Engulfed in Pool Fire

Transportation casks are idealized using stainless steel 304L pipes filled with an insulating material made of ceramic blanket. The dimensions of the casks immersed in pool fires are shown in Table 6.1. Experiments are conducted with diesel pool fires of diameters 0.5 m, 0.7 m and 1.0 m. The fuel pans are made up of 2 mm mild steel thick and 15 cm in depth. For each experiment, a cask is placed at a height of $0.2D$ to $0.4D$ both vertical and horizontal using stands as shown in Figs. 6.1 and 6.2. This location is chosen as the temperature of the pool fire is higher. The stands are made up of mild steel thin bars and are shaped in such a way there is a minimum contact between the stand the cask. The stands are insulated with ceramic cloth to insulate stands from casks thermally. Blockage ratio is defined as the ratio of the projected surface area of the cask in fire to the cross-sectional area of the pool. Blockage (B) for vertical and horizontal casks is given by:

$$\begin{aligned} B &= \frac{(\pi/4)\, d^2}{(\pi/4)\, D^2} \times 100, \quad \text{for vertical casks} \\ &= \frac{dl}{(\pi/4)\, D^2} \times 100, \quad \text{for horizontal casks} \end{aligned} \tag{6.1}$$

The blockage ratios of the casks used in this study for different pool fires are presented in Table 6.1. The real life thermal test blockage ratio is around 3% to 10% for vertical and horizontal orientations respectively. To study the influence of blockage on pool fire, mass burning in the presence of vertical casks are compared with the mass burning rates without casks. Mass burning rates are measured using a 250 kg platform type weighing scale. The pool is supported upon a stand made up of mild steel. Weighing scale and

the stand are separated by thick asbestos sheets. The supporting stand of the cask is insulated as shown in Figs. 6.1 and 6.2.

Table 6.1 Dimensions of the casks engulfed in pool fires

	Cask dimensions (mm)			Blockage ratio, B (%)	
D (m)	Diameter, d	Thickness, t	Length, l	Vertical	Horizontal
0.5	88.9	3.0	222.3	3.2	10.1
0.5	88.9	5.4	222.3	3.2	10.1
0.5	114.3	8.6	114.3	5.2	6.7
0.5	168.3	7.1	168.3	11.3	14.4
0.7	88.9	5.4	222.3	1.6	5.1
0.7	114.3	3.0	305.0	2.7	9.0
0.7	114.3	8.6	114.3	2.7	9.0
0.7	168.3	7.1	168.3	5.8	7.4
1.0	88.9	5.4	222.3	0.8	2.5
1.0	114.3	8.6	114.3	1.3	1.7
1.0	168.3	7.1	168.3	2.8	3.6
1.0	168.3	3.4	420.0	2.8	9.0

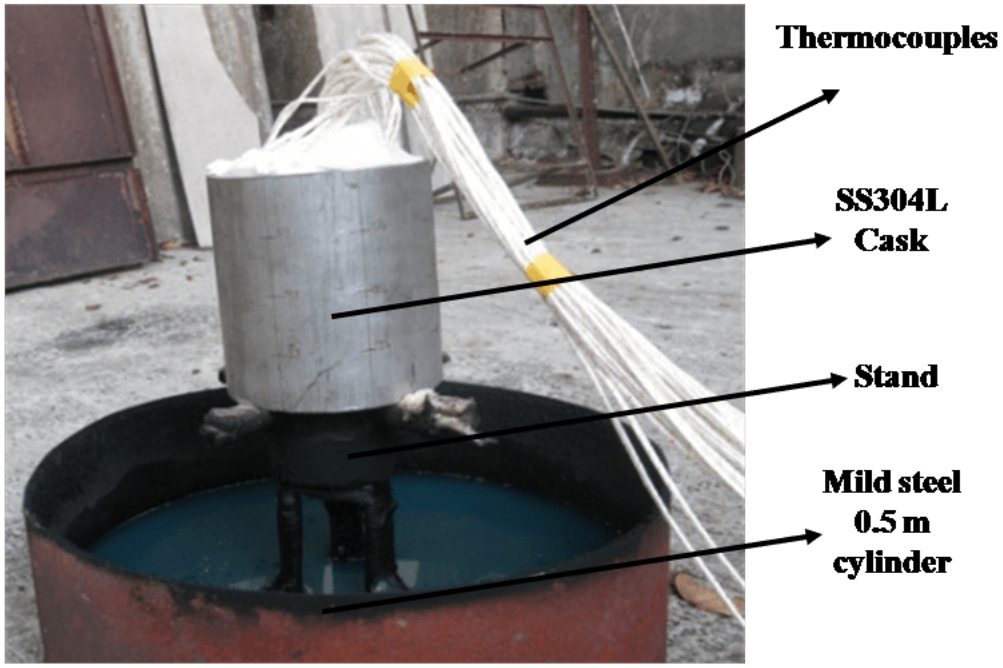

Fig. 6.1 Vertical cask in a 0.5 m pool fire

Fig. 6.2 Horizontal cask engulfed in 0.7 m diesel pool fire

Figure 6.3 shows the schematic of the cask and location of thermocouples inside the cask. Chromel-alumel (K type) thermocouples (0.7 mm diameter) are embedded to each cask. Twenty four of these thermocouples are spark welded to the inner wall of the cask at three different axial locations. The location of the thermocouples are chosen in such a way to capture the axial and circumferential temperature distribution of the cask. Three thermocouples are embedded inside the insulating material. The centerline thermocouples are required as an input to the inverse heat conduction solver. Hence, the thermocouples embedded inside the insulation are in the plane of the sub-surface thermocouples. The temperature of each thermocouple is measured for every second using a data acquisition system (Agilent 34970A).

6.3 Plate Thermometer

The heat transfer to a test specimen in a pool fire or in a test furnace at high temperature depends primarily on radiant flux rather than convection. Introducing water cooled sensors in fire environment is, if not impossible, very difficult. These devices should have large areas so that the radiant heat transfer dominates, and they must, at the same time, have a quick thermal response (Wickström, 1994). The plate thermometer is designed to have these properties. It consists of a thin inconel plate, 100 mm × 100 mm and 0.7 mm thick, with an insulating fiber board on one side. A thermocouple is welded at the center. Figure 6.4 shows a typical plate thermometer with insulation pad on its back side.

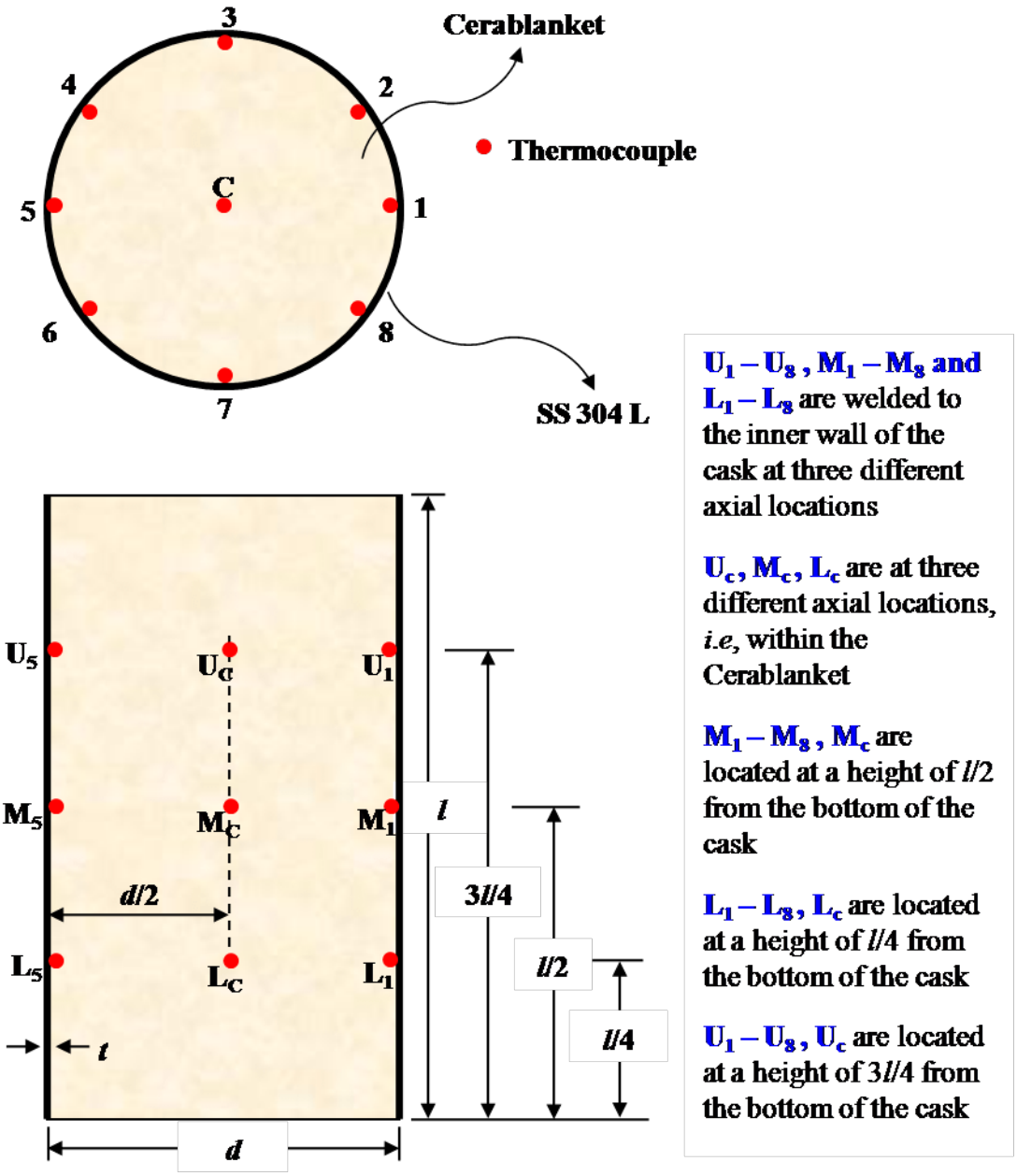

Fig. 6.3 Schematic of the cask showing the location of thermocouples

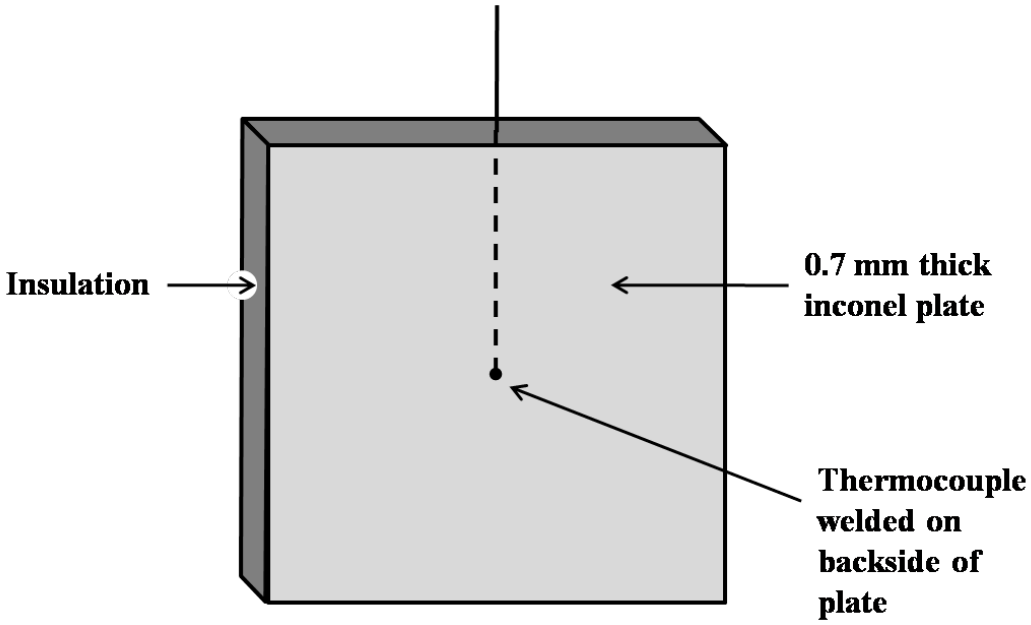

Fig. 6.4 The plate thermometer with insulation pad on its back side

6.3.1 Mathematical Modeling

The following mathematical modeling is based on theory outlined by Ingason and Wickström (2007). The radiation is assumed to be gray, *i.e.*, the emissivity is independent of wavelength.

Incident radiative heat flux

The incident heat flux by radiation to a surface from flames will be partly absorbed by the surface and partly be reflected. The absorbed heat can be expressed as:

$$\dot{q}''_{abs} = \varepsilon_{PT} \dot{q}''_{inc} \tag{6.2}$$

Also from Kirchhoff's identity, the reflected heat may be written as:

$$\dot{q}''_{ref} = (1 - \varepsilon_{PT})\, \dot{q}''_{inc} \tag{6.3}$$

The radiation the plate thermometer surface may be expressed as:

$$\dot{q}''_{emi} = \varepsilon_{PT} \sigma T^4_{PT} \tag{6.4}$$

where T_s is the surface temperature of plate thermometer. The net heat flux by radiation that is entering the surface is:

$$\dot{q}''_{rad} = \dot{q}''_{inc} - \dot{q}''_{emi} - \dot{q}''_{ref} = \varepsilon_{PT} \left(\dot{q}''_{inc} - \sigma T^4_{PT} \right) \tag{6.5}$$

Incident convective heat flux

Heat transfer by convection occurs due to the hot gases flow over the solid surface at different temperature. It depends on the temperature gradient near the surface and the thermal conductivity of the fluid and can be written as:

$$\dot{q}''_{conv} = h\left(T_f - T_{PT}\right) \tag{6.6}$$

where h is the convective heat transfer coefficient between the plate thermometer and the flame and T_f is the flame temperature.

Total incident heat flux

The total heat transfer is the sum of the net heat transfer by radiation and by convection:

$$\dot{q}''_{tot} = \dot{q}''_{rad} + \dot{q}''_{conv} \tag{6.7}$$

Using Eqs. (6.5) and (6.6) in Eq. (6.7):

$$\dot{q}''_{tot} = \varepsilon\left(\dot{q}''_{inc} - \sigma T_{PT}^4\right) + h\left(T_\infty - T_{PT}\right) \tag{6.8}$$

Heat balance at the plate thermometer surface

The incident heat flux by radiation to a plate thermometer can be obtained from the heat balance at the measuring point at the centre of the plate thermometer:

$$\dot{q}''_{tot} = \dot{q}''_{sto} + \dot{q}''_{cond} \tag{6.9}$$

where the first term in the right hand side represents the heat stored in the PT and the second term is a combination of heat losses due to two-dimensional conduction in the plane of the plate away from the thermocouple welding point in the center to the edges, and the heat losses by conduction through the insulation to the back side of the PT. The conduction losses can be written as:

$$\dot{q}''_{cond} = K_{cond}\left(T_{PT} - T_\infty\right) \tag{6.10}$$

where the conduction correction factor K_{cond} is determined experimentally in the applications. The first term on the left hand side of Eq. (6.9) can be written as:

$$\dot{q}''_{sto} = \rho_{PT} C_{PT} \delta \frac{\Delta T_{PT}}{\Delta t} \tag{6.11}$$

where ρ_{PT} and C_{PT} are the density and the specific heat capacity and δ is the thickness of the PT. Combining Eqs. (6.7) and (6.9) to (6.11), the incident heat flux by radiation can be written as:

$$\dot{q}''_{inc} = \left[\varepsilon_{PT}\sigma T_{PT}^4 + (h_{PT} + K_{cond})(T_{PT} - T_\infty) + \rho_{PT} C_{PT} \delta (\Delta T_{PT}/\Delta t)\right] / \varepsilon_{PT} \quad (6.12)$$

The conduction losses could be reduced by avoiding direct metal contact at the edges between the front and the back sides of the PT and by using thicker and more effective insulation pads. The inertia term could be reduced by using thinner steel plates.

Steady state measurements in a cone calorimeter

When the PT is put under the cone calorimeter, the temperature reaches a steady-state value within 2-3 min. Hence, the storage term in Eq. (6.12) can be neglected, *i.e.,*

$$\dot{q}''_{inc} = \left[\varepsilon_{PT}\sigma T_{PT}^4 + (h_{PT} + K_{cond})(T_{PT} - T_\infty)\right] / \varepsilon_{PT} \quad (6.13)$$

6.3.2 Construction of Plate Thermometer (PT)

To avoid the heat loss from behind the PT, commercially available CeraTex 3180 Blanket is used as insulation pad. CeraTex 3180 Blanket is a needled blanket that is made from high purity spun ceramic fibers, suitable for high temperature insulation (1260 °C) with a specific heat of 1.13 kJ/kg.K. Equation (6.13) gives the radiative heat flux on to the PT. It is dependent on the emissivity, h_{PT} and K_{cond} of the PT. To avoid the emissivity dependency, the PT is painted with pyromark, whose emissivity is constant within the temperature range of 30 °C to 1200 °C. Nakos and Keltner (1989) and Logenbaugh *et al.* (1990) have measured the emissivity of pyromark painted surface and reported that the emissivity is 0.86 ± 0.09. This emissivity is constant throughout the spectral range of 0.265 μm to 20.0 μm.

A specimen with pyromark has to be cured to make the paint adhere to the specimen at high temperatures. Pyromark is spray painted on each plate and then the painted plates are dried over night, cured at different temperatures. The paint has to be curing in a certain fashion to make the paint adhere to the plate. Two plates are painted with pyromark: one is not cured but dried over night and the other one is curing. Their temperature is raised to operating temperature. Figure 6.5a shows the plate with pyromark without curing. The paint peeled off the plate at 300 °C. Figure 6.5b shows the plate with Pyromark after curing. The curing procedure for pyromark is as follows:

- Paint the plate with spray nozzle
- Again paint (rotating the plate by 90 °) and left over night

(a) Pyromark wihtout curing at 300 °C

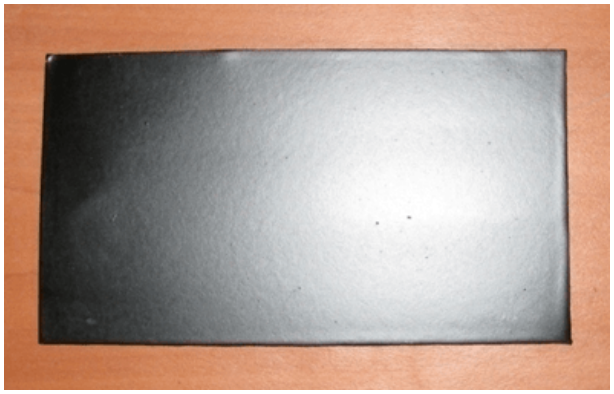

(b) Pyromark with curing at exposed to 900 °C

Fig. 6.5 Plate with pyromark exposed to high temperatures

- Curing is carried out at 300 °C for 2 hours by placing in a cone calorimeter
- Curing is done at 500 °C for 2 hours by placing in a cone calorimeter
- Vertified at 750 °C for 1 hour by placing in a cone calorimeter

Any temperature increment while curing should not exceed 10 °C per minute.

The other two parameters h_{PT} and K_{cond} are the properties of the plate material. Experiments are conducted on the stainless steel and inconel. Inconel showed a faster response and the time constants for inconel with and without pyromark are 100 s and 250 s respectively. Hence, inconel with pyromark is chosen as the PT material.

6.3.3 PT Calibration

The inconel PT has been calibrated under cone calorimeter. A cone calorimeter consists of a heating coil at the top, a sample holder. Figure 6.6 shows the typical cone calorimeter. The heat flux below the conical heater is calibrated using a Schmidt Boelter heat flux gauge. The calibration is carried out at a distance of 25 cm below the heating coil. The plate thermometer is placed 25 cm below the cone calorimeter. The heat flux under cone can be controlled from 0-90 kW/m^2. For different heat fluxes, the temperature of the plate thermometer is recorded in a computer via a data logger. Experiments are repeated at least four times to check the repeatability. Figure 6.7 shows the calibration chart of radiant heat flux variation with the PT temperature. The calibration chart shows that the relation between the radiant flux and the PT temperature as:

$$\dot{q}''_{rad} = 0.957 + 0.0017\,(T_{PT})^{5.57} \tag{6.14}$$

where T_{PT} is the PT temperature in degrees Celsius.

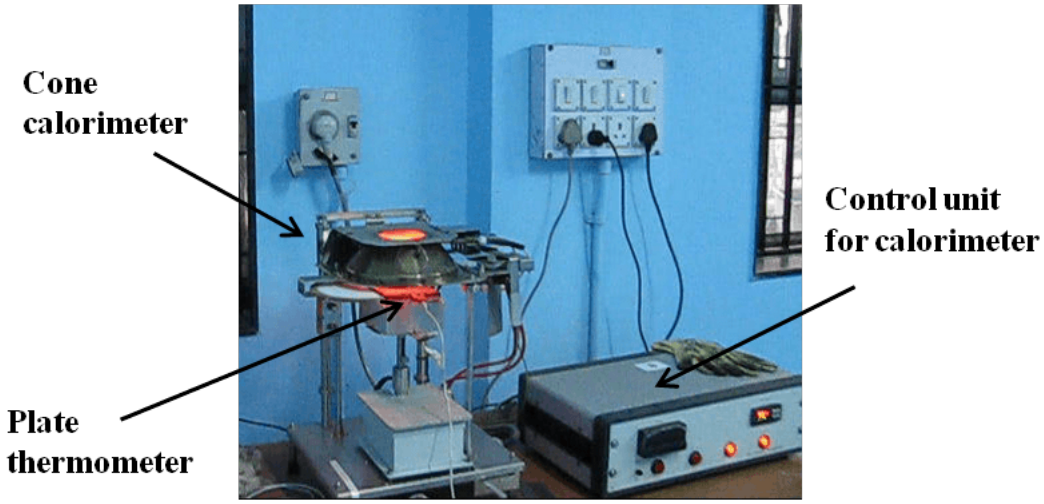

Fig. 6.6 Curing of plate thermometer under cone calorimeter (heater is ON)

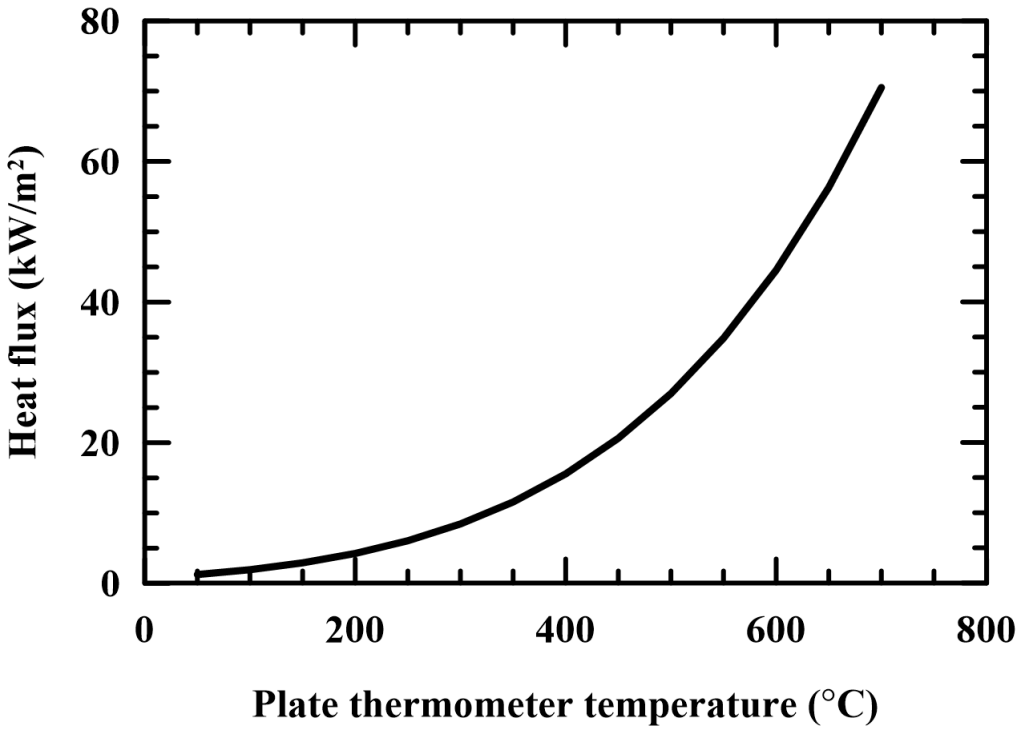

Fig. 6.7 Calibration chart for inconel plate thermometer

The calibration curve given in Fig. 6.7 is for radiative heat flux incident on the flame. Plate thermometers can be used for measuring the radiative heat flux from a source. Hence, plate thermometers can only be outside the flame environment where is no convective heat transfer from flame to the plate. The inherent problem with the implementation of plate thermometer is that tough this instrument is responsive to convective heat transfer, it is only calibrated for radiative environment. Calibration of plate thermometers under a mixed boundary condition (radiation and convection) is practically very difficult. The cone calorimeter provides only the radiative heat flux. So, the plate thermometers cannot be used to measure the heat flux inside the flame with the calibration chart provided in Fig. 6.7. Hence, the concept of adiabatic surface temperature is imposed on to the plate thermometer to measure an effective flame temperature both for radiation and convection.

6.4 Adiabatic Surface Temperature

Adiabatic surface temperature (AST) is the surface temperature of an ideal perfectly-insulated surface exposed to the same thermal conditions as the real surface under consideration (Wickström *et al.*, 2011). It is an effective boundary temperature that represents a combination of radiation and convection boundary conditions. Consider a body engulfed in fire. The surface of the body experiences convective and radiative heat flux from the flame as shown in Fig. 6.8.

The net heat flux received by the surface of the body is given by,

$$\dot{q}''_{net} = \dot{q}''_{rad} + \dot{q}''_{conv} \tag{6.15}$$

where $\dot{q}''_{rad}$ is the radiative heat flux and $\dot{q}''_{conv}$ is the convective heat flux. The convective heat flux can be written as:

$$\dot{q}''_{conv} = h\,(T_g - T_s) \tag{6.16}$$

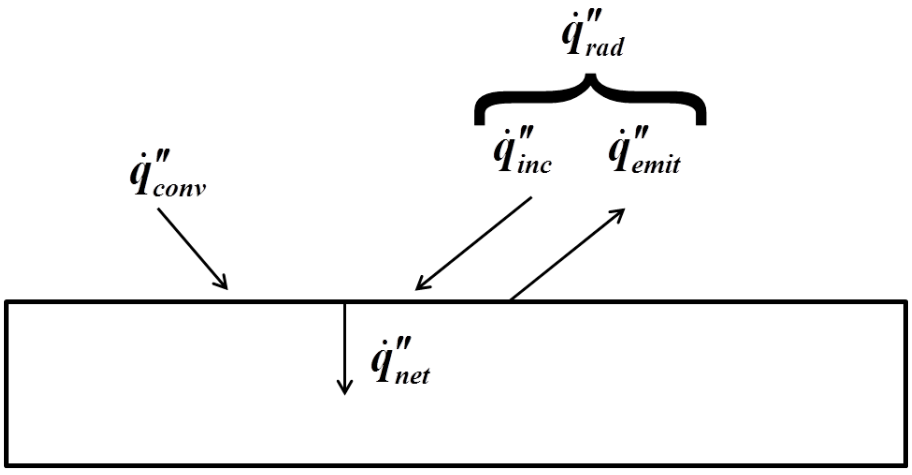

Fig. 6.8 Energy balance at the surface of a body engulfed in pool fire

where h is the convective heat transfer between the flame and the body and T_g is the surrounding gas temperature. The radiative heat flux can be written as:

$$\dot{q}''_{rad} = \dot{q}''_{recv} - \dot{q}''_{ems} \tag{6.17}$$

where $\dot{q}''_{recv}$ is the radiative heat flux received by the body and $\dot{q}''_{emi}$ is the radiative heat flux emitted by the body given as:

$$\dot{q}''_{emi} = \sigma \varepsilon_s T_s^4 \tag{6.18}$$

If $\dot{q}''_{inc}$ is the energy per unit area incident on to the surface of the body, then due to the absorptivity of the body only part of it is received:

$$\dot{q}''_{recv} = \varepsilon_s \dot{q}''_{inc} \tag{6.19}$$

where ε_s is surface emissivity of the body. In Eq. (6.19), the absorptivity and emissivity of the body are assumed to be same. If T_s is the surface temperature of the body then the net radiative heat flux received by the body is:

$$\dot{q}''_{rad} = \varepsilon_s \dot{q}''_{inc} - \sigma \varepsilon_s T_s^4 \tag{6.20}$$

$\dot{q}''_{inc}$ is the irradiance from the flame to the body.

Combining Eqs. (6.15), (6.16) and (6.20),

$$\dot{q}''_{net} = \varepsilon_s \left(\dot{q}''_{inc} - \sigma T_s^4 \right) + h \left(T_g - T_s \right) \tag{6.21}$$

If the body engulfed in the flames is adiabatic surface then by definition, $\dot{q}''_{net}$ vanishes and T_s becomes T_{AST}, *i.e.,*

$$0 = \varepsilon_s \left(\dot{q}''_{inc} - \sigma T_{AST}^4 \right) + h \left(T_g - T_{AST} \right) \tag{6.22}$$

Subtracting Eq. (6.22) from Eq. (6.23),

$$\dot{q}''_{net} = \sigma \varepsilon_s \left(T_{AST}^4 - T_s^4 \right) + h \left(T_{AST} - T_s \right) \tag{6.23}$$

Equation (6.23) acts as a boundary condition of a body engulfed in pool fire. From Eq. (6.23), T_{AST} is interpreted by the structural model as an effective black body radiation temperature for the purpose of computing the incident radiation and as the same gas temperature for the purpose of computing the convective heat flux. T_{AST} may also be seen as a single fictitious temperature being used commonly for calculating both convective and radiative heat transfer.

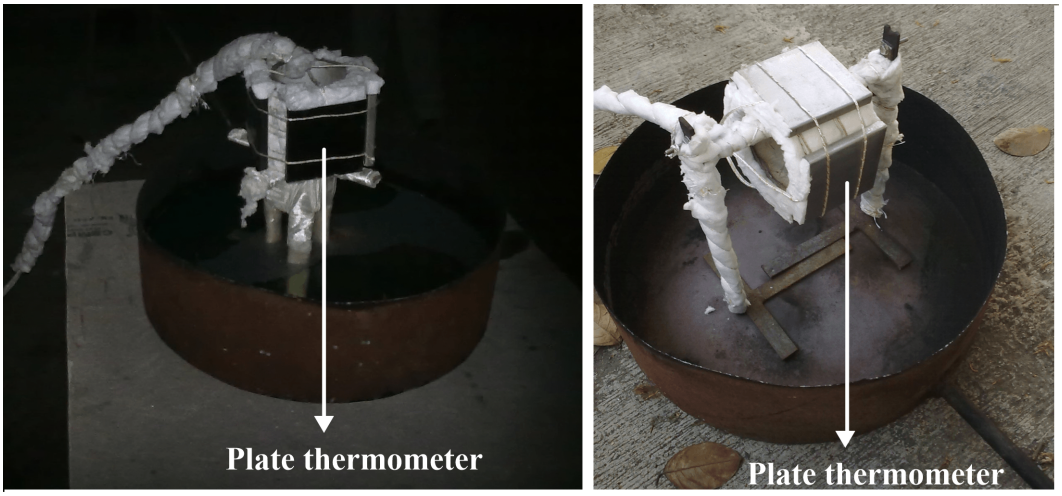

Fig. 6.9 Arrangement plate thermometer in pools

6.5 Estimation of AST from the Measured PT Temperatures

AST can be computed from the measured plate thermometer temperature as given by Wickström (1994) and Ingason and Wickström (2007). Four plate thermometers are used as shown in Fig. 6.9. The plates are fixed to a cylinder separated by an insulating material. All the four plates together form an approximate cylinder of diameter 0.17 m. Experiments are conducted with plate thermometers in vertical orientation. All the plate thermometers indicated reasonably same temperatures (2%) for a given diameter of the pool fire. Hence, average temperature distributions of plate thermometers (T_{PT}) for different pool sizes are shown in Fig. 6.10. It is observed that the plate thermometer temperatures increase with the increase in the diameter of the pool fire. This is because of the higher incident radiation and/or gas temperature due to the increase in the pool diameter.

Impose Eq. (6.23) on plate thermometer engulfed in a pool fire. T_s takes the form T_{PT} in Eq. (6.23), *i.e.*,

$$\dot{q}''_{net} = \sigma \varepsilon_{PT} \left(T^4_{AST} - T^4_{PT} \right) + h \left(T_{AST} - T_{PT} \right) \tag{6.24}$$

The net heat flux is the energy stored by the plate thermometer per unit area as a result of increase in plate thermometer temperature:

$$\dot{q}''_{net} = \rho \delta C_p \frac{dT_{PT}}{dt} \tag{6.25}$$

where δ is the thickness of the plate thermometer. In Eq. (6.25), the conduction heat loss to the insulation is neglected. Substituting Eq. (6.25) in Eq. (6.24),

$$\rho\delta C_p \frac{dT_{PT}}{dt} = \sigma\varepsilon_{PT}\left(T_{AST}^4 - T_{PT}^4\right) + h\left(T_{AST} - T_{PT}\right) \tag{6.26}$$

Equation (6.26) can be solved for T_{AST} using finite difference method.

$$\rho\delta C_p \frac{T_{PT}^{i+1} - T_{PT}^{i}}{\Delta t} = \sigma\varepsilon_P T\left[\left(T_{AST}^{i}\right)^4 - \left(T_{PT}^{i}\right)^4\right] + h\left(T_{AST}^{i} - T_{PT}^{i}\right) \tag{6.27}$$

In the Eq. (6.27), T_{PT} is a known function of time for every second (Fig. 6.9). The only unknown in the Eq. (6.27) is T_{AST}. The initial condition is

$$T_{AST}^{i=0} = T_{PT}^{i=0} \tag{6.28}$$

h is computed from the Nusselt number correlation for flow over a flat plate. By solving the Eq. (6.27), T_{AST} as a function of time is obtained.

Fig. 6.11 shows the AST computed using Eq. (6.27) for different pool fires. The time taken to reach steady state AST is less than 50 s. The repeatability of various experiments conducted in measuring AST is 4%. Transient temperature captures the development of pool fire gradually with time and hence the heat flux increases from zero to maximum. This fire growth may be not be much importance for several applications. Transient AST is given as the input in the numerical analysis. The total heat flux onto a cask, at any instant, is given by:

$$\dot{q}''_{net} = \sigma\varepsilon_s\left[\left(T_{AST}(t)\right)^4 - \left(T_s(t)^4\right)\right] + h\left[\left(T_{AST}(t)\right)^4 - T_s\right] \tag{6.29}$$

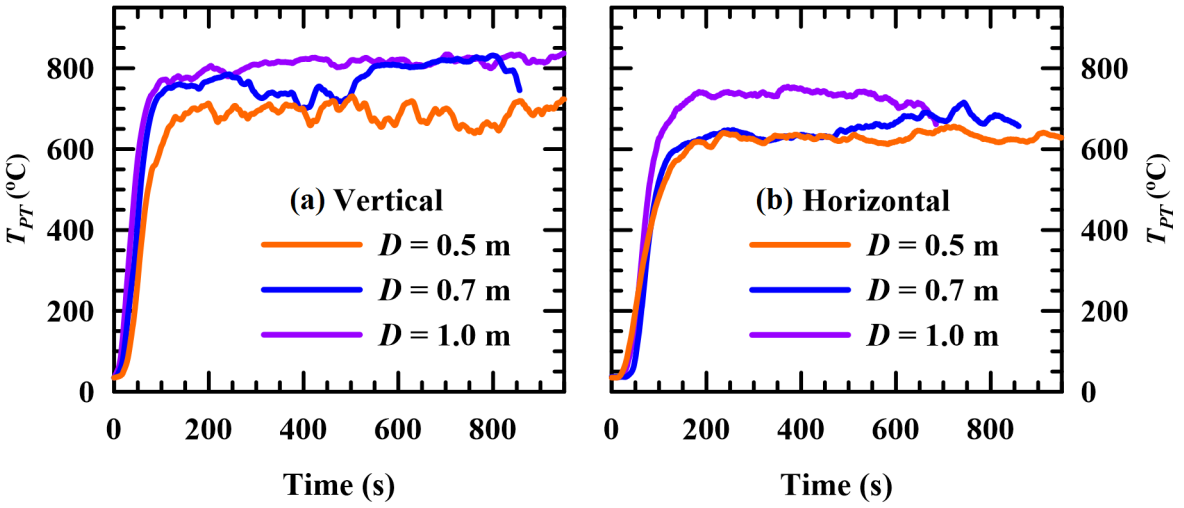

Fig. 6.10 Temperatures of the plate thermometers for different pool sizes

Soot gets deposited on to the surface of the cask. Hence, the emissivity of the soot of 0.9 is considered as the surface emissivity of the cask. The surface temperature (T_s) of the cask increases with time. This reduces the heat flux onto the cask with the increase in time as seen in Eq. (6.29). This heat flux can be given as an input to any solid modeling code to simulate the energy transfer in the body. This net incident heat flux changes with the surface temperature of the body. Hence, the problem of estimating temperatures of casks engulfed in fire reduces to a simple conduction problem.

6.6 Details of the Numerical Conduction Analysis of a Cask Using AST Concept

Numerical simulations are performed to predict the temperature distribution within the cask with AST as boundary condition. All the simulations are carried out in ANSYS FLUENT v13. Since the temperature distribution inside the pool fire is symmetric (Section 5.7), cask is simulated as a two dimensional axisymmetric model as shown in Fig. 6.12. The height of the total domain is $d/2$ and the thickness of the SS 304L is t. The exposed surface (top) of the SS 304L is subjected to a mixed boundary condition with T_{AST} as source temperature, *i.e.,* Eq. (6.29). The numerical domain is same both for horizontal and vertical orientations of the cask and also for different pool sizes. The input boundary condition, T_{AST} varies with the orientation and the pool size. The heat transfer from the fire to the cask through the small thickness, t is neglected. Hence, Both the side walls are considered to be adiabatic. All temperature dependent thermal properties of SS 304L are taken from Rempe and Knudson (2008). The thermal properties of SS 304L and Cerablanket are given in Table 6.2.

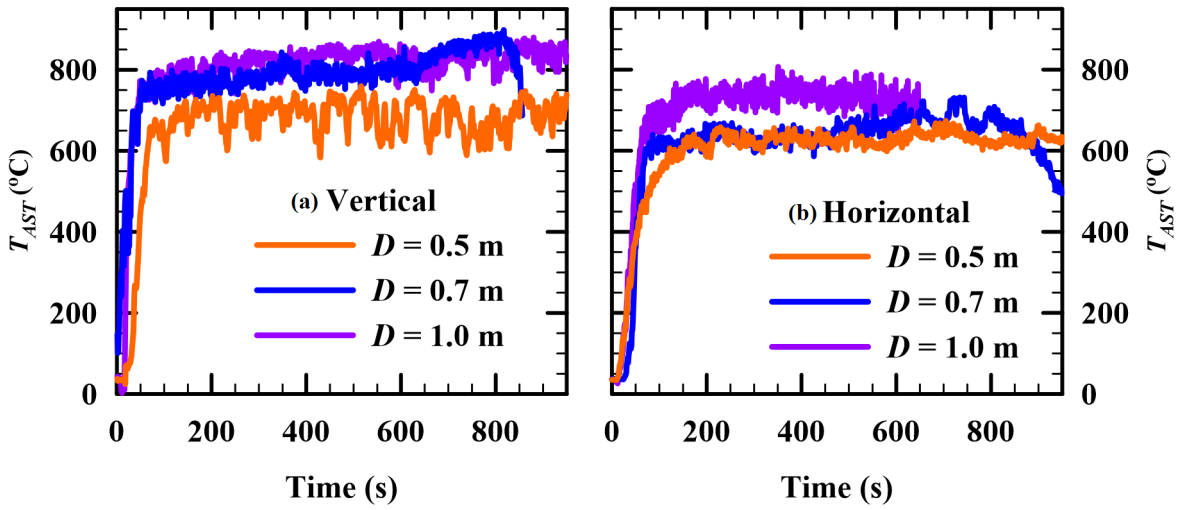

Fig. 6.11 Adiabatic surface temperatures for different pool fires

Table 6.2 Thermal properties of SS 304L and Cerablanket

Temperature	30 °C	100 °C	300 °C	500 °C	700 °C	900 °C
SS 304L						
Density, ρ (kg/m^3)	7776.32	7808.10	7860.80	7866.87	7838.79	7789.03
Specific heat, C_p (J/kg.K)	517.44	521.45	532.91	544.37	555.83	567.89
Conductivity, k (W/m.K)	15.47	16.46	19.28	22.10	24.92	27.74
Cerablanket						
Density, ρ (kg/m^3)	128	-	-	-	-	
Specific heat, C_p (J/kg.K)	1130.44	-	-	-	-	
Conductivity, k (W/m.K)	0.043	0.044	0.066	0.111	0.170	0.236

The Reynolds number for the configurations given in Table 6.1 vary from 8700 to 13100. For all the horizontal cask configurations the average Nusselt number correlation is given by (Ghisalberti and Kondjoyan, 1999):

$$\mathrm{Nu} = 0.57\ \mathrm{Re}^{0.52}\left(1 + 0.33\ \mathrm{Re}^{0.16}\right) \tag{6.30}$$

There is limited data for vertical casks in the range of Reynolds number 8700 to 13100. Studies on forced convective heat transfer from cylinders in axial flow are uncommon. Motlagh and Hashemabadi (2008) studied the heat transfer correlations using CFD modeling in different situations including axial-flow on finite cylinder. However, their study was carried out for a high Reynolds number in the range of 177000 to 617000. Hadad and Jafarpur (2011) presented dimensionless heat transfer correlations for forced convection from isothermal circular cylinders with different aspect ratios ($l/d \leq 8$). Reynolds number in their study varied from 1 to 100 for $l/d = 1$, from 1 to 160 for $l/d = 2$ and from 1 to 1000 for $l/d = 4$. Due to the lack of information regarding the heat transfer correlations for Reynolds number ranging from 8700 to 13100 for cylinders in axial flow, the correlations suggested by Hadad and Jafarpur (2011) are adopted. These relations are as follows:

For $l/d = 1$,

$$\mathrm{Nu} = 1.5828 + 0.5506\ \mathrm{Re}^{0.5}\ \mathrm{Pr}^{1/3} \tag{6.31}$$

for $l/d = 2$,

$$\mathrm{Nu} = 1.2564 + 0.4307\ \mathrm{Re}^{0.5}\ \mathrm{Pr}^{1/3} \tag{6.32}$$

for $h/d = 4$,

$$\mathrm{Nu} = 0.9854 + 0.2939\ \mathrm{Re}^{0.5}\ \mathrm{Pr}^{1/3} \tag{6.33}$$

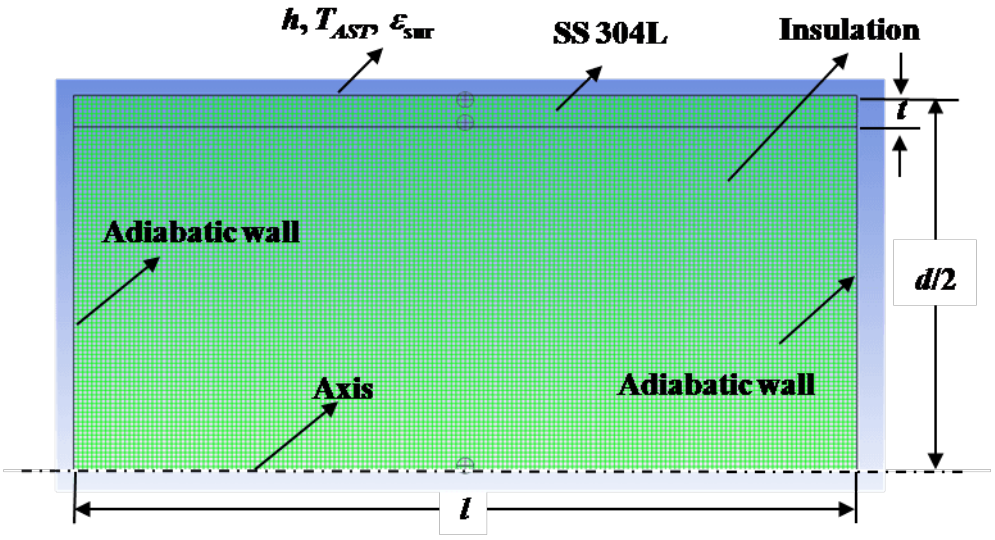

Fig. 6.12 Numerical grid to simulate a cask engulfed in fire

Ghisalberti and Kondjoyan (1999) presented the heat transfer correlations for $l/d = 1.2$ for Reynolds ranging from 1000 to 25000. The heat transfer coefficients computed using Eqs. (6.31) to (6.33) are in good agreement with the relations given in Ghisalberti and Kondjoyan (1999). Hence, the above correlations are used for all other l/d ratios. These correlations are used in modeling the thermal energy absorbed by the cask using FLUENT. Simulations are carried out with a time step of 0.5 s. Grid independent tests are conducted. Results are found to be independent of time steps chosen (0.01 s, 0.1 s, 0.5 s and 1 s).

6.7 Uncertainty Analysis

Experiments are exposed to atmosphere and no external means is provided to control the atmospheric wind. All of the experiments are conducted at around 6.30 AM to 8.00 AM in order to maintain the lower wind velocity (2 m/s). In spite of this low velocity, the fire tilts for a smaller duration during the entire length of the experiment, exposing the thermal cask to cooler atmosphere. The uncertainty in the measurement of the flame emissivity is 10% (Section 3.11). The uncertainty in the measurement of the mass burning rate is around 2% to 9%. The uncertainty in the measurement of the temperature is 5%. The micro-manometer is accurate by 1% of the reading. The uncertainty in the bi-directional probe constant for flows parallel to the probe axis is 0.07 (Bryant, 2009). In the numerical analysis, transient AST data is considered as input. The repeatability in the measurement of AST for the various experiments conducted is 4%. The numerical code overpredicted the initial heat flux values by 100% when the steady state AST is given as input. The temporal dependency of the properties of materials is very important in numerical analysis. It is observed that the predicted temperature values are very much dependent on the accuracy of the temporal dependency of the properties of materials.

6.8 Results and Discussions

Pool fire experiments on 0.5 m, 0.7 m and 1.0 m are conducted with diesel as a fuel. Table 6.1 shows all the cask sizes that are considered in this study. The mass burning rate of the pool fires is measured in the presence of casks. Inner wall temperature distribution of the casks is measured for different size of the casks engulfed in different pool fire diameters. FLUENT is used for simulating to dimensional axi-symmetric heat conduction in the cask engulfed in a pool fire. Mixed boundary condition is imposed on the wall exposed to the fire. This involves giving convective boundary condition (h, T_{AST}) and radiative condition (ε_s, T_{AST}). Numerical studies are conducted for all the twelve configurations shown in Table 6.1. The adiabatic surface temperature, T_{AST} is given from Fig. 6.11. Numerical simulations are solved for every time step of 0.5 s. These results are compared with the experimental results. The heat flux on to the surface of the cask is estimated using IHCP-1D code (Beck, 2012). The heat flux obtained from both IHCP and numerical simulations are compared for all the casks considered in this study.

6.8.1 Influence of the Blockage on the Mass Burning of the Pool Fire

A 250 kg platform type weighing scale interfaced to a computer is used to measure the mass burning rate. Mass burning rate of the pool fire in the presence of a cask is measured for a cask of diameter and length of 168 mm with a thickness of 7.1 mm. The uncertainty in the measurement of the mass burning rate is around 2-9%. A comparison of the steady state mass burning rate of pool fires with and without blockage is shown in Table 6.3. The blockages are computed using Eq. (6.1). The difference in the mass burning rate is within the uncertainty of the measurement. Hence, it may be concluded that there is no significant effect of the blockage on the mass burning rate for all the configurations considered in this study.

Table 6.3 Influence of blockage on mass burning rate
for a cask of size: d = 168 mm, t = 7.1 mm and l = 168 mm

		Vertical cask		Horizontal cask	
D (m)	$\dot{m}''$ (gm/m^2.s)	B (%)	$\dot{m}''_B$ (gm/m^2.s)	B (%)	$\dot{m}''_B$ (gm/m^2.s)
0.5	27.50	11.3	27.76	14.4	29.04
0.7	32.70	5.8	30.13	7.3	34.52
1.0	39.10	2.8	38.47	3.6	-

6.8.2 Comparison of Numerical Predictions with Measured Temperature Distributions

Figures 6.13 to 6.18 show the subsurface temperature distributions of different casks engulfed in pool fires: Figs. 6.13 to 6.15 are for vertical casks and Figs. 6.16 to 6.18 are for horizontal casks. In Figs. 6.13 to 6.18, the missing data is a result of thermocouple failure during a specific experiment.

Thermal Analysis on Vertical casks

Figures 6.13 to 6.15 show the subsurface transient temperature distributions of vertical casks engulfed in pool fires. All the measured temperatures in a given layer (upper, middle and lower) are averaged. U is the averaged temperature of all the thermocouples in the upper layer in Fig. 6.3, *i.e.,* U1 - U8. M is the averaged temperature of all the thermocouples in the upper layer in Fig. 6.3, *i.e.,* M1 - M8. L is the averaged temperature of all the thermocouples in the upper layer in Fig. 6.3, *i.e.,* L1 - L8. The temperatures inside the cask at different axial locations (inside the insulation) are also presented as Uc, Mc and Lc.

Figure 6.13 shows the temperature distribution inside casks engulfed in a 0.5 m vertical pool fire. The temperatures of the casks gradually increase and reach a steady temperature of around 705 °C. The larger cask in Fig. 6.13(d) took longer time to reach steady state compared to other smaller casks. This is because of the high thermal inertia of larger cask compared to that of smaller casks. In spite of their different sizes, all the casks reached a maximum temperature of around 705 °C. The temperatures inside the insulation started increasing only after 400 s in case of smaller cask (Fig. 6.13(a)) and 800 s in case of larger cask (Fig. 6.13(d)). This could be due to the thermal inertia of the cask due to its thickness. This makes the colder body to be in the fire for a longer time. The heat flux from flame to the body varies from cask to cask as this parameter depends on the temperature difference between the fire and the cask. Hence, any numerical simulation to simulate the boundary condition may not have a constant heat flux as the boundary condition. This is true for both vertical and horizontal orientations studied in this work.

From Fig. 6.13, it is observed that the numerical simulations slightly overpredicted the temperatures compared to the experimental results. The comparison of the averaged steady state temperatures is within 18% of the experimental data. In all the experiments conducted, the wind velocity measured is less than 2 m/s. In spite of this low velocity, it is observed that the cask is not fully engulfed in 0.5 m pool fire for the whole duration of the experiment. At times, some portion of the cask is exposed to atmosphere, cooling down the temperature of the cask at that location. However, the numerical analysis assumes that the cask is always engulfed by pool fire. This makes the numerically computed

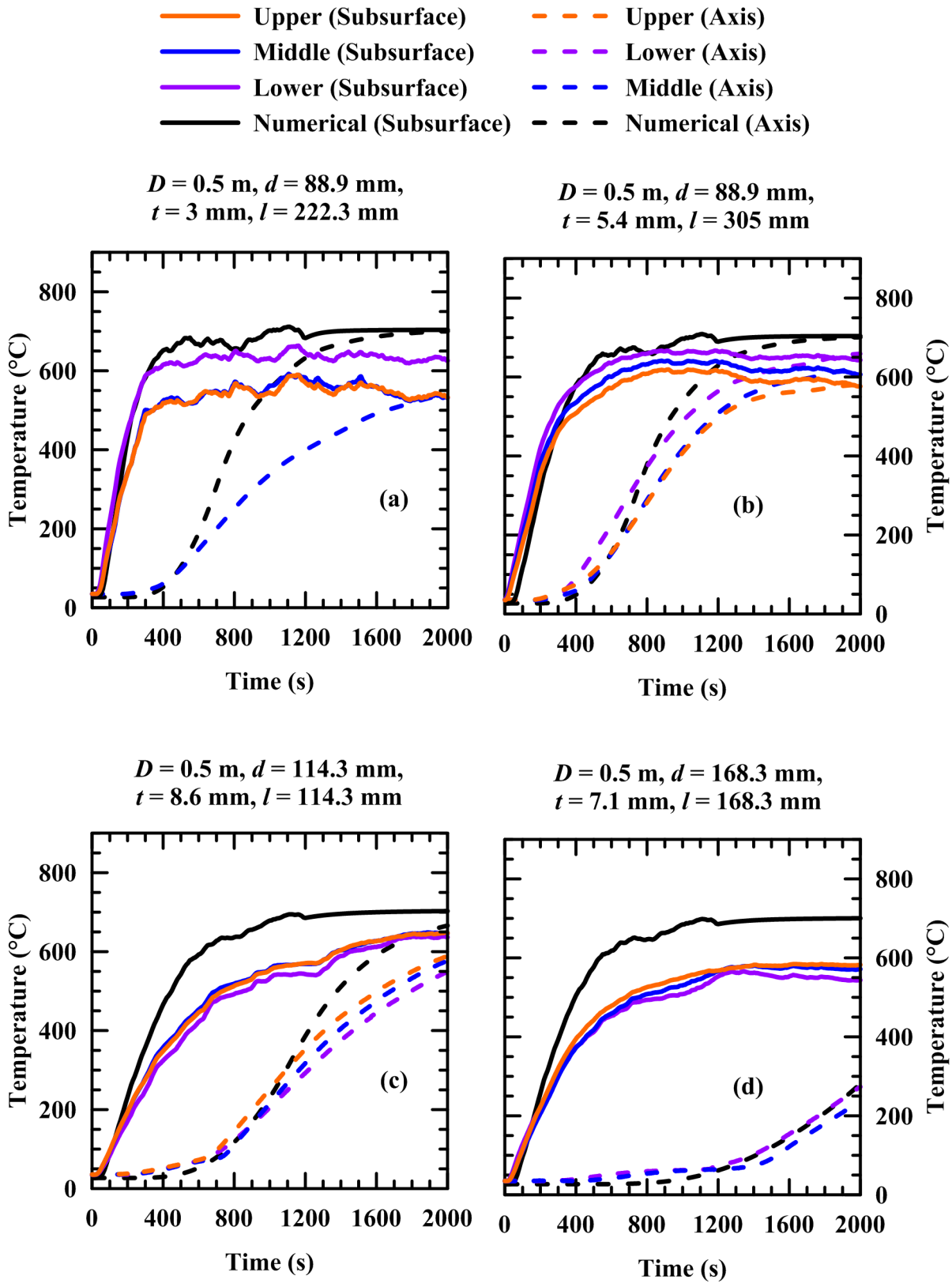

Fig. 6.13 Subsurface temperature distribution for vertical casks engulfed in a 0.5 m pool fire

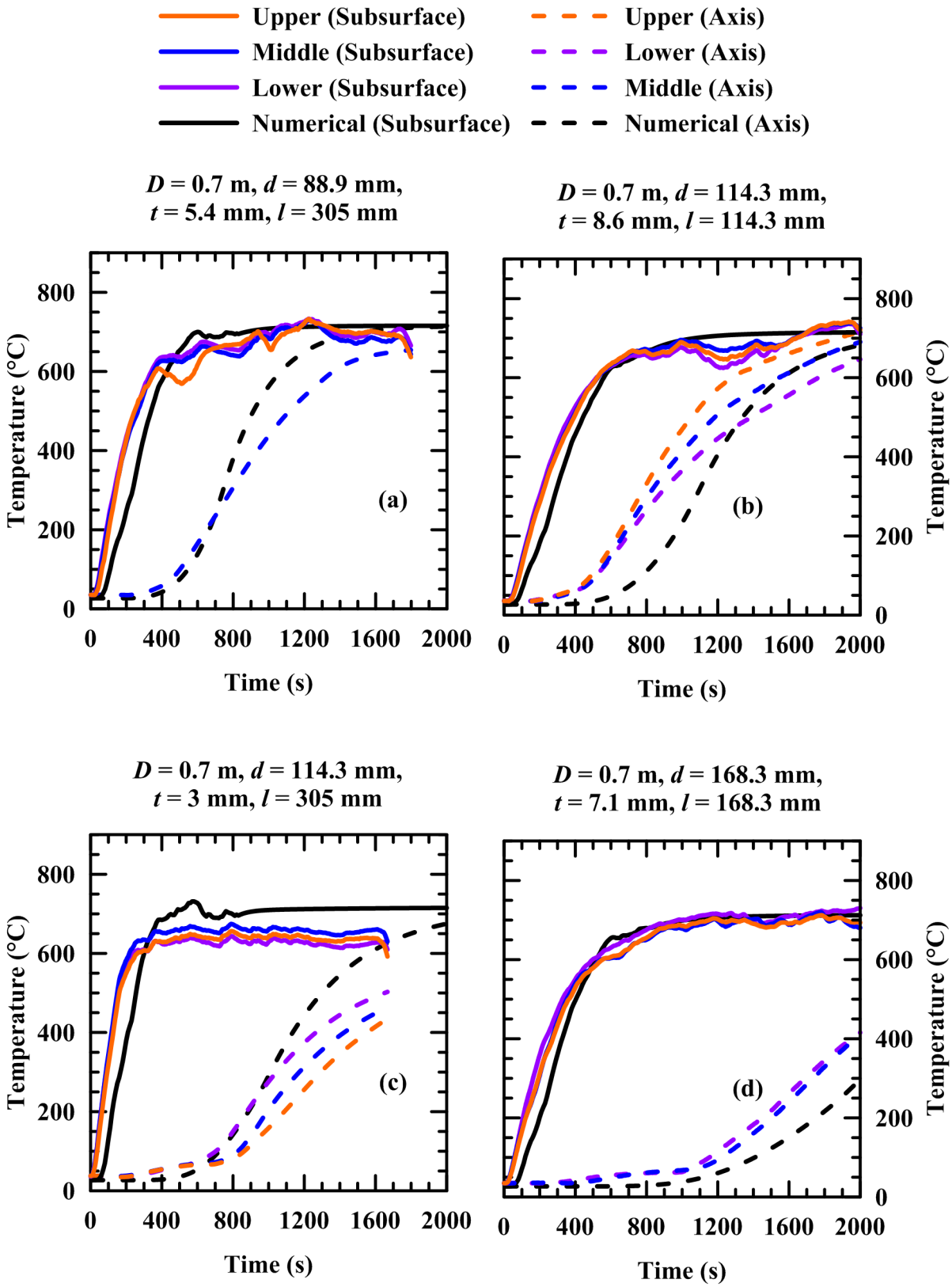

Fig. 6.14 Subsurface temperature distribution for vertical casks engulfed in a 0.7 m pool fire

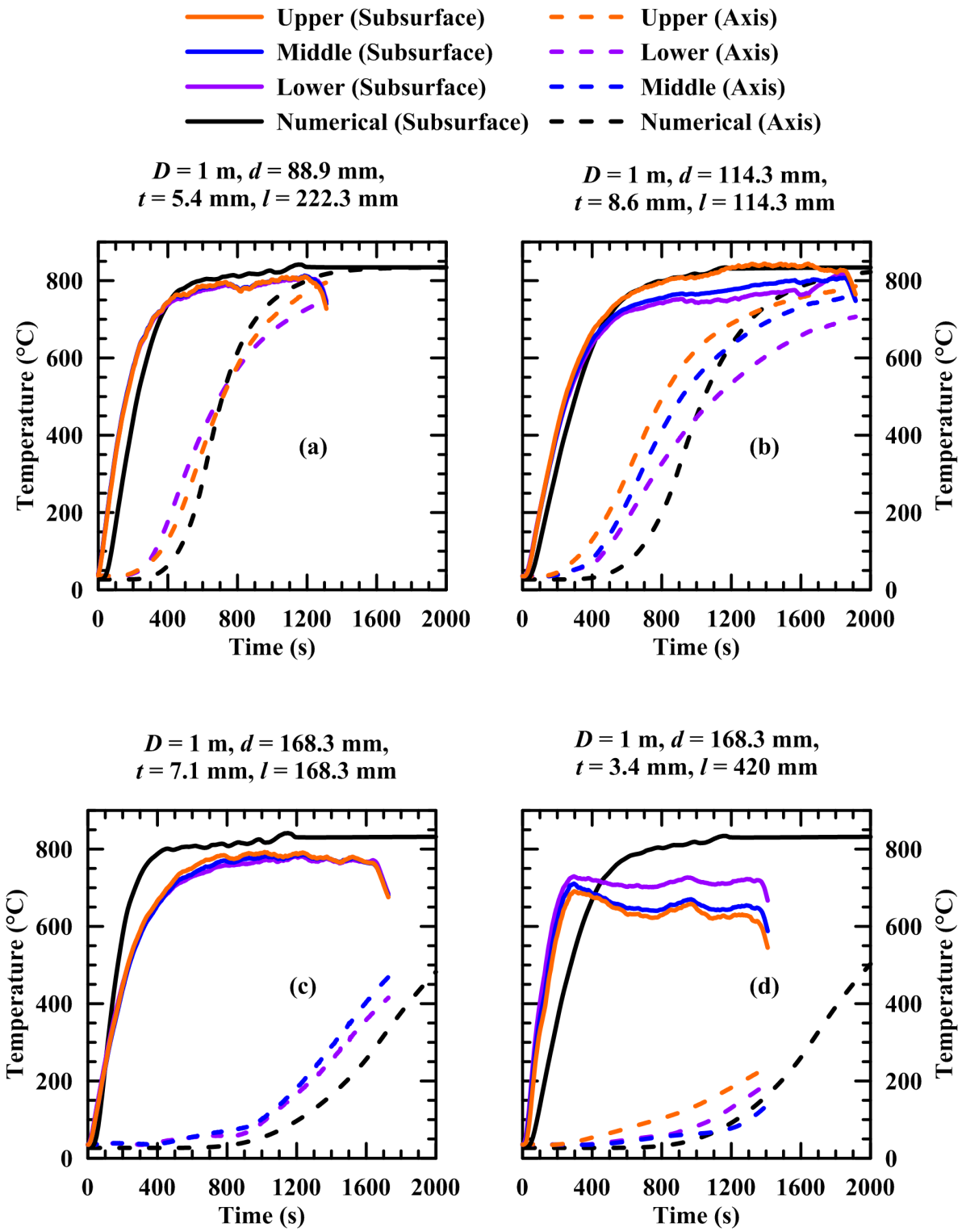

Fig. 6.15 Subsurface temperature distribution for vertical casks engulfed in a 1.0 m pool fire

temperatures to be overpredicting the temperatures when compared with the experimental measurements. This demonstrates that the numerical estimations are conservative.

Figure 6.14 shows the subsurface temperature distribution of various vertical casks engulfed in 0.7 m diesel pool fire. Numerical predictions of the averaged steady state subsurface temperature distributions are within 10% of the experimental results. The average temperatures at different locations ($3l/4, l/2$ and $l/4$ from the bottom of the cask) are almost the same in spite of their location inside the cask. This shows that the conduction is dominant in the radial direction compared to that in the axial direction. Figure 6.15 shows the subsurface temperature distribution of casks engulfed in a 1 m pool fire. Numerical predictions of the averaged steady state subsurface temperature distributions are within 7% of the experimental results. There is sudden drop of the temperatures in Fig. 6.15(d) at 285 s and is due to the sudden wind. This experiment is not repeated due to the costs involved in conducting the experiment. Figures 6.13 to 6.15 show that the temperature differences between the upper, middle and lower layers are significantly reduced for higher pool sizes (from 20% to less than 1%).

Thermal Analysis on Horizontal casks

Figures 6.16 to 6.18 show the subsurface transient temperature distributions of horizontal casks engulfed in pool fires. As there is a huge variation in the measured temperature distribution over the surface the cask, the worst case scenario is chosen for comparing with numerical simulations. And a corresponding insulation temperature is provided in all the Figs. 6.16 to 6.18. It is clearly observed that as the diameter increases, the numerical simulations are able to predict the temperature well. For a 0.5 m pool fire (Fig. 6.16), a maximum deviation of 8% is observed where as for a 1.0 m pool fire (Fig. 6.18), the maximum deviation is less than 3%. This shows that these simulations are conservative. All of these comparisons are with the maximum experimental subsurface temperature of the cask. In Fig. 6.17, there is a sudden dip in the predicted temperature data. This is because of the sudden drop in the T_{PT} value in Fig. 6.10 and hence the lower value of T_{AST} in Fig. 6.11.

As the size of the pool increases, there is a better chance for the casks to be completely engulfed with an uniformly distributed temperature. The measured transient temperature distributions of the casks presented in Figs. 6.13 to 6.18 serve as benchmark results.

6.8.3 Inverse Heat Conduction Problem

Heat flux on to the surface of the cylinder is measured using a commercial software Beck Engineers IHCP-1D (Beck, 2012). Beck IHCP-1D is applied for all the casks considered in this study (Table 6.1). This program provides a means for the numerical solution

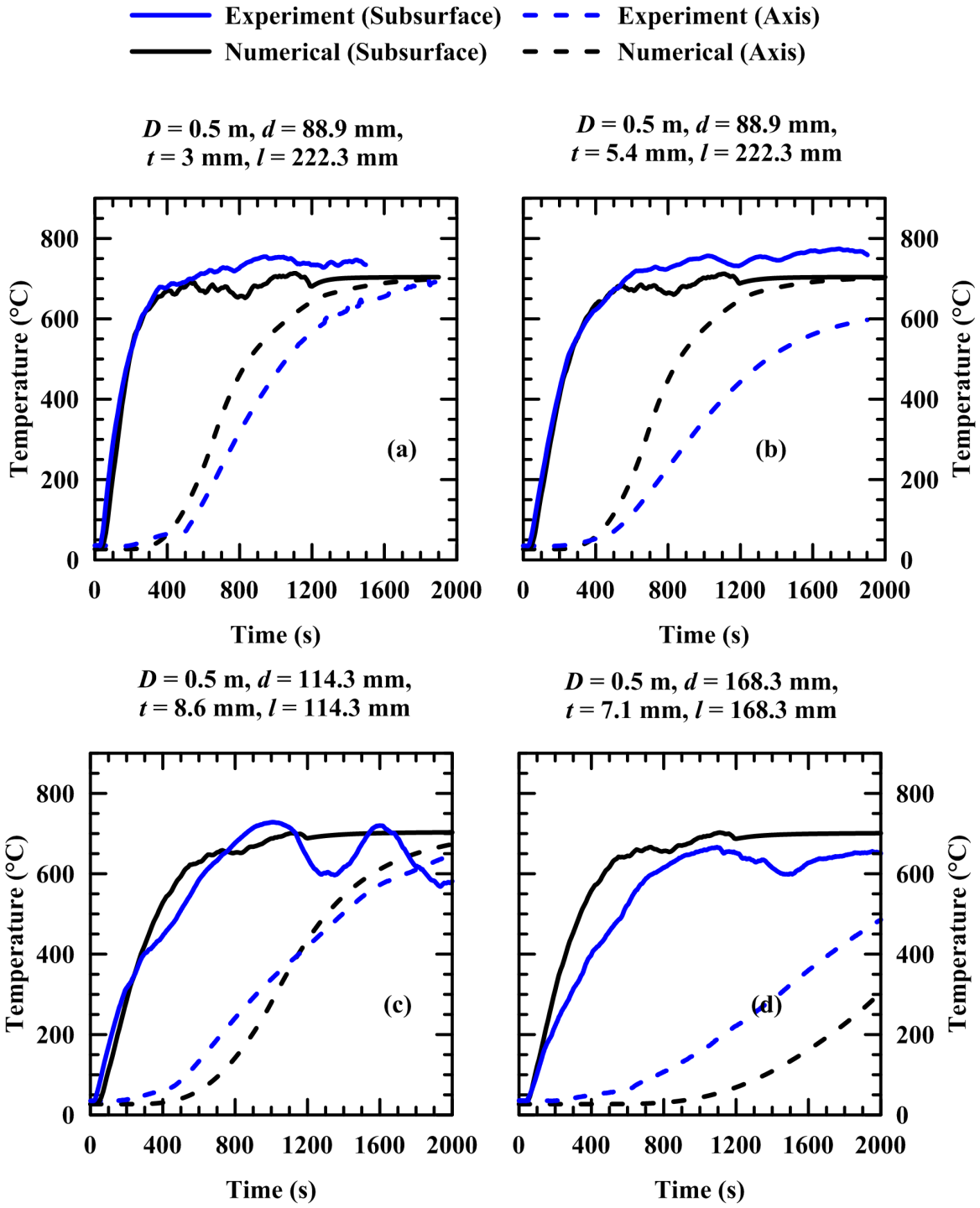

Fig. 6.16 Subsurface temperature distribution for horizontal casks engulfed in a 0.5 m pool fire

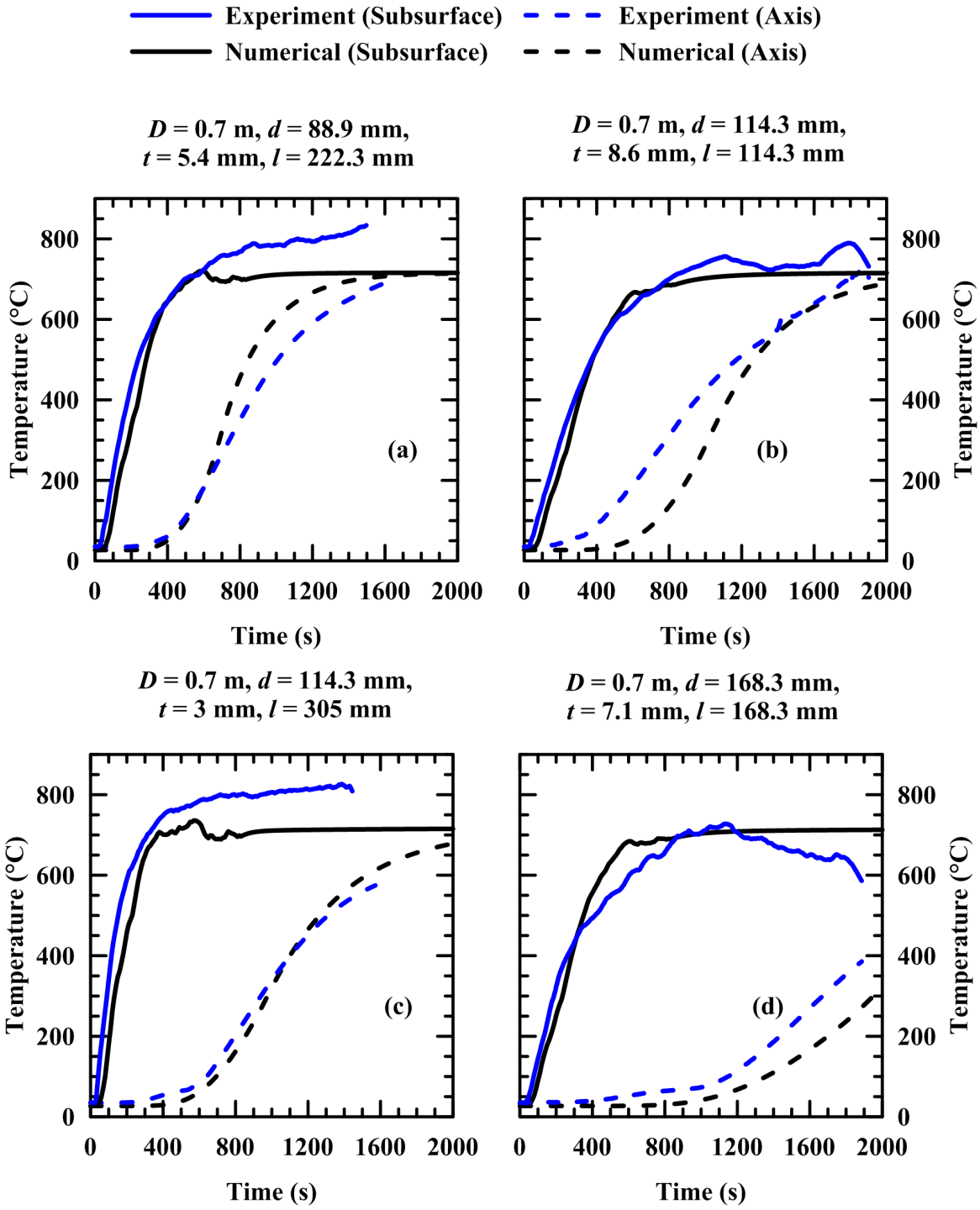

Fig. 6.17 Subsurface temperature distribution for horizontal casks engulfed in a 0.7 m pool fire

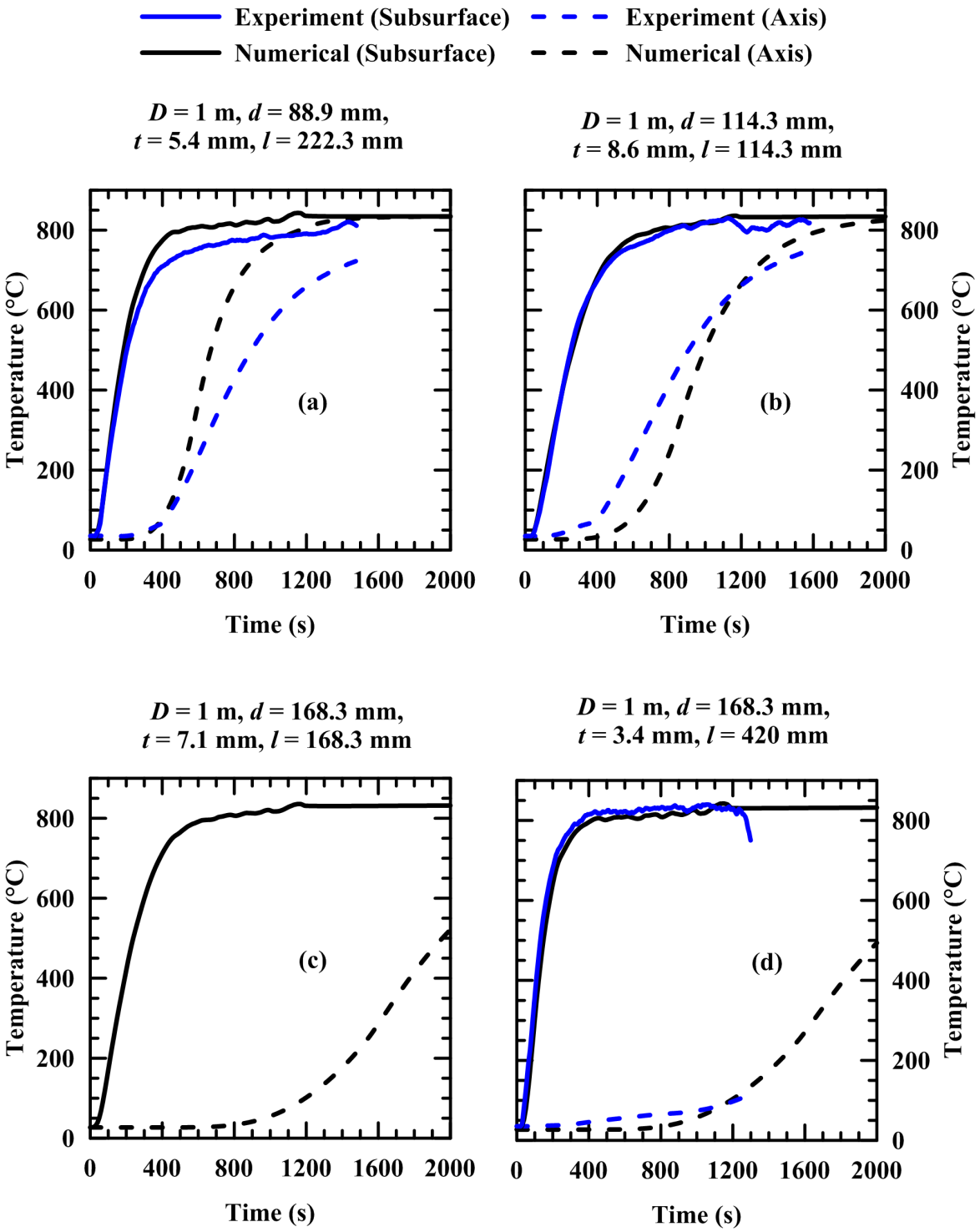

Fig. 6.18 Subsurface temperature distribution for horizontal casks engulfed in a 1.0 m pool fire

of the nonlinear, one-dimensional inverse heat conduction problem (IHCP) for planar, cylindrical and spherical geometries (Beck, 1962). Measured inner surface temperature of the cask (L, M or U) is given as one of the inputs to the program. Corresponding measured temperatures at the center of the insulation is given as another input to the program. Number of nodes per regions considered as 500. Five future time steps are considered and verified to be predicting the heat flux independent of number of future time steps (> 5). The properties of SS304L and insulation are shown in Table 6.2. This program predicts the incident heat flux onto the surface and the outer surface temperature of the cask.

Comparison of heat flux Estimated by IHCP using measured transient temperature distributions of the cask with the numerical predictions

Figures 6.19 to 6.24 show the estimated surface heat fluxes on to the casks by IHCP and the computed heat flux by numerical predictions. It is observed that the surface heat flux increases with the size of the pool fire and it varies with size of the cask engulfed in the fire. For larger pool diameters, the incident heat flux is higher than for the smaller diameters. Except for few configurations, the numerical results are well compared with the estimated heat flux results within the uncertainty limits.

Figures 6.19 to 6.24, show that the heat flux increasing from a lower value reaches a maximum and then decreases. Flame takes around 120 s to reach the steady state and during this period the heat flux on to the cask gradually increases as the flame is slowly ramping up. After reaching a steady state, because of the increase in the temperature of the cask surface temperature, the net heat flux from the flame to the cask decreases. Finally, when the cask surface reaches the temperature of the flame, the net heat flux to the cask surface becomes zero. From Fig. 6.19, for the vertical casks engulfed in 0.5 m diameter pool fire, the maximum heat flux is around 40 kW/m^2. For the horizontal casks engulfed in 0.5 m diameter pool fire (Fig. 6.22), the maximum heat flux is around 60 kW/m^2. A maximum heat flux of 60 kW/m^2 is both horizontal and vertical casks engulfed in 0.7 m pool fire. A maximum heat flux of 80 kW/m^2 is both horizontal and vertical casks engulfed in 1.0 m pool fire. Data is not smoothened and therefore, some coarseness in the heat fluxes are seen in the Figs. 6.19 to 6.24. The heat flux values are underpredicted when compared with IHCP results but are within the uncertainty of the IHCP simulations.

6.8.4 Partitioning of Heat Fluxes

The total incident heat flux in Eq. (6.23) consists of convection and radiation components. The first term of the RHS in Eq. (6.23) gives the radiative component where as the second term gives the convective component. These two components are computed at each time

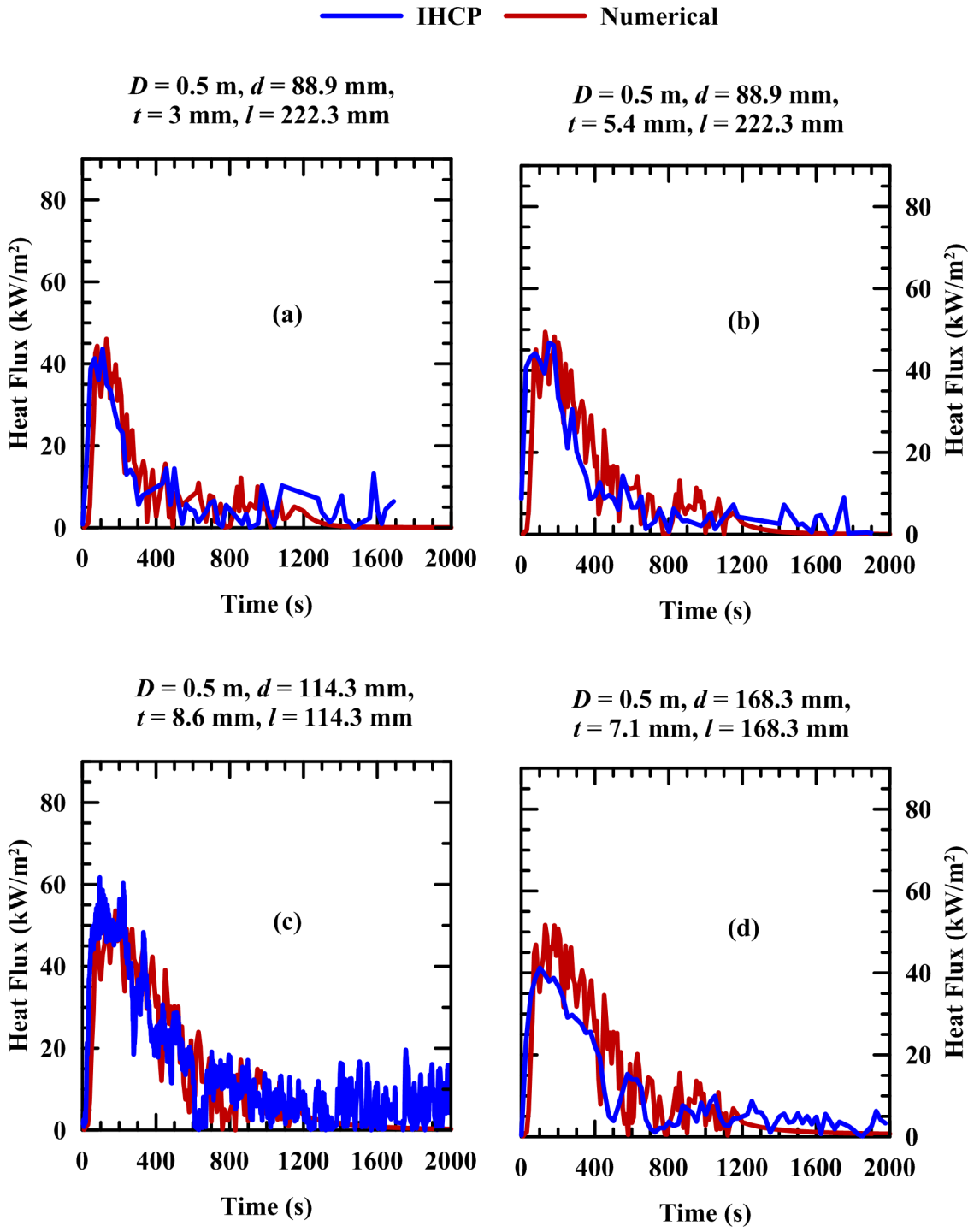

Fig. 6.19 Surface heat flux for vertical casks engulfed in a 0.5 m pool fire

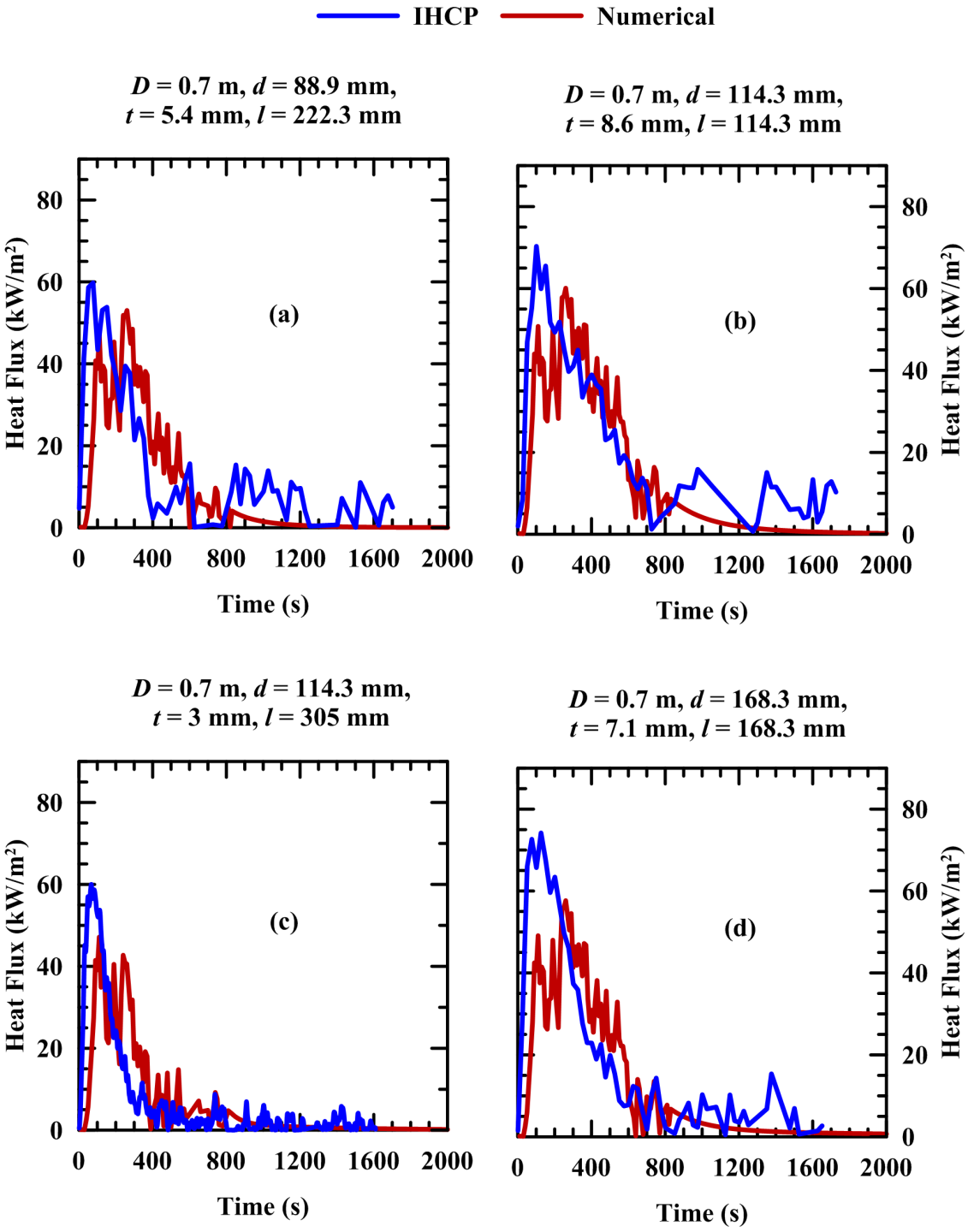

Fig. 6.20 Surface heat flux for vertical casks engulfed in a 0.7 m pool fire

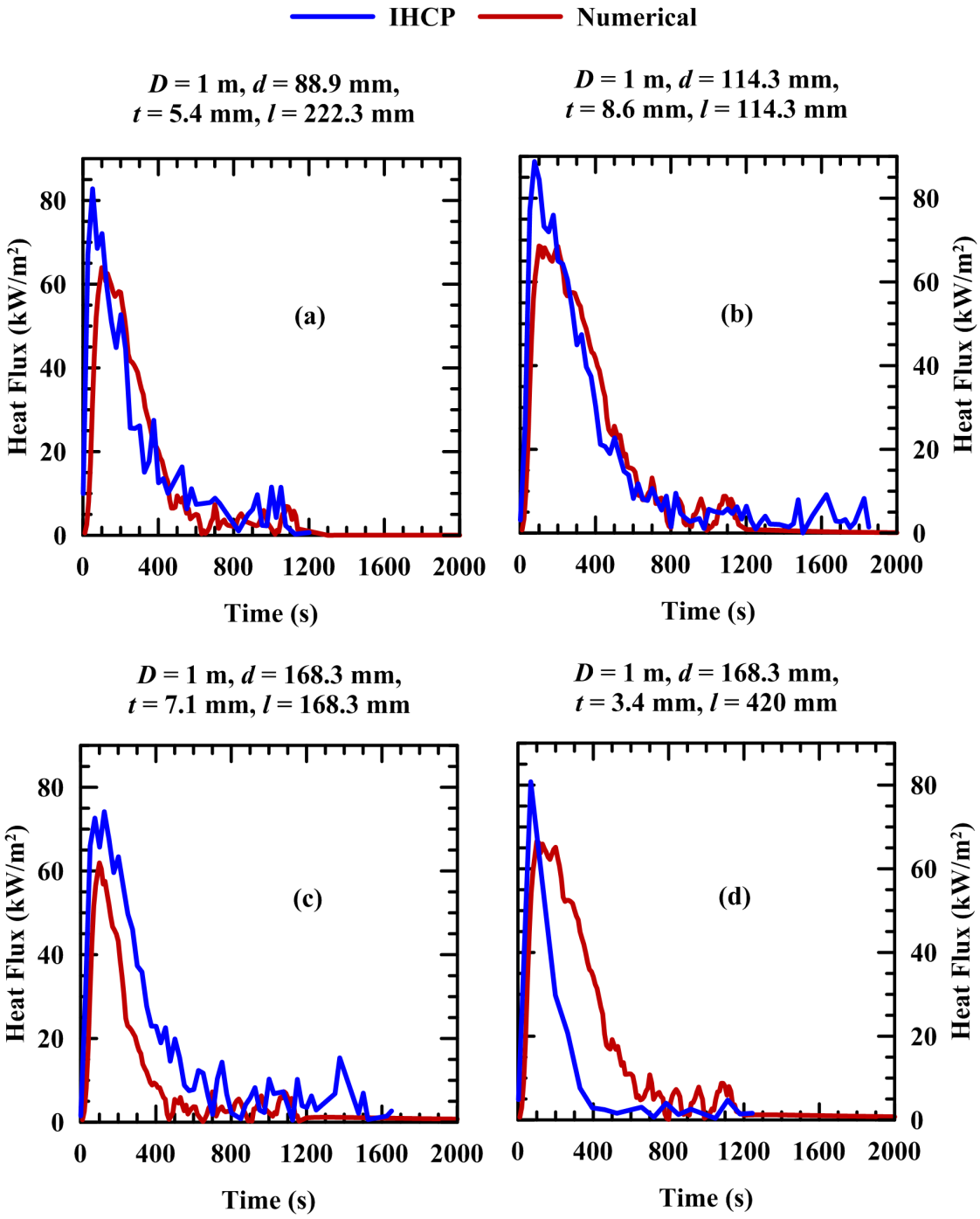

Fig. 6.21 Surface heat flux for vertical casks engulfed in a 1.0 m pool fire

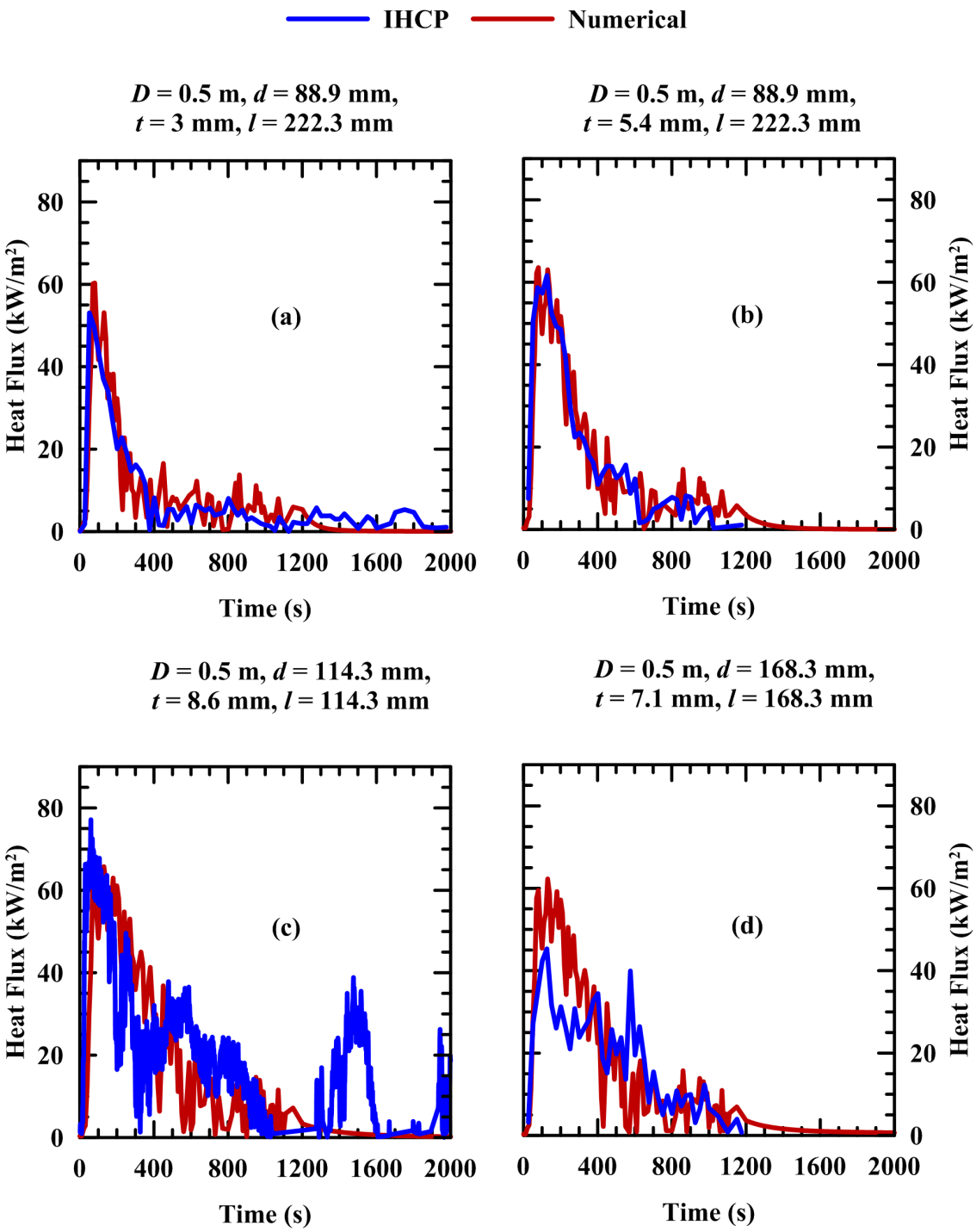

Fig. 6.22 Surface heat flux for horizontal casks engulfed in a 0.5 m pool fire

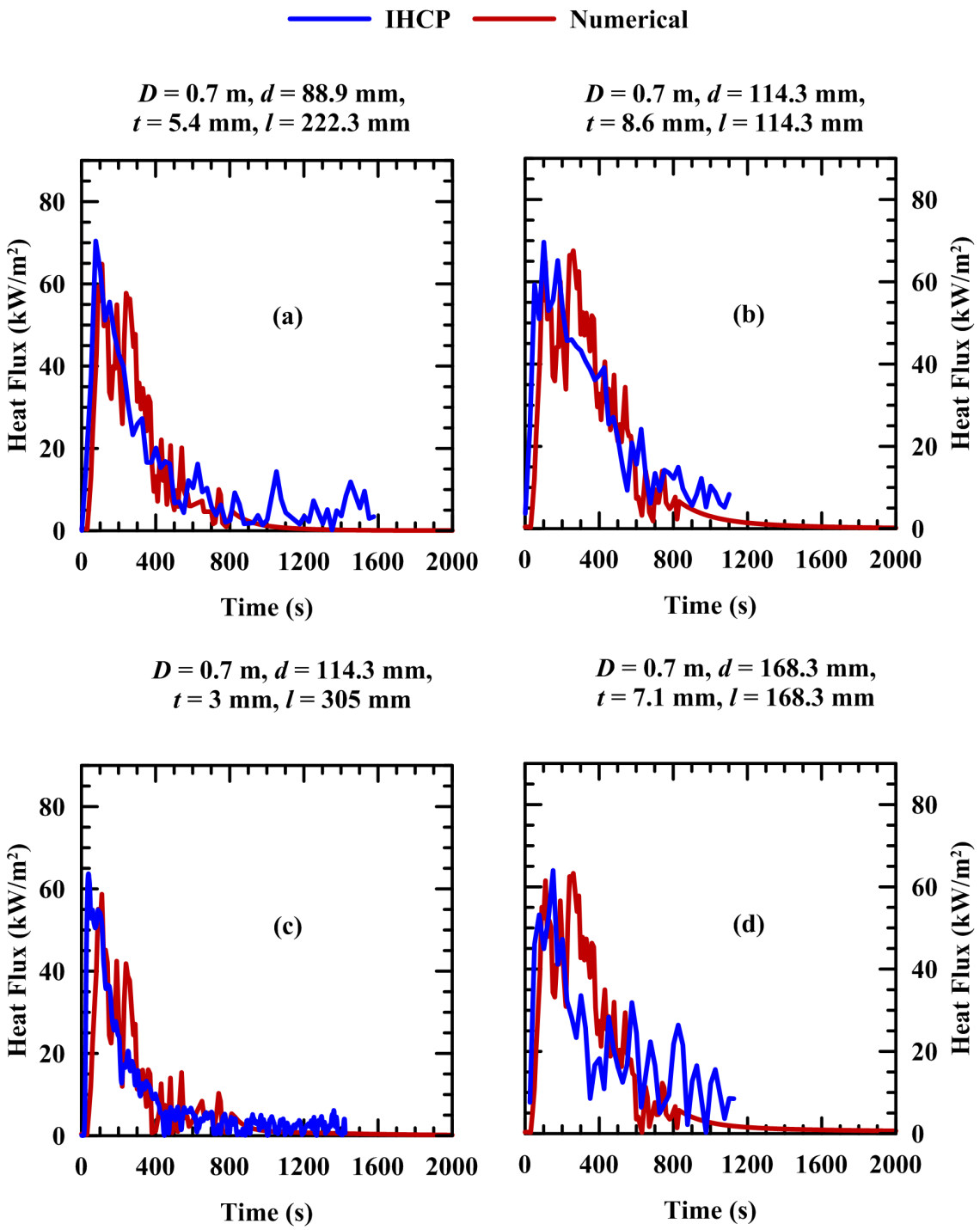

Fig. 6.23 Surface heat flux for horizontal casks engulfed in a 0.7 m pool fire

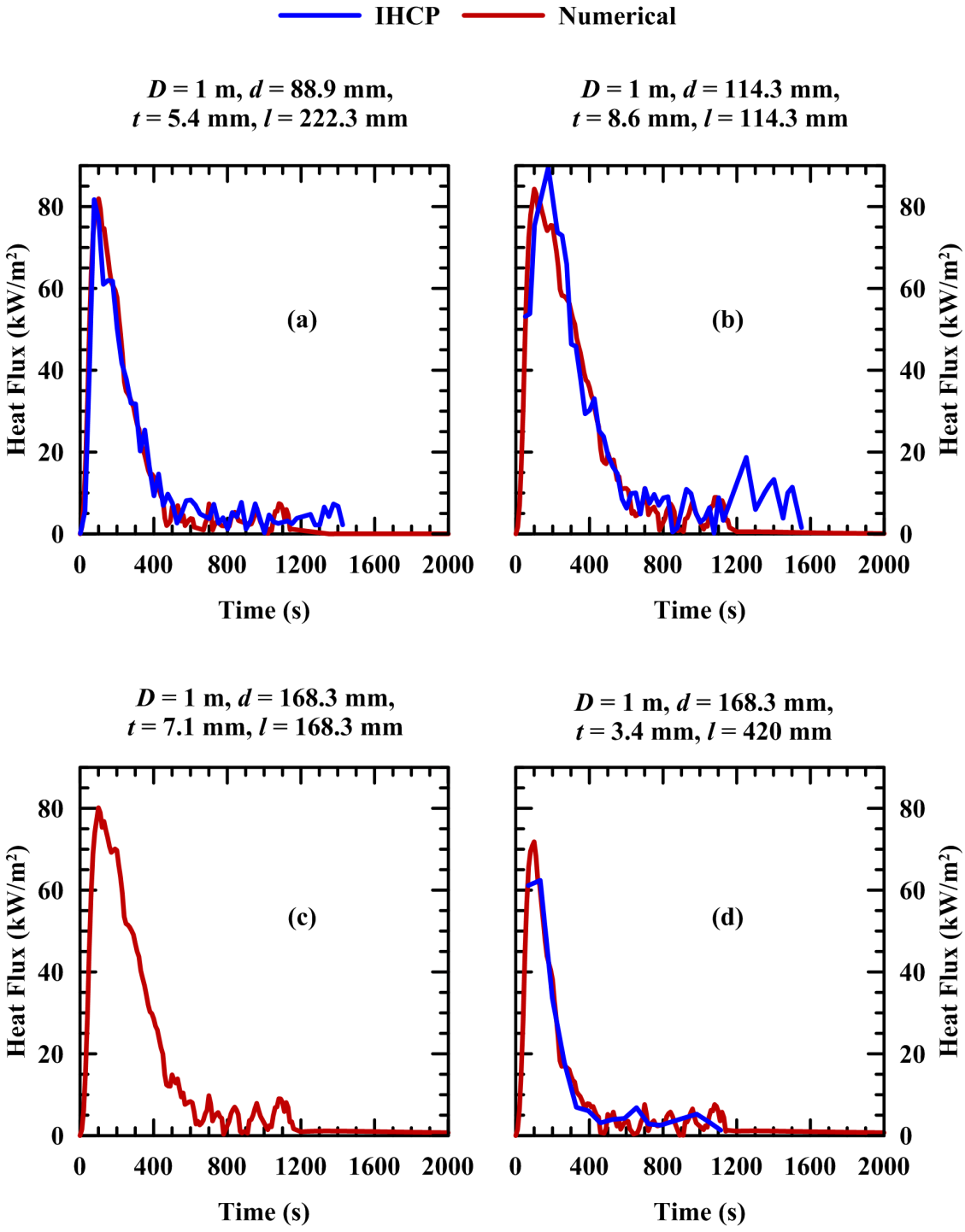

Fig. 6.24 Surface heat flux for horizontal casks engulfed in a 1.0 m pool fire

step. Since all the results gave a similar conclusion, only two blockages (minimum and maximum) are shown in this study. Figure 6.25 shows the convection and radiation heat flux components of the incident heat flux for two blockages 0.8% and 14.4% for vertical casks. Irrespective of the blockage, it is observed that the radiative component is more dominant than the convective component. The maximum convective component is 9.7 kW/m^2 in all the blockages covered in this work. Figure 6.26 shows the fraction of the heat flux component to the total heat flux experienced by the casks in 1 m pool fire in vertical and horizontal orientations. It is observed that the convective component is decreasing while the radiative component is increasing with the increase in time for all the blockages. At maximum total heat flux, the convective component is 10% and the radiative component is 90% for all the configurations considered in this study.

The present study shows that there is no influence of blockage ($0.8\% < B < 14.4\%$) on heat release rate. The measured velocity of pool fires are very low and of the order of 1.53 m/s to 1.79 m/s. Though the forced convective heat transfer is dominated than the free convection in this study, it is observed that radiation is dominant by 90% of the total heat transfer. The concept of adiabatic surface temperature is adapted to thermal tests and is validated with the experimental results. The numerically predicted results are within 10% of the experimental results.

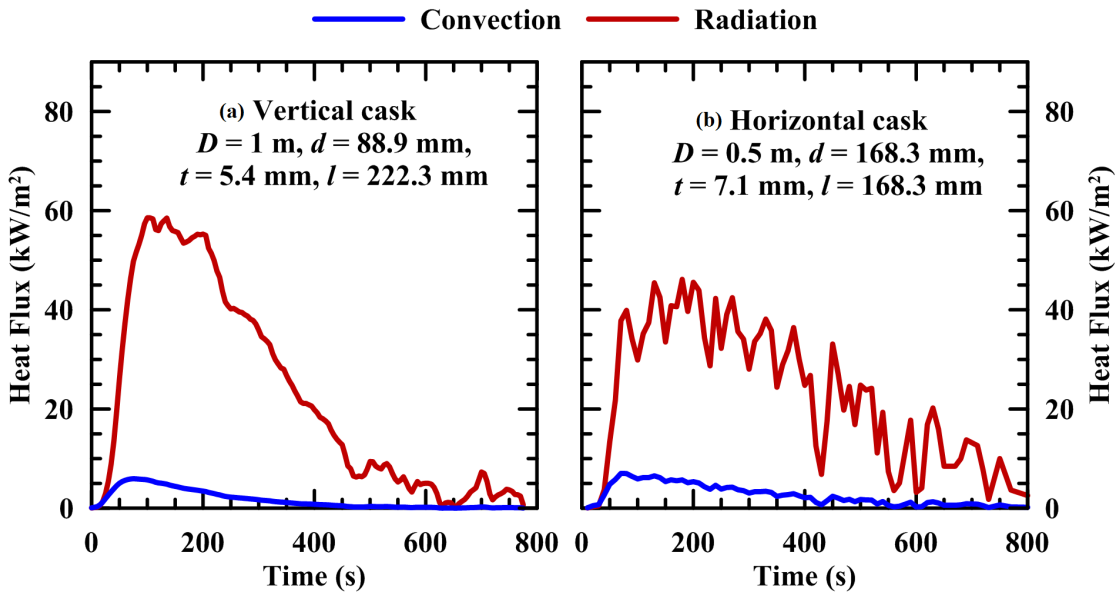

Fig. 6.25 Partitioning of heat fluxes for vertical and horizontal casks

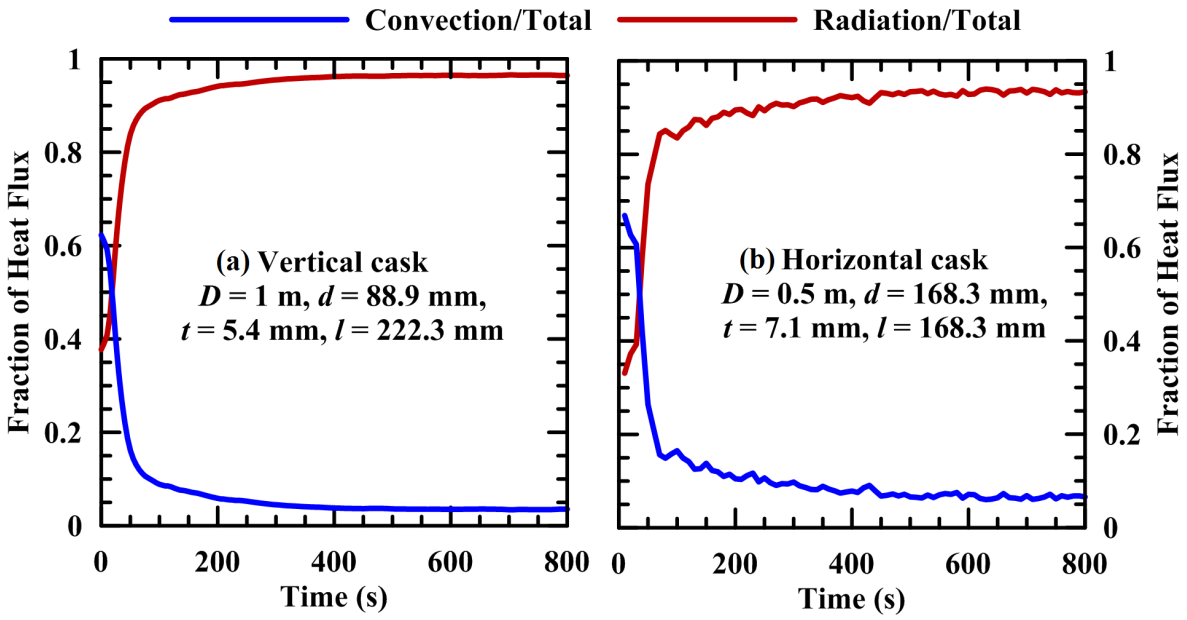

Fig. 6.26 Fraction of heat flux components for vertical and horizontal casks

6.8.5 Discussion on the Relevance of the Present Study as Against IAEA Standards

International Atomic Energy Agency standard specifies the pool fire temperature as 800 °C (IAEA, 2005). The standard does not specify about the size of the pool fire. It may be observed that the pool fire sizes used in various investigations reported in the literature varies from 2 m to 16 m. The maximum temperature of the flame varies with the size of the pool (Section 3.12). Hence, merely specifying 800 °C as the flame temperature may not be appropriate. This study demonstrates that using measured AST for thermal analysis is appropriate. AST varies with the pool fire diameter and fuel. For larger pool fires, AST needs to be measured and used for qualifying the casks.

6.9 Conclusions

Transportation package is idealized as a circular cask filled with an insulating material. For a blockage ratio of $0.8\% < B < 14.4\%$, the effect on the mass burning rate of diesel pool fires is not significant. Maximum heat flux onto the casks is around 40-45 kW/m^2, 60-70 kW/m^2 and 70-80 kW/m^2 for pool diameters of 0.5 m, 0.7 m and 1.0 m respectively. Radiation is dominant by 90% of the total heat transfer and hence the convective heat transfer can be neglected in heat transfer models for these blockage ratios.

The adiabatic surface temperature (AST) of diesel pool fires are computed from measured plate thermometer temperatures. By employing mixed boundary condition in a CFD

package, transient temperature distribution and heat flux to the casks are estimated. This present work demonstrates that the AST of the pool fires can be used to predict the behavior of the thermal casks engulfed in pool fires. This clearly obviates the necessity of computationally intensive modeling of open pool fires. The transient temperature distribution and heat flux distribution would serve as benchmark results for validating computational results.

CHAPTER 7

Numerical Simulations for Thermal Tests

7.1 Introduction

In the previous chapters, experimental studies on open pool fires are discussed. This chapter investigates numerical simulations of open pool fires using a CFD model, Fire Dynamics Simulator (FDS). It is a computational fluid dynamics model of fire-driven fluid flow (McGrattan *et al.*, 2007).

Real life cask testing involves the transportation cask being engulfed in a pool fire of $\geq$ 4 m pool fire. However, conducting experiments with 4 m pool fire is quite expensive. Hence, numerical experiments are carried out using FDS. FDS is validated using 1 m pool fire results. Then, results would be obtained by FDS for 4 m pool fire.

7.2 Mathematical Modeling in FDS

FDS solves numerically a form of the Navier-Stokes equations appropriate for low-speed, thermally-driven flow, with an emphasis on smoke and heat transport from fires. Partial derivatives of the conservation equations of mass, momentum and energy are approximated as finite differences, and the solution is updated in time on a three-dimensional, rectilinear grid. Thermal radiation is computed using a finite volume technique on the same grid as the flow solver. Lagrangian particles are used to simulate smoke movement, sprinkler discharge, and fuel sprays. In FDS, the gases are treated as incompressible. Also,

the flow is considered as the low speed flow *i.e.,* Mach number less than 0.3. Algorithm uses predictor corrector scheme which is second order accurate in time and space. Turbulence is treated with large eddy simulation model. The following conservation equations are solved for gas phase in FDS:

7.2.1 Continuity Equation

The continuity equation is given by:

$$\frac{\partial \rho}{\partial t} + \bigtriangledown \cdot \rho u = \dot{m}_b''' \tag{7.1}$$

where ρ is the density of the gas, u is the velocity, t represents time and $\dot{m}_b'''$ is the bulk mass source per unit volume. The gas phase mass conservation equation mentioned in Eq. (7.1) is not the conventional one because of the presence of extra source term, $\dot{m}_b'''$. This source term accounts for the pyrolysis of solid and evaporation of liquid fuel and water droplet, which enters a gas-phase control volume through the control volume surface. Explicitly, this takes into account the mass of gaseous vapour generated due to evaporation of liquid droplet.

7.2.2 Mass Transport Equation

The mass transport equation is given by:

$$\frac{\partial \rho Y_\alpha}{\partial t} + \bigtriangledown \cdot \rho Y_\alpha u = - \bigtriangledown \rho D_\alpha \bigtriangledown Y_\alpha + \dot{m}_\alpha''' + \dot{m}_{b\alpha}''' \tag{7.2}$$

where Y_α is the mass fraction, D_α is the diffusivity coefficient of species α and $\dot{m}_{b\alpha}'''$ is the bulk production rate of species α by evaporating droplets or particles per unit volume.. Here, α denotes species *i.e.,* CO_2, CO, H_2O, soot and fuel. The equation of mass transport accounts for the both the gas species generated due to chemical reaction as well as due to evaporation of liquid droplets or particle the source terms. Also, sum of Eq. (7.2) over all the species (α) results in $\sum Y_\alpha = 1$ and net rate of production or depletion of species becomes zero *i.e.,* $\sum \dot{m}_\alpha''' = 1$. Moreover for continuity equation to hold true, following conditions are to be satisfied:

$$\sum \dot{m}_{b\alpha}''' = \dot{m}_b''' \tag{7.3}$$

$$\bigtriangledown \rho D_\alpha \bigtriangledown Y_\alpha = 0 \tag{7.4}$$

7.2.3 Momentum Equation

The momentum equation is given by:

$$\frac{\partial \rho u}{\partial t} + \bigtriangledown \cdot \rho u v + \bigtriangledown = \rho g + f_b + \bigtriangledown \cdot \tau_{ij} \tag{7.5}$$

where p is the pressure and g is the gravity. The force tern f_b represents the external force such as drag force exerted by liquid droplet. The stress tensor τ_{ij} is given as

$$\tau = (\mu + \mu_{LES})(2S - \frac{2}{3}\delta_{ij}(\bigtriangledown \cdot u)) \tag{7.6}$$

$$\delta_{ij} = \begin{cases} 1, i = j \\ 0, i \neq j \end{cases} \tag{7.7}$$

FDS uses the large eddy simulation model (LES) for accounting the turbulence in flow field. In LES model, for the eddies having the scale greater than grid size are resolved directly while sub grid eddies are modeled. FDS incorporates Smagorinsky model for resolving the sub grid eddies in overall flow by evaluating the numerical viscosity (μ_{LES}) as per:

$$\mu_{LES} = \rho(C_s\Delta)^2(2S_{ij}S_{ij} - \frac{2}{3}\delta_{ij}(\bigtriangledown \cdot u)^2)^{0.5} \tag{7.8}$$

where C_s is smagorinsky constant, Δ is kronecker delta,

$$S_{ij} = \frac{1}{2}\left(\frac{\partial u_i}{\partial x_j} + \frac{\partial u_j}{\partial x_i}\right) \tag{7.9}$$

7.2.4 Energy Equation

The transport of sensible enthalpy equation is given by:

$$\frac{\partial}{\partial t}(\rho h_s) + \bigtriangledown \cdot \rho h_s u = \frac{Dp}{Dt} + \dot{q}''' - \dot{q}_b''' + \bigtriangledown \cdot \dot{q}'' + \varepsilon \tag{7.10}$$

where $\dot{q}'''$ is the heat release rate per unit volume, $\dot{q}_b'''$ the heat transferred to evaporating liquid droplet per unit volume, h_s is heat transfer coefficient and ε is dissipation rate. The heat flux $\dot{q}''$ accounts for conductive heat, heat because of species diffusion and radiative heat.

7.2.5 Combustion Model

FDS incorporates finite rate reaction model and mixture fraction model. Since in LES small scale diffusion processes are not resolved, mixture fraction model is invoked for calculating heat release rate and species mass fraction. Mixture fraction represents fraction of unburned fuel and burned fuel *i.e.,* product. Hence this variable is always conserved. Mixture fraction model assumes that combustion is mixing controlled and reaction between fuel and oxidizer is infinitely fast. Mixture fraction model assumed to follow:

$$\upsilon_F[F] + \upsilon_O[O] \rightarrow \sum \upsilon_P[P] \tag{7.11}$$

The stoichiometric coefficients υ_F, υ_O and υ_P can be obtained by element balance. Mixture fraction is conserved scalar property and defines fraction of gas present at any given point in the flow field. Mathematically, the mixture fraction (Z) may also be defined in terms of mass fraction of the fuel and carbon carrying product:

$$Z = \frac{1}{Y_F^1}\left[Y_F + \frac{W_F}{xW_{\mathrm{CO_2}}}Y_{\mathrm{CO_2}} + \frac{W_F}{xW_{\mathrm{CO}}}Y_{\mathrm{CO}} + \frac{W_F}{xW_s}Y_s\right] \tag{7.12}$$

It can be partitioned into unburned fuel and burned fuel which is converted into the products as:

$$Z_1 = \frac{Y_F}{Y_F^1} \tag{7.13}$$

$$Z_2 = \frac{W_F}{xW_{\mathrm{CO_2}}}Y_{\mathrm{CO_2}} + \frac{W_F}{xW_{\mathrm{CO}}}Y_{\mathrm{CO}} + \frac{W_F}{xW_s}Y_s \tag{7.14}$$

where W_α is molecular weight of species α. The local heat release is computed as:

$$Z_1^{n+1} = Z_1^n - \left[\frac{\dot{q}'''\Delta t}{\rho\Delta H}\right] \tag{7.15}$$

$$Z_2^{n+1} = Z_2^n + \left[\frac{\dot{q}'''\Delta t}{\rho\Delta H}\right] \tag{7.16}$$

From the mixture fraction variable Z_1 and Z_2, the species mass fractions can be determined, as mass fractions of the species (Y_α) is function of Z_1 and Z_2 only *i.e.,* $Y_\alpha = f(Z_1, Z_2)$. The relation between mass fractions of species and mixture fractions is defined as state relation.

7.2.6 Radiation Model

The gas generated due to combustion is considered as the non-scattering, hence, this results in the great simplification of radiation transport equation (RTE). The simplified RTE is expressed as:

$$s \cdot \bigtriangledown I_\lambda(x, s) = \kappa(x, \lambda)[I_b(x) - I_\lambda(x, s)] \tag{7.17}$$

where I is radiative intensity, λ is wave length, κ is absorption coefficient. The complete radiation band is divided into six or nine bands and RTE is solved over each discrete band wavelength. The band specific RTE are:

$$s \cdot \bigtriangledown I_n(x, s) = \kappa_n(x, \lambda)[I_{b,n}(x) - I_n(x, s)], n = 1, 2, 3, ...N \tag{7.18}$$

The total intensity is calculated by summing up the intensity obtained for individual bands. Moreover the radiative property like absorption coefficient is calculated using

RADCAL subroutine specifically developed for open pool fire simulations. More details on mathematical modeling of FDS are well presented in Wen *et al.* (2007), Xin *et al.* (2008), McGrattan and Klein (2007).

7.3 FDS Parameters

The FDS input parameters are classified as miscellaneous parameters, hydrodynamic parameters, combustion parameters, liquid fuel properties, radiation parameters and miscellaneous parameters. The hydrodynamic FDS input parameters are presented in Table 7.1. For large scale computations Courant Friedrichs Lewy (CFL) restricts the time step. It is defined as

$$\delta t = \max\left(\frac{|u|}{\delta x}, \frac{|v|}{\delta y}, \frac{|w|}{\delta z}\right) \tag{7.19}$$

The CFL conditions asserts that the solution of the equations cannot be updated with a time step larger than that allowing a parcel of fluid to cross a grid cell. Von Neumann number (VN) is a non dimensional number that controls the time step in case of fine grid, *i.e.,* it is only invoked in DNS simulation and in LES if grid size is smaller than 5mm. It is defined as

$$2\max\left(\mu, D, \frac{k}{\rho C_p}\right)\delta t\left(\frac{1}{\delta x^2}+\frac{1}{\delta y^2}+\frac{1}{\delta z^2}\right) < 1 \tag{7.20}$$

Turbulent Prandtl number is defined as the ratio of turbulent momentum diffusivity to turbulent thermal diffusivity. Turbulent Schmidt number is defined as the ratio of turbulent momentum diffusivity to turbulent mass diffusivity.

The combustion parameters for diesel pool fire are given in Table 7.2. The chemical composition of diesel is estimated by the CH (carbon, hydrogen) analysis. The results of CH analysis are given in Appendix B. CO yield is the fraction of mass of fuel that converted to carbon monoxide in kg of CO/kg of fuel. The value presented in Table 7.2 is from SFPE (2008). Soot yield is the fraction of mass of fuel that converted to soot in kg of soot/kg of fuel. Presence of soot plays dominant role in radiation energy transport. Critical or adiabatic flame temperature is defined as the highest value of temperature achieved when stoichiometric air fuel ratio mixture is burnt completely at constant pressure adiabatically.

The properties of the diesel liquid are given in Table 7.3. The fuel properties presented in Table 7.3 are from SFPE (2008). Absorption coefficient of liquid represents the absorption depth of thermal radiation. This parameter is important for mass burning rate prediction in FDS.

The FDS radiation parameters are given in Table 7.4. Gray band model assumes that all the radiative properties are independent of wave length and depend only on the tempera-

Table 7.1 Hydrodynamic FDS input parameters

Parameter	Description	Value
Simulator	Include gas phase flame extinction	.TRUE.
	Smagorinsky	0.2
	CFL region	0.8-1.0
	Von Neumann region	0.8-1.0
	LES	.TRUE.
	Turbulent Prandtl number	0.5
	Turbulent Schmidt number	0.5
	Baroclinic torque	.TRUE.
	Schmidt Number	0.5
	Pr	0.71
	Forced coefficient	0.037
	Horizontal coefficient	1.52
	Vertical coefficient	1.31
	Droplets disappear @ floor	.TRUE.

Table 7.2 FDS combustion input parameters for diesel vapor

Description	Parameter	Value
Diesel	Carbon	14
	Hydrogen	24
	Oxygen	0
	Nitrogen	0
	Other	0
	Ambient oxygen mass fraction, $Y_{O_2,\infty}$	0.23
	Mass fraction of fuel at burner, $Y_{F,0}$	1 kg/kg
Fire suppression	Limiting O_2	0.15 mol/mol
	Critical (Adiabatic) flame temperature	1427 °C
By products	Heat of combustion	42900 kJ/kg
	Ideal energy	.TRUE.
	Carbon monoxide fraction (CO yield)	0.012 kg/kg
	Soot fraction (soot yield)	0.1 kg/kg

Table 7.3 FDS input parameters for diesel liquid

Description	Parameter	Value
Thermal properties	Density	840 kg/m^3
	Specific heat of fuel	1.89 kJ/kg.K
	Thermal conductivity	0.18 W/m.K
	Emissivity	0.9
	Absorption coefficient	50000 1/m
Pyrolysis	Heat of combustion	42900 kJ
	Boiling temperature	300 °C
	Initial vapor	5×10^{-4} m^2/s
	Heat of vaporization	232.6 kJ/kg
	Fuel vapor yield	0
	Water vapor yield	0
	Residue yield	0
	Endothermic	.TRUE.

ture. Time step increment is the frequency of invoking radiation solver. Angle increment is the frequency at which the solid angle is changed. From Table 7.4, the radiation solver is invoked for every 6 time steps and solid angle is updated for every 5 time steps.

Table 7.5 shows the typical input miscellaneous parameters given in FDS. The simulations are run for 300 s. Burn away of solid represents whether fuel can be burn out in quantity or not. The parameter would set to .TRUE. when the mass burning rate is unknown and also it involves huge computational costs.

7.4 FDS Input Parameters that are Under Consideration

The FDS input parameters that are under consideration in study are grid size, solid angle and time step increment and type of radiation model. Figure 7.1 shows a typical computational domain used for studying sensitivity of input parameters on FDS output in open pool fires. A sensitivity analysis is performed on these parameters by observing their influence on centerline temperature and irradiance at $Z/D = 1$ for 0.3 m and 0.5 m diesel pool fire (Fig. 7.1). Irradiance is the heat flux from the flame incident at a given location. The temperature and irradiance values are averaged over the entire span of simulation time except for the initial ramp up period. The ramp up period in this study is 1 s. Table 7.6 shows various input parameters for diesel pool fires of 0.3 m and 0.5 m

Table 7.4 FDS radiation simulation parameters

Description	Parameter	Value
Radiation	RTE	.TRUE.
	Wide band model	.FALSE.
	Gray band model	.TRUE.
	Time step increment	6
	Angle increment	5
	Solid angles	500
	Polar angles	15
	Radiative source temp	1000 °C
	Absorption coefficient	1.2 1/m
	Radiative loss fraction	0.23
	Path length	0.3 m

Table 7.5 Miscellaneous FDS input parameters

Parameter	Description	Value
Time	Start time	0 s
	End time	300 s
	Initial time step	0 s
	Don't allow *dt* change	.FALSE.
	Don't allow *dt* exceed initial	.TRUE.
	Wall update increment	2 frames
Output	3D smoke visualization	.TRUE.
	Restart	300 s
Environment	Ambient temperature	25 °C
	Atmospheric pressure	1.01325×10^5 Pa
	Gravity (upward)	-9.81 m/s^2
Others	Burn away of solid	.FALSE.
	Thickness of liquid fuel	0.1 m

pool fire. As the simulation results for both the pool fires depict same conclusions, only 0.3 m pool fire results are presented in this report.

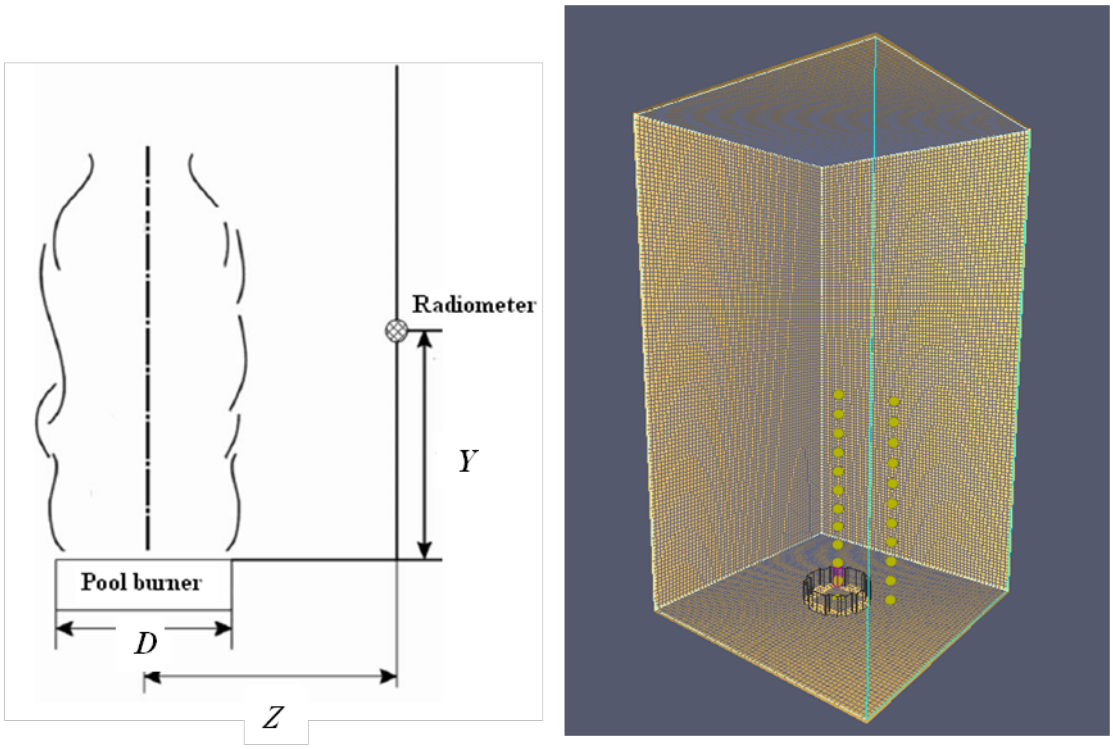

Fig. 7.1 Typical computational domain used for open pool fire simulations

Table 7.6 FDS input parameters for 0.3 m and 0.5 m diesel pool fires

	Pool diameter, *D*	
Parameter	**0.3 m**	**0.5 m**
Domain size (m^3)		
length × breadth × height	0.75 × 0.75 × 1.2	1.2 × 1.2 × 2.4
Angle increment, f_n	5	5
Time step increment, f_t	3	3
Radiation model	Gray band	Gray band
Mass burning rate	17 $gm/m^2.s$	27.5 $gm/m^2.s$
Time period	30 s	30 s

7.4.1 Influence of Grid Resolution on Centerline Temperature and Irradiance

Basing on the observations of Lin *et al.* (2010), the number of solid angles is taken as 500. The angle increment (f_n)and time step increment (f_t) are fixed as 5 and 3 respectively.

Influence of grid size on the centerline temperature and the irradiance computed at $Z/D = 1$ from the axis of pool is examined. For the purpose of representation, a non dimensional grid resolution is defined as follows. Non dimensional resolution,

$$R = \frac{\max(dx, dy, dz)}{\left(\frac{Q}{\rho_\infty C_p T_\infty \sqrt{g}}\right)^{2/5}} \tag{7.21}$$

This non dimensional grid size is used in order to make the sensitivity analysis independent of pool diameter and fuel used. Figure 7.2 shows the centerline temperature variation for 0.3 m diesel pool fire for different grid sizes. For a non dimensional resolution (R) of 0.076 and for further finer resolution, the temperatures practically are same. Figure 7.3 shows irradiance at $Y/D = 1$ for 0.3 m diesel pool fire for different grid sizes. For a non dimensional resolution (R) of 0.035 and for further finer resolution, the irradiance do not change. Hence, a non dimensional resolution, $R = 0.035$ or finer would provide satisfactory results.

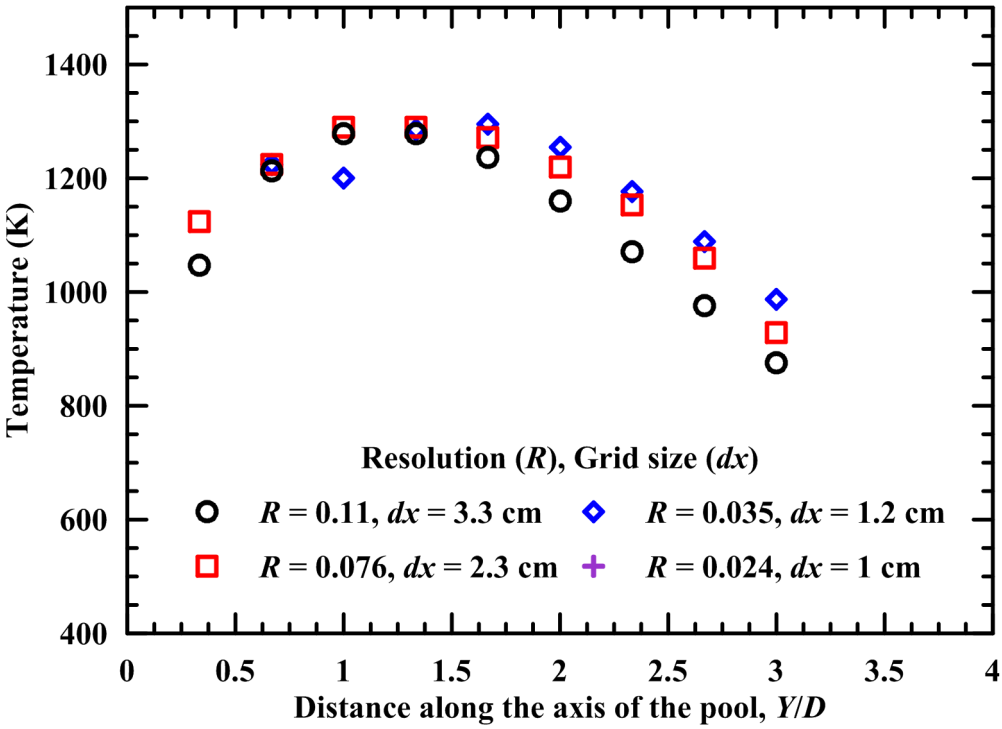

Fig. 7.2 Centerline temperature variation for different grid sizes in a 0.3 m diesel pool fire

7.4.2 Influence of Different Radiation Models on Centerline Temperature and Irradiance

The influence of different radiation models on centerline temperature and irradiance is studied for fixed grid size, solid angle, angle increment and time step increment. The

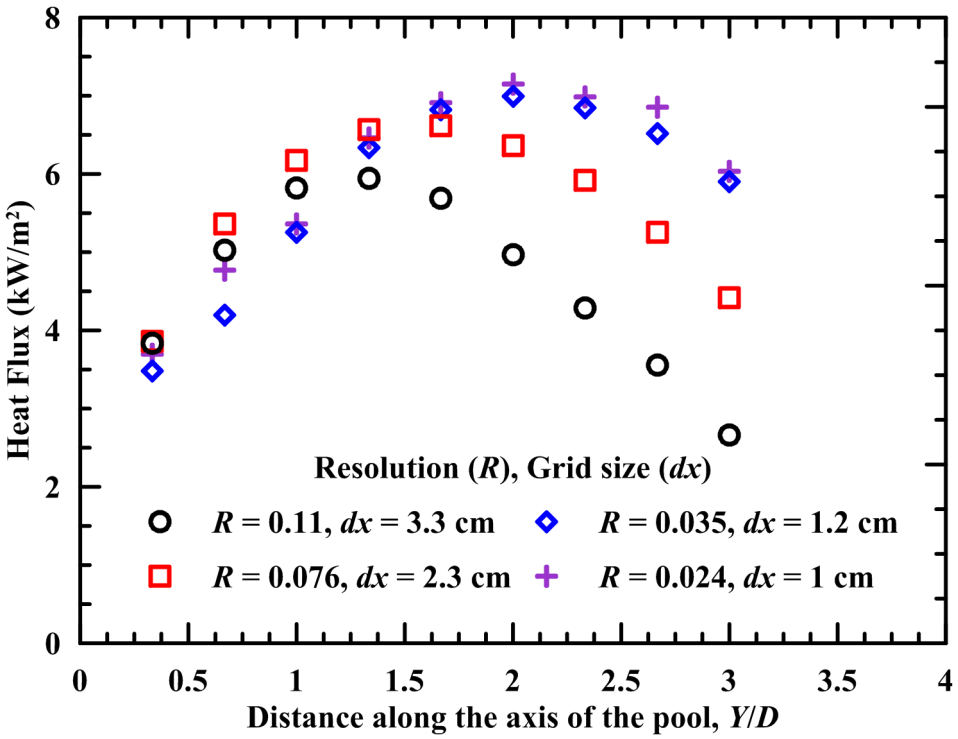

Fig. 7.3 Irradiance at $Y/D = 1$ along the height for different grid sizes in a 0.3 m diesel pool fire

radiation models available in FDS are gray band model and wide band model. Figure 7.4 shows the variation of centerline temperature for different radiation models in a 0.3 m diesel pool fire. Figure 7.5 shows the variation of irradiance for different radiation models in a 0.3 m diesel pool fire. The maximum deviations in temperature and irradiance are 6% and 4% respectively. The time for simulations with gray band model took 49 minutes, while the simulations with wide band model took 220 minutes. Gray band model works under the assumption that the gas properties are independent of wavelength. In spite of this assumption, Figs. 7.4 and 7.5 show that the gray band model is as capable as wide band model in numerical simulations. Hence, gray band model is chosen for further simulations in this work.

7.4.3 Influence of Number of Solid Angles on Centerline Temperature and Irradiance

For a fixed grid size, the number of solid angles are varied from $N = 100$ to $N = 700$. Gray model is chosen as radiation model. The angle increment (f_n)and time step increment (f_t) are fixed at 5 and 3 respectively. Figure 7.6 shows the centerline temperature variation for different number of solid angles for a 0.3 m diesel pool fire. It is observed that there is no influence of number of solid angles on centerline temperature in this range. Figure 7.7 shows the variation of irradiance at $Y/D = 1$ along the height for different solid angles.

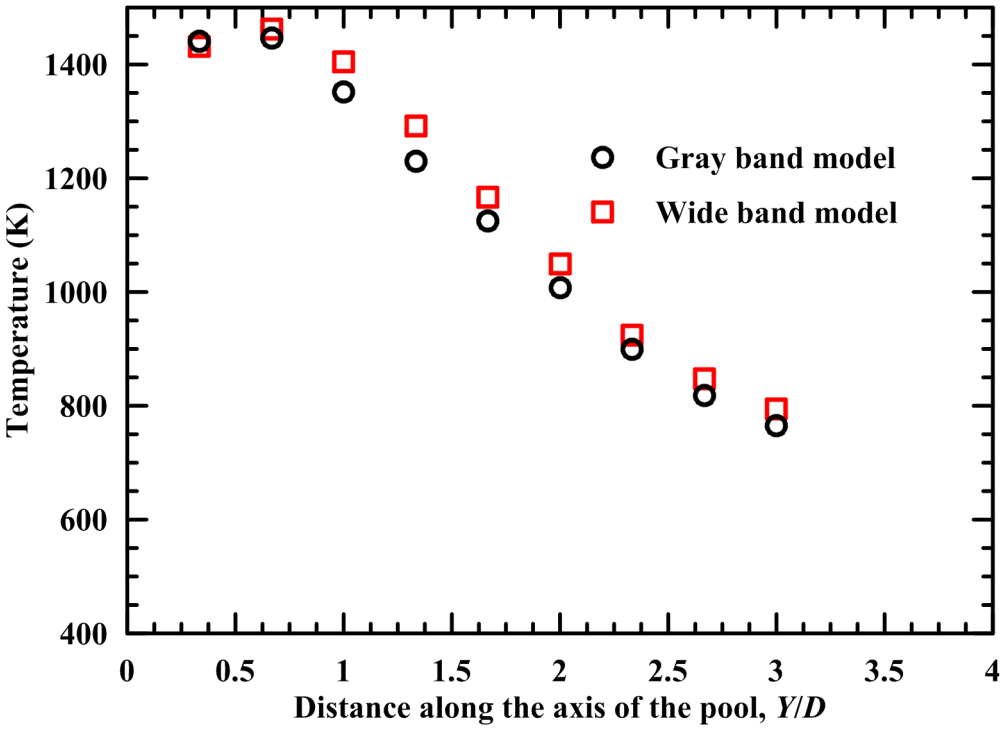

Fig. 7.4 Centerline temperature variation for different radiation models in a 0.3 m diesel pool fire

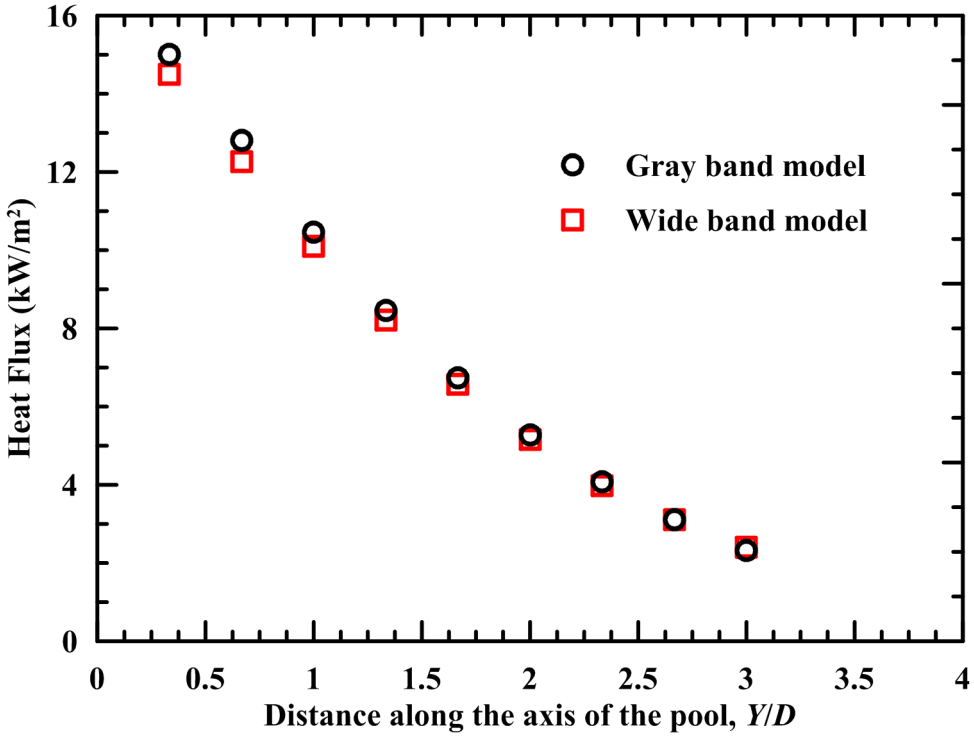

Fig. 7.5 Irradiance at $Y/D = 1$ along the height for different radiation models in a 0.3 m diesel pool fire

It is observed that the irradiance becomes independent for $N > 300$. Hence, number of solid angles, $N = 500$ is considered for further simulations

7.4.4 Influence of Time Step Increment and Angle Increment on Centerline Temperature and Irradiance

Lin *et al.* (2010) suggested that the time step increment and angle increment have less influence on the simulation results like centerline temperature, irradiance, velocity etc. Simulations are run for fixed solid angle, grid size and gray band radiation model. The time step increment (f_t) is varied from 3 to 6 while the angle increment (f_n) is fixed at 5. Then another simulation is run with time step increment of 1 and angle increment of 1. Figure 7.8 shows the variation of centerline temperature for different time step increments and angle increments for a 0.3 m diesel pool fire. Figure 7.9 shows the variation of irradiance for different time step increments and angle increments for 0.3 m diesel pool fire. It is observed that both the centerline temperature and irradiance are independent of angle increment and time step increment in this range. For the lower f_n and f_t, the computational time has doubled with significant change in the results. Hence, in the further simulations $f_n = 5$ and $f_t = 6$ are considered.

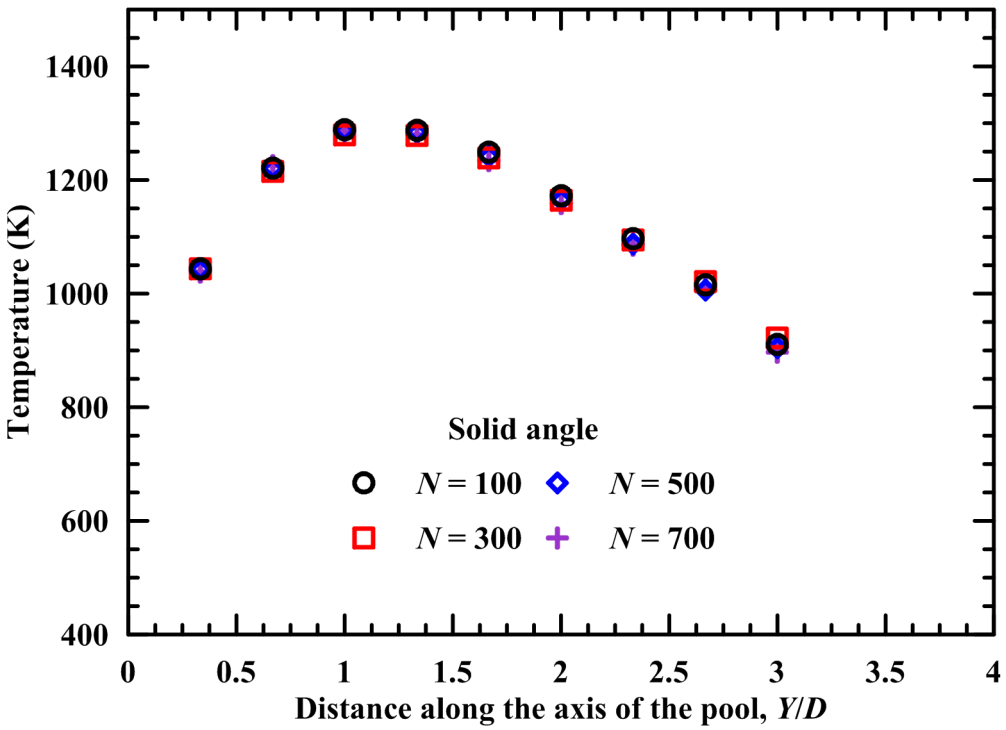

Fig. 7.6 Centerline temperature variation for different number of solid angles in a 0.3 m diesel pool fire

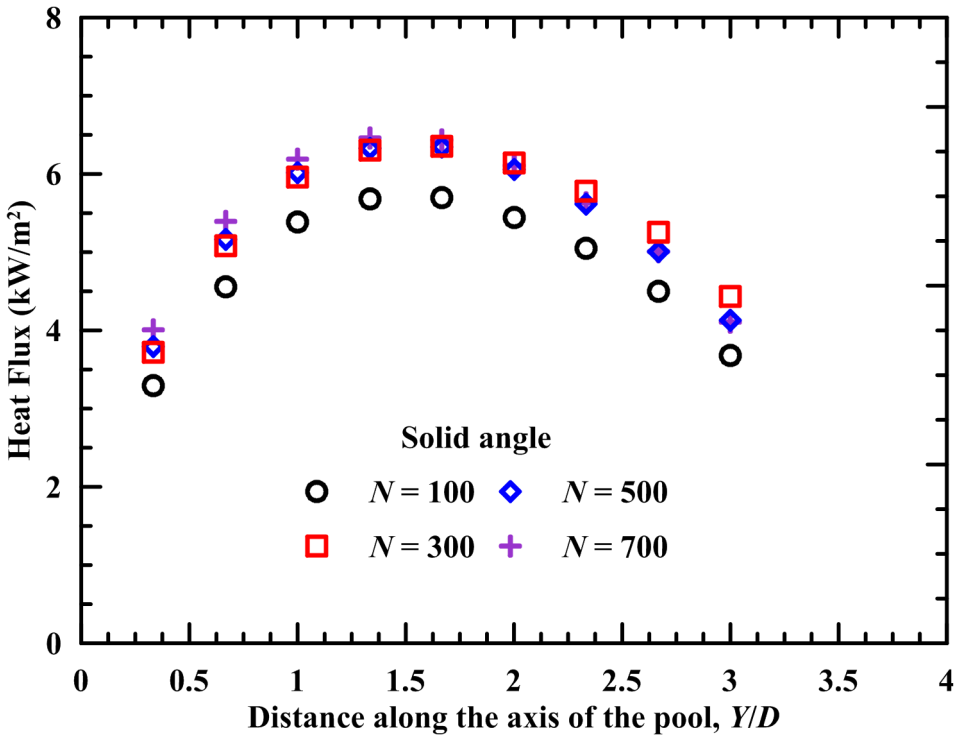

Fig. 7.7 Irradiance at $Y/D = 1$ along the height for different number solid angles in a 0.3 m diesel pool fire

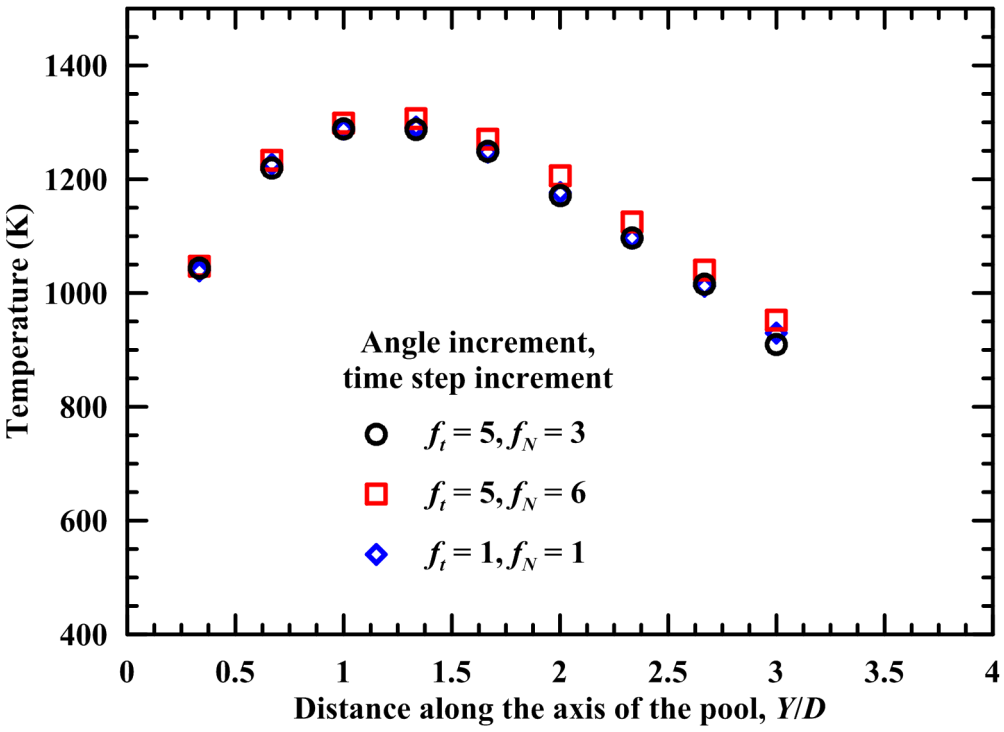

Fig. 7.8 Centerline temperature variation for different time step and angle increments of 0.3 m diesel pool fire

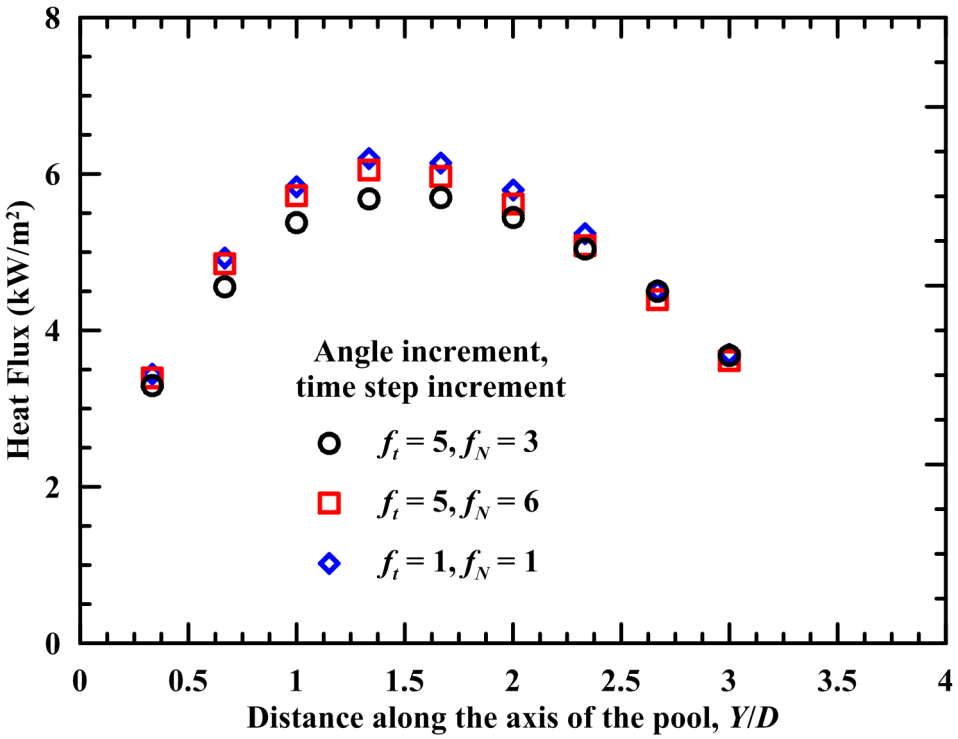

Fig. 7.9 Irradiance at $Y/D = 1$ along the height for different time step and angle increments and of 0.3 m diesel pool fire

7.4.5 Summary of Sensitivity Analysis

The simulation parameters obtained from the sensitivity analysis for 0.3 m and 0.5 m pool diameter are shown in Table 7.7. Both the gray band model and wide band model gave the same results within 6%. Gray band model is faster in terms of computational times. It is observed that the grid resolution has strong influence on the centerline temperature and irradiance. The number of solid angles only influenced the irradiance but not the centerline temperature. The angle increment and time step increment has least significance on the results but lower the numbers, higher the computational time.

Table 7.7 Summary of sensitivity analysis

Parameter	Value
Grid resolution, R	0.035
Solid angle, N	500
Angle increment, f_n	5
Time step increment, f_t	6
Radiation model	Gray band

7.4.6 FDS input parameters that Depend on Pool Size

The parameters shown in Table 7.7 are independent of pool size. Table 7.8 shows the pool size dependent FDS input parameters for diesel pool fires of different diameters. The radiative fraction in Table 7.8 are from the multi-location measurements as explained in Section 3.14.3.

Table 7.8 Pool size dependent FDS input parameters

	Diesel pool diameter, *D*			
Parameter	**0.3 m**	**0.5 m**	**0.7 m**	**1.0 m**
Mass burning rate, $\dot{m}''$ (gm/m^2.s)	17.0	27.5	32.7	39.1
Radiative fraction, χ_r	0.168	0.181	0.258	0.271

7.5 Numerical Simulations for 1 m Circular Diesel Pool Fire

Using the input parameters given in Tables 7.1 to 7.5, 7.7 and 7.8, simulations are run for a 1 m circular diesel pool fire. The grid size is chosen as $dx = 6$ cm that corresponds to resolution, $R = 0.035$. The time period of simulations is 30 s. The data for the last 26 seconds is averaged to obtain the steady state results. FDS version is used for the following simulations is 5.5.3.

7.5.1 Centerline Temperature

Ten thermocouple devices are placed along the axis each one separated by 20 cm in the simulations. Figure 7.10 shows the centerline temperature distribution from simulations compared to the thermal image data. The centerline temperature from the infrared camera is only a representative data but not the true temperature data. The emissivity to obtain this data is an average emissivity of 0.65. It is observed that the flame emissivity varies along the height as given in Section 3.9. Hence, the comparison given in Fig. 7.10 has to be view qualitatively but not quantitatively. The order of magnitude for simulation results and the thermal image are same.

Figure 7.11 shows the centerline temperature from the FDS compared to that obtained from the infrared camera. The variation of emissivity along the height is considered to obtain the thermal distribution. Hence, the thermal camera data presented in Fig. 7.11 differs from that presented in Fig. 7.10. This comparison shows that the FDS is able to capture the centerline temperature.

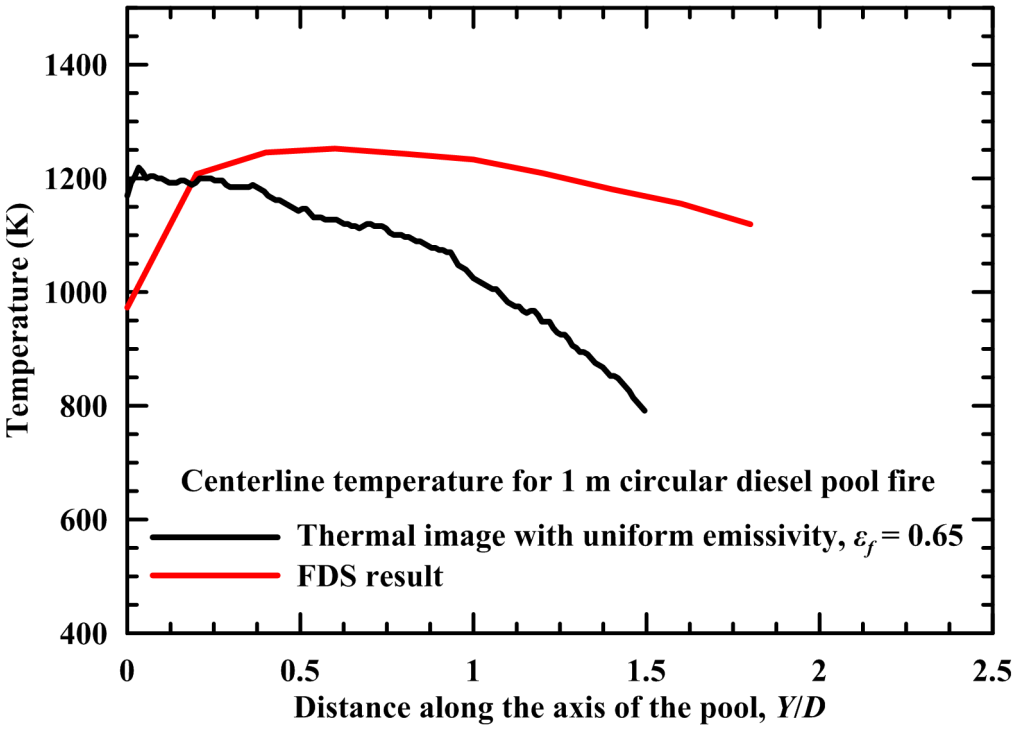

Fig. 7.10 Centerline temperature from FDS and infrared camera for 1 m circular diesel pool fire

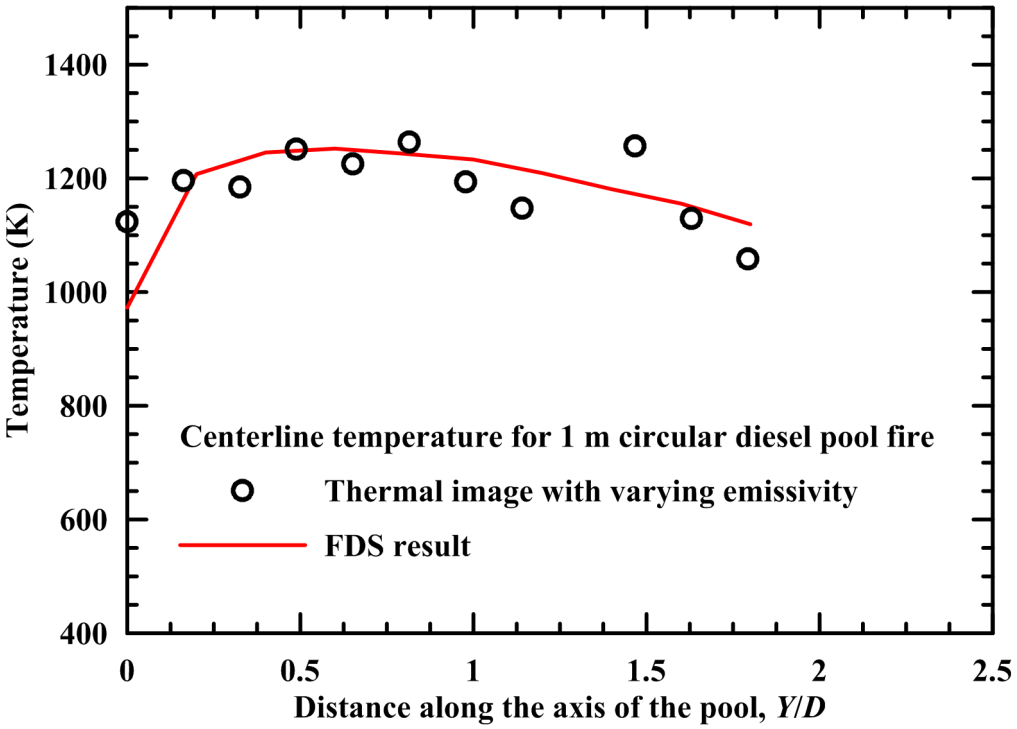

Fig. 7.11 Centerline temperature from FDS and infrared camera for 1 m circular diesel pool fire

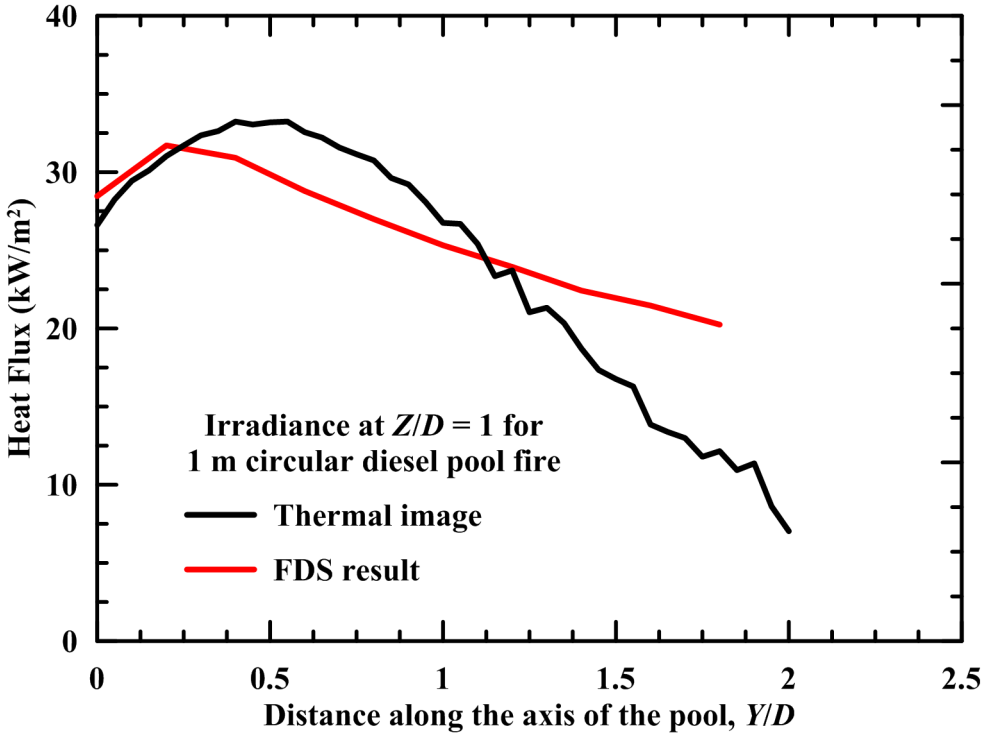

Fig. 7.12 Irradiance at $Y/D = 1$ along the height from FDS and infrared camera for 1 m circular diesel pool fire

7.5.2 Irradiance at $Z/D = 1$

Ten heat flux measuring devices are placed along the axis each one separated by 20 cm in the simulations. Figure 7.12 shows the irradiance from 1 m circular diesel pool fire at a distance of $Z/D = 1$ away from the pool center. The irradiance presented in Fig. 7.12 are from FDS simulations and from the thermal images. The maximum deviation of simulation results is within 12% from the results obtained from thermal image. This shows that FDS is capable of simulating open pool fires with blended fuels like diesel.

7.5.3 Vertical Velocity at $Y/D = 0.2$

The vertical velocity at a height of $Y/D = 0.2$ is computed using a velocity probe in the simulations. The average vertical velocity obtained from simulations is 2.14 m/s. The velocity obtained from bidirectional probe is 1.79 m/s. Though the difference is 20%, the predictions are in the order of magnitude of experimental results. The inherent problem in measuring such a low velocity might have been the problem in the experimental results.

7.5.4 Adiabatic Surface Temperature

The advantage of FDS over experiments is that, the adiabatic surface temperature (AST) can be at different locations. A cask of 114 mm diameter and 114 mm height is generated

inside the pool fire as shown in Fig. 7.13. The adiabatic surface temperature on the side of the cask is computed to be 855.98 °C. The steady state AST for 1 m diesel pool fire is experimentally measured as 831 °C. The heat transfer coefficient along the side wall of the cask in FDS simulations is obtained as 12.76 W/m^2.K. The heat transfer coefficient for this configuration obtained using Eq. (6.31) (Hadad and Jafarpur, 2011) is 15.23 W/m^2.K. This shows that the numerical prediction of AST is as good as experimental results.

The computed AST from FDS simulations is given as input to solve the heat transfer in the cask. The input is a mixed boundary condition. Due to the similarities in the results, only the results of one cask are discussed. The dimensions of the cask are: d = 114 mm, h = 114 mm and t = 8.6 mm. Figure 7.14 shows the subsurface temperature distribution from conduction code using the AST obtained from FDS simulations (d = 114 mm, h = 114 mm and t = 8.6 mm). Figure 7.15 shows the surface heat flux from numerical simulations using the AST obtained from FDS simulations.

Figures 7.14 and 7.15 shows the comparison of FDS results with the experimental results for a 1 m diesel pool fire. The maximum deviation is around 10% in the subsurface temperature. The deviation of temperature values inside the insulation is may be due the variaion of thermal properties of the insulation. The density of the insulation might change while placing inside the cask. The predicted heat flux values are inline with the experimental results. This comparison affirms that the FDS is capable of simulating heat transfer in casks engulfed in open pool fires along with a conduction code.

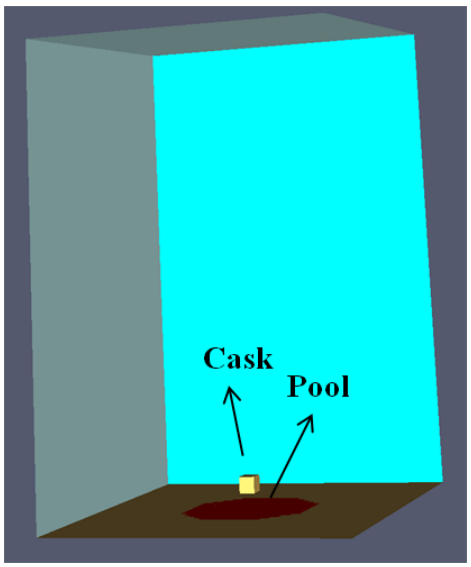

Fig. 7.13 Typical computational domain used for a cask engulfed in 1 m circular diesel pool fire

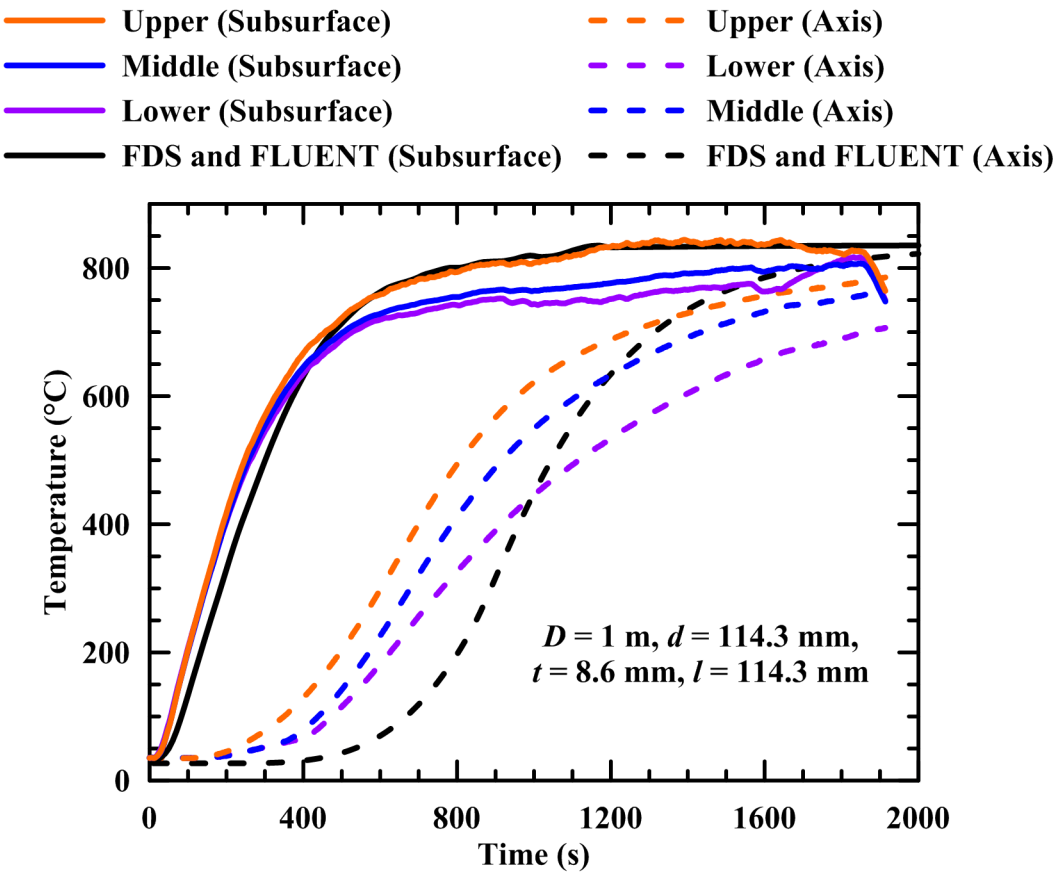

Fig. 7.14 Subsurface temperature distribution using AST from FDS simulations

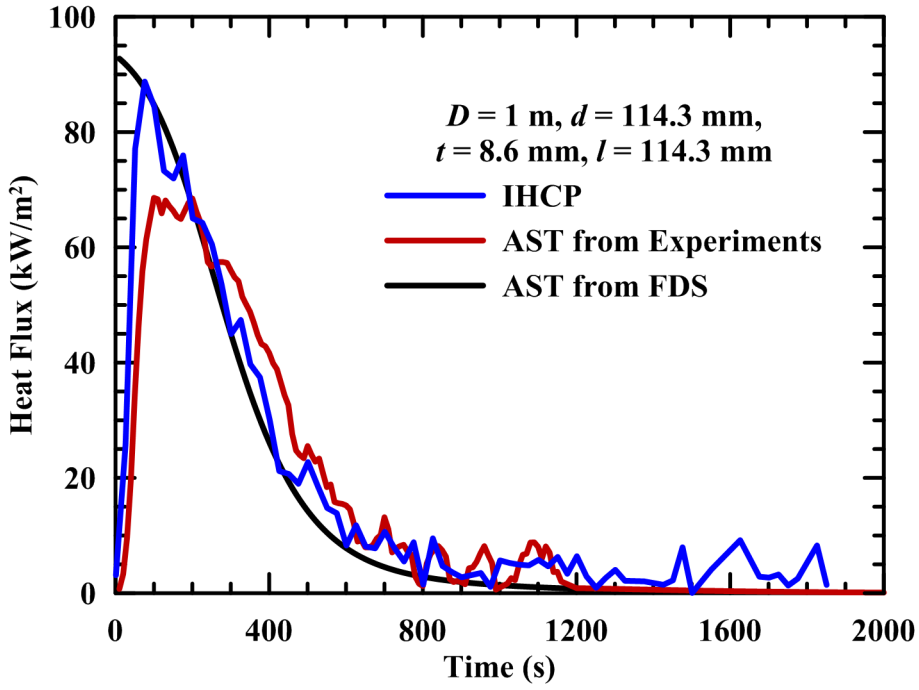

Fig. 7.15 Surface heat flux for a cask using AST from FDS simulations

7.6 Boundary Conditions for Thermal Tests Using FDS

It has been demonstrated that FDS is capable of simulating open pool fires. Hence, FDS can be safely employed for thermal tests. The following are the steps to get the boundary conditions from FDS for thermal tests for $B < 14.4\%$:

- Obtain the pool size and find the mass burning rate using $\left(1 - e^{-\kappa\beta D}\right) \dot{m}''_{\infty}$. $\dot{m}''_{\infty}$ and $\kappa\beta$ for different fuels are given in Table 3.1 and Section 3.10 respectively.
- Obtain the radiative fraction for the pool fire. χ_r values for different sizes are given in Table 7.8 and Section 3.14.3.
- Generate FDS domain for a grid resolution of at least $B = 0.035$.
- Create an object of the same size as the thermal cask.
- Create adiabatic surface temperature measuring devices at different locations on the surface of the object.
- Create devices to measure the heat transfer coefficient at the surfaces of the object.
- Run FDS simulations for a time period of 30 s.
- This AST along with the heat transfer coefficient becomes the mixed boundary condition for further conduction or any other analysis.

As it has been demonstrated that the pool fires are radiation dominant, measurement of heat transfer coefficient can be neglected for better computational times.

7.7 AST for large pool fires

Adiabatic surface temperature is numerically computed for pool fires of large pool sizes. A cylinder of 1 m diameter and 1 m height is considered as the blockage for $D \geq 1$ m. The blockage is placed at a height of around $0.2D$ from the pool base. Table 7.9 shows the AST and convective heat transfer coefficient for large pool sizes, 2 m $\leq D \leq$ 8 m. It is the observed that the AST increases with the pool diameter. Also for this cask, AST measured horizontally and vertically are almost the same (within 4%). A linear curve fit for this data is given in the last row of Table 7.9. This AST can be given as boundary condition for the thermal analysis of a cask engulfed in pool fire.

Table 7.9 AST for different diesel pool fires

Pool diameter, (m)	Cask orientation			
	Vertical		horizontal	
	AST (°C)	h (W/m².K)	AST (°C)	h (W/m².K)
2	914.3	10.6	871.9	11.3
4	964.3	12.4	934.8	13.1
5	1030.6	10.2	1016.5	10.0
6	1089.0	10.0	1082.3	10.1
7	1100.9	10.1	1088.5	10.8
8	1151.3	10.1	1159.0	10.7
D	$AST_{avg} = 44.8D + 794.9$			

7.8 Conclusions

Sensitivity analysis for various FDS input parameters is performed. The simulations results are very much influenced by the grid resolution and least influenced by the angle increment and time step increment. FDS simulations are validated using experimental results for diesel open pool fires. The irradiance results are within 6% of the experimental data. It is concluded that FDS is capable of simulating non-premixed flames even for complex fuel such as diesel. It is demonstrated that the FDS is capable of simulating heat transfer in casks engulfed in open pool fires along with a conduction code. The adiabatic surface temperature values predicted by FDS simulations compares well with the experimental results.

CHAPTER 8

Conclusions and Scope for Future Work

8.1 Conclusions

Open pool fires are studied to optimize the thermal tests. Pool fire characteristics like flame emissivity, temperature and emissive power distributions are measuring. An optimized methodology for carrying out thermal tests is proposed. The summary of these studies are presented below:

1. Mass burning rates of hydrocarbon pool fires are measured for different pool sizes. The mass burning rate increases for pool sizes in range of 0.1 m to 1.0 m diameter.

2. The average flame emissivity can be inferred from the mass burning rate. The flame emissivity at a particular location can be measured using infrared thermography. Average flame emissivity increases with the pool size for pool diameters in the range of 0.1 m to 1.0 m.

3. Emissivity of the flame along the axis of the pool fire is studied. Emissivity of the flame at different locations can be measured using infrared thermography. Emissivity of the flame decreases along the axis of the pool from the pool surface.

4. Temperature and emissive power distributions of different pool fires are studied. The temperature and the emissive power values increase with the pool size. The temperature and emissive powers for hexane pool fires are higher than gasoline. The

temperature and emissive powers for gasoline pool fires are higher than diesel pool fires.

5. Radiative fraction is measured using single-location measurement and multi-location measurement. The single-location measurement underpredicts the radiative fraction values. Radiative fraction of diesel pool fires increases with the pool size of diameters in the range of 0.3 m to 1.0 m.

6. The visual images of the diesel pool fires are studied. The flame height of diesel fires is 2.13 times of the pool diameter for diameters in the range of 0.3 m to 1.0 m. There is no much variation in the flame height with the pool size.

7. The gas velocity in diesel pool fires is measured using bidirectional probe. The gas velocity is in the range of 1.53 m/s to 1.79 m/s for pool fires of diameters 0.5 m to 1.0 m.

8. Fire safety distances for different pool fires are studied. Hexane pool fires are more dangerous than diesel and gasoline pool fires. The fire safety distances range from 5.7 to 9.5 times pool equivalent diameter for the pool sizes studied.

9. Different modes of heat transfer to a body engulfed in a pool fire are studied. The convective heat transfer from the flame to the body is less than 10% of the total heat transfer to the body. Radiation is the dominant mode of heat transfer to a body engulfed in a pool fire.

10. Thermal tests are studied in diesel pool fires for blockages in the range of 0.8% to 14.4%. Vertical and horizontal orientations of the casks are studied. There is no influence of blockage on the heat release rate of the pool fires. The transient temperature and heat flux distributions would serve as benchmark results for validating computational results.

11. A three dimensional approach is studied, to predict the temperature distribution of a body engulfed in open pool fires. The circular pool fires are symmetric along the pool axis, in terms of temperature distribution. The two dimensional thermal images give the apparent temperature distribution of the pool fire. However, these temperature distributions cannot be used as true temperature distributions inside the flames.

12. The thermal tests are reduced to simple conduction problem using adiabatic surface temperature (AST) concept. Plate thermometers are constructed to measure the AST of a given pool fire. The measured AST is given as mixed boundary condition

to a conduction code to predict the subsurface temperatures and heat flux to the cask. The AST approach for carrying thermal tests reduces the computational costs.

13. Fire Dynamics Simulator (FDS) is capable of simulating open pool fires even for a blended fuel like diesel. FDS can be employed to estimate the AST for large pool fires.

8.2 Contributions from the Present Work

The following are the contributions from the present work:

1. Pool fire experiments are conducted for pool diameters 0.5 m, 0.7 m and 1.0 m and fuels diesel, gasoline and hexane. These are real hydrocarbons. In the literature, most of the data is available for JP-4. Hence, there was a need for data which would serve as benchmark results for numerical work (FDS).

2. Pool fire properties like flame emissivity, temperature distribution, emissive power distribution, radiative fraction and flame velocity are measured in this report. Measured mass burning rate and radiative fraction would serve as an input data to FDS. Giving mass burning rate as an input eliminates the one step chemical kinetics and reduces computational time.

3. It is demonstrated that the pool fires are radiatively dominant for diameters larger than 0.5 m.

4. Computed fire safety distances would guide in planning the experiments.

5. Conventionally, to simulate thermal tests, coupling of fire models and conduction models is required. FDS do not have conduction model and fire models in commercial packages take enormous computational time. Hence, there was a need for reducing the computational time. The proposed concept of AST as a mixed boundary condition simplifies the problem to conduction analysis and thereby reduces the computational costs.

6. International atomic energy agency standard (IAEA) specifies the pool fire temperature as 800 °C but does not specify the test conditions in terms of power. This report shows that the maximum temperature of flame varies with the size of the pool fire and hence suggests the need for correction in the IAEA standard specifications for thermal tests.

8.3 Scope for Future Work

The following aspects may be considered for future work:

1. The effect of pool shape can be studied on the severity of the thermal tests.
2. The flame emissivity distribution of the pool fires can be measured using either infrared thermography or a visual camera.
3. A methodology to reconstruct the flame (tomography) can be developed. This can be done by predicted the flame inner temperatures while maintaining the symmetry and the cumulative apparent temperature. This requires the knowledge of the distribution of soot volume fraction in the flame.
4. A generalized equation can be made for mass burning rate, flame emissivity, temperature distributions for different pool fires.
5. The AST at different locations inside the flame can be studied. The AST can be generalized for different fuels and pool sizes.
6. A numerical model can be developed using the temperature distributions to predict the AST of a pool fire.
7. An experimental study can be performed to measure the temperature distribution with different blockages at different locations. This involves the understanding the air entrainment and chemical reactions.
8. A furnace can be modeled to simulate a pool fire. The thermal tests would be reduced to simple furnace problem.
9. A plug-in can be developed for FDS to simulate three-dimensional conduction along with fire model. The influence of flame shape can be studied using FDS.

Appendices

APPENDIX A

Temperature and Emissive Power Distributions for Gasoline and Hexane Pool Fires

This chapter presents the experimental results for gasoline and hexane pool fires. The flame emissivity is measured using the mass burning rate and infrared thermography (Chapter 3 for gasoline and hexane pool fires of pool diameters 0.3 m, 0.5 m, 0.7 m and 1.0 m. The thermal images are taken for both gasoline and hexane pool fires for diameters 0.3 m, 0.5 m, 0.7 m and 1.0 m. In each set of experiments, thermal images of the flame are captured using a thermal camera (VisIR Ti200) at a rate of 12 fpm. Using emissivity values measured on the basis of mass burning rate (Fig. 3.4), these thermal images are converted to corresponding temperature contour plots. For each diameter around 20 to 40 temperature plots are averaged.

A.1 Gasoline Pool Fires

A.1.1 Variation of Emissivity with Height

As explained for diesel pool fires in Section 3.9, the flame emissivity measured at five locations along the axis using infrared thermography. Figure A.1 shows the variation of emissivity of the gasoline pool fire along the height for different diameters. It is observed that the emissivities at the flame tip are lower than the emissivities at the base of the pool fire. In all the measurements using infrared thermography, ε_t is taken as 0.85.

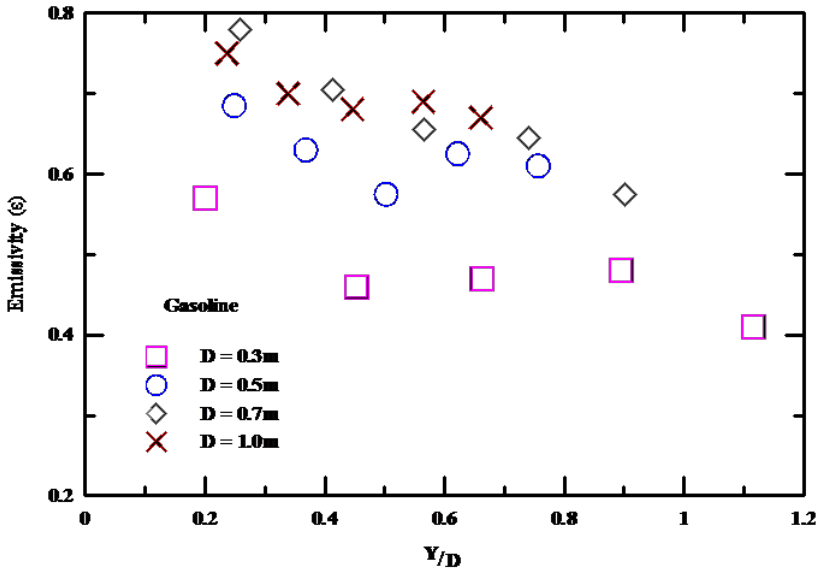

Fig. A.1 Variation of emissivity along the height of gasoline pool fires

A.1.2 Temperature and Emissive Power Distributions for Gasoline Pool Fires

Figures A.2 and A.3 show the temperature distributions for gasoline pool fires of 0.3 m, 0.5 m, 0.7 m and 1.0 m diameters. The origin in all these figures is chosen at the center of the base of the pool. The horizontal and the vertical axis are non-dimensionalized by dividing the axis with diameter of the pool fire. Peak values are observed at $Y/D = 0.1$ (X/D varies -0.2 to 0.2) and along the centerline of the pool for all the diameters that are considered. Figures A.4 and A.5 show the emissive power distributions for gasoline pool fires of 0.3 m, 0.5 m, 0.7 m and 1.0 m diameters.

A.1.3 Validation of Temperature Measurements Using Thermal Camera

A series of experiments are conducted using thermocouples for a pool fire of diameter 0.3 m to validate the temperature measurements. A set of 20 K-type thermocouples are placed along the center line of the pool axis, each is separated by 0.025 m from the other. All the thermocouples are connected to the computer for the data collection via data logger. An estimation of error can be derived from an energy balance equation on the thermocouple junction. Figure A.6 shows the center line temperature distribution obtained from thermocouples (after correction) and the averaged thermal image for gasoline pool fire of 0.3 m diameter. This shows a reasonably good agreement in the temperature values inferred from thermal images.

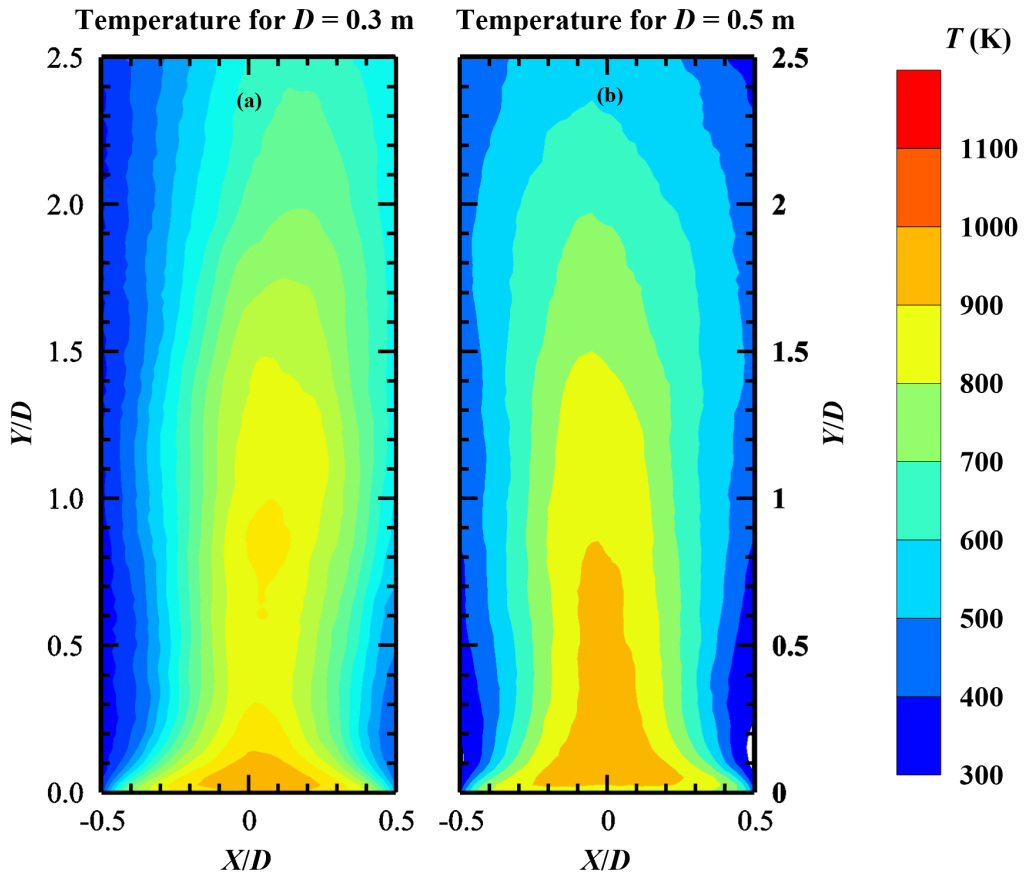

Fig. A.2 Temperature distribution of 0.3 m and 0.5 m gasoline pool fire

A.1.4 Validation of Heat Flux Measurements at a Distance

Experiments are conducted on a pool fire of 0.3 m diameter using Schmidt Boelter gauge. The heat flux gauge is traversed along the vertical axis from a distance of 0.3 m from the pool center. In each position measurements are made for a period of 30 seconds to get time averaged heat flux at that location. Figure A.7 shows the comparison of heat flux measurements at $Z/D = 1$ with heat flux transducer and camera for 0.3 m diameter pool fire.

A.2 Hexane Pool Fires

Figures A.8 and A.9 show the temperature distributions for hexane pool fires of 0.3 m, 0.5 m, 0.7 m and 1.0 m diameters. The origin in all these figures is chosen at the center of the base of the pool. The horizontal and the vertical axis are non-dimensionalized by dividing the axis with diameter of the pool fire. Peak values are observed at $Y/D = 0.1$ (X/D varies -0.2 to 0.2) and along the centerline of the pool for all the diameters that are considered. Figures A.10 and A.11 show the emissive power distributions for hexane pool fires of 0.3 m, 0.5 m, 0.7 m and 1.0 m diameters.

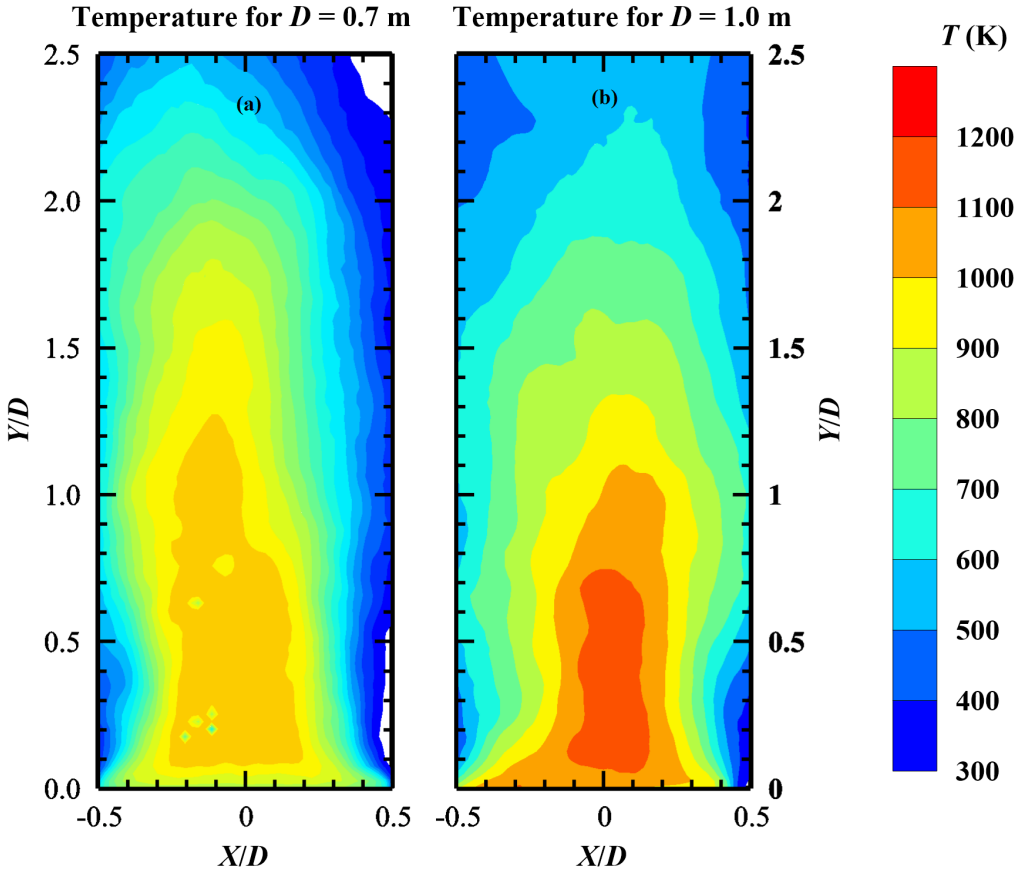

Fig. A.3 Temperature distribution of 0.7 m and 1.0 m gasoline pool fire

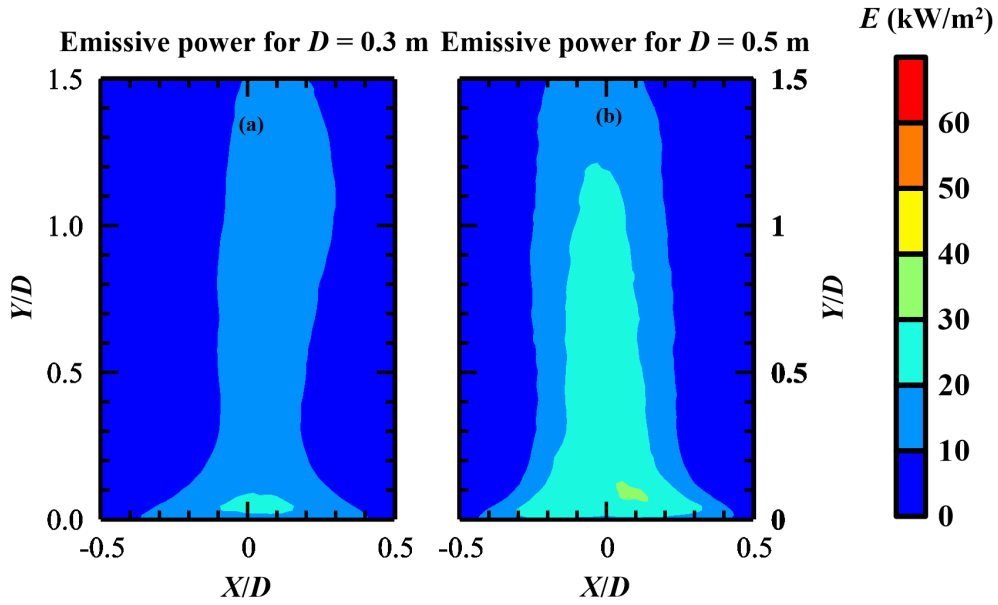

Fig. A.4 Emissive power distribution of 0.3 m and 0.5 m gasoline pool fire

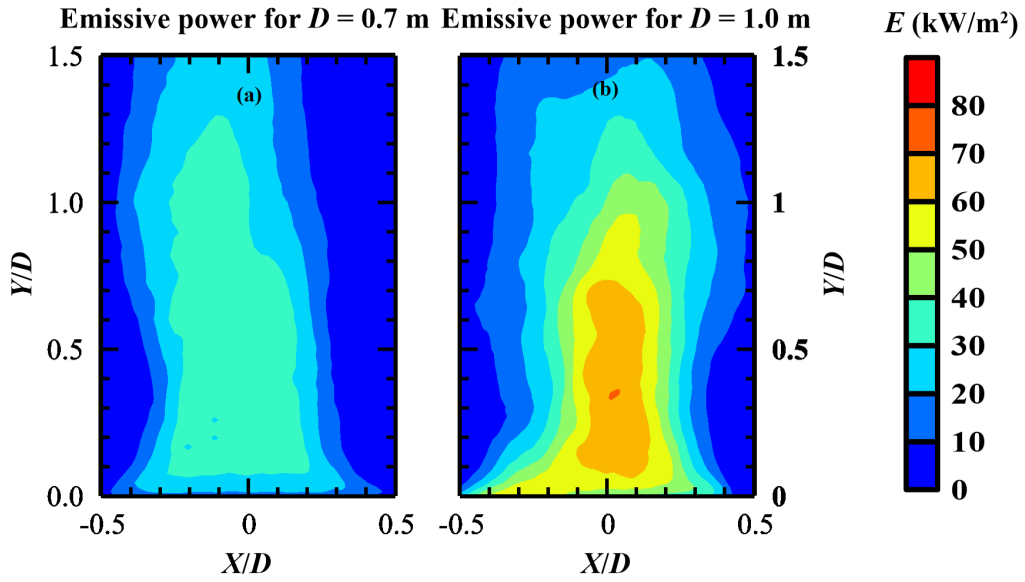

Fig. A.5 Emissive power distribution of 0.7 m and 1.0 m gasoline pool fire

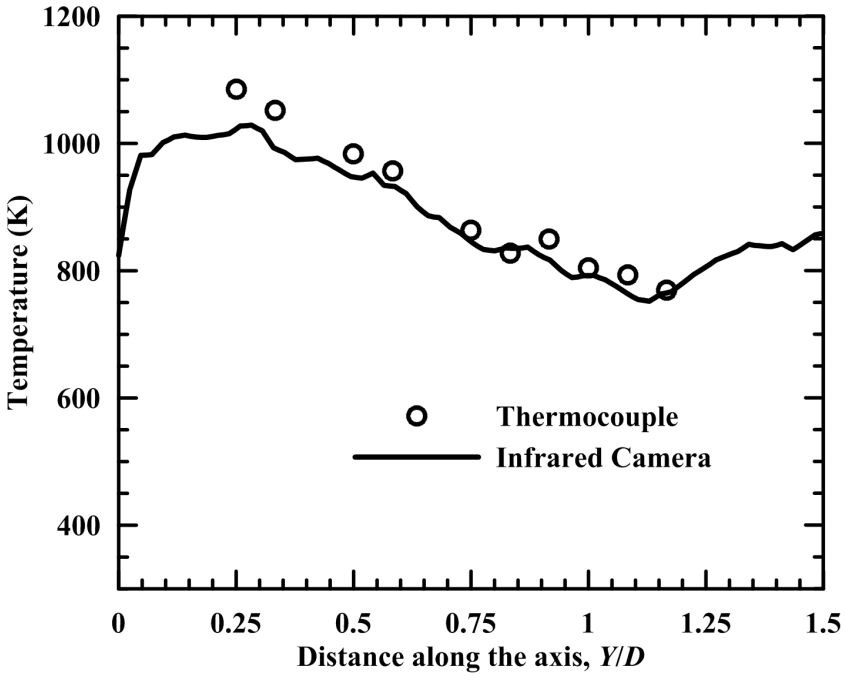

Fig. A.6 Centerline temperature distribution for 0.3 m gasoline pool fire

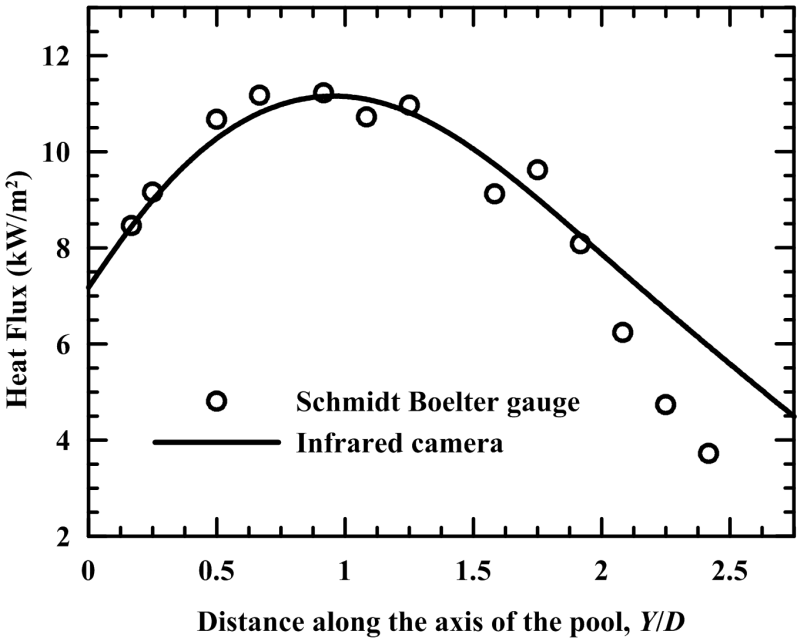

Fig. A.7 Comparison of Heat Flux measurements at $Z/D = 1$ using Schmidt Boelter gauge and infrared camera for 0.3 m gasoline pool fire

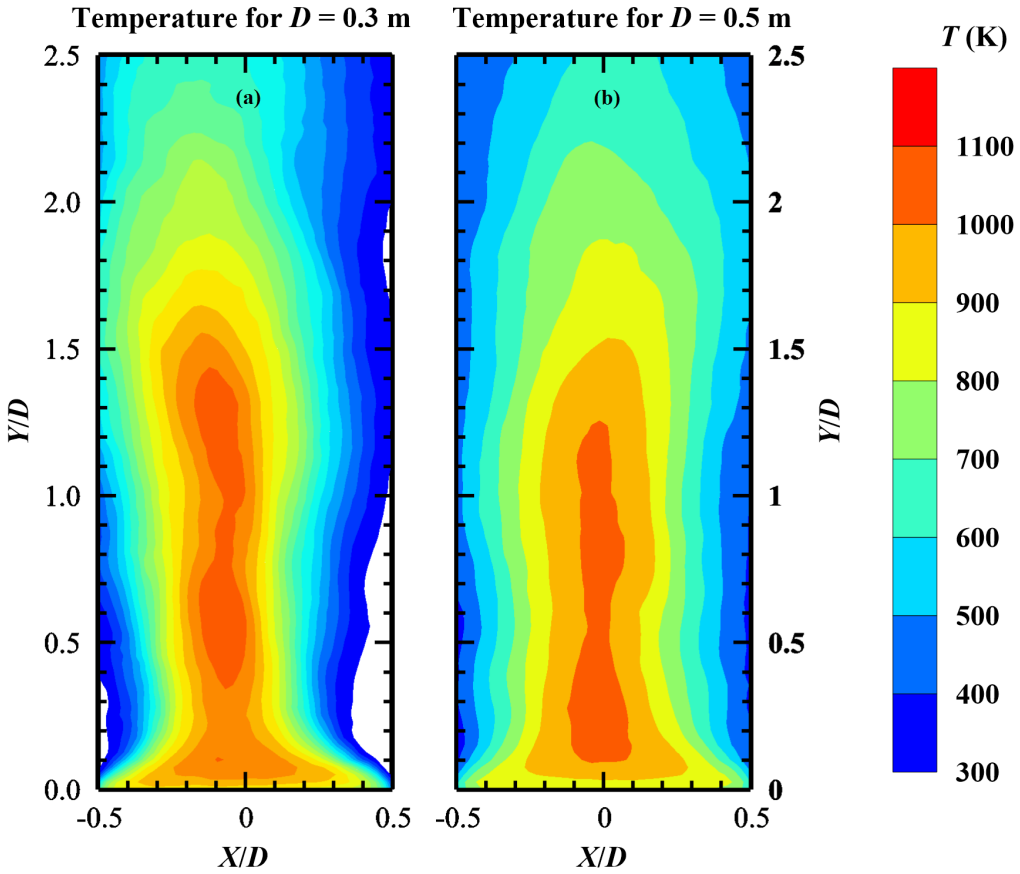

Fig. A.8 Temperature distribution of 0.3 m and 0.5 m hexane pool fire

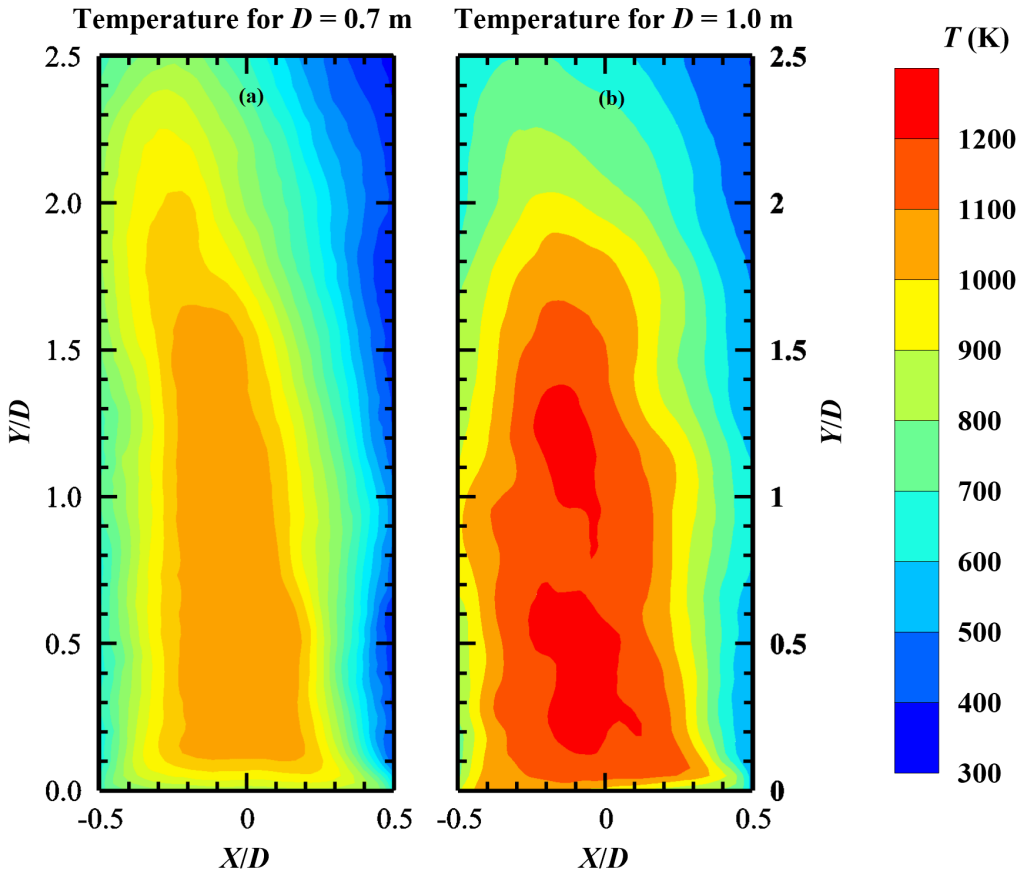

Fig. A.9 Temperature distribution of 0.7 m and 1.0 m hexane pool fire

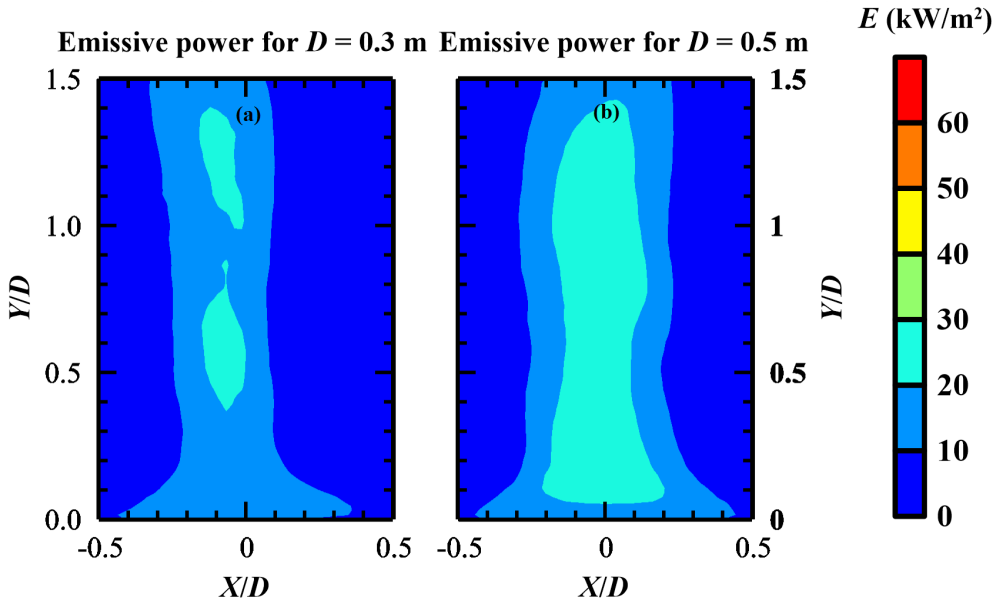

Fig. A.10 Emissive power distribution of 0.3 m and 0.5 m hexane pool fire

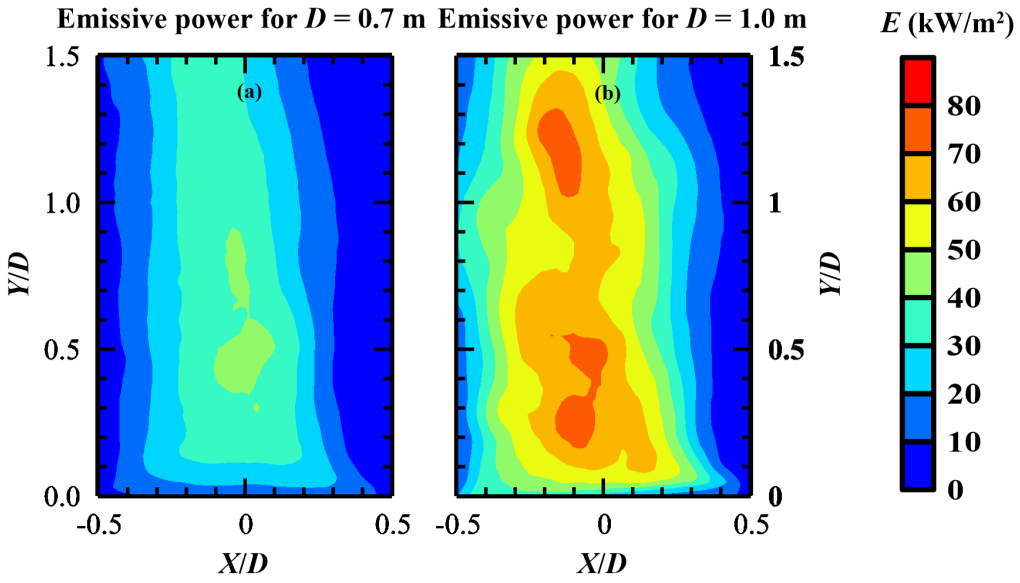

Fig. A.11 Emissive power distribution of 0.7 m and 1.0 m hexane pool fire

APPENDIX B

Elemental Analysis of Diesel

This appendix provides the Carbon, Hydrogen and Nitrogen (CHN) analysis of diesel. Samples of diesel is sent to Sophisticated analytical instrument facility at Indian institute of technology, Bombay. The analyzer used for the analysis is Thermo finnigan make FLASH EA 1112 series. Figure B.1 provides the results of this report. The chemical composition of diesel is estimated to be $C_{14}H_{24}$.

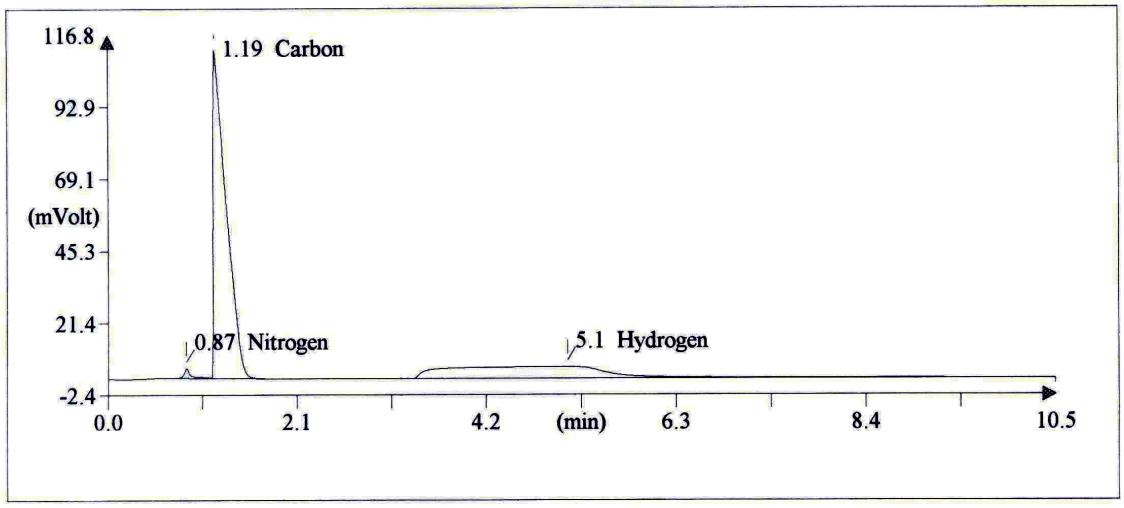

Peak Number (#)	Retention Time (min)	Area (.1*uV*sec)	Element %	Compon
1	0.867	179871	2.306	Nitrog
2	1.192	10733170	83.417	Carbon
3	5.100	4959228	12.321	Hydrog
		15872270	98.044	

Fig. B.1 CHN analysis of diesel

Bibliography

Agueda, A., Perez, Y., Planas, E. and Pastor, E. (2006). Evaluating the Effect of Long-Term Forest Fire Retardants on Thermal Properties: Fuel Heat Content and Flame Emissivity. In *Fifth International Conference on Forest Fires Research*, Coimbra, Portugal.

Akafuah, N.K., Salazar, A.J. and Saito, K. (2010). Infrared Thermography-Based Visualization of Droplet Transport in Liquid Sprays. *Infrared physics and Technology*, **53**, 218–226.

Akers, S.M., Conkle, J.L., Thomas, S.N. and Rider, K.B. (2006). Determination of the Heat of Combustion of Biodiesel Using Bomb Calorimetry. *Journal of Chemical Education*, **83**, 260–262.

Ali, S.M., Verma, V., Markandeya, S.G., Ghosh, A.K. and Kushwaha, H.S. (2004). Thermal Analysis of a Marine Products Irradiator and Its Transportation Cask. In *12^{th} International Conference on Nuclear Engineering*, Arlington, India.

Arakawa, A., Saito, K. and Gruver, W.A. (1993). Automated Infrared Imaging Temperature Measurement with Application to Upward Flame Spread Studies Part I. *Combustion and Flame*, **92**, 222–230.

Atallah, A. and Allan, D.S. (1971). Safe Separation Distanecs from Liquid Fuel Fires. *Fire Technology*, **7**, 47–56.

Babrauskas, V. (1983). Estimating Large Pool Fire Burning Rates. *Fire Technology*, **19**, 251–261.

Babrauskas, V. and Peacock, R.D. (1992). Heat Release Rate: The Single Most Important Variable in Fire Hazard. *Fire Safety Journal*, **18**, 255–272.

Bainbridge, B.L. and Keltner, N.R. (1988). Heat Transfer to Large Objects in Large Pool Fires. *Journal of Hazardous Materials*, **20**, 21–40.

Beck, J.V. (1962). Calculation of Surface Heat Flux from an Internal Temperature History. *ASME Paper*, **62-HT-46**.

Beck, J.V. (2012). Beck Engineering Consultants Company. http://wwwbeckengcom/.

Bejan, A. (1993). *Heat Transfer*. John Wiley & Sons Inc .

Billaud, J.L., Y Kaiss and Consalvi, B.P. (2001). Monte Carlo Estimation of Thermal Radiation from Wildland Fires. *International Journal of Thermal Sciences*, **50**, 2–11.

Blanchat, T., O'Hern, T., Kearney, S., Ricks, A. and Jernigan, D. (2009). Validation Experiments to Determine Radiation Partitioning of Heat Flux to an Object in a Fully Turbulent Fire. *Proceedings of Combustion Institute*, **32**, 2511–2518.

Blinov, V.I. and Khudyakov, G.M. (1961). *Diffusion of Burning Liquids*. U S Army Engineering Research and Development Laboratories (English Translation), (T-1490a-c ASTIA, AD296762).

Brötz, W., Schönbucher, A., Bandhardt, V. and Sciess, N. (1983). Periodische und statische Eigenschaften kohärenter Kurzzeit-Strukturen in Tankflammen. *Berichte der Bunsengesellschaft für physikalische Chemie*, **87**, 997–1004.

Bryant, R.A. (2009). A Comparison of Gas Velocity Measurements in a Full-Scale Enclosure Fire. *Fire Safety Journal*, **44**, 793–800.

Buch, R., Hamins, A., Konishi, K., Mattingly, D. and Kashiwagi, T. (1997). Radiative Emission Fraction of Pool Fires Burning Silicone Fluids. *Combustion and Flame*, **108**, 118–126.

Burgess, M.H. and Fry, C.J. (1990). Fire Testing for Package Approval. *International Journal of Radioactive Materials Transport*, **1**, 7–16.

Butler, B.W. and Cohen, J.D. (1988). Firefighter Safety Zones: A Theoretical Model Based on Radiative Heating. *International Journal of Wildland Fire*, **8**, 73–77.

Byram, G.M. and Nelson, R.M. (1970). The modeling of pulsating fires. *Fire Technology*, **6**, 102–110.

Bystrom, A., Wickström and Veljkovic, M. (1988). Use of Plate Thermometers for Better Estimate of Fire Development. *Applied Mechanics and Materials*, **8**, 73–77.

Cetegen, B.M. and Ahmed, T.A. (1993). Experiments on the Periodic Instability of Buoyant Plumes and Pool Fires. *Combustion and Flame*, **93**, 157–184.

Chatris, J.M., Quintela, J., Folc, J., Planas, E., Arnaklos, J. and Casak, J. (2001). Experimental Study of Burning Rate in Hydrocarbon Pool Fires. *Combustion and Flame*, **126**, 1373–1383.

Chun, H., Wehrstedt, K., Vela, I. and Schönbucher, A. (2009). Thermal Radiation of Di-tert-butyl Peroxide Pool Fires - Experimental Investigation and CFD Simulation. *Journal of Hazardous Materials*, **167**, 105–113.

Ciro, W.D., Eddings, E.G. and Sarofim, A.F. (2006). Experimental and Numerical Investigation of Transient Soot Buildup on a Cylindrical Container Immersed in a Jet Fuel Pool Fire. *Combustion Science and Technology*, **12**, 51–80.

Cong, B., Guangxuan, L. and Zhen, H. (2009). Extinction Limit of Diesel Pool Fires Suppressed by Water Mist. *Journal of Fire Sciences*, **27**, 5–27.

Consalvi, J.L., Pizzo, Y., Porterie, B. and Torero, J.L. (2007). On the Flame Height Definition for Upward Flame Speed. *Fire Safety Journal*, **42**, 384–392.

Croce, P.A. and Mudan, K.S. (1997). Calculating Impacts for Large Open Hydrocarbon Fires. *Fire Safety Journal*, **11**, 99–112.

Cuchi, E.P. and Casal, J. (1998). Modelling Temperature Evolution in Equipment Engulfed in a Pool-fire. *Fire Safety Journal*, **30**, 251–268.

Cuchi, E.P., Casal, J., Lancia, A. and Bordignon, L. (1996). Protection of Equipment Engulfed in a Pool Fire. *Journal of Loss Prevention in the Process Industries*, **9**, 231–240.

Cuchi, E.P., Montiel, H. and Casal, J. (1997). A Survey of the Origin, Type and Consequences of Fire Accidents in Process Plants and in the Transportation of Hazardous Materials. *Process Safety and Environmental Protection*, **75**, 3–8.

Cuchi, E.P., Chatris, J.M., Lopez, C. and Arnaldos, J. (2003). Determination of Flame Emissivity in Hydrocarbon Pool Fires Using Infrared Thermography. *Fire Technology*, **39**, 261–273.

Cumber, P.S. (2011). Measuring Radiation Heat Fluxes from a Jet Fire Using a Lumped Capacitance Model. *Fire Technology*, **47**, 655–685.

Dupuy, J.L., Vachet, P., Marechal, J., Melendez, J. and Castro, D.A.J. (2007). Thermal Infrared Emission-Transmission Measurements in Flames from A Cylindrical Forest Fuel Burner. *International Journal of Wildland Fire*, **16**, 324–340.

Emori, R.I. and Saito, K. (1983). A Study of Scaling Laws in Pool and Crib Fires. *Combustion Science and Technology*, **31**, 217–231.

Francis, J. and Yau, T.M. (2004). On Radiant Network Models of Thermocouple Error in Pre and Post Flashover Compartment Fire. *Fire Technology*, **40**, 277–294.

Gardon, R. (1953). An Instrument for the Direct Measurement of Intense Thermal Radiation. *Review of Scientific Instruments*, **24**, 366–370.

Ghisalberti, L. and Kondjoyan, A. (1999). Convective Heat Transfer Coefficients Between Air Flow and a Short Cylinder Effect of Air Velocity and Turbulence Effect of Body Shape, Dimensions and Position in the Flow. *Journal of Food Engineering*, **42**, 33–44.

Hadad, Y. and Jafarpur, K. (2011). Laminar Forced Convection Heat Transfer from Isothermal Cylinders with Active Ends and Different Aspect Ratios in Axial Air Fows. *Journal of Heat and Mass Transfer*, **47**, 59–68.

Hamins, A., Kashiwagi, T. and Burch, R.R. (1995). Characteristics of Pool Fire Burning. In *American Society for Testing and Materials (ASTM),Fire Resistance of Industrial Fluids*, Gaithersburg, MD, ASTM STP 1284.

Hayasaka, H. (1996). Radiative Characteristics and Flame Structure of Small-Pool Flames. *Fire Technology*, **32**, 308–322.

Hayasaka, H., Koseki, H. and Tashiro, Y. (1992). Radiation Measurements in Large-Scale Kerosene Pool Flames Using High-Speed Thermography. *Fire Technology*, **28**, 110–122.

Hostikka, S., McGrattan, K.B. and Hamins, A. (2003). Numerical Modeling of Pool Fires Using LES and Finite Volume Method for Radiation. In *Proceedings of the Seventh International Symposium on Fire Safety Science*, 383–394, Worcester, MA.

Hottel, H.C. and Sarofim, A.F. (1967). *Radiative Transfer*. New York: McGraw Hill.

Howell, J.R. (2008). A Catalog of Radiation Heat Transfer@online. http://thermalhuborg/resources/32.

IAEA (2005). Regulations for the Safe Transport of Radiactive Material. *International Atomic Energy Agency, IAEA Safety Standards Series No TS-R-1*.

Imber, M. (1973). A Temperature Extrapolation Method for Hollow Cylinders. *The American Institute of Aeronautics and Astronautics Journal*, **11**, 117–118.

Incropera, F.P. and DeWitt, D.P. (2002). *Fundamentals of Heat and Mass Transfer*. John Wiley & Sons Inc .

Ingason, H. and Wickström, U. (2007). Measuring Incident Radiant Heat Flux Using the Plate Thermometer. *Fire Safety Journal*, **42**, 161–166.

Jolly, S. and Saito, K. (1992). Scale Modeling of Fires with Emphasis on Room Flashover Phenomenon. *Fire Safety Journal*, **18**, 139–182.

Koseki, H. (1989). Combustion Properties of Large Liquid Pool Fires. *Fire Technology*, **25**, 241–255.

Koseki, J.A., Gritzo, L.A., Kent, L.A. and Wix, S.D. (1996). Actively Cooled Calorimeter Measurements and Environment Characterization in a Large Pool Fire. *Fire and Materials*, **20**, 69–78.

Kramer, M.A., Greiner, M., Koski, J.A., Lopez, C. and Suo-Anttila, A. (2003). Measurements of Heat Transfer to a Massive Cylindrical Calorimeter Engulfed in a Circular Pool Fire. *Journal of Heat Transfer*, **125**, 21–40.

Kuo, C.H. and Kulkarni, A.K. (1991). Analysis of Heat Flux Measurement by Circular Foil Gages in a Mixed Convection/Radiation Environment. *Journal of Heat Transfer*, **113**, 1037–1040.

Lam, C.S. and Weckman, E.J. (2009). Steady-State Heat Flux Measurements in Radiative and Mixed RadiativeConvective Environments. *Fire and Materials*, **33**, 303–321.

Lin, C., Ferng, Y. and Hsu, W. (2010). Investigations on the Characteristics of Radiative Heat Transfer in Liquid Pool Fires. *Fire Technology*, **46**, 321–345.

Logenbaugh, R.S., Sanchez, L.C. and Mahoney, A.R. (1990). Thermal Response of A Small Scale Cask-Like Test Article to Three Different High Temperature Environments. *Sandia National Laboratories Report to Federal Rail Administration*, DOT/FRA/ORD-90/01.

Luo, M. (1997). Effects of Radiation on Temperature Measurement in a Fire Environment. *Journal of Fire Sciences*, **15**, 443–461.

Ma, T. and Quintiere, J. (2003). Numerical Simulation of Axi-Symmetric Fire Plumes: Accuracy and Limitations. *Journal of Fire Safety*, **38**, 467–492.

McCaffrey, B.J. (1979). *Purely Buoyant Diffusion Flames: Some Experimental Results*. Center for Fire Research, NBS.

McCaffrey, B.J. and Heskestad, G. (1976a). A Robust Bidirectional Low-Velocity Probe for Flame and Fire Application. *Combustion and Flame*, **26**, 125–127.

McCaffrey, B.J. and Heskestad, G. (1976b). A Robust Bidirectional Low-Velocity Probe for Flame and Fire Application. *Combustion and Flame*, **26**, 125–127.

McGrattan, K. and Klein, B. (2007). Fire Dynamics Simulator (version 5) User's Guide. *National Institute of Standards and Technology Special Publication*, **1019-5**.

McGrattan, K., Hostikka, S. and Klein, B. (2007). *Fire Dynamics Simulator (Version 5) User's Guide*. U S Government Printing Office, Washington.

Mishra, K.B. (2010). *Experimental Investigation and CFD Simulation of Organic Peroxide Pool Fires (TBPB and TBPEH)*. Ph.D. thesis, University of Duisburg-Essen.

Mishra, K.B. and Wehrstedt, K. (2011). Interpretations of Temperature Measurements in Organic Peroxide Pool Fires. *5th European Combustion Meeting 2011 -ECM- (Proceedings)*, 1–5.

Mishra, K.B. and Wehrstedt, K. (2012). Decomposition Effects on the Mass Burning Rate of Organic Peroxide Pool Fires. *Journal of Loss Prevention in the Process Industries*, **25**, 224–226.

Modest, M.F. (2003). *Radiative Heat Transfer*. Chemical, Petrochemical & Process, Academic Press.

Montes, C.G., Rojas, E.S., Viedma, A. and Rein, G. (2009). Experimental Data and Numerical Modelling of 1 3 and 2 3 MW Fires in a 20 m Cunic Atrium. *Building and Environment*, **44**, 1827–1839.

Moorhouse, J. and Pritchard, M. (1982). Thermal Radiation Hazards from Large Pool Fires and Fireballs. *A Literature Review, I Chem Symp* , **71**, 123–125.

Motlagh, A.H.A. and Hashemabadi, S.H. (2008). CFD Based Evaluation of Heat Transfer Coefficient from Cylindrical Particles. *International Communications in Heat and Mass Transfer*, **35**, 674–680.

Muñoz, M., Arnaldos, J., Casal, J. and Planas, E. (2004). Analysis of the Geometric and Radiative Characteristics of Hydrocarbon Pool Fires. *Combustion and Flame*, **139**, 263–277.

Muñoz, M., Planas, E., Ferrero, F. and Casal, J. (2007). Predicting the Emissive Power of Hydrocarbon Pool Fires. *Journal of Hazardous Materials*, **144**, 725–729.

Mukta, G. (2011). Jaipur Fire and its Environmental Effects. In *12th Esri India User Conference*, New Delhi, India.

Mukunda, H.S. (2009). *Understanding Combustion 2nd Edition*. Orient Blackwan.

Mulholland, G.P., Gupta, B.P. and San, M.R.L. (1975). Inverse Problem of Heat Conduction in Composite Media. *ASME Paper*, **75-WA/HT-83**.

Nakos, J.T. (2005). Uncertainty Analysis of Steady-State Incident Heat Flux Measurements in Hydrocarbon Fuel Fires. SAND2005-7144.

Nakos, J.T. (2010). Description of Heat Flux Measurement Methods Used in Hydrocarbon and Propellant Fuel Fires at Sandia. *Sandia National Laboratories*, SAND2010-7062.

Nakos, J.T. and Keltner, N.R. (1989). The Radiation-Convective Partitioning of Heat Transfer to Structures in Large Pool Fires. *Sandia National Laboratories*, **106**, 381–387.

Ojha, M., Dhiman, A.K. and Guha, K.C. (2012). Simulation of Thermally Protected Cylindrical Container Engulfed in Fire. *Journal of Loss Prevention in the Process Industries*, **25**, 391–399.

Parag, S. and Raghavan, V. (2009). Experimental Investigation of Burning Rates of Pure Ethanol and Ethanol Blended Fuels. *Combustion and Flame*, **156**, 997–1005.

Portscht, R. (1975). Studies on Characteristic Fluctuations of the Flame Radiation Emitted by Fires. *Combustion Science and Technology*, **10**, 73–84.

Qian, C. (1995). *Flame Spread Over Vertical Corner Walls*. Ph.D. thesis, Department of Mechanical Engineering, University of Kentucky, Lexington.

Qian, C. and Saito, K. (1995). Measurements of Pool-Fire Temperature Using IR Technique. In *Gore JP (ed) Joint Technical Meeting Proceedings, Combusion Fundamentals and Applications*, 81–86, San Antonio, TX.

Qian, C., Ishida, H. and Saito, K. (1994). Upward Flame Spread along PMMA Vertical Corner Walls Part II: Mechanism of "M" Shape Pyrolysis Front Formation. *Combustion and Flame*, **99**, 331–338.

Quintiere, J.G. (1998). *Principles of Fire Behavior*. Career Education Series, Delmar.

Rashbash, D.J., Rogowski, Z.W. and Stark, G.W.V. (1956). Properties of Fires of Liquids. *Fuel*, **35**, 94–107.

Rempe, J.L. and Knudson, D.L. (2008). High Temperature Thermal Properties for Metals Used in LWR Vessels. *Journal of Nuclear Materials*, **372**, 350–357.

Rew, P.J., Hulbert, W.G. and Deaves, D.M. (1997). Modelling of Thermal Radiation from External Hydrocarbon Pool Fires. *Process Safety and Environmental Protection*, **75**, 81–89.

Saito, K. and Emori, R.I. (1980). Theoretical Prediction for the Applicable Range of Scaling Laws on Tank Fire Model Experiment. In *Fifth Joint Meeting US-Japan Panel on Fire Research and Safety, UJNR*, Washington, DC.

Sandia (2013). How SAFE are Radioactive Material Packages? http://wwwsandiagov/tp/SAFE_RAM/WHATHTM.

Schälike, S., Wehrstedt, K. and Schönbucher, A. (2012). Flame Heights of Di-tert-butyl Peroxide Pool Fires - Experimental Study and Modelling. *Chemical Engineering Transactions*, **26**, 363–368.

Schneider, M.E. and Kent, L.A. (1989). Measurements of Gas Velocities and Temperatures in a Large Open Pool Fire. *Fire Technology*, **25**, 51–80.

Seo, D., Jung, S., L, S.J., Feng, Z.C., Chen, J.K. and Yuwen, Z. (2011). Fabrication and Electrical Properties of Polymer Derived Ceramic (PDC) Thin Films for High Temperature Heat Flux Sensors. *Sensors and Actuators A: Physical*, **165**, 250–255.

SFPE (2008). *SFPE Handbook of Fire Protection*. 4 Edition, National Fire Protection Association.

Sibulkin, M. and Hansen, A.G. (1975). Experimental Study of Flame Spreading over a Horizontal Fuel Surface. *Combustion Science and Technology*, **10**, 85–92.

Siegel, R. and Howell, J.R. (2002). *Thermal Radiation Heat Transfer*. Taylor & Francis Group.

Silvani, X. and Morandini, F. (2008). Fire Spread Experiments in the Field: Temperature and Heat Fluxes Measurements. *Fire Safety Journal*, **44**, 279–285.

Stolz, G. (1960). Numerical Solutions to an Inverse Problem of Heat Conduction for Simple Shapes. *Journal of Heat Transfer*, **82**, 20–26.

Tewarson, A. (2004). Combustion Efficiency and Its Radiative Component. *Fire Safety Journal*, **39**, 131–141.

Tunc, M. and Venart, J.E.S. (1984). Incident Radiation from an Engulfing Pool Fire to a Horizontal Cylinder – Part I. *Fire Safety Journal*, **8**, 81–87.

Wen, J.X., Kang, K.T., Donchev, T. and Karwatazki, J.M. (2007). Validation of FDS for the Prediction of Medium-Scale Pool Fires. *Fire Safety Journal*, **42**, 127–138.

Wickström, U. (1994). The Plate Thermometer-A Simple Instrument for Reaching Harmonized Fire Resistance Tests. *Fire Technology*, **30**, 195–208.

Wickström, U., Robbins, A. and Baker, G. (2011). The Use of Adiabatic Surface Temperature to Design Structures For Fire Exposure. *Journal of Structural Engineering*, **2**, 21–28.

Williams, S.D. and Curry, D.M. (1977). An Analytical Experimental Study for Surface Heat Flux Determination. *Journal of Spacecraft*, **15**, 632–637.

Xin, Y., Rehm, R. and Gore, J. (2005). Fire Dynamics Simulation of a Turbulent Buoyant Flame Using a Mixture-Fraction-Based Combustion Model. *Combustion and Flame*, **141**, 329–335.

Xin, Y., Filatyev, S.A., Biswas, K., Gore, J.P., Rehm, R.G. and Baum, H.R. (2008). Fire Dynamics Simulations of A One-Meter Diameter Methane Fire. *Combustion and Flame*, **153**, 499–509.

Yang, J.C., Hamins, A. and T, K. (1994). Estimate of the Effect of Scale on Radiative Heat Loss Fraction and Combustion Efficiency. *Combustion Science and Technology*, **96**, 183–188.

Zarate, J., Arnaldos, J. and Casal, J. (2008). Establishing Safety Distances for Wildland Fires. *Fire Safety*, **43**, 565–575.

Zhang, J., Dembele, S. and Wen, J. (2009). Investigation of Turbulence Models for CFD Simulations of Gas and Liquid Pool Fires. *Journal of Fire Sciences*, **27**, 157–182.

List of Publications and Patents

Journal Papers

1. Sudheer, S. and Prabhu, S.V. (2013). Heat Transfer in Vertical Casks Engulfed in Open Pool Fires. *Journal of Fire Sciences* (Accepted).

2. Sudheer, S., Desai, S. and Prabhu, S.V. (2012). Physical Experiments and Fire Dynamic Simulations on Gasoline Pool Fires. *Journal of Fire Sciences* (Accepted).

3. Sudheer, S. and Prabhu, S.V. (2012). Characterization of Hexane Pool Fires using Infrared Thermography. *Journal of Fire Sciences*, **31**, 143-165.

4. Sudheer, S. and Prabhu, S.V. (2012). Measurement of Flame Emissivity of Hydrocarbon Pool Fires. *Fire Technology*, **48**, 183-217.

5. Sudheer, S. and Prabhu, S.V. (2010). Measurement of flame emissivity of gasoline pool fires. *Nuclear Engineering and Design*, **240**, 3474-3480.

6. Saket, S., Sumeet, S., Sudheer, S. and Prabhu, S.V. Performance of intumescent coatings in cone calorimeter and open pool fire (Under review).

7. Sudheer, S. and Prabhu, S.V. Fire Safety Distances for Open Pool Fires (Under review).

8. Reddy, V.M., Sudheer, S., Prabhu, S.V. and Kumar, S. Design of a Probe for Measuring Radiative Heat Flux of Combustion Systems (Under review).

9. Sudheer, S. and Prabhu, S.V. Investigations to determine the Heat Flux to an Object Engulfed in Diesel Pool Fires (Under review).

Conferences Papers

1. Sudheer, S. and Prabhu, S.V. (2012) Thermal Interaction Between A Circular Pipe And Diesel Pool Fire. *ASME 2012 International Mechanical Engineering Congress and Exposition*, Houston, USA (Presented).

2. Sudheer, S. and Prabhu, S.V. (2011) Behavior of Small Lumped Bodies Immersed in Diesel Pool Fire. *Fire Science & Technology - Research and it's Implementation*, CBRI, Roorkee, 266-276 (Presented).

3. Sumeet, S., Saket, S., Sudheer, S. and Prabhu, S.V. (2011) Influence of External Heat Flux and Coating Thickness of Intumescent Coatings on the Fire Resistance to Stainless Steel. *Fire Science & Technology - Research and it's Implementation*, CBRI, Roorkee, 67-76.

4. Sudheer, S. and Prabhu, S.V. (2010) Characterization of Hexane Pool Fires using Infrared Thermography. *Eighth Asia-Pacific Conference on Combustion*, Hyderabad, 674-681 (Presented).

5. Desai, S., Sudheer, S. and Prabhu, S.V. (2010) Fire Dynamic Simulations and Physical Experiments on Gasoline Open Pool Fires. *Eighth Asia-Pacific Conference on Combustion*, Hyderabad, 689-696 (Presented).

6. Sudheer, S. and Prabhu, S.V. (2010) Measurement of Emissivity of Small Diameter Open Pool Fires Using Infrared Thermography. *Proceedings of the 20^{th} National and 9^{th} International*, ISHMT-ASME Heat and Mass Transfer Conference, Mumbai (Presented).

Patents

1. Reddy, V.M., Sudheer, S., Prabhu, S.V. and Kumar, S. Design of a Probe for Measuring Radiative Heat Flux of Combustion Systems (In Process).

Acknowledgments

"*...may the LORD reward you for your kindness... to me.*" -Ruth 1:8

Throughout this adventure, I felt as if *I was only chasing the moments of fire that were already predefined meticulously by Someone.* I am thankful to that **Marvelous Creator** for encouraging me in accomplishing this thesis.

A best teacher would invigorate the passion of a student. My deep sense of gratitude and profound thanks to my supervisor **Prof. S.V. Prabhu**, for his valuable guidance, patience, encouragement and the freedom given to me in carrying out research. Throughout my PhD tenure, he is always approachable and helpful. Discipline has been put as our first priority and this played a vital role in the success of this thesis.

"Plans fail for lack of counsel, but with many advisers they succeed" Prov. 15:22. I express my heartfelt gratitude to my Research Progress Committee members, Prof. R.P. Vedula, Prof. K.N. Iyer and Prof. A.K. Sridharan for their evaluation and support in my work. The staff of the laboratory and in particular Mr. Prakash, Mr. Raju and Mr. C.V. Jakka who contributed enormously to the experimental part of this project and might be responsible for the timely availability of the instrumentation and completion of the experimental part of this dissertation. I would like to thank, Bhabha Atomic Research Center, for funding the entire project. Also, I would like to thank Mr. B. Klein of Thunder head engineering, USA for providing free licenses for the PYROSIM which is preprocessor to the FDS.

Life in metropolitan city of Mumbai became homely and friendly. It is a great pleasure to thank my friends in the lab: Mr. Lokendra, Mr. S. Desai, Mr. S. Saketh, Mr. A. Venugopal, Mr. V.M. Reddy and Mr. J. Manish. Their creation of joyful atmosphere has made my progress well. I thank Mr. Timothy, Mr. S. Madhu, Mr. B. Anil, Mr. P. Prajish, Mr. J. Rajesh and Mr. H. John for their continual fellowship. I thank everyone in *IITBCF*, *CAP* and *PP* for giving me such a godly fellowship. I also thank all the elders who were available for any kind of advise and counseling: Rev. Dr. C. Cecil, Ps. P. Lonnie, Prof. J. John, Prof. T.V. Mathew, Prof. J. Sameer and Mr. K. Viswas. Especially, I thank Mr. Solomon for giving me opportunities in helping some of the children of this great city.

A big $\mathcal{THANK\ YOU}$ to my parents and my brother's family for their love and care.

S Sudheer